

Solar Flare Induced Power Variation of Oscillations Around an Active Region.

By

Teresa Antoinette Monsue

Dissertation

Submitted to the Faculty of the
Graduate School of Vanderbilt University
in partial fulfillment of the requirements

for the degree of

DOCTOR OF PHILOSOPHY

in

PHYSICS

December 15, 2018

Nashville, Tennessee

Approved:

William Dean Pesnell, Ph.D.

Professor Andreas Berlind, Ph.D.

Frank Hill, Ph.D.

David J. Ernst, Ph.D.

David A. Weintraub, Ph.D.

*Copyright © 2018 by Teresa Antoinette Monsue
All Rights Reserved*

*This work is dedicated to my dear mother.
A woman whom I had the greatest privilege to know in my life.
Who later was not only a mother to me but became my best friend.
She taught me how to be independent, strong and able to fight adversity with the greatest
attitude.*

ACKNOWLEDGMENTS

There is an African proverb that says; “*it takes a village to raise a child*”, and I made a profound discovery that it also takes a village to produce a doctoral scholar. During the past seven and a half years this village has offered me mentoring or scholarly training through their various areas of expertise. My scientific village comprised of teachers, mentors, post-docs, administrators, fellow graduate students and family. There are several individuals who contributed in some way to this dissertation, to whom I would like to express my sincere gratitude and appreciation.

First and foremost, Dr. William Dean Pesnell, my research advisor at NASA GSFC, for his crucial role in transforming my mind in order to grasp the fundamentals of Heliophysics. It is with great appreciation and respect that I was afforded the opportunity to work with such a great mind.

I owe deep gratitude to Dr. Frank Hill, Associate Director at the National Solar Observatory, for his introduction and guidance into the field of Helioseismology and in developing the solar physics project that evolved from my Masters Thesis. It has been an interesting journey of challenge and discovery.

A very special thank you and appreciation for a mentor and advisor who had my interest at heart, Dr. Andreas Berlind. Many years ago he introduced me to the Solar Dynamics Observatory at NASA. And now, in hindsight, one of life’s grand ironies has me working with SDO’s Principal Investigator, Dr. William Dean Pesnell!

My warm and sincere thanks to Dr. David Ernst for sharing his wisdom, experience and personal guidance with me through the years. He has a wonderful way of putting things in perspective through his stories.

Thanks Dr. David Weintraub for serving on my committee and believing in my potential to carry this work to its completion. Very much appreciated!

Additionally, I would like to send a special thank you to Dr. Carolyn Ng, in the He-

liophysics Science Division at NASA GSFC. Through your actions you have greatly contributed to the positive karmic outcome of my graduate career. Bless you!

I would also like to thank the postdocs and those who worked with me along my journey and provided me with the skills I need to pursue this field. Thank you Dr. Michael Kirk at NASA GSFC. Thanks to Dr. Nathan DeLee, a past postdoc, who contributed by his guidance towards my Master's Thesis work that eventually evolved into my dissertation. My sincere thanks to Dr. Rudolfo Montez for his coding assistance, his moral support and steadfast encouragement through those challenging times as I struggled through the early days of programming. Thanks to Dr. Keivan Stassun for introducing me to Solar Physics and his vision of diversity – never lose hope in that.

I would like to sincerely thank the major funding contributors over my entire journey such as NASA's Solar Dynamics Observatory (SDO) through Catholic University of America. I would like to deeply thank NASA's Minority University Research and Education Program (MUREP) through their Harriet G. Jenkins Fellowship, a prestigious graduate fellowship awarded to me through the years 2013 to 2017. The Fisk-Vanderbilt Masters-to-Ph.D. Bridge Program in funding me and believing in me to pursue doctoral studies.

I would like to thank my friends who supported me through my tough times. You know who you are.

Last but not least, I would like to thank my family. My little dog Snow, a really small doggie with such an enormous heart. And especially my dear mother, Sheila 'Shanti' Monsue, for her endless love and support. For the unwavering faith she has always had in me, even more so during my doctoral journey. Mom, from the bottom of my heart I thank you and I could not have done this without you. You are my best friend and I thank God for you.

TABLE OF CONTENTS

	Page
DEDICATION	iii
ACKNOWLEDGMENTS	iv
LIST OF TABLES	xi
LIST OF FIGURES	xii
1 Understanding Helioseismology	1
1.1 Introduction	1
1.2 Historic Helioseismology	2
1.3 Global Helioseismology	7
1.3.1 p -modes, g -modes and f -modes	7
1.3.2 Wave modes and Power Spectra	9
1.4 Local Helioseismology	14
1.4.1 Data Observations in Local Helioseismology	14
1.4.2 Techniques in Observational Local Helioseismology	17
1.4.2.1 Fourier-Hankel Method	17
1.4.2.2 Ring-diagram Analysis	17
1.4.2.3 Time-distance Helioseismology	19
1.4.2.4 Helioseismic Holography	20
1.4.2.5 Direct Modeling	20
1.5 Oscillatory Waves Around Active Regions	21
1.5.1 The significance of p -modes from the Surface to the Chromosphere	21
1.5.2 Magnetic Flux Emergence	22

1.5.3	Acoustic power around solar active regions	24
1.5.4	Excitation of p-modes by solar flares	25
1.6	Advances in Helioseismic Wave Response From Solar Flares	30
1.6.1	Sunquakes	30
1.6.2	Magnetohydrodynamic Waves around Sunspots and in the Solar At- mosphere	31
1.7	Introduction to the Dissertation	34
2	Methodology: GONG	36
2.1	Part I: GONG Methodology	36
2.1.1	Experimental Research Purpose	36
2.1.2	GONG Data Set	36
2.1.3	Data Analysis Utilizing the Interactive Data Language (IDL) and the FFT	38
2.1.4	Candidate Selection	39
2.2	Part I: Data Analysis – IDL Code Stages	42
2.2.1	Stage 1 – Extract pixel information	43
2.2.2	Stage 2 – Correction on missing frames	47
2.2.3	Stages 3 and 4 – Power Map Movie wrapper	48
2.2.4	Stage 5 – Periodograms	50
3	Temporal Evolution of Chromospheric Oscillations in Flaring Regions – A Pilot Study	51
3.1	Introduction	51
3.2	Observational Data	53
3.3	Data Analysis and Reduction Methods	57
3.4	Results	61
3.4.1	AR3	61

3.4.1.1	Inner Flaring Regions – <i>Locations 3, 4, and 7 in AR3</i>	63
3.4.1.2	Outer Flaring Regions – <i>Locations 2 and 5 in AR3</i>	65
3.4.1.3	Quiescent Regions – <i>Locations 1 and 6 in AR3</i>	67
3.4.2	AR1	69
3.4.3	AR2	73
3.5	Discussion and Conclusions	77
4	Methodology: AIA Image Processing	81
4.1	Data Acquisition (JSOC) - <i>A Step-by-Step Tutorial</i>	82
4.2	Stage 1 Image Processing - Uncompressing and Dividing by the Image Exposure Time	93
4.3	Stage 2 Image Processing - Linear Interpolation on Missing Frames	95
4.4	Stage 3 Image Processing - Creating Superpixel Images	102
4.5	Stage 4 Image Processing - Image Average Subtraction	103
5	Methodology: higher resolution, higher cadence images (SDO data)	107
5.1	Power Map Movies of SDO AIA 1700 Å, 1600 Å and 304 Å	107
5.2	Random Sampling Method	109
5.2.1	Data Analysis Procedure	109
5.2.2	Results: Random Sampling Method	111
5.3	Triangulation Tracking of a Radially Propagating MHD Wave in the AIA 1600 Acoustic Power Maps in Active Region 12193	115
5.3.1	Results: Additional Areas for Triangulation Tracking	118
5.4	Caveats and lessons learned from previous methods	121
6	Methodology: Sector Sampling Method Around Active Region AR12192	123
6.1	Sector Sampling Concept Philosophy	123
6.2	Windowing or Apodization on Time Series	131
6.2.1	Windowing and the Uncertainty Principle	131

6.2.2	Window Functions	134
6.3	Data Analysis Procedures	143
6.3.1	Creating sector time series data (in IDL)	143
6.3.2	Running the FFT on sector time series (in Python)	147
6.4	Results: Sector Sampling Method	153
6.4.1	Sector Sampling Method Interpretations	153
6.4.2	Sector Sampling Method - Multi-wavelength Annular Sampling	161
6.5	Results: Time-Distance Helioseismology Measurements on AR12192	170
7	Conclusion	177
Appendix A Scientific and Mathematical Background		179
A.1	Wave Fundamentals	179
A.1.1	Fundamentals – the Anatomy of a Wave	179
A.1.2	Spherical Harmonics and Eigenvalues	180
A.2	Time Series Data Techniques	182
A.2.1	Fourier analysis and the classical Fourier transform	183
A.2.2	The Discrete Spectrum and the FFT	187
A.3	Linearity of the FFT	188
Appendix B Mathematical Formulas and Proofs		189
B.1	Euler’s equation and the Fourier Transform	189
B.2	Laplace’s Equation and Conformal Mapping (Proof)	191
B.3	Heisenberg’s Uncertainty Principle and the Fourier Transform	196
Appendix C Important Procedures		199
C.1	Normalizing IDL’s FFT to Python’s Numpy FFT procedure	199
C.1.1	FFT Normalization	199
C.1.2	IDL Normalization	199

C.1.3 Numpy Normalization	200
BIBLIOGRAPHY	201

LIST OF TABLES

Table	Page
1.1 AIA wavelength bands (LMSAL-AIA, 2010).	16
3.1 Table of observational information of the three data sets.	56
A.1 Harmonic order of the fundamental frequency, nodes and anti-nodes of dif- ferent order standing waves	180

LIST OF FIGURES

Figure	Page
1.1 First observations of velocity fields by Leighton <i>et al.</i> in 1962	4
1.2 Supported evidence to Leighton <i>et al.</i> (1962a) by Evans and Michard (1962)	5
1.3 Predictions made by Ulrich (1970) and then confirmed by Deubner (1975) .	6
1.4 Theoretical frequencies of solar oscillations (p-modes, g-modes and f-modes)	9
1.5 $\ell - \nu$ diagrams obtained as an azimuthal average of the three-dimensional power spectra from the Solar Oscillations Investigation (SOI) and the Taiwan Oscillation Network (TON).	11
1.6 Solar Power Spectrum of the South Pole campaign (1994) and from SOHO MDI (1996).	12
1.7 Power Spectral Density (PSD) function for low-degree solar oscillations . .	13
1.8 The ring-diagram analysis.	19
1.9 Transportation of energy by magnetic flux tubes within active regions . . .	23
1.10 Photospheric and chromospheric LOS velocity power spectra in the observed plage region.	24
1.11 First observation of helioseismic waves produced by a flare.	26
1.12 The correlation of solar flares flux with p-mode oscillation power.	28

1.13 MDI and GOLF data taken of an X17.6 flare on October 28, 2003	29
1.14 Observations of sunquakes from two solar flares. X3-class on 16-July-2004 and X1-class flare on 15-January-2005.	31
2.1 GONG Network Detectors	37
2.2 GONG H α Network.	37
2.3 Fulldisk location on candidate selection	40
2.4 GONG image quality	42
2.5 Power Map Movies creation diagram.	43
2.6 Stage 1 flowchart	45
2.7 GONG file processing order.	46
2.8 Plots for each corresponding pixel text file written out in the 1_PLOTDIR directory.	46
2.9 Stage 2 flowchart	48
2.10 Stage 3 and 4 flowchart	50
3.1 GONG H α image of AR11504, Region of Interests AR1 and AR2, 13 June 2012	55
3.2 GONG H α image of AR11520, Region of Interests AR3, 12 July 2012 . . .	57

3.3	Individual PMM frames of each binned frequency band of the X1.4 flare on 2012 July 12 in region AR3	60
3.4	AR3 ROI with eight sampled subregions	62
3.5	Time-frequency power plots of three subregions AR3_3, AR3_4, and AR3_7 with the corresponding average intensity and <i>GOES</i> X-ray flux	64
3.6	Time-frequency power plots of two subregions AR3_2 and AR3_5 with the corresponding average intensity and <i>GOES</i> X-ray flux	66
3.7	Time-frequency power plots of the two quiescent subregions AR3_1 and AR3_6 with the corresponding average intensity and <i>GOES</i> X-ray flux	68
3.8	AR1 ROI with seven sampled subregions	70
3.9	Time-frequency power plots of three subregions AR1_5, AR1_6, and AR1_7 with the corresponding average intensity and <i>GOES</i> X-ray flux	72
3.10	AR2 ROI with six sampled subregions	74
3.11	Time-frequency power plots of three subregions AR2_3, AR2_4, and AR2_5 (a quiet region) with the corresponding average intensity and <i>GOES</i> X-ray flux	76
4.1	Huge sunspot group AR12192 in 1700 Å, 1600 Å and 304 Å wavelengths	82
4.2	JSOC Lookdata site window.	84
4.3	JSOC Series Select Tab Window.	86

4.4	JSOC RecordSet Select window.	88
4.5	JSOC Values Display window.	89
4.6	JSOC Export Data window.	90
4.7	JSOC Data Export Request Generation window.	91
4.8	JSOC <i>im_patch</i> field for image processing for cutouts.	93
4.9	Uncompressed AIA image files for each AIA analyzed wavelength.	95
4.10	Stage 1 image processing images are placed in the C1IMAGES directory.	96
4.11	Linear interpolation illustration. Case for three missing images.	98
4.12	Linear interpolation done on three missing frames within the time series.	100
4.13	Stage 2 image processing images are placed in the C12IMAGES directory.	101
4.14	Stage 3 image processing images are placed in the C123CoIMAGES directory.	103
4.15	Stage 4 image processing images are placed in the C1234CoIMAGES directory.	105
4.16	AIA image processing flowchart.	106
5.1	PMM enhancement seen in the AIA 304 Å wavelength Power Map Movies.	109
5.2	Three sampled regions around and X3 flare in AR12192.	111
5.3	Multi-wavelength image of AR12192 at sample R1.	112

5.4	Multi-wavelength image of AR12192 at sample R2.	113
5.5	Multi-wavelength image of AR12192 at sample R3.	114
5.6	(Left) PMM frame (the region is measured in power) in the 2–3 mHz band, windowed at 30–90 minutes. (Right) Spectrogram plots of corresponding regions, A1, A3, O3, O1, MA12 and MA13.	117
5.7	Additional sampled regions for the three vertices A1, A2 and A3 and their corresponding midpoints MA12, MA23, MA13.	119
5.8	Additional sampled regions for the three vertices O1, O2 and O3 and the corresponding midpoints MA12, MA23, MA13.	120
6.1	Conformal mapping preserves the angles on different coordinate systems. .	126
6.2	Sector sampling method.	128
6.3	The distance between the radii in the sector sampling will vary therefore conserving the value of the pixels contained in each sector region.	129
6.4	The Uncertainty Principle in Windowing	133
6.5	Periodic signal function $x(t)$ with discontinuities	135
6.6	Rectangular window function (Boxcar).	136
6.7	Hanning (raised cosine) window function.	137
6.8	Cosine taper window (Tukey) function.	138
6.9	Frequency response of window functions.	140

6.10 Window Functions	142
6.11 Sector sampling area map for the 304 Å	147
6.12 Spectrogram for sector region A1 in the 1600 Å wavelength.	152
6.13 1600 Å sector region A, where the sampling was taken between $0^\circ \leq \theta \leq 45^\circ$.156	
6.14 1600 Å sector annulus 1 sampling.	158
6.15 Multi-wavelength region E1 in AIA 1700 Å, 1600 Å, 304 Å	160
6.16 Multi-wavelength region C0 in AIA 1700 Å, 1600 Å, 304 Å	161
6.17 Multi-wavelength Annulus 0 (1700 Å (lower photosphere), 1600 Å (upper photosphere), 304 Å (chromosphere)).	163
6.18 Multi-wavelength Annulus 1 (1700 Å (lower photosphere), 1600 Å (upper photosphere), 304 Å (chromosphere)).	164
6.19 Multi-wavelength Annulus 2 (1700 Å (lower photosphere), 1600 Å (upper photosphere), 304 Å (chromosphere)).	165
6.20 Multi-wavelength Annulus 3 (1700 Å (lower photosphere), 1600 Å (upper photosphere), 304 Å (chromosphere)).	166
6.21 Multi-wavelength Annulus 4 (1700 Å (lower photosphere), 1600 Å (upper photosphere), 304 Å (chromosphere)).	167
6.22 Multi-wavelength Annulus 5 (1700 Å (lower photosphere), 1600 Å (upper photosphere), 304 Å (chromosphere)).	168

6.23	Multi-wavelength Annulus 6 (1700 Å (lower photosphere), 1600 Å (upper photosphere), 304 Å (chromosphere)).	169
6.24	Time-distance plot between $315^\circ \leq \theta \leq 320^\circ$	172
6.25	Time-distance plot between $225^\circ \leq \theta \leq 230^\circ$	174
6.26	Time-distance plot between $90^\circ \leq \theta \leq 95^\circ$	176
A.2	Contour plots for the real part of spherical harmonics $Y_\ell^m(\theta, \phi)$ projected on the solar disk.	185
B.1	Conformal mapping and Laplace's equation.	191

Chapter 1

Understanding Helioseismology

1.1 Introduction

Our nearest star, the Sun, is a chaotic dynamic system affecting the entire Solar System. Space weather is a concern for our society which depends almost entirely on technology. Solar flares can affect spacecraft, cause surges in the electrical power grid and inhibit satellite and telecommunications (Lindsey and Braun, 2000b). It is important for us to understand such a chaotic system for us to be able to create more flare predictive models. Helioseismology helps us understand this system. Helioseismology is the study of how waves propagate around and within the Sun. These waves bounce around the interior of the Sun, helping scientists understand how they interact with surface structures and the solar atmosphere. There are three types of wave modes: p, g, and f-modes. P-modes, also known as acoustic modes, are predominantly driven by pressure fluctuations in the photosphere originating from the turbulent convective flows deep below. Once these waves reach the photosphere they reflect off the surface where the density and pressure rapidly decrease. Some of those waves become trapped and are refracted back below the surface where the temperature is much higher, causing an increase in the velocity and then traveling back to the surface. These trapped waves make the Sun vibrate in millions of different modes. These waves travel up to the surface and vary by their velocity as they travel throughout the Sun. P-modes are found within the frequency range of $1.0 < \nu < 8.0$ mHz with most modes occurring in the 3.33 mHz ($=3300 \mu\text{Hz}$) or a period of 5 minutes. They can live for a few hours to months and so far, millions of p-modes have been identified and characterized (Christensen-Dalsgaard, 2003).

1.2 Historic Helioseismology

The goal of helioseismology is to investigate the solar interior, surface structures and atmospheric wave propagation by understanding the properties of these acoustic oscillations. The field of helioseismology has largely been driven by observations (Christensen-Dalsgaard, 2002). The origins of helioseismology began with first indications of solar oscillation detection in the early 1900s through ground based observations by Plaskett in 1916 and the roots of seismology detection on Earth. Plaskett (1916) first observed fluctuations on the solar surface by Doppler velocity measurements of the solar rotation rate. Plaskett noted that the changes in variations took three forms: (1) rapid changes within a day; (2) slower changes, extending over several weeks; and (3) a secular change in variation from 1913 to 1916. However, it was not clear whether the fluctuations were solar in nature or they were induced by atmospheric distortion of light scattered in the Earth's atmosphere and in the telescope. Meanwhile in the 1930s, Pekeris blended work with Earth seismology and nonradial oscillations on stars would evolve into the field of helioseismology. Pekeris (1939) determined the excitation of propagating waves within the Earth's atmosphere brought on by the Krakatoa eruption of 1883. The solar origin of fluctuations observed by Plaskett (1916) was established by Hart (1954, 1956) through line-of-sight spectral velocity measurements of the equatorial photosphere taken near the limb of the Sun between October 1950 through June 1952 and in May 1953. Hart concluded that the atmospheric effects of light scattered in the Earth's atmosphere and in the telescope was negligible. Hart was able to find conclusive proof of the existence of a velocity field through his measurements.

The first definitive observations of the 'velocity field' on the solar surface (see Figure 1.1) were oscillatory in nature by Leighton *et al.* (1962a). The behavior of the velocity field had two distinct classes: large-scale horizontal cellular motions, which they called *supergranulation*, and vertical *quasi-periodic oscillations*. By analyzing early Doppler images, Leighton *et al.* (1962a) established that the velocity fields have a period of around

300 seconds (or 5 minutes), a lifetime of a few seconds and a velocity amplitude of around 0.4 km s^{-1} . Interestingly, Leighton *et al.* (1962a) suggested the potential for utilizing the observed period to probe the properties of the solar atmosphere, such as: the temperature, the vertical temperature gradient, or the mean molecular weight. The observations of Leighton *et al.* (1962a) also led to the detection of convective motion on supergranular scales. Leighton *et al.* (1962a) stated the oscillations might be excited in the Sun's granulation layer, and accounted for a part of the energy transfer from the convection zone into the chromosphere. The detection made by Leighton *et al.* (1962a) was confirmed by Evans and Michard (1962) very near 300 seconds, agreeing with the period of 296 second period first derived by Leighton *et al.* (1962a). Evans and Michard (1962) applied the same autocorrelation procedure to Leighton *et al.* (1962a) spectroheliographic photographs of the velocity field. Evans and Michard (1962) most important complement to Leighton *et al.* (1962) was studying individual oscillatory waves with measured velocities, $(v(t))$, see Figure 1.2) and phase relationships between motions at two different levels or between velocities and granulation (in the continuum or line spectrum) (Kosovichev, 2011).

The physical nature of the oscillations were uncertain during this time. Additionally, the questions on whether the oscillations were acoustic or gravity waves, or if the waves represented traveling or standing waves remained unanswered for almost a decade after the discovery of Leighton *et al.* (1962a) (Kosovichev, 2011). Developing on understanding the nature of the 'velocity fields' and their structure were attempted by such authors as Frazier (1968) through Fourier transforms of the oscillations as a function of position and time. Frazier (1968) found power spectra as a function of wave number and frequency; this in turn showed some localization of power. The 'velocity fields' (see Figure 1.1) were later theorized as trapped standing acoustic waves (or p-modes) at the sub-photospheric layer (Ulrich, 1970; Leibacher and Stein, 1971) and the power output by these waves could be responsible for the processes causing the heating of the chromosphere and the corona (Ulrich, 1970). Measurements done by Deubner (1975) on Doppler velocities of the low pho-

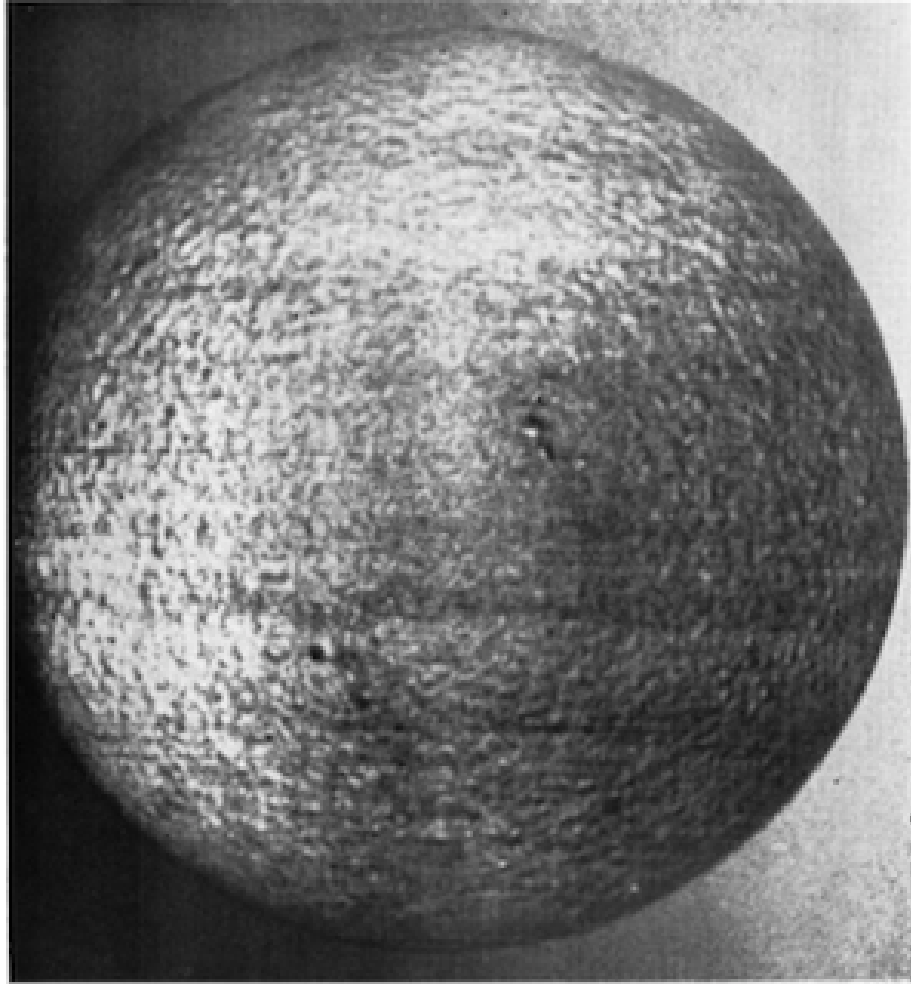


Figure 1.1: Velocity fields, first observed in 1962 from data taken on June 15, 1960, 14h11m U.T., were described as “large cell” of horizontally moving material moving with an outward flow (Leighton *et al.*, 1962a). These velocity fields were later described as standing acoustic waves by (Leibacher and Stein, 1971; Ulrich, 1970).

ospheric CI 5380 line confirmed the theoretical predictions of Ulrich (1970) and Leibacher and Stein (1971); by resolving the lower modes for the five minute oscillations;* confirming the power in the oscillations were concentrated at discrete frequencies for low wavenumber nonradial acoustic eigenmodes (see Figure 1.3).

*The next section on *Global Helioseismology* goes further in explaining the anatomy of the eigenfunction wave modes and power spectra.

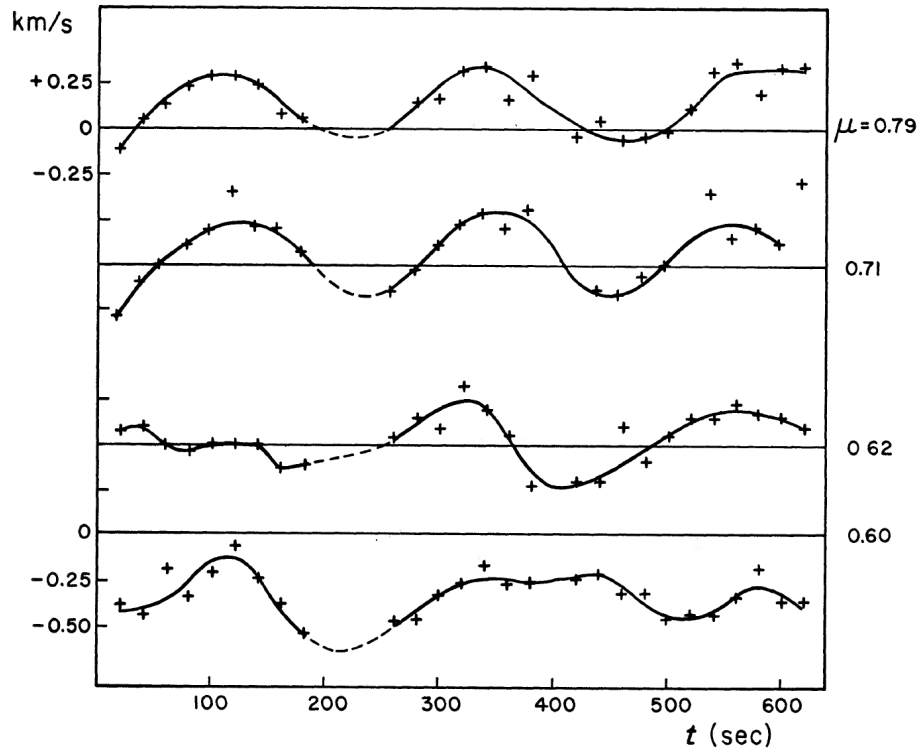


Figure 1.2: Supported evidence to Leighton *et al.* (1962a) by Evans and Michard (1962). A study of individual oscillatory waves with measured velocities. The two clearest ($\mu = 0.79, 0.71$) and the two most doubtful ($\mu = 0.62, 0.60$) oscillating $v(t)$ curves away from the center of the solar disk (Evans and Michard, 1962).

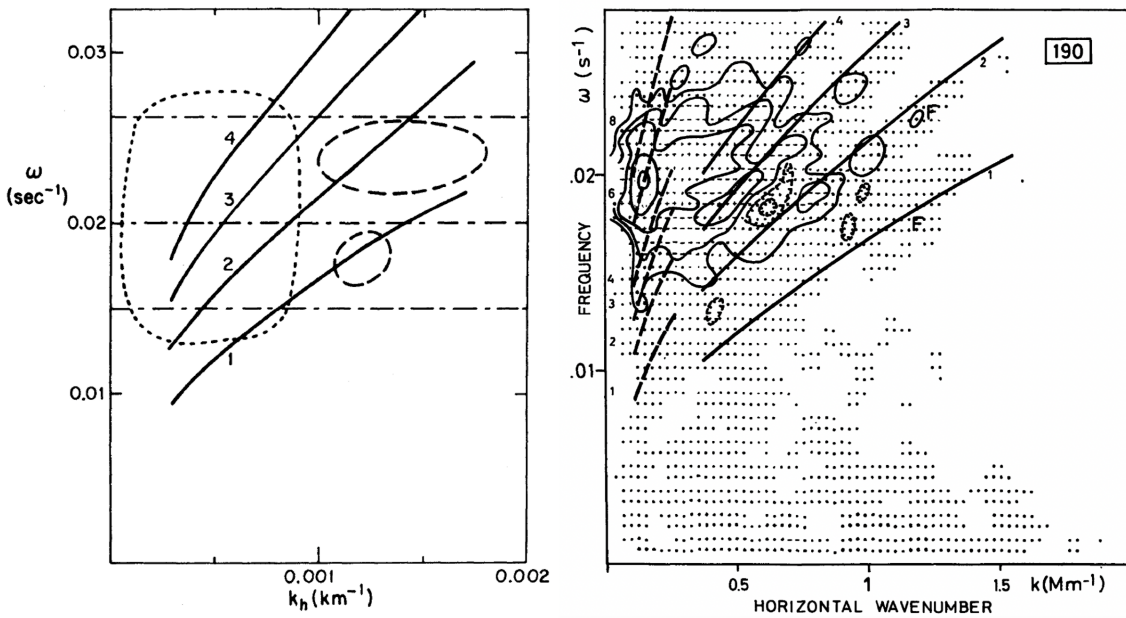


Figure 1.3: The predictions made by Ulrich in 1970 (left) were confirmed by Deubner in 1975 (right).

The next major developmental step in helioseismology was the identification of modal structure in 5-minute oscillations by Claverie *et al.* (1979). Their observations involved 300 hours of Doppler-velocity observations of integrated light over the entire solar disk at two observatories, Izana, on Tenerife, and Pic du Midi in the Pyrenees. In the 5-minute oscillations power spectra, several equally spaced lines corresponding to oscillations in the lower modes were observed. With such observations there is a sensitivity in observing oscillations of the lowest spherical harmonic degree. These types of oscillations of angular degree of $\ell = 0$, $\ell = 1$ and $\ell = 2$ will propagate deeper into the solar structure; therefore providing information about the structure of the solar core.[†] Additionally, Gough (1982) indicated that the small separation was related to the curvature of the sound speed in the solar core, providing further evidence for mixing of material within the solar core. The connection to the gap between the observations of 5-minute oscillations at both low degree and at high wave number was filled by Duvall and Harvey (1983). They made detailed observations of the wave modes at intermediate degrees. This in turn allowed a definite identification of the order of the modes, adding the low degree and by establishing the connection with the high-degree modes in which the order could not be directly determined. There was now complete information of the full range of modes, furthering subsequent observations and opening the opportunities for detailed deductions of the properties of the solar interior, such as the internal solar rotation studied by Duvall *et al.* (1984) and the sound speed by Christensen-Dalsgaard *et al.* (1985) (Kosovichev, 2011).

1.3 Global Helioseismology

1.3.1 p -modes, g -modes and f -modes

The convective currents below the solar surface are thought to be the driving mechanism of solar oscillations. The theoretical spectrum of solar oscillations covers a wide

[†]Further explanation on observing lower modes in the integrated light can be found in section *Wave modes and Power Spectra* under *Global Helioseismology*.

range of frequencies and angular degrees (see Figure 1.4). There are three classifications of solar oscillations in which two classes are of interior oscillations and the third is a special class of surface modes – *acoustic (p) modes*, *surface gravity (f) modes*, and *internal gravity (g) modes*. Sound waves or pressure modes are in essence standing acoustic waves, where the dominant restoring force is *pressure* (rather than buoyancy), hence the name p-modes. All the solar oscillations that are used for inferences about the interior are p-modes, with frequencies between about 1 and 5 mHz. They span angular degrees (ℓ) from $\ell = 0$ (purely radial motion) to $\ell >$ several hundred. Gravity modes are lower-frequency modes that are confined exclusively to the interior. The restoring force is buoyancy and thus indirectly gravity, from which they take their name *g*-modes. *G*-modes are evanescent in the convection zone and therefore have tiny amplitudes at the surface (Appourchaux *et al.*, 2010). No individual *g*-modes have been detected but indirect detections have been claimed (García *et al.*, 2007; Fossat *et al.*, 2017). The lowest frequency ridge ($n = 0$) is for fundamental modes or *f*-modes and are surface gravity waves, analogous to waves on deep water. To good approximation, they follow the same dispersion law: $\omega = gk_h$ where ω is the angular frequency, g is the surface gravity and k_h is the horizontal wavenumber. Surface gravity modes observed on the Sun are all of very high degree ($\ell \geq 80$) (Duvall and Gizon, 2000; Gizon and Birch, 2005).

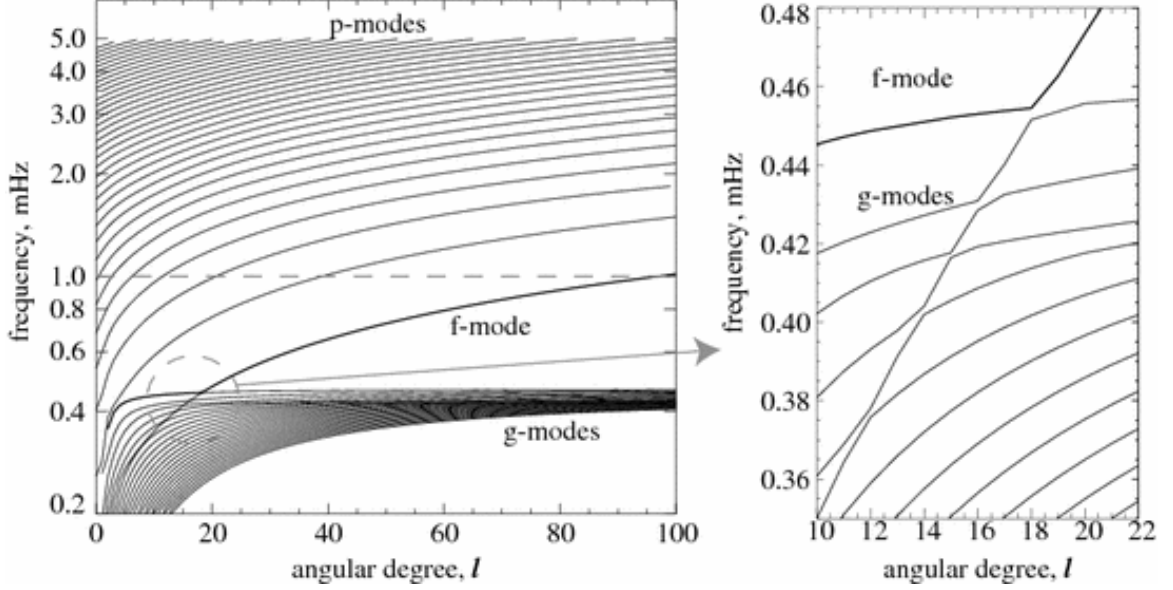


Figure 1.4: (Left) Theoretical frequencies of solar oscillations (p-modes, g-modes and f-modes) by the standard solar model for angular degree ℓ from 0 to 100, and for the frequency range 0.2 mHz to 5 mHz. The dashed gray horizontal line indicates the low-frequency observational limit – only modes above this line have been observed reliably. (Right) The area of the avoided crossing of f-modes and g-modes (indicated by the gray dashed circle in the left panel.) (Kosovichev, 2011).

1.3.2 Wave modes and Power Spectra

Small oscillations of a sphere can be represented by a linear superposition of wave modes or eigenmodes, characterized by a set of three indices: the radial order n , the spherical harmonic degree ℓ , and the azimuthal order m . For example, the radial displacement of a fluid element can be written as:

$$\delta r(r, \theta, \phi, t) = \sum_n \sum_{\ell, m=-\ell}^{\ell} a_{n\ell m} \xi_{n\ell}(r) Y_{\ell}^m(\theta, \phi) e^{i\omega_{n\ell m} t} \quad (1.1)$$

where r is the radius, θ and ϕ are spherical-polar coordinates (colatitude and longitude), and t represents time. The Y_{ℓ}^m are spherical harmonics[‡], $a_{n\ell m}$ is a complex mode amplitude, and $\xi_{n\ell}(r)$ is the radial eigenfunction of the mode with frequency $\omega_{n\ell m}$. The index n corresponds to the number of nodes of the radial eigenfunction, ℓ indicates the total number of

[‡]See Appendix A.1.2 for more details on Spherical Harmonics.

nodal lines on the sphere, and m tells how many of these nodal lines cross the equator. A spherical harmonic star would produce a spectrum of azimuthally degenerate frequencies. However, rotation and other perturbations lift the $(2\ell + 1)$ -fold degeneracy of the frequency of nonradial mode (n, ℓ) . The power spectra of m -averaged solar oscillations are shown in Figures 1.5 and 1.6. Each ridge in the power spectrum corresponds to a different radial order n . The lowest frequency ridge ($\ell = 0, n = 0$) is for f -modes. The ridges above the f -mode ridge are the p -modes denoted by p_n , where the ridge immediately above the f -mode is p_1 , and then p_2 continuing on to p_n . Wave modes of low- ℓ and high- n penetrate deeper inside the Sun. For frequencies above the acoustic cutoff frequency of 5.3 mHz, acoustic waves are not trapped inside the Sun and can propagate to the surface and beyond in the solar atmosphere. Acoustic modes with equal values of $\omega_{n\ell m}/\ell$ propagate to similar depths inside the Sun. For degrees larger than around 150, wave damping becomes significant and modes are not resolved and appear as continuous ridges (Gizon and Birch, 2005).

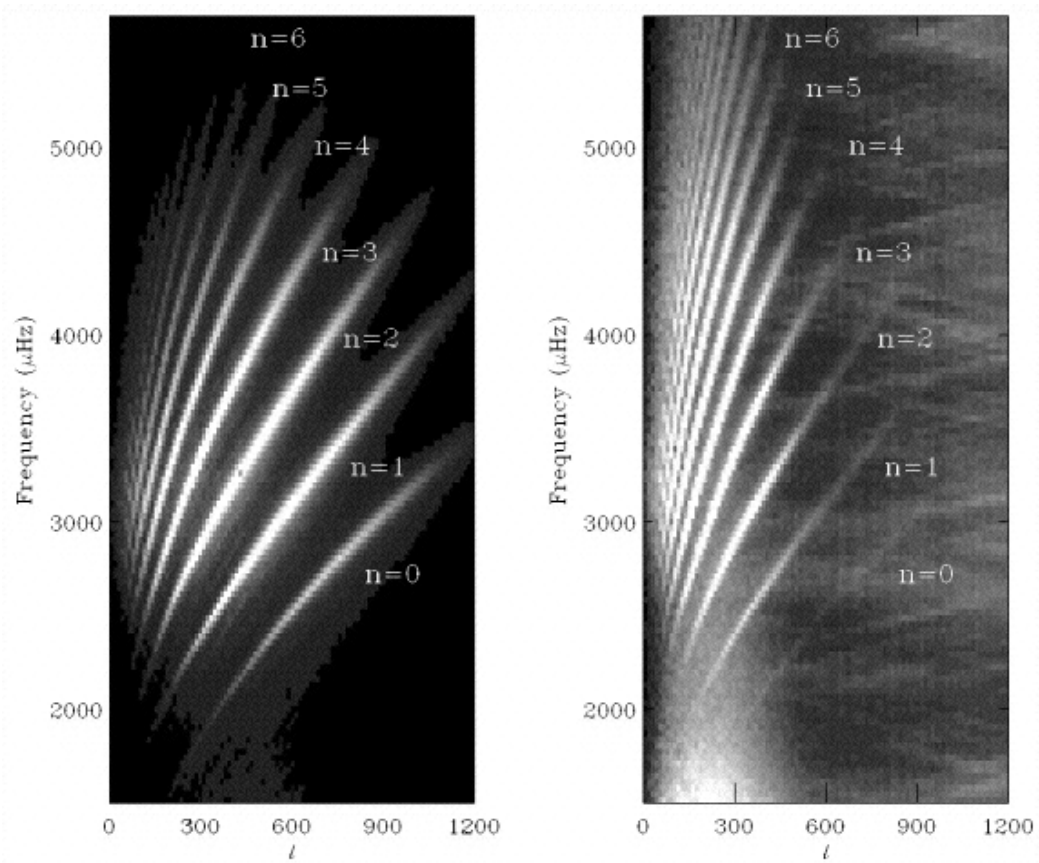


Figure 1.5: $\ell - \nu$ diagrams obtained as an azimuthal average of the three-dimensional power spectra obtained with the Solar Oscillations Investigation (SOI) and the Taiwan Oscillation Network (TON) instruments. On the left, the SOI diagram is shown, and the TON one is on the right. The n labels have been situated in the same position in both diagrams as a reference. The power has been enhanced multiplying by k^2 . (Gonzalez Hernandez *et al.*, 1998).

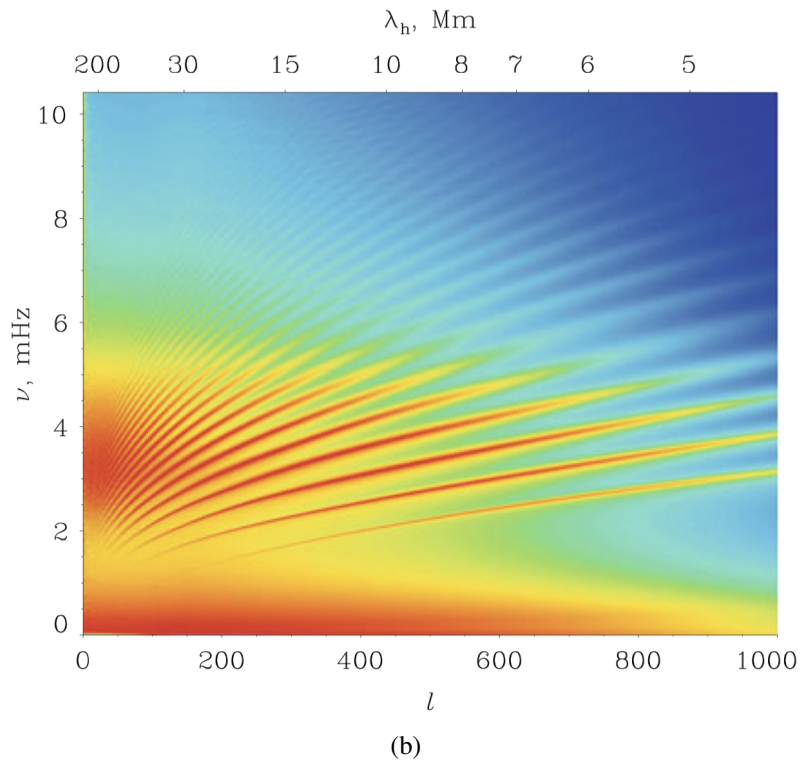
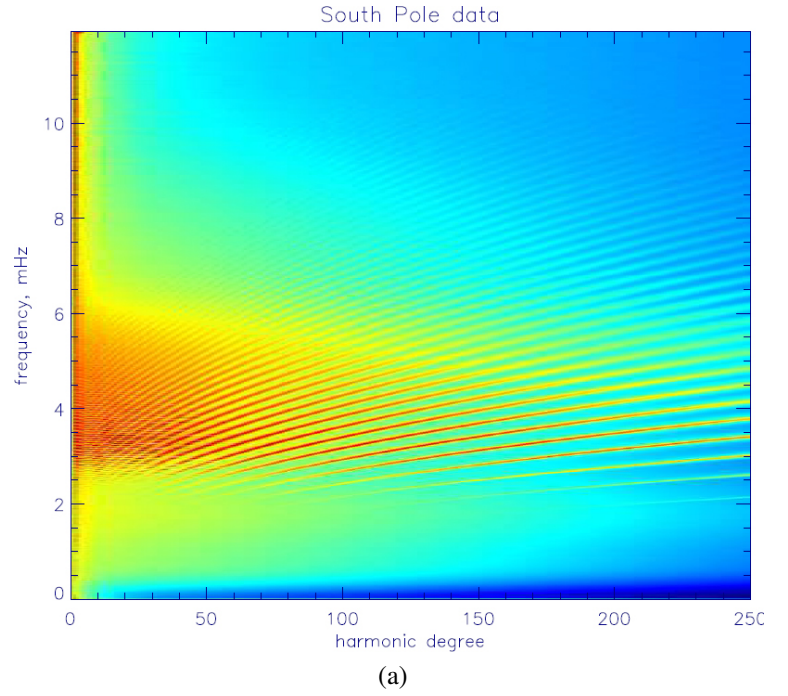


Figure 1.6: (a) Power spectrum of solar oscillations from data collected during the 1994 south pole campaign in Ca II K_1 line, 6 Å bandpass (Gizon and Birch, 2005). (b) Power spectrum for 6-day time series, in 1996, of solar oscillation data from the SOHO MDI instrument; ν is the cyclic frequency of the oscillations, ℓ is the angular degree, λ_h is the horizontal wavelength in megameters (Kosovichev, 2011).

When the total or spectral solar irradiance is observed the oscillatory power is concentrated in low angular degree modes, see Figure 1.7. The frequency pattern with regularly spaced peaks agreed with theoretical predictions by Vandakurov (1968), where the estimated spacing between the modes was $67.8 \mu\text{Hz}$. This spacing corresponds to the inverse time it takes the acoustic waves to travel from the surface of the Sun through the center to the opposite side and then return. Therefore, the frequency spacing offers an important constraint on the internal structure of the Sun.

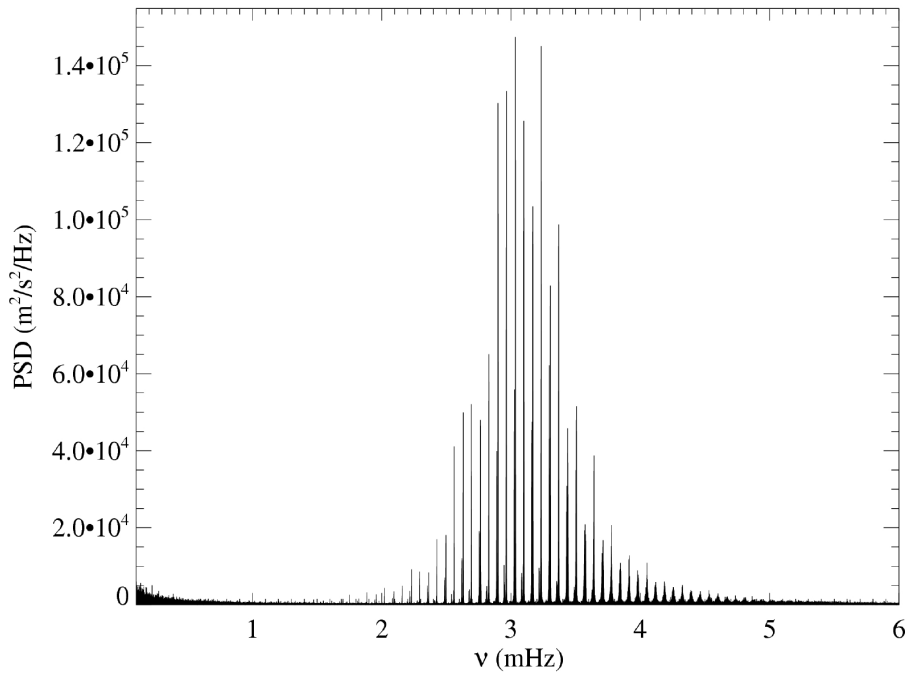


Figure 1.7: Power Spectral Density (PSD) function for low-degree solar oscillations by the GOLF instrument onboard SOHO, from 4-November-1996 to 7-August-2008. Notice the concentrated distribution of acoustic oscillations around the p-mode frequency band $\nu = 3.33 \text{ mHz}$, between 2 and 4 mHz (Kosovichev, 2011).

1.4 Local Helioseismology

By combining the frequencies of global waves modes, localized information about the structure and rotation to limited regions in radius and latitude can be obtained. This information can then provide inferences about the variation of localized properties with respect

to position within the Sun (Christensen-Dalsgaard, 2002). Local helioseismology observations began with a study of p-mode acoustic absorption by sunspots in the photosphere by Braun *et al.* (1987). The study involved the analysis of three sunspots and a quiet area from data taken with the 512 channel magnetograph of NSO’s vacuum telescope, located at Kitt Peak, to see if the strong magnetic fields and temperature variations around the sunspot “produce measurable effects upon p-mode oscillations” (Braun *et al.*, 1987). The analysis examined the traveling waves in the interior of the sunspots, about which very little was known at the time, and compared the results to the incoming and outgoing traveling waves on the outside of the sunspot where the properties were understood. The results showed a difference in power of the incoming and outgoing traveling waves around sunspots. In addition, there was found a difference of 50% absorption of incoming waves (Braun *et al.*, 1987) and the amplitude of incoming waves were higher than the outgoing waves – this was the first time viable information on local surface structures were obtained from p-modes (Hill, 2008).

1.4.1 Data Observations in Local Helioseismology

High-resolution Doppler images of the Sun are the fundamental data of modern helioseismology (Gizon and Birch, 2005). With the advent of high-resolution data from space-based and ground-based networks, helioseismology is constantly developing. The main datasets utilized in helioseismology are the Helioseismic Magnetic Imager (HMI) aboard NASA’s Solar Dynamics Observatory (SDO), the Global Oscillation Network Group (GONG), the Michelson Doppler Imager (MDI) aboard ESA/NASA’s SOHO, and the Taiwan Oscillation Network (TON). Additionally, the 1600 Å and 1700 Å bandpasses from SDO’s Atmospheric Imaging Assembly (AIA) are now known to capture oscillations of p-modes as well as waves propagating upwards from the photosphere up through the chromosphere (Rajaguru *et al.*, 2013).

Launched on 11-February-2010, SDO is the main NASA *Living with a Star* mission to

understand the influence of the Sun on the Earth and near-Earth space by studying the solar atmosphere on small scales of space and time and in many wavelengths simultaneously. There are three instruments onboard the SDO, the AIA, HMI and the Extreme Ultraviolet Variability (EVE). SDO's 4096×4096 square pixel spatial resolution gives it a tremendous advantage over earlier missions with unprecedented detail. The first instrument, HMI maps magnetic and velocity fields on the surface of the Sun. HMI measures the Doppler shift of the Fe I 617.3 nm spectral line to determine the photospheric surface velocity over the Sun's entire visible disk. HMI creates a full-disk Dopplergrams every 45 seconds with a two-pixel resolution of $1''$. These Dopplergrams are then used to study the surface and the inside of the Sun (Scherrer *et al.*, 2012). HMI uses the Zeeman effect of the same spectral line to measure the Stokes parameters required to create full-disk longitudinal magnetic-field measurements (LOS magnetogram) and full-disk vector photospheric magnetic-field maps (vector magnetogram). The LOS magnetograms have a cadence of 45 seconds with a two-pixel resolution of $1''$ resolution and the vector magnetograms have a 12-minute cadence; thus HMI provides the first rapid-cadence measurements of the strength and direction of the solar magnetic field over the visible disk of the Sun. The second instrument, the AIA (see Table 1.1) is an array of four telescopes that observes the surface and atmosphere of the Sun. AIA was built to obtain full-disk images of the solar atmosphere with a field of view of at least 40 arcmin and a two-pixel resolution of $1.2''$. Filters on the telescopes cover ten different wavelength bands that include seven extreme ultraviolet (304 Å, 171 Å, 193 Å, 211 Å, 335 Å, 94 Å and 131 Å), two ultraviolet (1600 Å, 1700 Å), and one visible (4500 Å) light band to reveal key aspects of solar activity. The wavelength bands were chosen to yield diagnostics over the range of 6000 K to 3×10^6 K. AIA uses multi-layer coatings combined with foil filters to isolate the desired spectral bandpasses for each telescope (Pesnell *et al.*, 2012).

GONG, an international network of six extremely sensitive and stable solar velocity imagers, provides nearly continuous observations of solar oscillations. The system

Table 1.1: AIA wavelength bands (LMSAL-AIA, 2010).

AIA wavelength	Source	Solar Atmosphere Region	Characteristic Temperature	Image Cadence (seconds)
White light	continuum	Photosphere	5000 K	3600
1700 Å	continuum	Temperature minimum, photosphere	5000 K	24
304 Å	He II	Chromosphere & transition region	50,000 K	12
1600 Å	C IV + continuum	Transition region & upper photosphere	10^5 & 5000 K	24
171 Å	Fe IX	Quiet corona, upper transition region	6.3×10^5 K	12
193 Å	Fe XII, XXIV	Corona & hot flare plasma	1.2×10^6 & 2×10^7 K	12
211 Å	Fe XIV	Active region corona	2×10^6 K	12
335 Å	Fe XVI	Active region corona	2.5×10^6 K	12
94 Å	Fe XVIII	Flaring regions	6.3×10^6 K	12
131 Å	Fe VIII, XX, XXIII	Flaring regions	$4 \times 10^5, 10^7$ & 1.6×10^7 K	12

became operational in October 1995. The GONG instruments, which are Michelson-interferometer-based Fourier tachometers, observe in the Ni I 6768Å line. In addition to intensity and Doppler images every minute, GONG provides full-disk magnetograms nominally every 20 minutes. The original instruments used 256×256 pixel CCD cameras, which were replaced in 2001 by 1024×1024 square-pixel cameras (Leibacher, 1999).

The MDI has provided line-of-sight Doppler velocity images since 1996 with an excellent duty cycle. MDI Dopplergrams are obtained by combining 4 filtergrams on the wings and core of the Ni 6788 Å absorption line, formed just above the photosphere. Dopplergrams are available at a one minute cadence. MDI operates under several observing modes. The Dynamics Program runs for 2 to 3 months each year and provides 1024×1024 full-disk Doppler images; the plate scale is 200 per pixel, or 0.12 heliographic degrees (1.45 Mm at disk center). The Structure Program provides continuous coverage: full-disk images are binned onboard into a set of about 20,000 regions of roughly similar projected areas on the Sun to make use of the narrow telemetry channel. The Structure Program data are used to measure mode frequencies up to spherical harmonics degrees of 250. MDI can also operate in High-Resolution mode by zooming on a 110 square field of the Sun with a plate scale of $0.62500''$ per pixel and a diffraction-limited resolution of $1.2500''$ (Scherrer *et al.*, 1995; Gizon and Birch, 2005).

The TON (Chou *et al.*, 1995) is a ground-based network to measure solar K-line in-

tensity oscillations to study the internal structure of the Sun. The TON consists of six identical telescopes at appropriate longitude around the globe. The TON system uses a 3.5-inch Maksutov-type telescope to observe the K-line images. The data are series of 1080×1080 full-disk intensity images recorded at a rate of one image per minute. The TON obtains data on the intermediate and high-degree p-mode oscillations.

1.4.2 Techniques in Observational Local Helioseismology

1.4.2.1 Fourier-Hankel Method

The Fourier–Hankel spectral method was originally used to search for wave absorption by sunspots. The method probed the nature of sunspots by detecting their influence of high-degree p-mode oscillations in the surrounding photosphere. The analysis decomposed the observed oscillations into radially propagating waves described by Hankel functions within an annular region in a cylindrical coordinate system centered on the sunspot. Braun *et al.* (1987) were able to take measurements of three sunspots by taking the differences in power between waves traveling outward and inward. Braun *et al.* (1987) found that sunspots appear to absorb $\sim 50\%$ of the incoming acoustic waves. And that the absorption increases linearly with the horizontal wave number (Braun *et al.*, 1987).

1.4.2.2 Ring-diagram Analysis

Gough and Toomre (1983) proposed frequency changes of local perturbation effects on oscillation frequencies, brought on by the meridional horizontal subsurface flows on the Sun. The ring-diagram analysis (Hill, 1988), first introduced by Frank Hill in 1988 was a practical tool developed to infer the speed and direction of the horizontal flows, by observing the doppler shifts of the local acoustic waves from power spectra computed over patches of the solar surface (typically $15^\circ \times 15^\circ$) (Gizon and Birch, 2005). Thus, the ring-diagram analysis is a generalization of global helioseismology applied to local areas on the Sun. For example, the sound speed and adiabatic index can be compared within

magnetically active and inactive (quiet Sun) regions (Basu *et al.*, 2004). The computed local power spectra was taken as a function of frequency, ω , along with the individual longitude and latitude components (k_x, k_y) of the horizontal wave vector number, k . In three dimensional $\omega - k_x - k_y$ space, the results appear like “trumpetlike” surfaces, obtained by rotating the ridges of the power spectra, shown in Figures 1.5 and 1.6, around the frequency axis (Christensen-Dalsgaard, 2002). When slices of “trumpets” are taken at fixed frequency, the cross sections of the trumpets form rings shown in Figures 1.8 (Hill, 1988). The sets of rings each correspond to a ridge in the $\ell - \nu$ diagram. The shifts in the rings are a result of the underlying horizontal flow field, and the variations in the subsurface sound speed cause a distortion of the rings (Christensen-Dalsgaard, 2002).

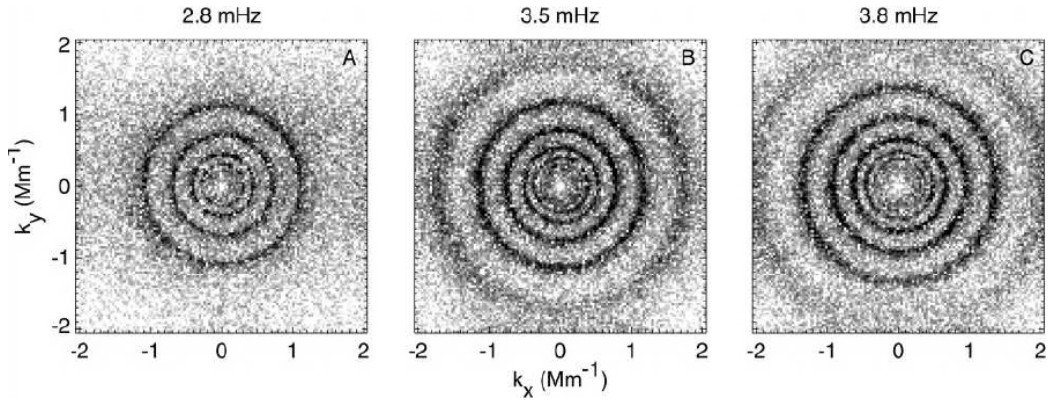


Figure 1.8: The ring-diagram analysis involves cuts at constant frequency through the three-dimensional power spectrum, $\omega - k_x - k_y$, appearing as rings. Panels A, B and C correspond to cuts at frequencies, ν , 2.8, 3.5 and 3.8 mHz, where the outermost ring corresponds to the f-mode and the inner rings corresponds to $p_1, p_2, p_3, \dots, p_n$. Displacements of the rings are caused by horizontal subsurface flows, and distortions of the rings are caused by variations in the subsurface sound speed (Gizon and Birch, 2005).

1.4.2.3 Time-distance Helioseismology

A common procedure used in geoseismology is to measure the travel time for waves between a known source and a detector. Earthquake travel times are used to investigate the global structure of the Earth (Christensen-Dalsgaard, 2002). Time-distance Helioseismology (Duvall *et al.*, 1993) aims to measure and interpret the travel times of acoustic waves

between any two locations on the solar surface from a cross-covariance function. The cross-covariance function will produce a maximum value when the cross-correlated time lags between the two signal locations coincide with the travel time of the acoustic waves (Gizon and Birch, 2005; Kosovichev, 2011). Inhomogeneities near the ray path connecting the two locations perturb the travel time between those two points. An inverse problem must then be solved to infer the local structure and dynamics of the solar interior (Jensen, 2003).

1.4.2.4 Helioseismic Holography

Helioseismic holography first introduced by Lindsey and Braun (1990) for the purpose of far-side (magnetic) imaging, is a special case of phase-sensitive holography. A more recent theoretical introduction to helioseismic holography can be found in Lindsey and Braun (2000a). The idea is to image the sunspots on the back of the Sun by using the acoustic wavefield, basically the line-of-sight Doppler velocity observed at the solar surface, on the visible solar disk and combine with the phase information. The idea can be used to make an estimate of the acoustic wavefield at any location in the solar interior at any instant in time. Similar to the seismic migration technique in geophysics, this technique has been used to produce a seismic image of a solar flare (Donea *et al.*, 1999). Furthermore, the method has been used mainly to investigate the subsurface structure and acoustic properties of active regions (e.g., Braun *et al.* (1998), Chen *et al.* (1998), Lindsey and Braun (1998), Lindsey and Braun (2000b), Braun and Lindsey (2001)).

1.4.2.5 Direct Modeling

In direct modeling, Woodard (2002) introduced a concept to estimate subsurface flows from direct inversion of the frequency-wavenumber correlations seen in the acoustic wavefield in the Fourier domain and the underlying supergranular flow. The central concept is that there is no correlation from horizontal and uniform steady models with no flow

Fourier components of the acoustic wavefield and can therefore introduce correlations into the acoustic wavefield produced by perturbations. Woodard (2002) demonstrated the ability of the technique to recover near-surface flows from the f-mode spectrum (Gizon and Birch, 2005).

1.5 Oscillatory Waves Around Active Regions

1.5.1 The significance of p-modes from the Surface to the Chromosphere

In the Sun, 5-minute p-mode oscillations seem to be the dominant frequencies, with their major source of excitation belonging to the convection zone, where these waves are trapped oscillations. As these p-modes approach the surface and above, there is a transition region where there is an acoustic cutoff at about 5.3 mHz. Apart from the 5-minute oscillations, higher frequency p-modes, or frequencies above 5.3 mHz, have been detected. However, the source of these high-frequency waves is still not known. So far, two models have been proposed to try to explain these oscillations with frequencies above the acoustic cut-off. The first model proposed by Balmforth and Gough (1990) suggests that these waves are partially reflected at the transition region rather than the ordinary p-modes that are reflected from the photosphere. In the other model, by Kumar and Lu (1991) the high-frequency waves are an interference phenomenon between ingoing and outgoing waves from a local source under the photosphere. In comparison, the amount of energy stored in the high-frequency waves is much less than the energy stored in the 5-minute p-modes – due to the power of the strong turbulence in the convective zone. Therefore, solar flares will have a larger effect on the high-frequency waves. Also, the waves are not only pure acoustic waves, but are acousto-gravity waves, and so detection is more effectual to investigate the acoustic velocity oscillations in the solar atmosphere (Kumar *et al.*, 2010).

1.5.2 Magnetic Flux Emergence

Even though the mechanism of the solar flares is not yet understood, efforts are being made to try to understand them by investigating for a change in magnetic flux (Kumar and Ravindra, 2006; Lara *et al.*, 2000). One of the many important processes responsible for such dynamical processes such as large solar flares, is the emergence of the magnetic flux from the solar interior in active regions and the change in the coronal magnetic field in response to the emergence. However, it is still unclear exactly how the magnetic fields rise through the convection zone of the Sun and emerge through the photosphere and the chromosphere into the corona. Understanding that process could be an initial step in unravelling the mechanism behind solar flares (Archontis, 2008). Solar flares take place above active regions or sunspots on the Sun. These huge magnetic storms on the surface of the Sun are caused by the interaction of the magnetic field with convection currents below the surface. Deep below in the convection zone the magnetic field is too weak to produce any significant change in the oscillation eigenfrequencies; however, closer to the surface the magnetic field becomes more significant (Hindman and Brown, 1998). Wave propagation can carry energy between different atmospheric heights efficiently and dissipate it (Martínez González *et al.*, 2011). It has been established that active regions such as sunspots and plages are formed by the emergence of magnetic flux tubes (Figure 1.9) – cylindrical structures where the magnetic field travels from the solar interior up to the upper atmosphere (Mason *et al.*, 2006; Shibata *et al.*, 1989). Khomenko *et al.* (2008) demonstrated through a model study that the peak in the power spectrum of the 5 minute oscillations is due to the leakage of oscillations from the photosphere to the chromosphere through small vertical magnetic flux tubes. Their theoretical model (Figure 1.10) correlated with observations of a plage around an active region, taken from the German Vacuum Tower Telescope (VTT) of the Observatorio del Teide on July 14, 2002 using the Tenerife Infrared Polarimeter (Khomenko *et al.*, 2008).

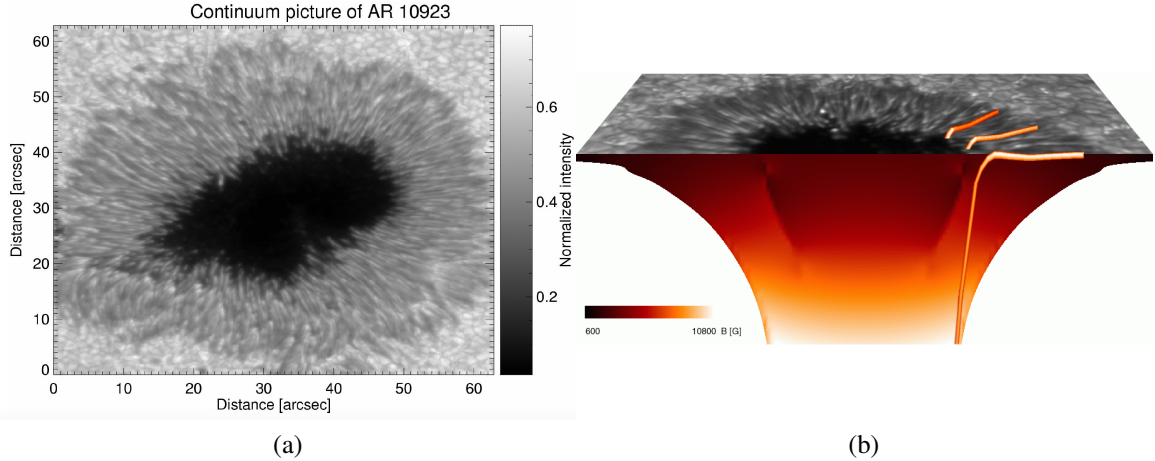


Figure 1.9: (a) Map of intensity of sunspot (12 Nov 2006, $\theta = 30^\circ$) taken with the spectropolarimeter SP attached to the SOT onboard Hinode (Rempel and Schlichenmaier, 2011). (b) Within active regions, such as sunspots, magnetic flux tubes could be a way to transport energy in the form of acoustic modes to the upper regions, such as the chromosphere (Martínez González *et al.*, 2011; Khomenko and Collados, 2015).

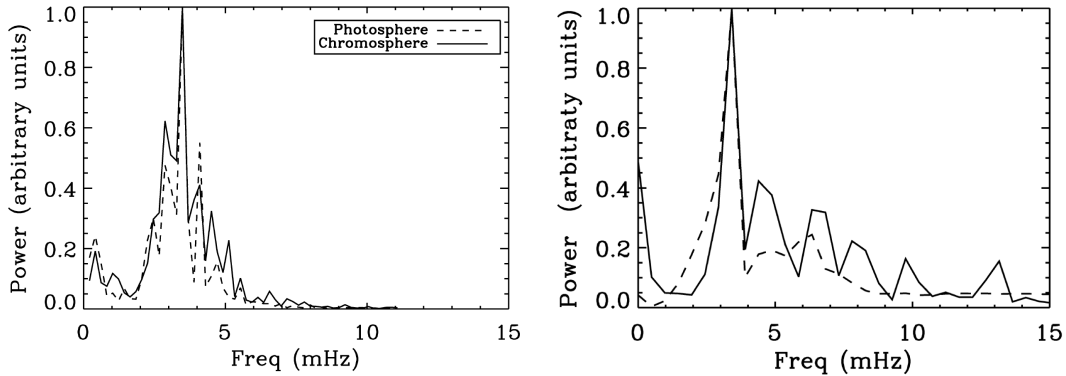


Figure 1.10: (Right) Photospheric (dashed line) and chromospheric (solid line) LOS velocity power spectra in the observed plage region. (Left) Photospheric (dashed line) and chromospheric (solid line) power spectra obtained from the simulation with τ_{RR} equal to 10 s. (Khomenko *et al.*, 2008).

1.5.3 Acoustic power around solar active regions

It has been accepted that around magnetically concentrated active regions, such as sunspots, p-mode oscillations are influenced by these magnetic structures – the p-mode power is suppressed or absorbed (Braun *et al.*, 1987; Jain *et al.*, 2011). However, solar flares commonly occur in active regions. Flares are known to drive oscillations within

certain frequency oscillation bands, $5.2 < \nu < 7.0$ mHz (Kumar and Ravindra, 2006). However, in the chromosphere, the acoustic cutoff frequency for p-modes is 5.33 mHz; beyond this level no waves should be able to propagate to the upper atmosphere (Heggland *et al.*, 2011). Additionally, the acoustic power in magnetically active regions is lower than that of a quiet region because of the absorption, emission, and suppression of the acoustic waves (Chou *et al.*, 2009a,b).

1.5.4 Excitation of p-modes by solar flares

Solar Flares are energetic explosions on the Sun brought on by highly twisted magnetic fields around active regions. These magnetic fields originate from below the Sun's surface and extend through the corona into the solar system. The high level of twist of these fields initiates the flares (Komm and Hill, 2009). These flares release large amounts of energy exciting p-mode oscillations in active regions, including the magnetically dominated regions of the sunspots. The oscillations that are excited are at high frequencies (5–6.5 mHz) (Kumar and Ravindra, 2006). A characteristic of sunspots is that they are known to absorb broadband p-mode power (Braun *et al.*, 1987), but power may show significant enhancement in the frequency range of 5–6 mHz but not in the lower frequency ranges of 2–4 mHz (Kumar *et al.*, 2010; Kumar and Ravindra, 2006).

Even though the basic mechanism by which a flare excites acoustic oscillations is still not yet known, it is believed that these flares can excite velocity oscillations in active regions, especially those regions where a higher class solar flare has taken place (Kumar and Ravindra, 2006). Wolff (1972) theorized that large solar flares could heat the relative area of the photosphere resulting in stimulating p-modes around the Sun (Gizon and Birch, 2005; Wolff, 1972). Solar flares release large amounts of energy at different levels of the atmosphere on the Sun. So it is expected that major solar flares would be able to excite p-mode oscillations, therefore changing the characteristics, such as the wave amplitude of the p-modes (Ambastha *et al.*, 2003b). The first clear observations of helioseismic waves

produced by a flare is by Kosovichev and Zharkova (1998), taken from data with the SOHO Michaelson Doppler Imager, see Figure 1.11.

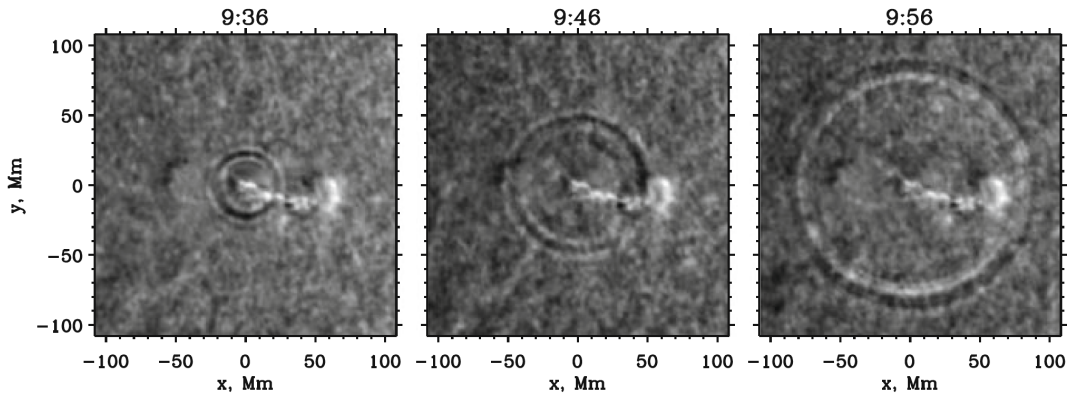
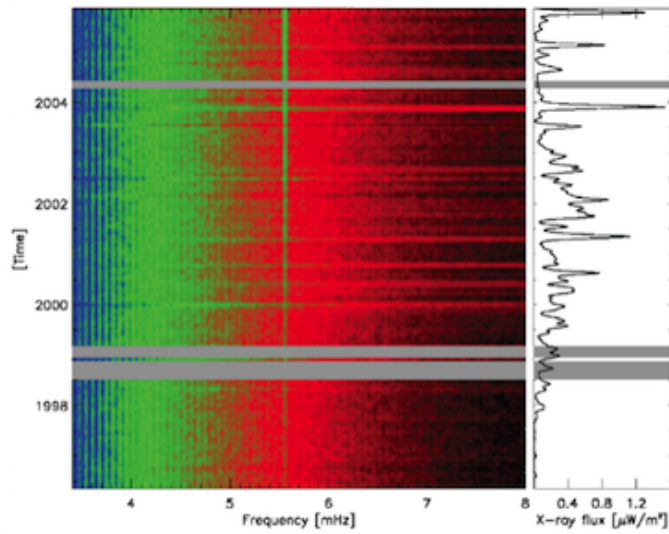


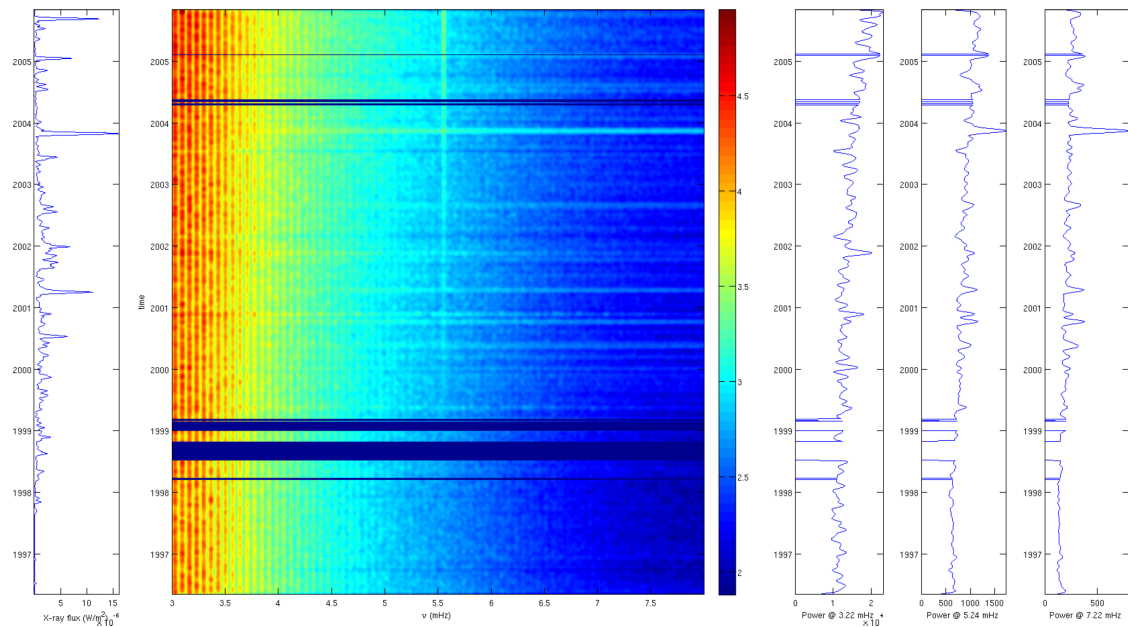
Figure 1.11: Observations of helioseismic waves produced by a flare (Kosovichev and Zharkova, 1998). Observations of the seismic response (“sunquakes”) of the solar flare of 9 July, 1996, showing a sequence of Doppler-velocity images, taken by SOHO/MDI. The signal amplitude of expanding ripples is enhanced by a factor 4 in the these images perturbations (Kosovichev, 2011).

Flares not only affect the immediate active regions during the short term of the event but also excite long lasting global oscillations. Karoff and Kjeldsen (2008) supported the theoretical idea by Wolff (1972), by observationally showing a correlation between the high frequency ($5.3 < \nu < 8.3$ mHz) global oscillation power spectra from 8 years of data from the VIRGO (Variability of Solar Irradiance and Gravity Oscillations) instrument onboard SOHO, and the GOES (Geostationary Operational Environmental Satellite) solar X-ray flux at $1-8 \text{ \AA}$ (Figure 1.12a) (Chakraborty *et al.*, 2011; Karoff and Kjeldsen, 2008). Chakraborty *et al.* (2011) reproduced the method of Karoff and Kjeldsen (2008) by calculating frequency-time plots for acoustic data from VIRGO, using a longer time series of 10 years, and then correlating the power spectra with GOES X-ray flux data and found that there was a correlation (Figure 1.12b). However, Richardson *et al.* (2012) could not confirm these findings, moreover, these results cannot reflect individual flares, where a shorter time series is needed to associate the flare (Richardson *et al.*, 2012). And so, researchers have looked into a correlation of acoustic oscillations of major X-class flares and the X-ray flux, by studying their acoustic power in localized areas of the active regions around the

flare (Kumar *et al.*, 2006, 2011). What they found was that there was an enhancement in acoustic power (see Figure 1.13), not only for the higher-frequency p-modes, but also for the 5-minute and lower p-modes (Kumar *et al.*, 2010; Kumar and Ravindra, 2006).



(a)



(b)

Figure 1.12: The correlation of solar flares flux with p-mode oscillation power in (a) the method by Karoff and Kjeldsen (2008) in the utilization of frequency-time plots, with a time series of 8 years, and (b) Chakraborty *et al.* (2011) with a longer time series of 10 years.

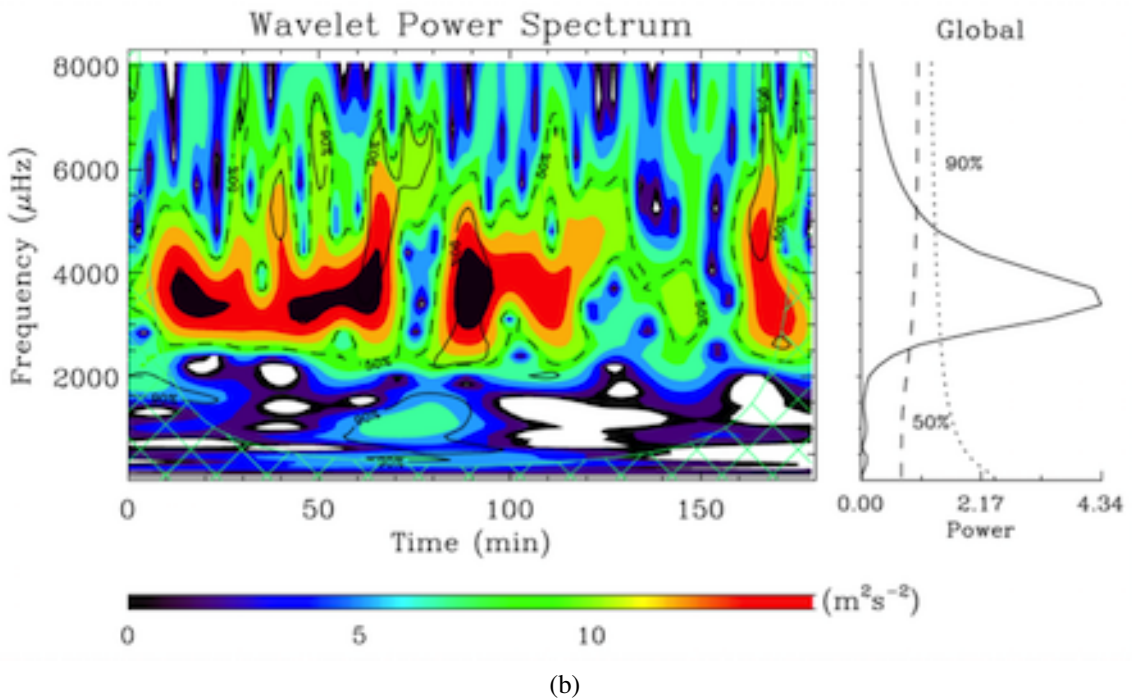
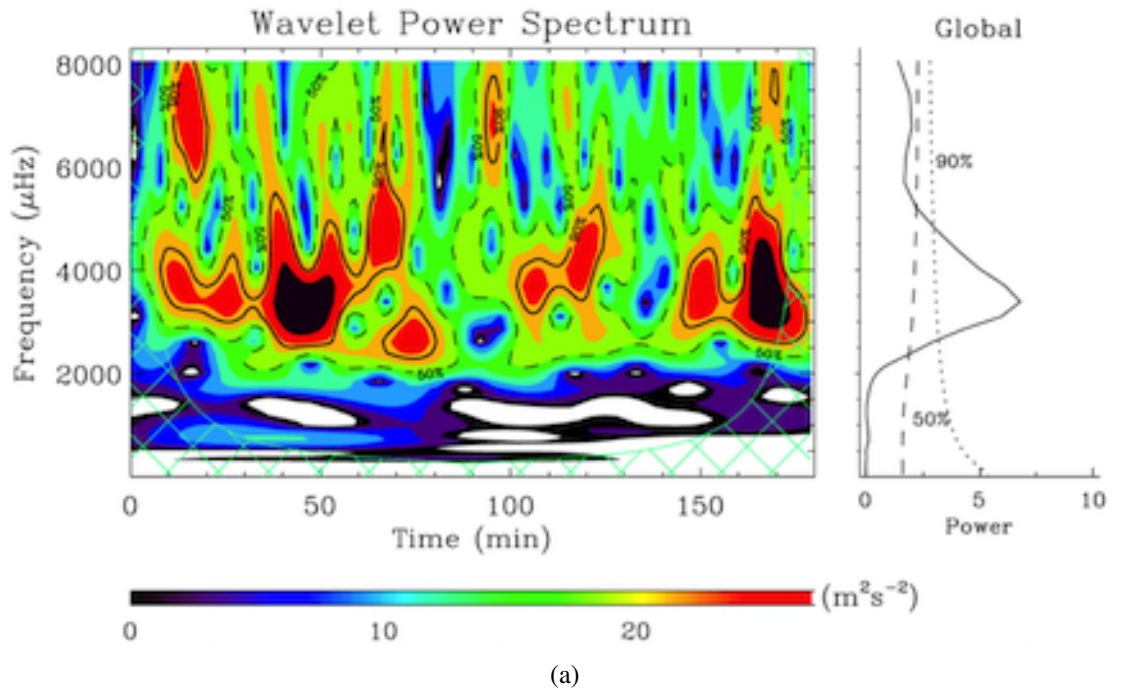


Figure 1.13: (a) MDI data taken of an X17.6 flare on October 28, 2003, with a time series of 10:00-13:00 UT, using a Wavelet Power Spectrum (WPS) and the Global-Wavelet Power Spectrum (GWPS). In the WPS, the solid lines correspond to regions with 90% confidence level and the hatched region indicates the cone of influence. The color scale is for the wavelet power. In the GWPS, the dotted line is for 90% significance level and the dashed line is for 50% significance level. (b) Same as above, but using GOLF (Global Oscillations at Low Frequency) data (Kumar *et al.*, 2010).

1.6 Advances in Helioseismic Wave Response From Solar Flares

With the advent of multi-wavelength detectors such as the instrumentation onboard the Solar Dynamics Observatory (SDO), the solar atmosphere can now be explored by correlating data at different heights. Multi-wavelength observations can be explored in order to understand the processes taking place within different layers of the solar atmosphere. The AIA 1600 Å and 1700 Å wavelengths are now known to capture clear oscillation signals due to acoustic oscillations as well as waves propagating up through to the chromosphere (Rajaguru *et al.*, 2013). Howe *et al.* (2012) studied the local power distribution for a 15-degree region around NOAA active region 11072 by observing in different wavelengths of the AIA and HMI channels to understand the interactions of waves and magnetic fields within the different layers of the photosphere. They observed changes in the suppression of power within the AIA and HMI wavelength channels. Analyses of multi-wavelength observations also built up evidence that magnetoacoustic waves above certain frequencies can travel up in the chromosphere and transition region (McIntosh and Jefferies, 2006).

1.6.1 Sunquakes

Sunquakes are caused by the strong hydrodynamic impacts during a flare. The helioseismic waves produced from the impulsive phase of the flare propagate out as expanding circular ripples (see Figure 1.11). These waves can be detected in Dopplergram movies as a characteristic ridge in the time distance diagrams (see Figure 1.14, Kosovichev, 2011). .

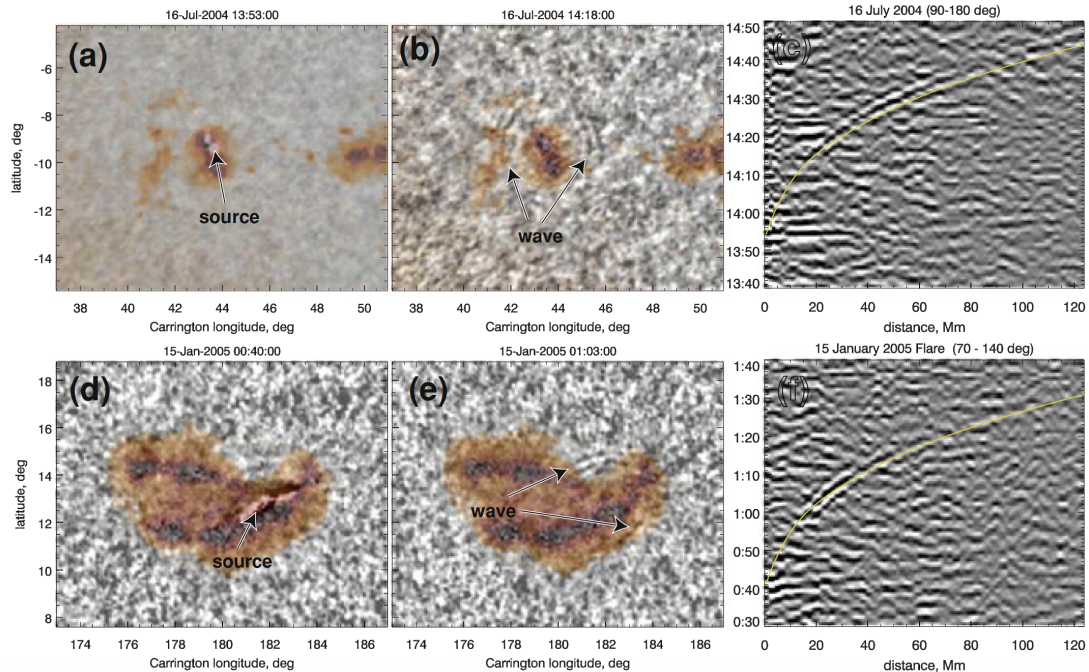


Figure 1.14: Observations of sunquakes from two solar flares: a–c) X3-class on 16-July-2004 and d–f) X1-class flare on 15-January-2005. The left panels show the images of active regions and the location of the seismic wave source from a superposition of MDI white-light images. The right panels show the time-distance diagrams of these events. The thin yellow curves in the right panels are a theoretical time-distance relation for helioseismic waves for the standard solar model (Kosovichev, 2006, 2011).

1.6.2 Magnetohydrodynamic Waves around Sunspots and in the Solar Atmosphere

Observations and theoretical modeling of sunspots have made significant progress in recent years. Observational capabilities make it possible to study sunspot waves from the photosphere up through the corona. It has been clearly established that umbral and penumbral waves have different properties originating from ground based observations operating in visible and near-infrared wavelengths. This result is related to their different magnetic configuration, with a magnetic field that is mainly vertical in the umbra and highly inclined in the penumbra. Waves above sunspots have also been shown to have a different behavior at the photosphere, chromosphere and above, where the amplitudes or periods of the disturbances have different values. The most prominent oscillations in sunspots have periods that are of the order of a few minutes. Global oscillations of sunspots as a whole also exist

and have periods that range from hours to days (Khomenko and Collados, 2015).

In observations, wave properties can be determined using spectroscopic or imaging instruments. Complementarily, imaging instruments have the advantage that the spatial coherence of waves can be studied and their apparent propagation in the plane of the sky can be determined. The comparison between the fluctuations observed with a number of filters that include lines of different temperature sensitivity, facilitates the study of the propagation of disturbances with varying heights. From the ground, radio observations also make possible the observation of the corona above sunspots, but the real impulse for the study of waves in this region comes from space based missions. In the upper layers, instruments like SMM (Gurman *et al.*, 1982), SUMER onboard SOHO (Wilhelm *et al.*, 1997) and the IRIS mission De Pontieu *et al.* (2014) have made possible the observation of emission spectra of ultraviolet lines formed in the high chromosphere, transition region and low corona. Sunspot waves can now be detected in these high atmospheric layers with adequate temporal and spatial resolutions (Khomenko and Collados, 2015).

With all this information, a global picture can be made of how the waves propagate through the three-dimensional sunspot atmosphere. Many observations point in the direction that wave phenomena at different layers of the sunspots are related to each other. To theoretically understand the observed wave properties, one has to take into account that different wave modes can exist in a magnetized medium (for example, fast and slow magnetoacoustic modes and the Alfvén wave modes in a homogeneous atmosphere). These waves have different dominant restoring forces in the wave equation, such as magnetic Lorentz force, gas pressure gradient or buoyancy. The photosphere and low chromospheres of sunspots are regions where restoring forces are of the same order of magnitude, making arbitrary the division into pure wave modes and complicating theoretical models (Khomenko and Collados, 2015).

There are unanswered questions on the general picture of how p-mode waves make their way into the higher atmosphere, how waves of different frequencies behave during the up-

ward propagation, and where the ultimate sources of these p-mode waves are located. Different types of waves, mostly MHD, are abundant in the atmosphere of and above sunspots (Zhao *et al.*, 2016; Bogdan and Judge, 2006). Utilizing a helioseismic analysis Zhao *et al.* (2015) were able to detect a new type of wave in the photosphere, traveling from inside sunspots and around the vicinity with a speed around $40\text{-}60\text{ km s}^{-1}$. This was supported by direct observations from Löhner-Böttcher and Bello González (2015). Because the speed of $40\text{-}60\text{ km s}^{-1}$ was too fast for any MHD wave to sustain in the photosphere, Zhao *et al.* (2015) suggested that the observed waves correspond to wavefronts, of p-mode waves excited about 5 Mm beneath the sunspot's surface, sweeping across the photosphere. Due to the limited spatial and temporal scale of the wave, aliasing is hard to avoid when performing Fourier transform and calculating the power spectrum. The $k - \nu$ power-spectrum diagram shows a dominant power in the range of 2.5–4.0 mHz, indicating that the oscillation frequency of this fast-moving wave falls into the category of a five-minute oscillation, same as the typical acoustic waves in the photosphere. The frequency-dependent power distribution at the subsurface locations is determined by the local atmospheric properties and is expected to be different from the power distribution observed at the photosphere. It is unclear what causes those disturbances beneath sunspots. Some past helioseismic analyses indicated that the depth of 5Mm (5Mm - 5000km) was approximately where the sunspot's downdraft meets the upward flow (e.g., Zhao *et al.*, 2010), and plasma collisions near this depth may cause disturbances that generate the magnetoacoustic waves (Zhao *et al.*, 2015).

P-modes could be the driver of magnetoacoustic waves observed above the photosphere. It is becoming increasingly evident that all the above phenomena detected in different layers of the solar atmosphere are actually inter-connected and most likely produced by the same upwardly propagating slow magnetoacoustic waves, which present themselves according to the local physical conditions (Krishna Prasad *et al.*, 2015). Theoretically, the photospheric p-modes are likely the source of propagating slow magnetoacoustic waves in sunspots that are guided up to coronal heights along the strong umbral field lines, perme-

ating coronal fans before becoming dissipated (Krishna Prasad *et al.*, 2015; Hindman and Jain, 2008; Jain *et al.*, 2014). The role of the MHD mode conversion may be insignificant for explaining the power deficit of 5-min photospheric oscillations in sunspots. However, the mode conversion is expected to be significantly higher in the solar atmosphere where magnetic forces become dominant (Kosovichev, 2011).

1.7 Introduction to the Dissertation

The main theme of this study is to observe the effects of solar flares on oscillations and investigate p-mode and other wave mode oscillations frequency and power in active regions and quiet regions with varying imaging techniques such as power map movies, and sampling techniques to study the power frequency distribution. The goal of this dissertation is to develop a new way of investigating various wave mode frequency oscillations around solar flares and to examine how these frequencies evolve through time. The study will involve taking a survey of several active flaring regions, to observe whether there will be a difference in the frequency distribution. The main objective in this study will be to investigate the flare in different frequency bands, observing if there are any changes.

This helioseismic study involved both ground based and space based observations. Ground based investigations involved the GONG (Leibacher, 1999) $H\alpha$ detectors which image the chromosphere. Space based investigations involved data from NASA's SDO mission (Pesnell *et al.*, 2012), utilizing several wavelengths of the AIA. This multi-wavelength approach enables this study to compare the wave mode behaviors at several heights in the solar atmosphere.

The next two chapters, Chapters 2 and 3 involve analyses with the GONG data sets. Chapter 3 discusses the results of the study and was disseminated in a publication. Chapters 4 through 6 covers analyses utilizing data from SDO AIA and HMI. Chapter 4 discusses the image processing procedures of the AIA JSOC cutout images. Chapter 5 will discuss two fundamental sampling techniques where active regions were either randomly sampled

or a triangulation procedure was performed. In Chapter 6, a more advanced technique built from the fundamentals learned from the GONG study and the previous sampling methods, will be discussed. Chapter 7 contains conclusive statements.

Chapter 2

Methodology: GONG

2.1 Part I: GONG Methodology

2.1.1 Experimental Research Purpose

Our original study aimed to take a survey of various M and X-Class flares utilizing NSO's GONG $H\alpha$ data. The study was done to understand how the active regions around flares affect varying frequencies of p-mode oscillations. To obtain power spectra for individual pixels around a region of interest, a Fast Fourier Transform technique was utilized. In the chromosphere there is a cutoff frequency of 5.33 mHz, but with the $H\alpha$ data set it should be quite possible to observe these frequencies. This would then prove that there is leakage, and that p-modes travel vertically along magnetic field lines up to the chromosphere. The following sections will describe the experimental procedures and the data processing detailed in the study with the GONG $H\alpha$ data.

2.1.2 GONG Data Set

GONG or Global Oscillation Network Group, is a network of detectors located globally to monitor the Sun 24/7 providing 1 minute full disk 2048 by 2048 pixel CCD images, and is owned and operated by the National Solar Observatory (NSO) and funded by AURA. The data utilized in the initial GONG study consisted of NSO's GONG $H\alpha$ data from two of the six GONG detector sites – Cerra Tololo and El Tiede, see Figures 2.1 and 2.2. The original GONG data study consisted of one M and one X-class flare, each confined to the same day of universal time, and the corresponding GONG detector.

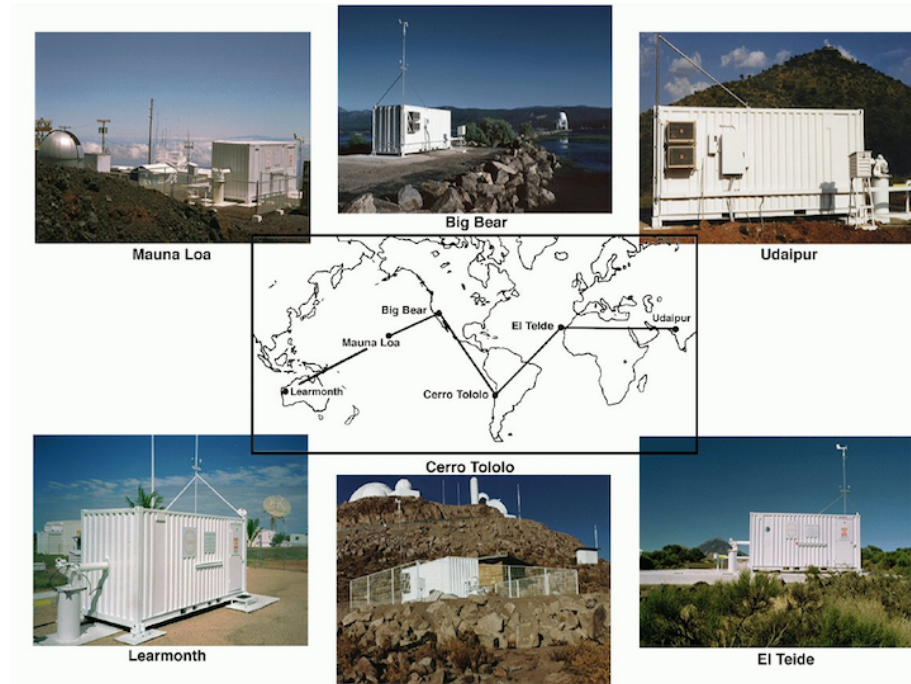


Figure 2.1: GONG Network Detectors.

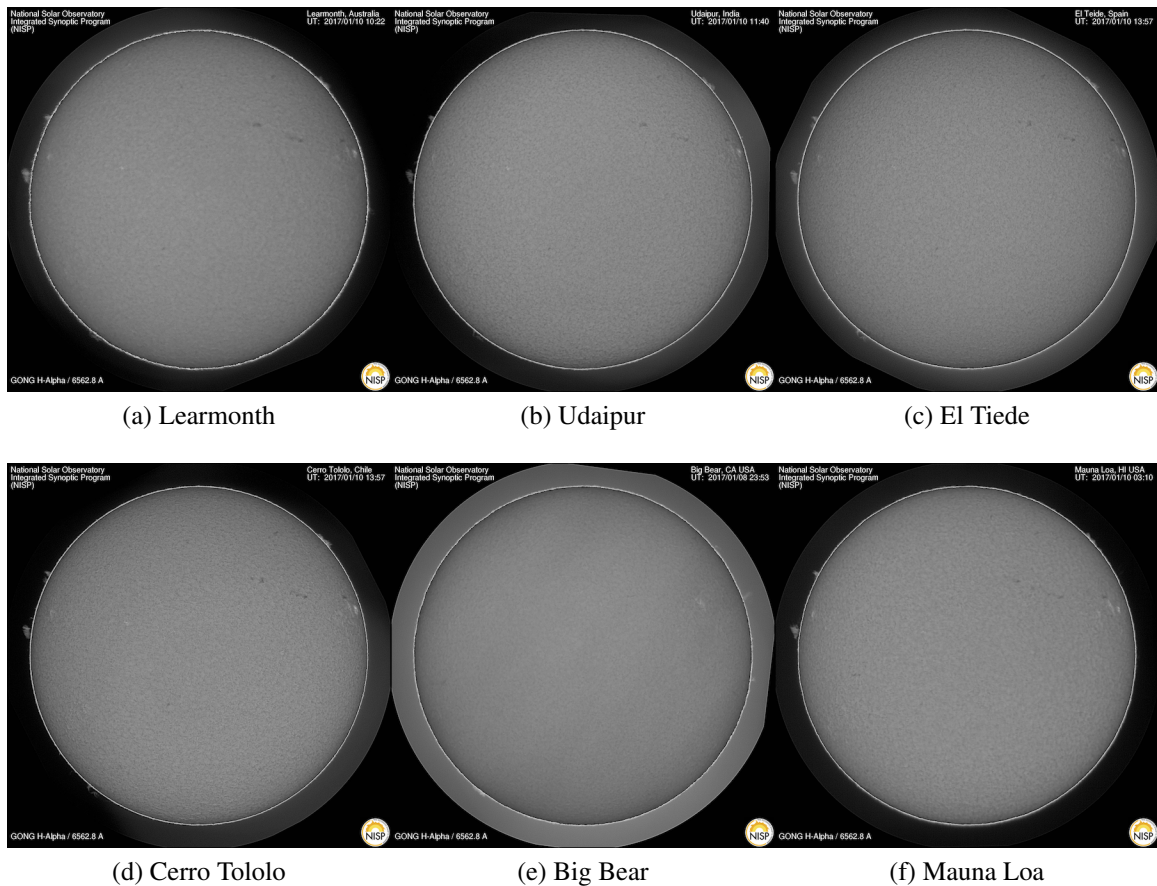


Figure 2.2: GONG H α Network.

2.1.3 Data Analysis Utilizing the Interactive Data Language (IDL) and the FFT

In image processing, the most popular method to represent pixel location is in the spatial domain by *column* (x), *row* (y), and z (*value*). The spatial domain is then transformed to the frequency domain to analyze any repeating patterns or extract features. In the frequency domain, x and y are now the frequencies and the z -value represents its corresponding amplitude or power. A large peak in the center of the data often shows the lowest frequencies. An efficient method, preserving all the original data while it fully transforms to the frequency domain, is the FFT or Fast Fourier Transform. The FFT decomposes an image into its fundamental sines and cosines (Harris Geospatial Solutions, 2017).

IDL or Interactive Data Language is a programming language used in data analysis in astronomy, especially in the field of solar physics. IDL was developed in 1981 and was birthed out of the FORTRAN language. The language's utilization as an array-oriented data analysis is what makes it ideal in analyzing images (Gumley, 2001). In the analysis of a time series of the GONG H α data set, IDL's FFT algorithm will calculate the complex, discrete Fourier transform of each spatial pixel in the time array. The result is a single- or double-precision complex array. The algorithm of the discrete Fourier transform (DFT), $F(U)$, of an N -element, one-dimensional function, $f(x)$ is:

$$F(U) = \frac{1}{N} \sum_{x=0}^{N-1} f(x) e^{-\frac{j2\pi ux}{N}} \quad (2.1)$$

Since the direction is negative for the forward transform and positive for the inverse transform,

$$f(x) = \frac{1}{N} \sum_{x=0}^{N-1} F(u) e^{\frac{j2\pi ux}{N}} \quad (2.2)$$

The FFT function can calculate functions up to eight dimensions. For example, if a function has n -dimensions, IDL will perform a transform separately in each dimension starting with the first dimension then on to the next, calculating the row by row arrays and

then column by column to the specified dimension. The FFT will return a complex array that has the same dimensions as the inputted array. If an array is not of the complex type it will be converted to complex and the dimensions will stay the same. In IDL the syntax is:

$$Result = \mathbf{FFT}(Array[, Direction][, DIMENSION = vector] \quad (2.3)$$

$$[, /DOUBLE][, /INVERSE][, /OVERWRITE])$$

In equation 2.3 the **DIMENSION** keyword is set to the dimension in which to calculate the FFT. The **DOUBLE** keyword specifies what form the result should be in, a double precision complex type. The **INVERSE** keyword specifies whether to calculate the inverse Fourier transform, thereby changing the direction to positive. And the **OVERWRITE** keyword tells the transform to overwrite the previous contents of the variable, therefore setting the transform to be done “in-place” (Gumley, 2001; Harris Geospatial Solutions, 2017). The power spectrum can then be calculated by taking the square of the absolute value of the result array divided in half – since there are identical peaks on the other side of the frequency domain. An example of the code syntax is shown in equation 2.4,

$$\mathbf{Power} = (ABS(POWER[0 : (\mathbf{ResultArray})/2]))^2 \quad (2.4)$$

2.1.4 Candidate Selection

Certain criteria were set in choosing solar flares for analysis. At the time of the initial study, the GONG H α data set was a young data set of nearly three years starting in Solar Cycle 24, when the sunspot activity should have started to ramp up. However, the age of the data set limited the choice in candidates. One criterion for solar flares choice was that the flare has to be class X and high class M, since ground-based detectors are more susceptible to measurements of these upper level flares. An additional criterion, is the location of the flare on the full disk image. The ideal candidate location is near the center and not on the edge or limb of the image, Figure 2.3. This is taken into consideration to not have any

“projection effects” in the analysis of the data, and to analyze the data as if the Sun was flat to ignore sphericity – especially when dealing with local areas (Gizon and Birch, 2005).

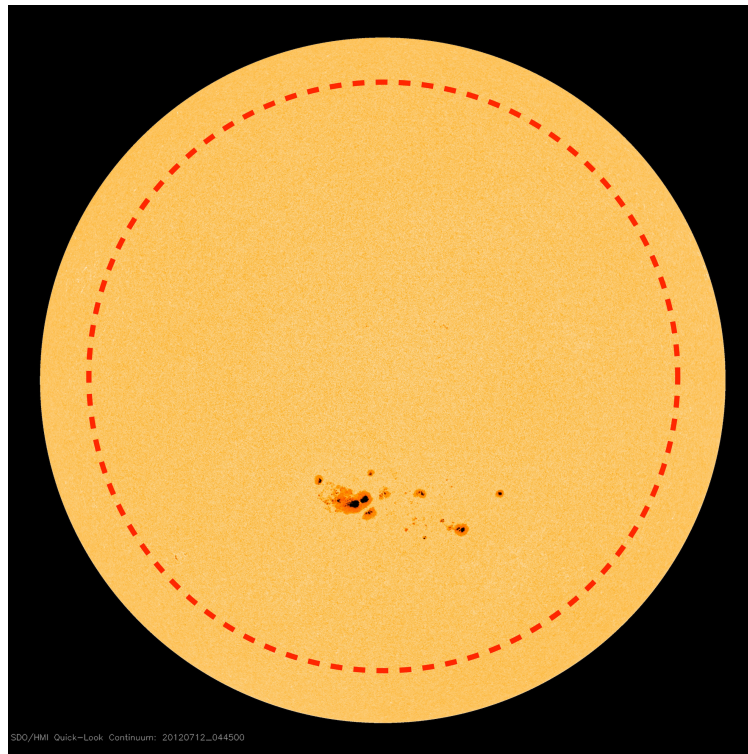


Figure 2.3: Location is taken into consideration when choosing the ideal candidate for analysis. Active regions should be chosen within the dashed red circular region such that the closer to the central meridian will eliminate any projection effects and the sphericity of the Sun which could affect the power spectra results(Gizon and Birch, 2005). HMI continuum of active region AR11520, a region that unleashed an X1.4-class solar flare on 12-July-2012 at 16:53 UT. Image Credit: SDO/HMI

There are six GONG detectors, positioned at different locations, focusing on the Sun constantly and configured to take data as the Earth rotates. Therefore, start times for each detector will be different. For the GONG study, only one time set data per detector, in one universal time date was considered. The unpredictability of solar flare events and the coordination of the time of the event to the detector measurement time, limit the choice of candidates even further. For example, a flare that takes place ten minutes before the end of the time the detector switches to the next detector, is not an ideal candidate.

And finally, another criterion to select solar flares in this study is the image quality of

the GONG images. Since, these are ground based detectors, weather has to be taken into consideration. And even though care was taken in choosing data from higher altitude detectors, such as Cerra Telolo, the images might not be as clear if it is cloudy during detection times. In order to test the image quality in the time series, an IDL code – *surfplot.pro*, was designed to check the pixel quality and also to check the intensity of the flare and view the region of interest of study, see Figure 2.4. In the program, a region was extracted and then made into a movie and also a three-dimension surface plot was run on the region. If there were any jumps in the Y-direction as the animated image sequence runs, that would indicate that the image quality changed. We would then investigate the *fits* image frames where a jump had occurred, using image software such as SAOImage DS9, and check the quality of the full disk images.

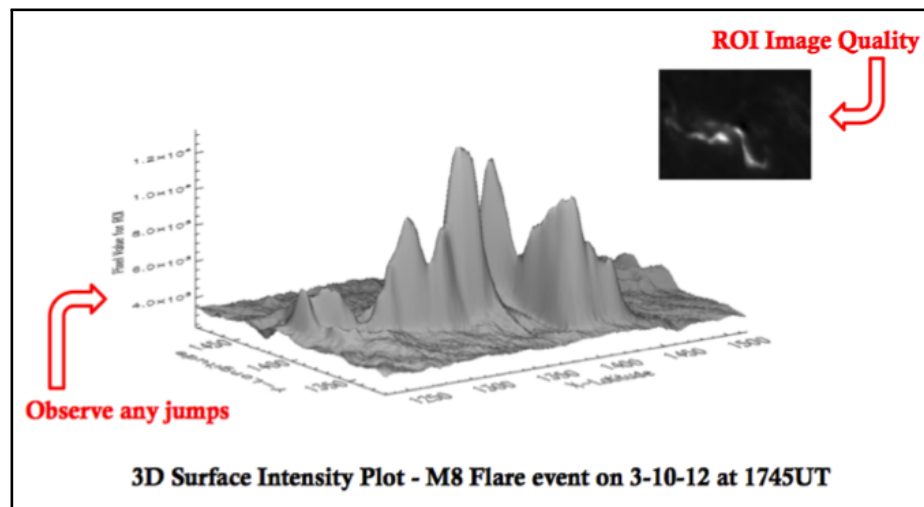


Figure 2.4: An IDL code, *surfplot.pro*, was designed on this project to check the image quality.

2.2 Part I: Data Analysis – IDL Code Stages

In this section, an explanation of the experimental methodology will be used as a guide to follow through the procedural pipeline in order to obtain the power map movie. The power map movie is a series of time evolved stacked images of the frequency domain, or the power spectra of the original GONG $H\alpha$ time series images. From these images analysis of the changes in power around active regions can be observed in the frequency domain per pixel location, basically a moving power map of the region, see Figure 2.5. In order to obtain the periodograms from sampling regions of the power map movie there are a total of six stages of computer codes. There are several stages where one code will call another; these will either be in the form of ROI codes or wrapper codes. This is the most effective way to handle the data since many text files containing the data arrays need to be handled in order to process the information of many pixels. The code workflow will be illustrated by flowcharts.

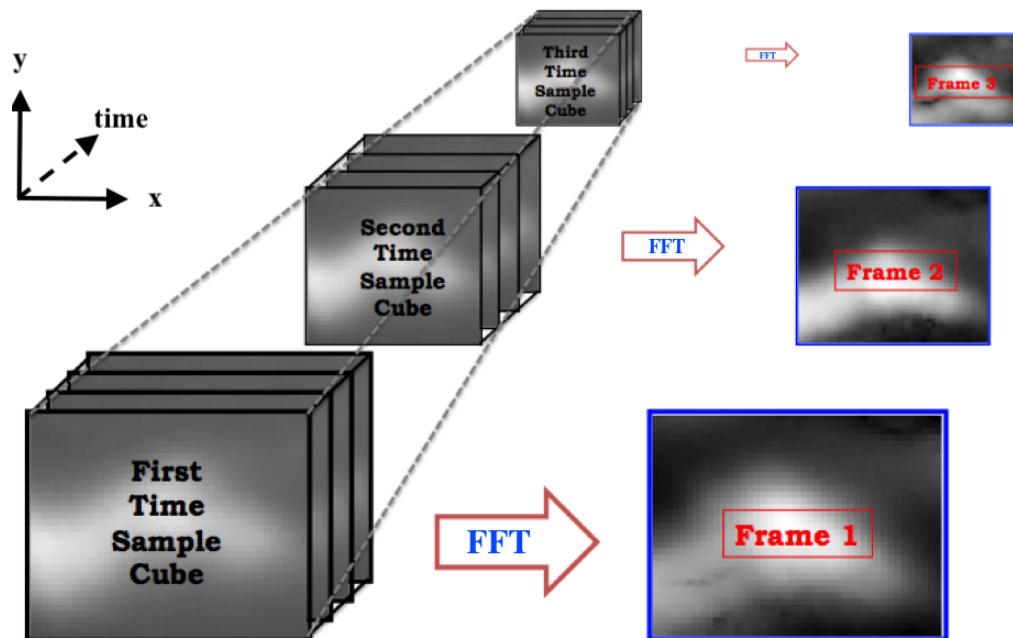


Figure 2.5: Power Map Movies creation diagram.

2.2.1 Stage 1 – Extract pixel information

In the initial stages there is a stack of $H\alpha$ full disk time series intensity images, produced each minute by the appropriated GONG detector. The stack of images will then be in the form of the 3-dimensional data cube, where X and Y are the 2-dimensional image with each pixel location being (X, Y) and the Z -dimension is the time series evolutions of the images. In the IDL code, this stacked set of intensity images will eventually form the original data cube. The first stage, *makefluxfast.pro*, takes the time series set of GONG images and then extracts an inputted region of interest (ROI) for analysis. Along with the ROI the code extracts the value of the intensity of each pixel through time, or the virtual Z direction of the data cube – creating a time rod in a specific location, in which there is a corresponding intensity value for each time series frame. In order for the *makeflux.pro* procedure to do this, it must have an embedded *ROI* code, *ROI.pro*, built into the main *makefluxfast.pro* code, which calls a double forloop, see Figure 2.6 for a flow chart of the Stage 1 procedures. To process the time information, values of the observational universal time in the image header files are extracted and then transformed into a fundamental time in seconds, otherwise known as *zerotime*. This is used to reference and output a time array for each intensity to the corresponding pixel location, with the first frame now starting at zero seconds. *makefluxfast.pro* makes the data cube, and then extracts the intensity information for each pixel in the ROI. The output would be two arrays, one containing the *time-step* in seconds of the images and the other the *intensity value* of the pixels. For each pixel in the ROI, an individual file is written out into the 1_FILEDIR in text format with two arrays, time and intensity flux, see Figure 2.7. There are also plots for each corresponding pixel text file written out the 1_PLOTDIR directory, that plots the intensity per time per file number, see Figure 2.8.

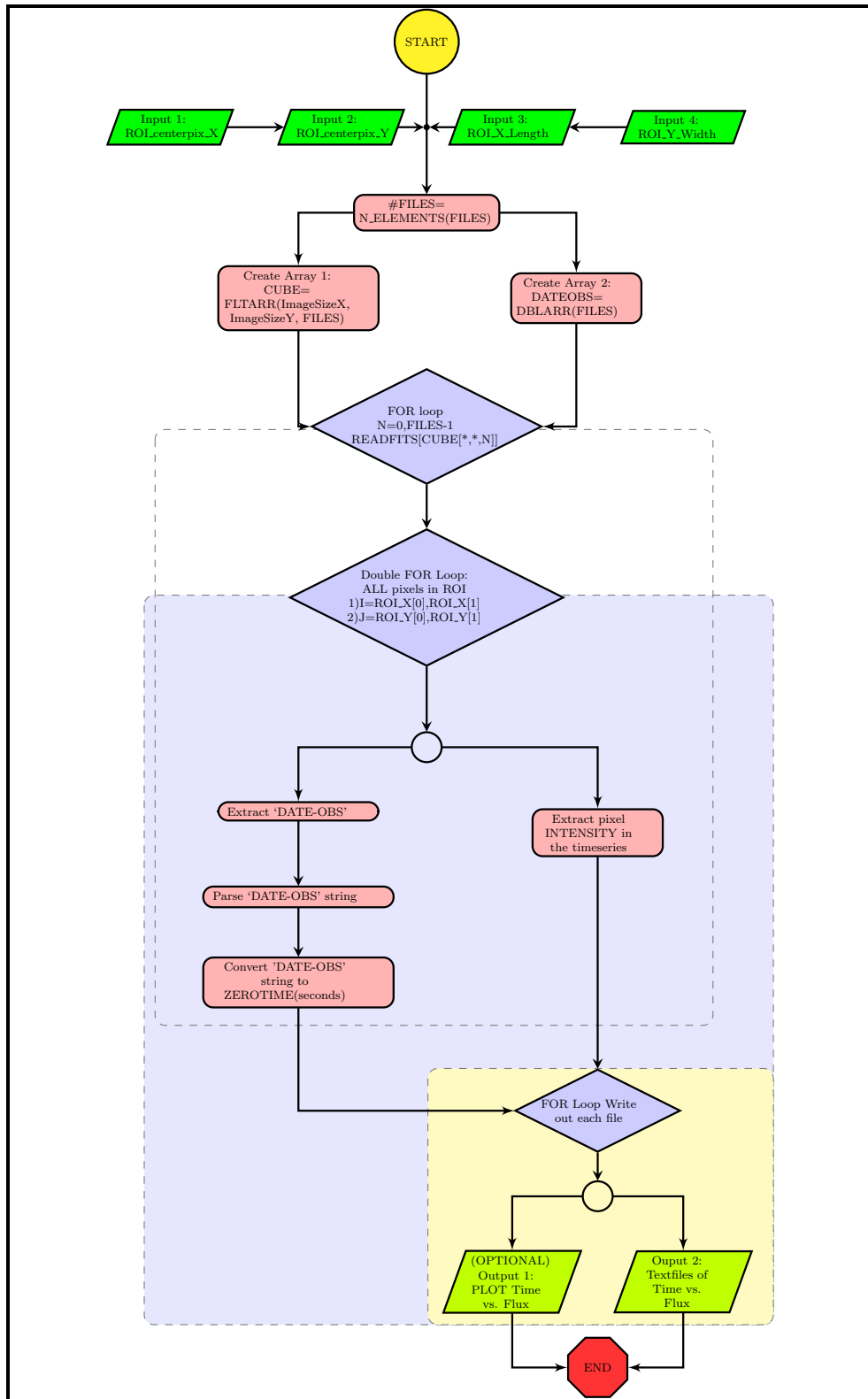


Figure 2.6: Stage 1 flowchart.

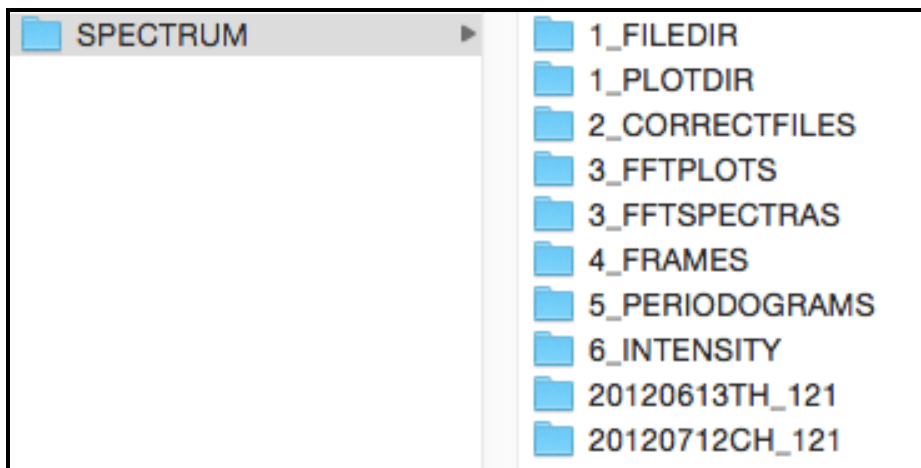


Figure 2.7: GONG file processing order.

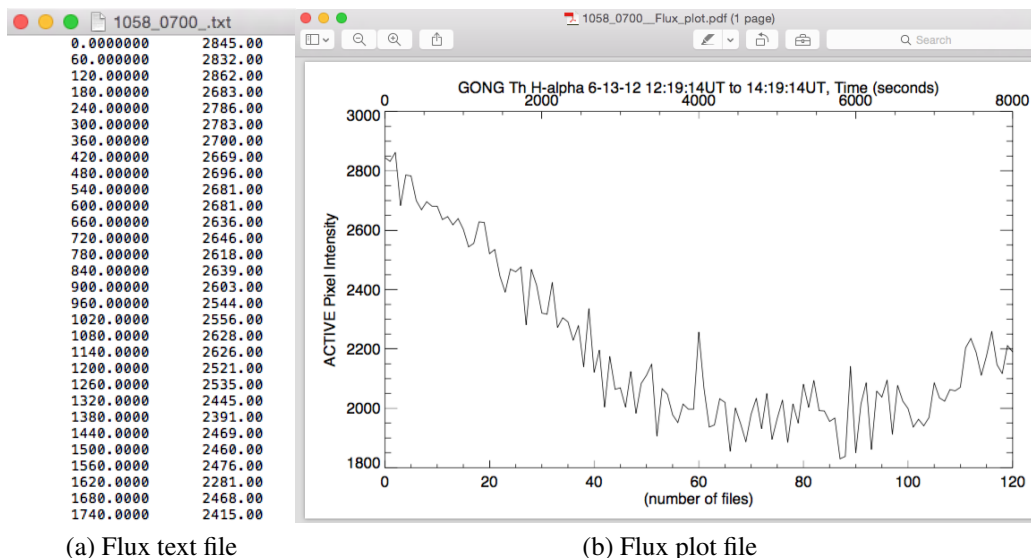


Figure 2.8: Plots for each corresponding pixel text file written out in the 1_PLOTDIR directory, that plots the intensity per time per file number

2.2.2 Stage 2 – Correction on missing frames

However, the time series of images may not be perfect, so some of the frames may be missing; especially if there were discrepancies on the images caused by the weather or an instrumentation glitch. So stage two corrects for this, placing the missing values in the time array and filling in the missing flux values with zeros. This therefore, creates a blank image frame of zeros and substitutes it into the missing time image. The first code that does this for an individual pixel is the *fillervals* function code, see flowchart in Figure 2.9. But this has to be done for each pixel in the ROI and so a calling procedure is written into the second code: *correctroi.pro* wrapper. This will call the *fillervals* function to repeat it's procedure for each pixel in the ROI. The corrected flux data is written in a two array text file containing the time array that is corrected, and the zero intensity value substituted into the missing file. Each of these files corresponds to a pixel in the ROI and is then written into the 2_CORRECTFILES directory. It is important to note that for the candidates chosen, in Chapter 3, no frames within the two hour time series for each candidate were missing. The author preferred not to use zero frames in the data for this study. Later the *correctroi.pro* will be useful as a time series quality check for the SDO images in Chapter 4.

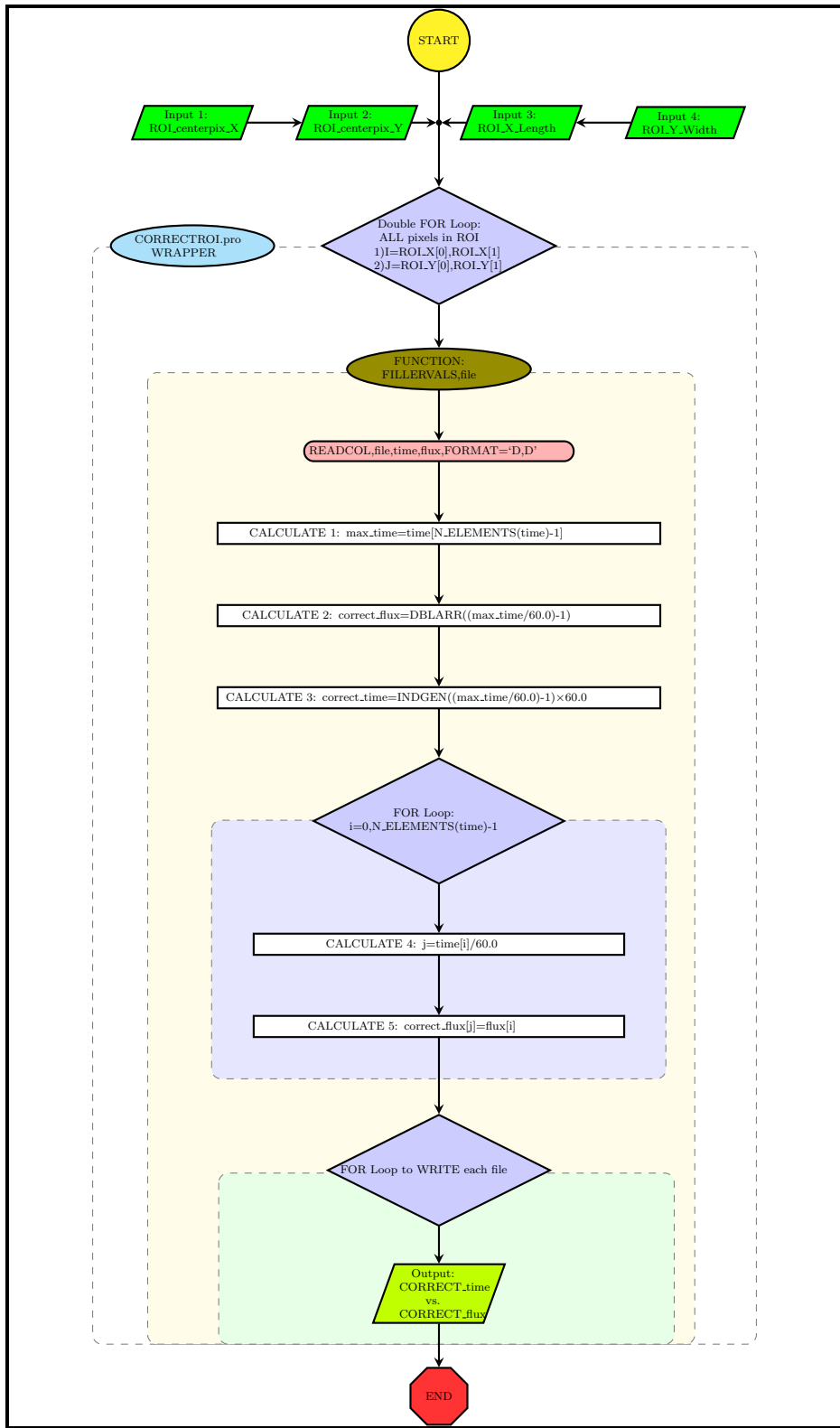


Figure 2.9: Stage 2 flowchart.

2.2.3 Stages 3 and 4 – Power Map Movie wrapper

The third stage of the coding pipeline encompasses a group of programs containing the algorithms to calculate the power spectrum in a specified frequency range and also calculate the average of the power values. There are a total of five codes in this stage: two sets are calling each other and a wrapper program encompasses the two sets of codes, see flowchart in Figure 2.10. The first step in stage three, *fftspectrum*, takes the corrected files produced in stage two and then does the FFT on a pixel time rod. This transforms the time domain array of those files into the frequency domain, along with their corresponding intensity values into power. The *fftspectrum* program does this for one pixel and then writes the two arrays, frequency and power, out to a text file. The *fftroi* program does this for all pixels in the ROI and a calling procedure is written into the program that calls the *fftspectrum* code, repeatedly for each pixel in the ROI. The output is written to a directory in the form of a text file for each pixel coordinate in the ROI. The frequency-power plot has a limit ~ 8.4 . This is the Nyquist limit and is based on the sampling frequency.

The next set of codes in stage three calculates the average of the power spectrum. *freqavg* averages the power in the inputted frequency value range. The *freqavgroi* program calls the *freqavg* program to do this for all the pixels in the ROI. The output is a fits file image of the power spectrum, known as a periodogram. The wrapper program *makeframe* calls the four sets of code to repeat and make a power map or one single frame of the power map movie. The power map movie was automated by creating another wrapper program *pmmovie.pro* to call the *makeframe* program to automatically make the frames of the power map movie. So each frame of the power map movie is a sampling of the complete time series. In other words, it is a sequence of data cubes sampled along a time domain. For the GONG data the time sampling is jumped one minute for each data cube. This is to evolve the frequency power maps through the time domain and study the behavior of the power in different regions.

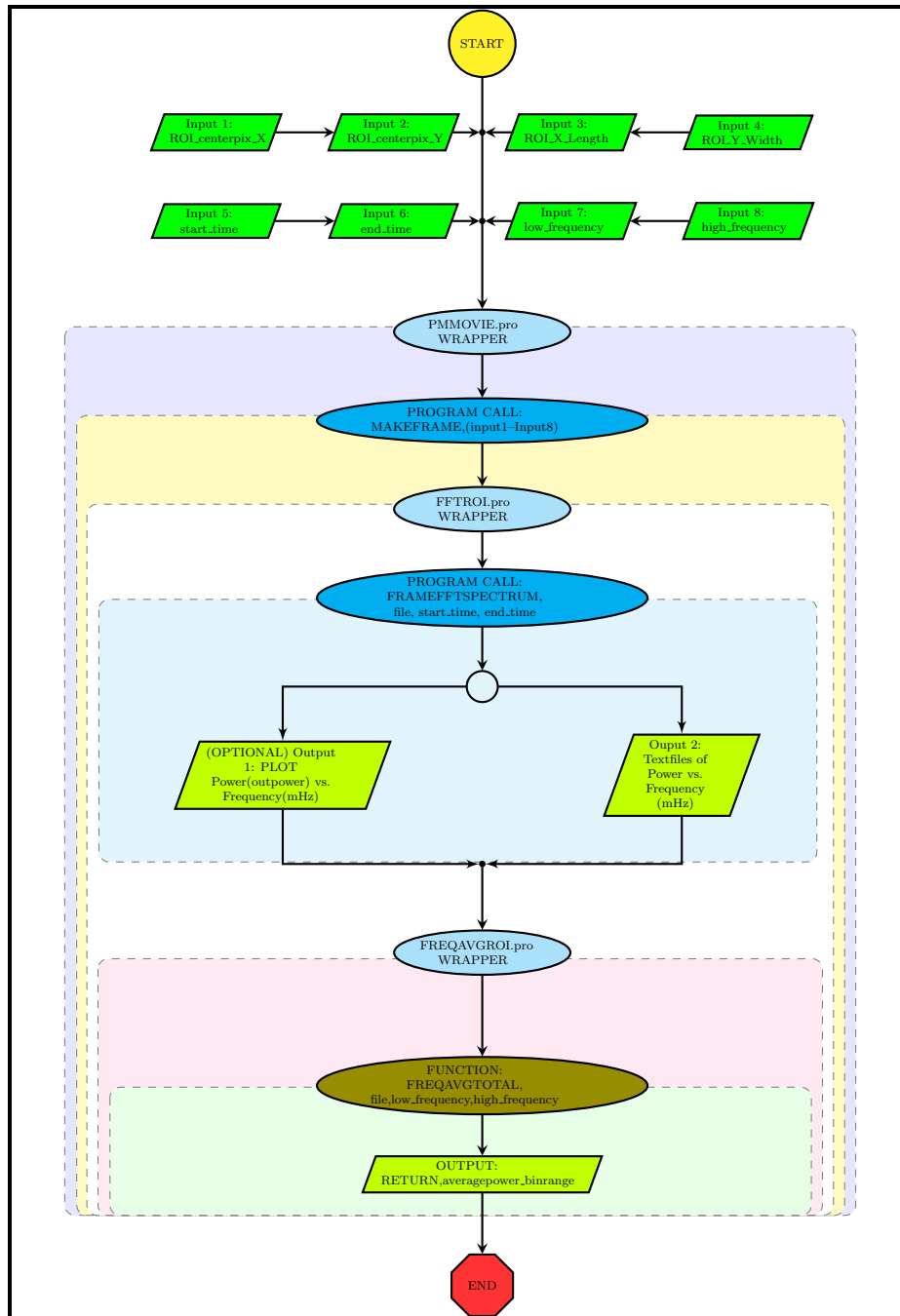


Figure 2.10: Stage 3 and 4 flowchart.

2.2.4 Stage 5 – Periodograms

The fourth stage consists of analysis codes. The *color fits* code colorizes the original greyscaled image frame and adds the X and Y axis labels. It also writes the images out

into a png (Portable Network Graphics) file format to make for visual presentation. The other series of analysis codes are the codes to study regions in $H\alpha$ by taking a smaller pixel region and calculating the average on a 3 by 3 pixel region and then plots the results.

Chapter 3

Temporal Evolution of Chromospheric Oscillations in Flaring Regions – A Pilot Study

Published in: *The Astronomical Journal (AJ)*, Volume 152, Issue 4 (2016)

DOI: 10.3847/0004-6256/152/4/81

3.1 Introduction

The relationship between solar acoustic oscillations, active regions, and energetic flares remains an open question in solar physics. A fundamental question is whether acoustic oscillations are enhanced, suppressed, or perhaps both, in active regions and by flares, and how these power enhancements and/or suppressions behave as functions of time before, during, and after energetic flaring events. Solar flares release great amounts of energy and so in principle are capable of exciting acoustic oscillations in the magnetically active sunspot regions, perhaps by exciting velocity oscillations in regions where a higher-class solar flare has taken place (Kumar and Ravindra, 2006). The first clear observations of helioseismic waves produced by a flare were by Kosovichev and Zharkova (1998) using data from the Michelson Doppler Imager on board the Solar and Heliospheric Observatory space mission. It is expected that this production of waves will change the characteristics, such as the power, of the p-modes (Ambastha *et al.*, 2002, 2003b,a; Kumar and Ravindra, 2006; Kumar *et al.*, 2006, 2010, 2011).

In addition, Braun *et al.* (1987) and others have observed that sunspots absorb acoustic power in the photosphere. These authors found that outgoing waves were reduced in amplitude by 50% compared to incoming waves (Braun *et al.*, 1987).

Observations of acoustic modes in the chromosphere using the H α line were first carried out by Elliott (1969) and later by Harvey (1993). Observations of H α intensity os-

cillations in solar flares were performed by Jain *et al.* (1999). Chromospheric oscillations in the 3.4 mHz and 5.6 mHz p-mode frequencies were found, confirming Elliott’s study of their existence and also agreeing with Kneer and von Uexkuell (1983). They surveyed 18 locations around two flares with Fourier power spectra and clearly found prominent 5 and 3 minute modes in H α (Jain and Tripathy, 1998). Furthermore, the observation of short-time variations of the Sun’s chromosphere observed in H α , contributes to our understanding of the atmospheric dynamics and could reveal progenitors for chromospheric heating mechanisms (Kneer and von Uexkuell, 1985).

We are interested in studying the acoustic frequency spectrum to investigate energy transfer in the chromosphere (Kneer and von Uexkuell, 1983). Our method incorporates a short time-series analysis to study the time variations in the Sun’s chromosphere observed in H α . Studying the chromosphere in the Fourier spectrum, and observing the temporal evolution gives us an advantage in that it provides a way to trace the temporal behavior of specific structures involved in the flare, which can be rather difficult to follow over the course of several minutes or hours otherwise (Kneer and von Uexkuell, 1985).

A technique for studying the p-mode excitation due to solar flares in a three-dimensional Fourier analysis was devised by Jackiewicz and Balasubramaniam (2013) in their “*frequency-filtered amplitude movies (FFAMs)*”. This method is simple and powerful in that it preserves the initial 3-dimensional information in the inputted time series by incorporating a moving power map method. Here we employ this novel approach to the Global Oscillation Network Group H α data set to create power-map movies (PMMs). From these PMMs we investigate the H α oscillatory modes across the frequency band ($0 < \nu < 8.33$ mHz) and characterize the temporal and spatial evolution of these oscillations in flaring regions.

In Section 3.2 we describe the X-ray flare data and the GONG H α time-series data that we employ in our analysis. We specifically study three active regions, directly over sunspots, in which M- or X-class flares occurred on 2012 June 13 and 2012 July 12. Section 3.3 describes our data reduction and analysis methods. In Section 3.4 we then present

the results of how the frequency distribution evolves temporally and spatially by constructing a PMM of each region. We find that, in the core regions of all three flares, the low-frequency power ($\sim 1\text{--}2$ mHz) is substantially enhanced immediately prior to and after the flare, and that power at all frequencies up to 8 mHz is depleted at flare maximum. This depletion is both frequency- and time- dependent. These variations are not observed outside the flaring region. In addition, dark lanes of reduced wave power are also visible in the power maps. Finally, in Section 3.5 we conclude with a discussion of these results. The observations may indicate that acoustic energy is being converted into thermal energy at flare maximum, while the low-frequency enhancement may arise from an instability in the chromosphere and provide an early warning of the flare onset. We also suggest that the dark lanes observed may arise from the interaction of the acoustic waves and the magnetic field. Suggestions for next steps to advance this work are also provided.

3.2 Observational Data

The data set used here comprises GONG $H\alpha$ intensity images centered at a wavelength of 6562.8 \AA . The GONG $H\alpha$ network became operational in 2010; it consists of a set of six detectors placed around the Earth for nearly continuous solar full-disk observations. The images have a cadence of 1 minute and a format of 2048×2048 pixels.

Our initial study analyzes two individual data sets taken from two different GONG stations; El Tiede and Cerro Tololo. Each data set covers approximately two hours of time (121 images) around two solar flare events that occurred on 2012 June 13 at 13:19UT and 2012 July 12 at 16:53UT (Table 3.1). Each data set was centered in time on flare maximum, and started one hour before the event. The June 13 flare had an NOAA classification of M1 in active region AR11504, and the July 12 flare was an X1.4 in active region AR11520. The two detector data sets were not missing any time frame images.

We also use X-ray flux from the NOAA Space Weather Prediction Center (SWPC), obtained every minute with the Solar X-ray Imager (SXI) instrument on board the NOAA

Geostationary Operational Environmental Satellite 15 (GOES-15) spacecraft. We compare the GONG time-series data with the X-ray flux in the 1-8 Å wavelength band.

We carry out an analysis on active regions directly over sunspots during a flare. There are a total of three regions of interest: AR1 and AR2 in the June 13 flare (Figure 3.1), and AR3 in the July 12 flare (Figure 3.2). The regions were chosen to be located close to the central meridian to reduce projection effects (Gizon and Birch, 2005). We restrict the GONG data to the same day of universal time (UT), and to one site for image stability.

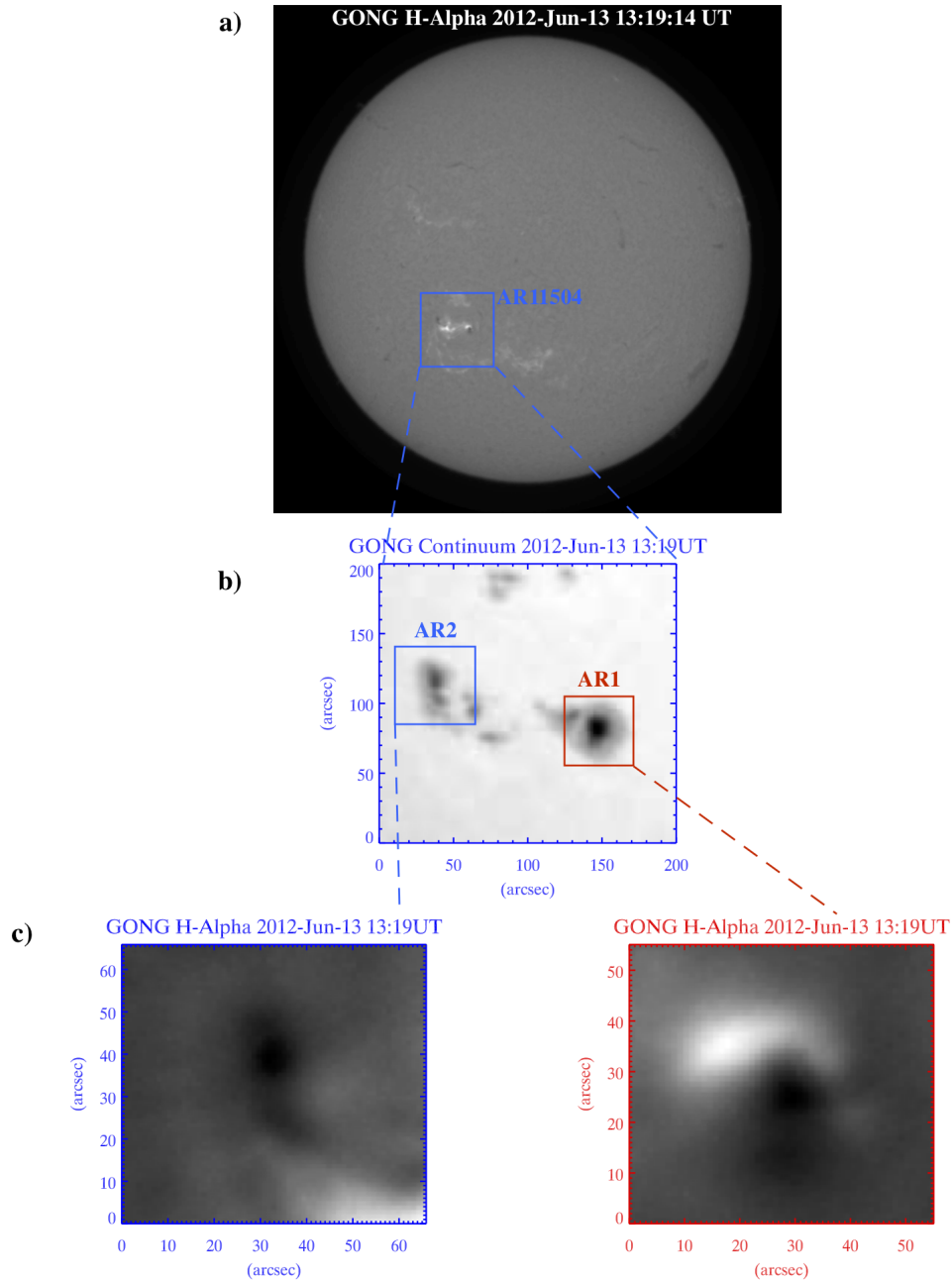


Figure 3.1: Analysis was done on solar flare regions directly over sunspots where the magnetic field was concentrated. a) The event is the M1 flare that occurred on 2012 June 13 at 13:19UT. b) Our region of interest is AR1, an ideal candidate with an active flaring region directly over a sunspot in AR11504, and the smaller active region AR2, a companion sunspot within that region. c) The main regions of interest have a rectangular area of approximately between $55'' \times 55''$ for AR1, and $65'' \times 65''$ for AR2.

Table 3.1: Table of observational information of the three data sets.

Data Set	Date	Active Region (AR)	Average Locations	Flare Locations	AR Class	Event Time (UT)	Images	GONG Station	Cadence [min]
AR1	13-June-2012	AR11504	S17E26 (-399",-375")	S17E26 (-399",-375")	M1	13:19	121	El Teide	1
AR2	13-June-2012	AR11504	S17E26 (-399",-375")	S17E26 (-399",-375")	M1	13:19	121	El Teide	1
AR3	12-July-2012	AR11520	S17W08 (126",-385")	S17W08 (126",-385")	X1.4	16:53	121	Cerro Tololo	1

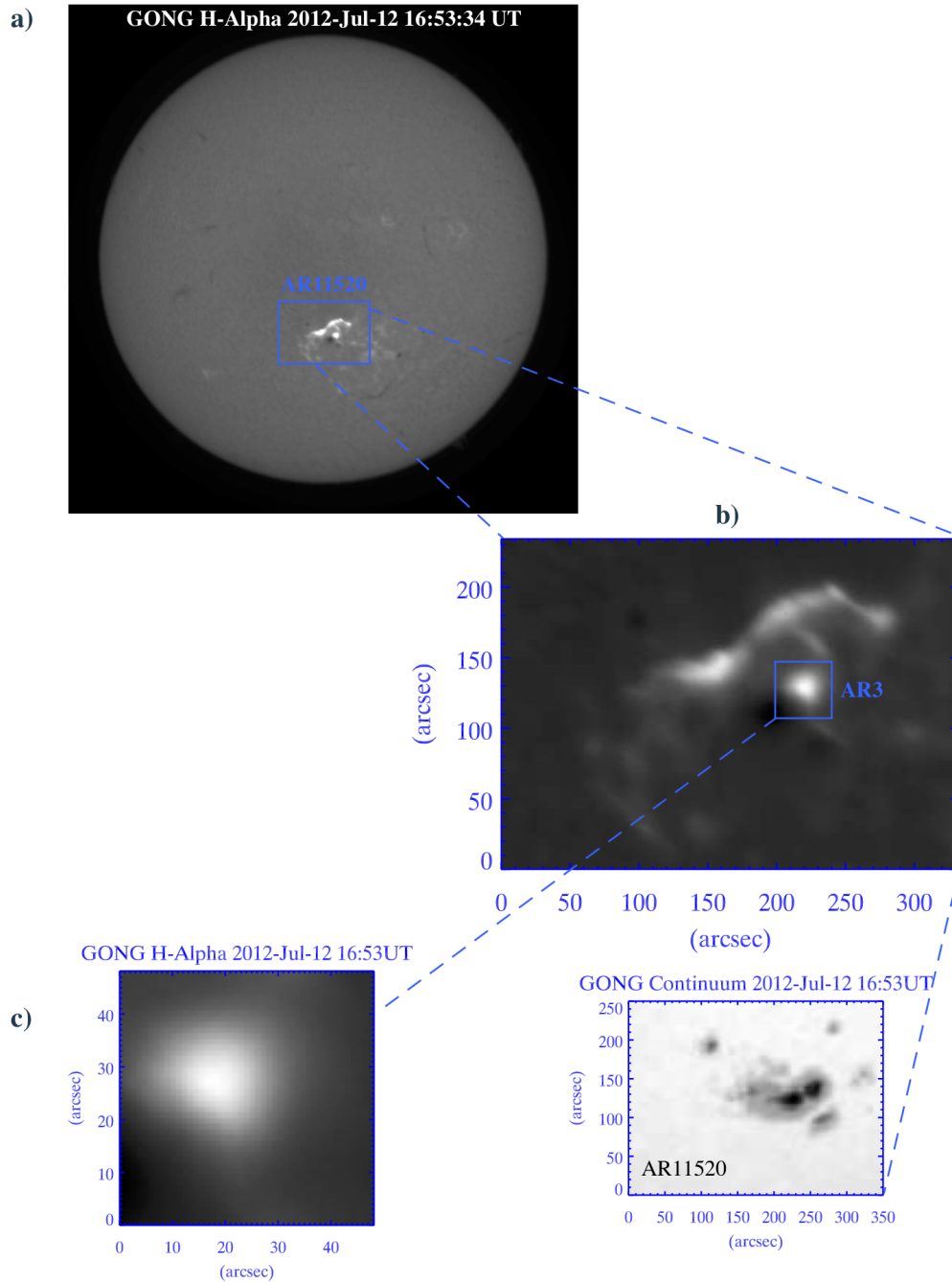


Figure 3.2: Analysis was done on solar flare regions directly over sunspots where the magnetic field was highly concentrated. a) The event is the X1.4 flare that occurred on 2012 July 12 at 16:53UT. b) Our region of interest, AR3, was a nearly spherical flaring region directly over a sunspot in active region AR11520. The sunspot morphology of AR11520 is depicted in the GONG continuum image below. c) The main region of interest, AR3, has a rectangular area of approximately $48'' \times 48''$.

3.3 Data Analysis and Reduction Methods

We employ a technique similar to the “*FFAMs*” (Jackiewicz and Balasubramaniam, 2013) to construct a PMM. In summary, a PMM consists of a time series of acoustic power maps that show wave power as a function of frequency and space, but with an initial starting time that is systematically offset. For a given starting time, the power maps are created by applying a fast Fourier transform (FFT) in the temporal direction for each pixel in the region of interest. The starting time is then shifted by one minute and the procedure is repeated.

In detail, we start with a time series of GONG H α intensity images, $I(x, y, t)$ in a data cube with a cadence of 1 minute. We define a region of interest (I_{ROI}) covering the area $x_1 \leq x \leq x_2$ and $y_1 \leq y \leq y_2$ within the large data cube. We extract the time series at each ROI pixel over a temporal length N starting at time t_i . Missing images are replaced by a value of zero. The input data for the PMM are constructed by incrementing t_i . Explicitly, we have

$$I_{ROI}(x', y', t', t_i) = I(x_1 \leq x \leq x_2, y_1 \leq y \leq y_2, t_i \leq t \leq t_i + N) \quad (3.1)$$

For our analysis here, t_i is incremented by one minute, $0 \leq t_i \leq 60$, and $N = 60$, producing a set of 61 time series, each an hour long, that start at one hour prior to flare maximum, and end at one hour after flare maximum.

To create a single frame, P , in the PMM, we apply an FFT in the temporal direction to the time series for each spatial pixel in I_{ROI} , and then take its modulus, producing

$$P(x', y', \nu, t_i) = |FFT(I_{ROI}(x', y', t', t_i))|^2 \quad (3.2)$$

where ν is the temporal frequency. The power P is then averaged in frequency bins ν_i , producing one frame in the PMM, Equation (3.3).

$$PMM(x', y', \nu_j, t_i) = \frac{\Delta\nu}{\nu_2 - \nu_1} \sum_{\nu_1 < \nu_j < \nu_2} P(x', y', \nu, t_i) \quad (3.3)$$

where $\Delta\nu$ is the frequency resolution of the power spectrum ($277.8 \mu\text{Hz}$) and ν_1 and ν_2 are the lower and upper limits respectively of frequency bin j . We define a set of seven bins ν_j of width 1 mHz starting at 1 mHz, with the highest band covering 7–8.33 mHz.

Within the areas AR1–AR3, we extract a number of smaller regions of 3×3 pixels, or approximately $3.2''$ in length, and then average the PMM values within these small areas. Averaging the pixels over a smaller region improves the signal-to-noise ratio and allows us to isolate different physical conditions. We kept all subregions the same size to maintain consistency within the experiment.

To compare the PMM data with the intensity, we carry out a 60 minute running average of the intensity that is incremented by one minute to provide the same sampling as the PMM. Figure 3.3 shows a power-map frame for region AR3 for each ν_j along with the averaged intensity. The sampling window in Figure 3.3 is from 32 to 92 minutes in the total time series.

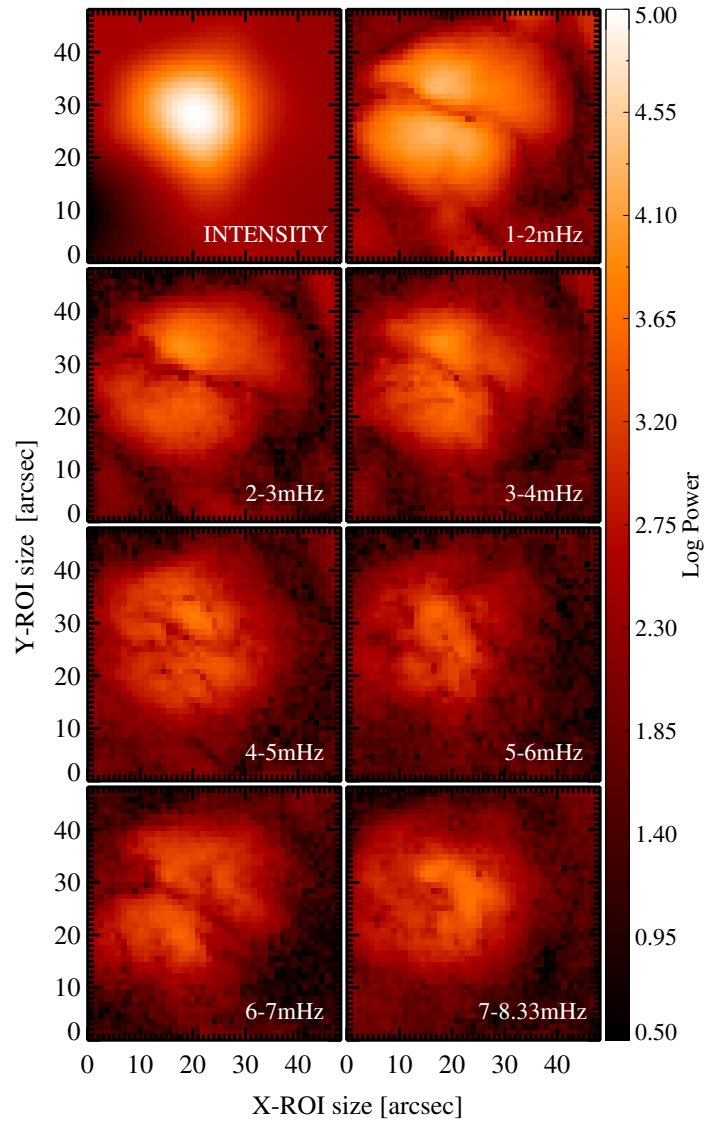


Figure 3.3: The flare intensity and frequency-binned PMM frames of the X1.4 flare on 2012 July 12 in region AR3. The PMM frames are in the time window of 32–92 minutes. Dark lanes are seen in each frame and are sharper in the 1–2 mHz and 2–3 mHz ranges. The power is measured in arbitrary instrumental units.

3.4 Results

In this section, we present the results of our time-series power spectrum analysis on each of the three flaring active regions defined in Section 3.2. Within each of the three main analysis regions—AR1, AR2, and AR3—we define several subregions in and around the centers of the active regions in order to relate the temporal behavior of the oscillation power to different spatial positions. As we discuss below, the overall results for all three analysis regions are qualitatively similar, so we describe the results for one of the three regions in detail and then more briefly summarize the similar results for the other two regions. We find that, in the core regions of all three flares, the low-frequency power (~ 1 – 2 mHz) is substantially enhanced immediately prior to and after the flare, and that power at all frequencies up to 8 mHz is depleted at flare maximum. This depletion is both frequency- and time-dependent. We also observe dark lane features in the power maps. We defer a discussion and interpretation of these general findings to Section 3.5.

3.4.1 AR3

There are three main groups of subregions for area AR3. Figure 3.4 shows seven rectangular subregions, each approximately $3.2'' \times 3.2''$, distributed around the solar flare and the dark lanes. The subregions are selected to probe the temporal behavior at various levels of overall power and at various positions relative to the center of the active region. We present the results by grouping the subregions accordingly. Obviously these are not the only subregions that could be selected; we emphasize that this selection of subregions is made arbitrarily, and on the basis of visual impression, but in an attempt to sample the active region at various representative locations relative to the peak of activity. The regions with the lowest power (log power 0.5 to 2.0), are AR3_1 and AR3_6 (Figure 3.7 (a) and (b)). The regions with mid-level power levels (log power 2.0 to 3.0) are AR3_2 and AR3_5 (Figure 3.6 (a) and (b)). The regions located in the middle of the flare (AR3_3, AR3_4

and AR3_7) exhibited the greatest amount of power (Figure 3.5(a)–(c)), with logarithmic values from 3.0 to 4.5.

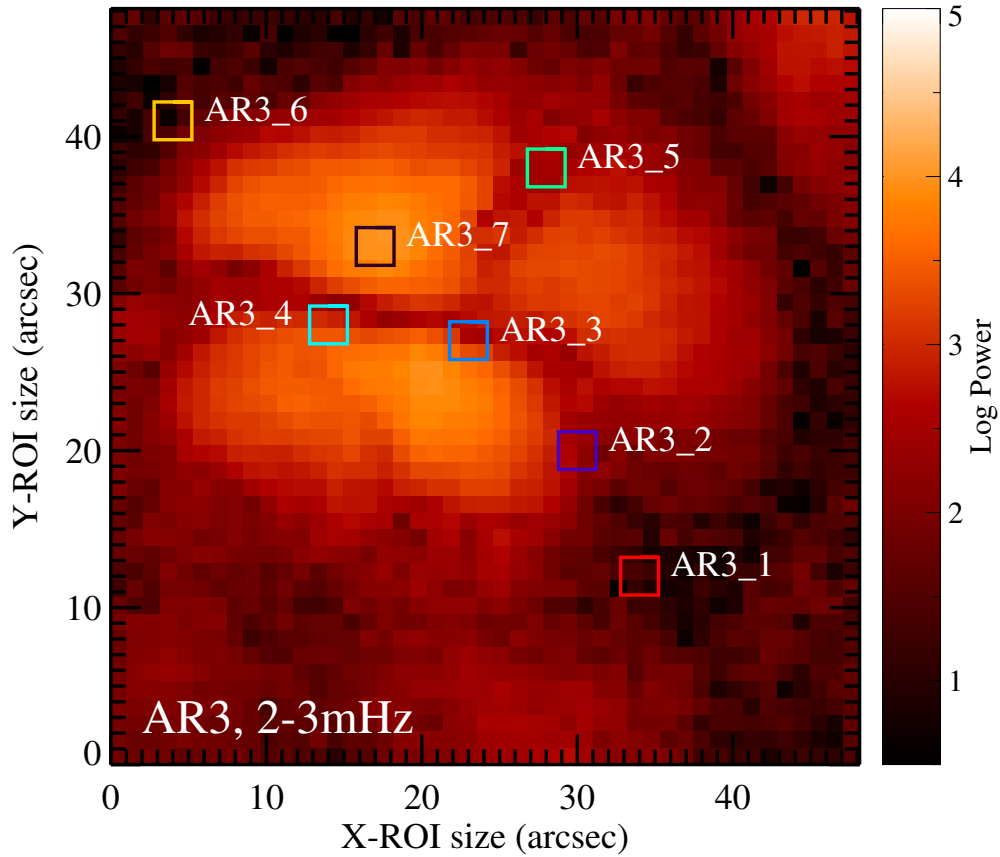


Figure 3.4: Region AR3 has a rectangular area of approximately $48.15'' \times 48.15''$. There are seven subregions sampled in AR3 for the X1 solar flare on 2012 July 12. The subregions are approximately $3.2'' \times 3.2''$ in size. In the above figure representing AR3, the PMM frame depicted is in the time window of 34–94 minutes.

3.4.1.1 Inner Flaring Regions – Locations 3, 4, and 7 in AR3

These three subregions are placed along the dark lanes and in a bright region in the flare. Figure 3.5(a)–(c) shows the power as a function of time and frequency in these subregions. We observe an increase in power across the entire frequency band once the flare begins. However, as the intensity increases in each subregion, we observe a suppression of power

that begins first at the higher frequencies, and then moves toward lower frequencies as time progresses. Maximum power suppression at all frequencies occurs at the time of the maximum local intensity. The power then increases back toward pre-flare levels, with the lower frequencies recovering first. The result is the appearance of a “V”-shaped feature in the color plots of Figure 3.5. For each subregion, the lowest frequency band (1–2 mHz) shows the greatest power.

The overall temporal extent of the “V”-shaped decrease in power is shortest for subregion AR3_4, which might be a consequence of the narrow spatial width of the dark lane in that region. The suppression in power in AR3_3 (Figure 3.5(a)) is wider in time, perhaps due to the larger width of the dark lane in that area. AR3_7 (Figure 3.5(c)), free of dark lanes, shows the longest time period of power suppression. Figure 3.5(d) shows the total average intensity variations for each of the three regions along with the *GOES* X-ray flux.

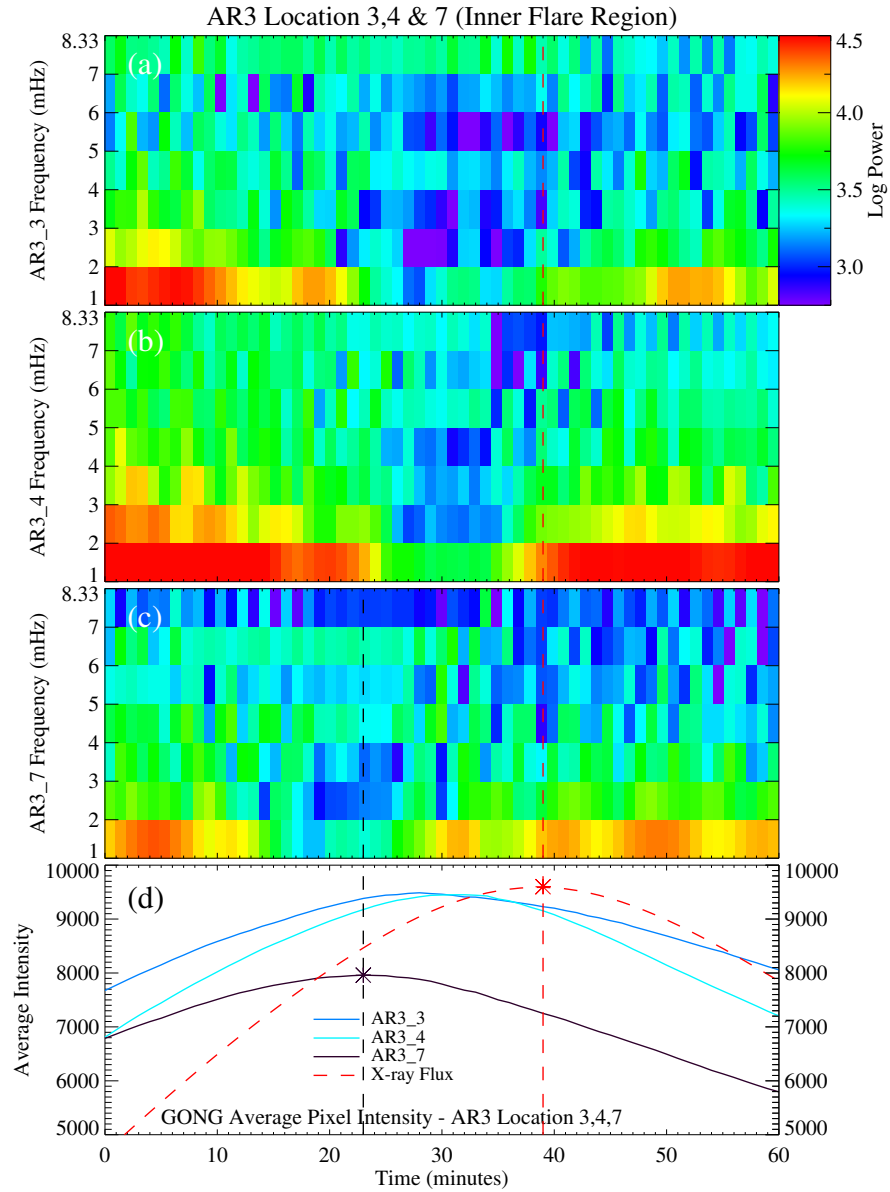


Figure 3.5: Time-frequency power plots of the three subregions AR3_3 (a), AR3_4 (b) and AR3_7 (c) along with the corresponding average intensity (d). The *GOES* X-ray flux is scaled as a reference for the overall solar flare event. The red dashed line indicates the time of flare maximum in the time series at 39 minutes.

3.4.1.2 Outer Flaring Regions – *Locations 2 and 5 in AR3*

Regions AR3.2 and AR3.5 both lie on the outer edge of the dark lanes, as shown in Figure 3.4. The overall power for these two regions are in the middle range of log power, 2.0–3.0. The corresponding time-frequency plots are shown in Figure 3.6.

These plots have a substantially different qualitative nature compared to those in Figure 3.5. Here, there is no sign of the “V” shape in these time-frequency images. For region AR3.2 (Figure 3.6(a)) there is an overall increase in power for the 4–5 mHz frequency band, with logarithmic values in the range of 2.6 to 3.0 - also observed in region AR3.1 (Figure 3.7(a)). A decrease in power for frequencies above 5 mHz (Figure 3.6(a)) is present at the start of the time series and persists to around 35 minutes. There appears to be a trend of increasing power late in the time series in the frequency band of 1–2 mHz. For region AR3.5 (Figure 3.6(b)) there are three areas of power suppression within the 1–2 mHz band. A period of fluctuating suppression is also observed in the 5–6 mHz band.

Figure 3.6 shows that these two subregions have substantially lower levels of average intensity variations than those in Figure 3.5. This suggests that rapid changes in the average intensity are at least partially responsible for the power variations in the oscillations.

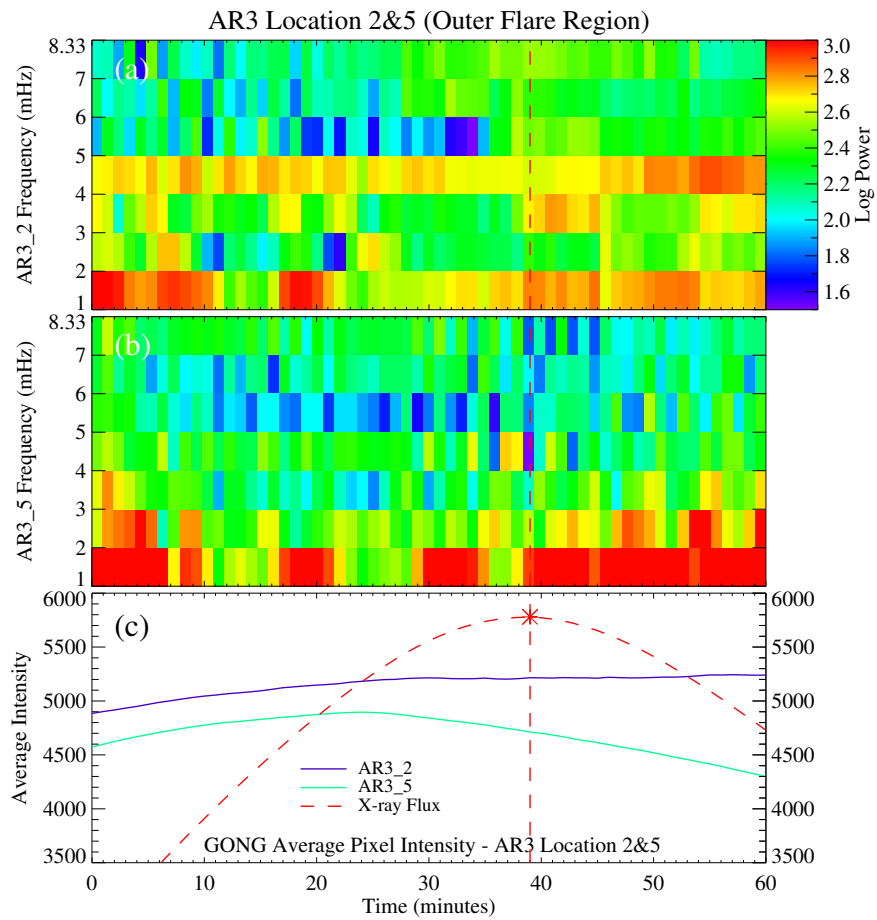


Figure 3.6: Analysis of the two outer flare regions, AR3.2 (a) and AR3.5 (b), along with the corresponding pixel intensity and *GOES* X-ray flux (c). The *GOES* X-ray flux is scaled as a reference for the overall solar flare event. The red dashed line indicates the solar flare event in the time series at 39 minutes.

3.4.1.3 Quiescent Regions – *Locations 1 and 6 in AR3*

Regions AR3_1 and AR3_6 both lie on the outer edge of the solar flare and in very dark outer regions. The overall logarithmic power for these two regions is in the lowest range of 0.6–2.0, Figure 3.7.

These areas also do not show the “V”-shape suppression feature. For region AR3_1 (Figure 3.7(a)) there is an overall increase in the power in the frequency band of 1–6 mHz. Some power suppression is apparent in the time period of about 8–42 minutes. The overall power has a maximum in the 5–6 mHz band.

Region AR3_6 (Figure 3.7(b)) shows an overall suppression of power in all frequency bands that starts at the time of maximum X-ray intensity. This region also shows a substantially higher power level at frequencies of 1–3 mHz than at 6–8 mHz.

As in Figure 3.6(c), the curves of average intensity curves in Figure 3.7(c) do not show much relative variation. This is consistent with the hypothesis that the “V” shape is related to the presence of strongly varying intensity.

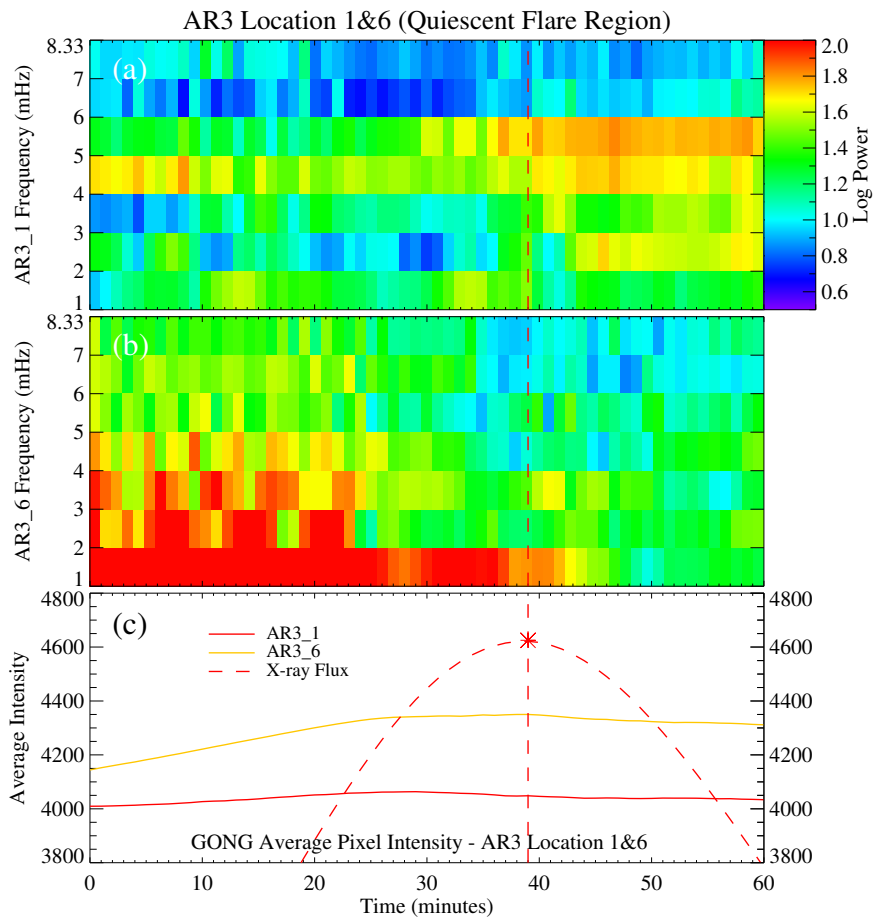


Figure 3.7: Analysis of the two quiescent flare regions: AR3_1 (a) and AR3_6 (b), along with the corresponding pixel intensity and *GOES* X-ray flux (c). The *GOES* X-ray flux is scaled as a reference for the overall solar flare event. The red dashed line indicates the solar flare event in the time series at 39 minutes.

3.4.2 AR1

Region AR1 has an area of approximately $55'' \times 55''$ (Figure 3.8). As with AR3, we select seven subregions intended to probe the temporal evolution of the flaring event at various spatial locations relative to the center of the active region. Each of the seven subregions samples a rectangular area with $3.2''$ per side. AR1 displays similar behavior to that of AR3 and so only the most significant of results (Figure 3.9) will be discussed. We present the results for locations AR1_5, AR1_6 and AR1_7, the regions where the M1 flare on 2012 June 13 was the most intense.

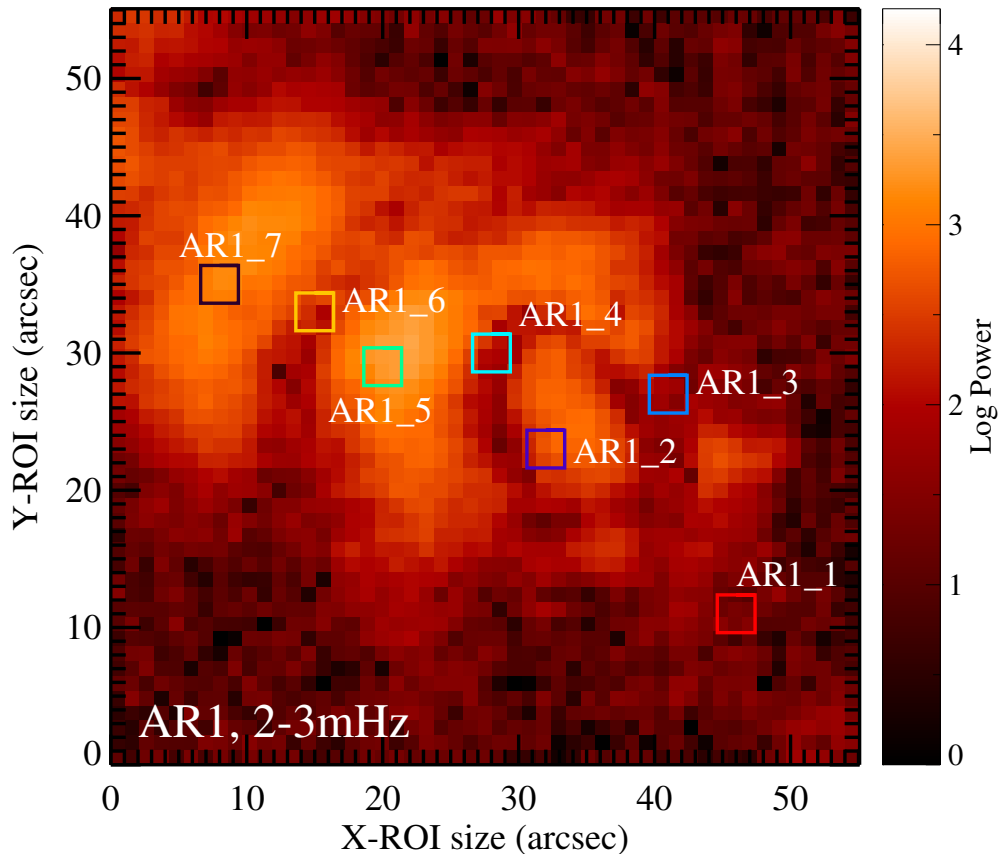


Figure 3.8: AR1 has an area of approximately $55'' \times 55''$. There are seven subregions in AR1 for the M1 solar flare occurring on 2012 June 13. In this figure, the PMM frame depicted is in the time window of 32 to 92 minutes.

The subregions where the M1 flare in AR1 was the strongest were AR1_5, AR1_6, and AR1_7. The relationship between the peak of the intensity and the suppression of power is clearly observed in Figure 3.9. The X-ray flux of the flare is scaled and plotted along with the intensity to show the time of maximum overall flaring activity (Figures 3.9(d)). The suppression of power is observed as a “V” shape for locations AR1_5 and AR1_6 (Figure 3.9(a) and (b)) with results similar to AR3_3, AR3_4 and AR3_7 (Figure 3.5). Again we see a relatively large variation in average intensity, with the point of the “V” corresponding to the intensity maximum in Figure 3.9(d).

Figure 3.9(c), shows a rather different situation with a clear indication that the power is suppressed not only at the peak of the intensity but also near a minimum. This will be discussed later.

Once again, as seen in almost all of our time-frequency power plots, the power is greatest at low frequencies below 2 mHz.

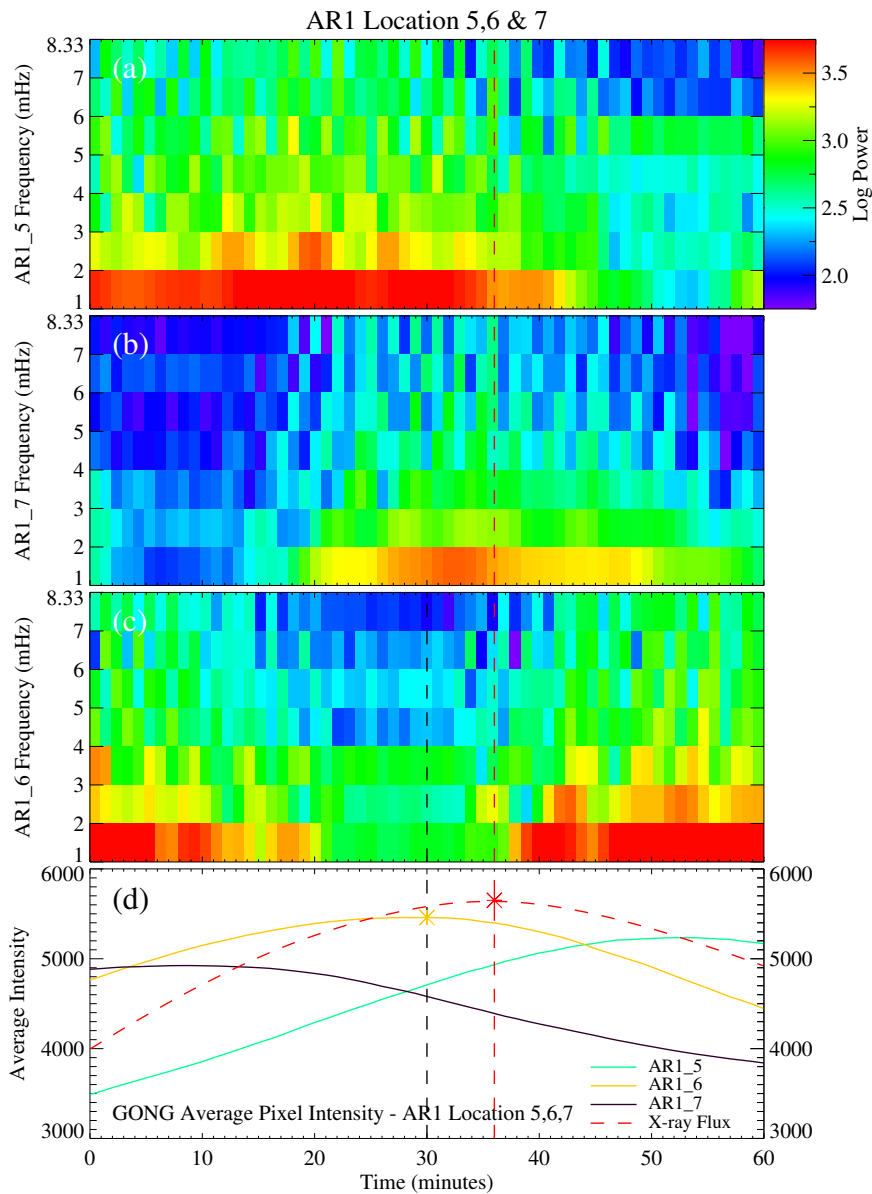


Figure 3.9: Time-frequency power plots for regions AR1_5, AR1_6, and AR1_7, showing the suppression of power in plots (a)–(c), correlating with the peak intensity (d). All three regions exhibit a peak in power around 3.75 at the lowest frequency bands of 1–2 mHz and then gradually decreasing as the frequency bands increase. The *GOES* X-ray flux is scaled as a reference for the overall solar flare event in the time series at 36 minutes.

3.4.3 AR2

Region AR2 is approximately $66'' \times 66''$ in size (Figure 3.10). This was the smaller sunspot region involved in the M1 solar flare on 2012 June 13 (Figure 3.1). Once again, we defined several subregions in order to probe the temporal behavior of the activity at various spatial positions relative to the visual center of the activity. Six subregions of $3.2''$ in size were analyzed. AR2 displayed results similar to those of both AR1 and AR3. Here we present an analysis of two of the subregions close to the center of the active region (Figure 3.11, (a) and (b)), and a control quiet subregion for comparison (Figure 3.11(c)).

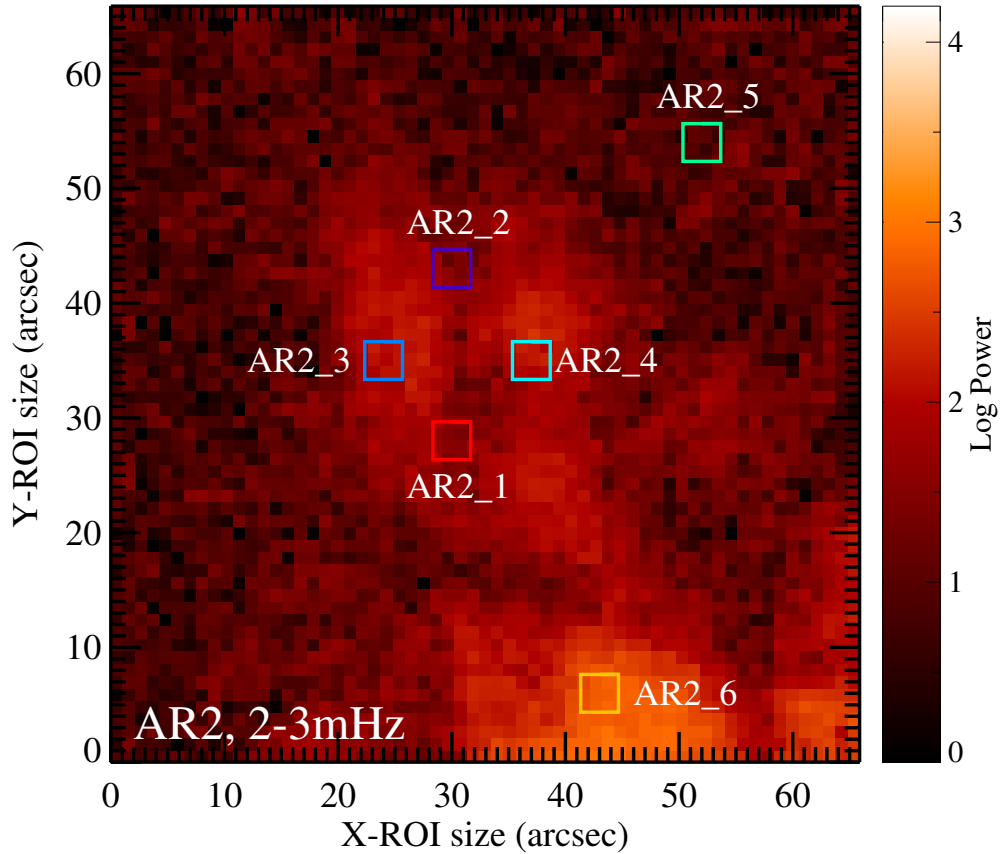


Figure 3.10: AR2 has a rectangular area of approximately $66'' \times 66''$. There are six subregions in total in AR2 for the M1 solar flare on 2012 June 13. In this figure, the PMM frame depicted is in the time window of 32–92 minutes.

Region AR2 provides observations of the oscillatory power behavior when the average intensity is slowly varying. In Figure 3.11(d) the intensity for AR2_3 is slowly increasing, while it is decreasing for AR2_4. The corresponding time-frequency images show power suppression slowly increasing for AR2_3 and decreasing for AR2_4, suggesting that the rate of change of the intensity is related to the rate of change of the oscillatory power. Again the lower frequency bands below 3 mHz show higher power levels than the bands above 3 mHz. The relatively low signal-to-noise ratio in these panels can be increased by enlarging the size of the selected subregions.

Region AR2_5 (Figure 3.10) is a quiet region that provides an observation of the acoustic power characteristics outside flaring regions. This control region shows a constant oscillatory power with no systematic temporal changes within the frequency bands (Figure 3.11 (c)). While it does show higher power at lower frequencies, the enhancement is much lower than that seen in the flare regions. Quasi-periodic fluctuations are also seen with a periods of ~ 7 minutes in the 1–2 mHz band and ~ 1 minute above 5.0 mHz. However, these may be a result of a low signal-to-noise ratio.

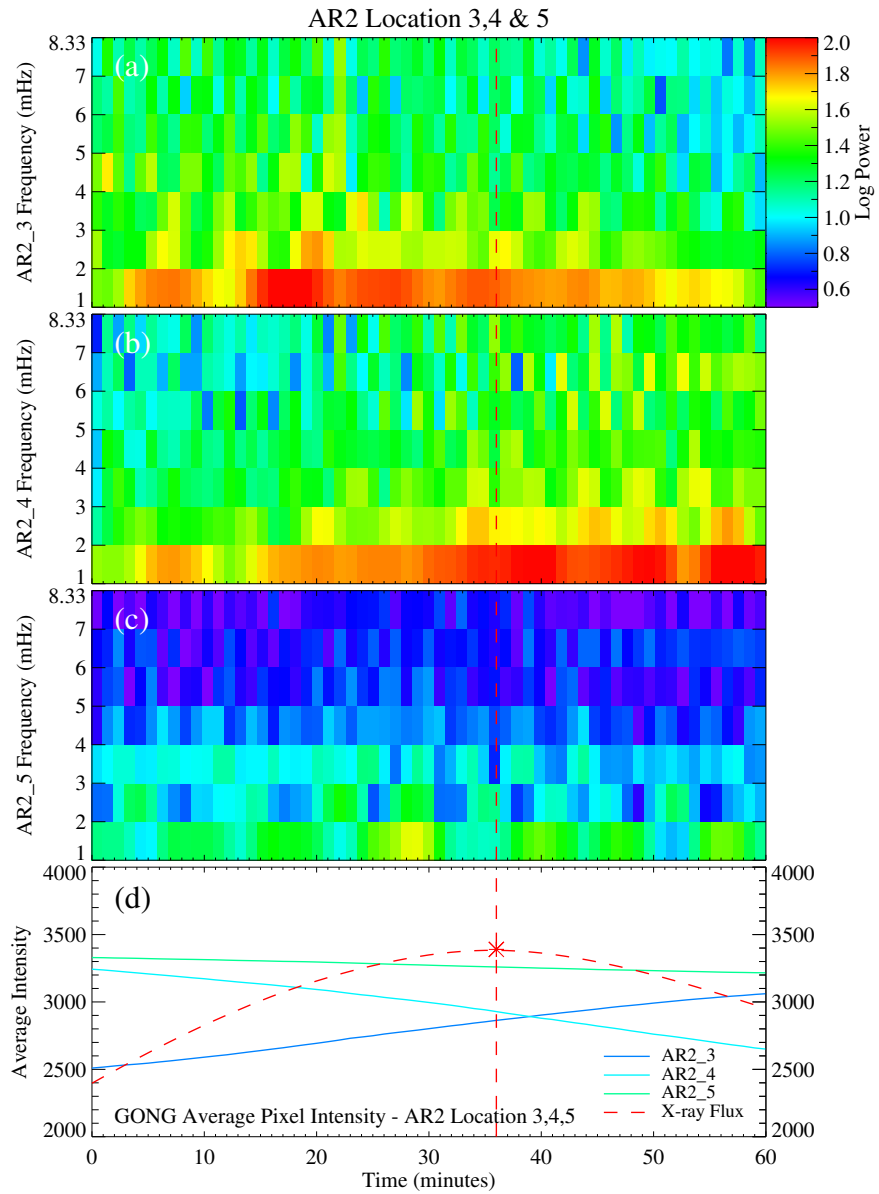


Figure 3.11: Acoustic power observations for regions AR2_3, AR2_4, and AR2_5, showing the suppression of power in plots (a) and (b) and a quiet region for reference (c). The *GOES* X-ray flux is scaled as a reference for the overall solar flare event in the time series at 36 minutes.

3.5 Discussion and Conclusions

The results in this paper demonstrate that $H\alpha$ observations of chromospheric oscillations in the p-mode band can provide information about the physical processes occurring in flaring regions. In particular, variations in the oscillatory power as a function of frequency, spatial position, and time can be used to probe energy transport at different heights within a flare.

Figures 3.5 and 3.9 show a suppression of power that first migrates in time from high to low frequencies in a flare, with a subsequent restoration of the power starting at low frequencies and progressing back to high frequencies. This produces a “V”-shaped feature in the images of the power as a function of frequency and time. The shape can be understood as a consequence of the nature of the observations, the behavior of the $H\alpha$ spectral line during a flare, and the height dependence of the frequency of the maximum oscillation amplitude. Wang *et al.* (2000), with their high-cadence $H\alpha$ observations from the Big Bear Solar Observatory, found high-frequency fluctuations that correlate with HXR elementary bursts. These hard X-ray emissions could be signatures of sites of fine structures where individual magnetic reconnection processes are taking place (Wang *et al.*, 2000).

One of the earliest results of studies of solar oscillations showed that the frequency at which the waves reach their maximum amplitude increases with height in the solar atmosphere (Leighton *et al.*, 1962b). In the photosphere, the maximum amplitude occurs at periods around five minutes (frequency near 3.3 mHz), while in the chromosphere the maximum occurs at periods of three minutes (frequency near 5.5 mHz). It is also known that the wings of a spectral line are formed at lower heights in the solar atmosphere than the core of the line, thus observations of oscillations obtained in the wing of a spectral line will be dominated by lower-frequency power than observations in the core of the line.

The observations discussed here are obtained with a filter that is centered on the wavelength of the $H\alpha$ line core in the quiet Sun. During the course of the flare, the motion of the plasma will change the wavelength of the line due to the Doppler effect, so that the filter

bandpass will admit a higher proportion of light from the wings of the spectral line rather than from the core. Since the wings of the line are formed at lower heights in the solar atmosphere, and since the peak amplitude of the p-modes occurs at lower frequencies at lower heights, the net effect is to reduce power at high frequencies. This reduction moves to lower frequencies as the flare progresses and the spectral line is increasingly Doppler-shifted. The overall observed intensity also increases as the brighter wings contribute a larger portion of the signal. As the flare energy decreases, the solar plasma motions die out and the spectral line core moves back toward the center of the filter bandpass, restoring the visibility of the high-frequency power and decreasing the overall intensity. A plasma velocity of 5 km s^{-1} , easily created in a flare, would move the line core by 0.1 \AA , which is a substantial fraction of the 0.6 \AA bandpass of the GONG filter.

The dark lanes in wave power, also observed by Jackiewicz and Balasubramaniam (2013), could be where the magnetic field absorbs or scatters the acoustic waves. In the photosphere, sunspots are known to be areas of suppressed acoustic mode power (Braun *et al.*, 1987). The appearance of the dark lanes depends on frequency, as seen in Figure 3.3, which may provide information on the structure of the magnetic field as well as aspects of energy transport during the flare. In addition, the time-frequency maps of subregions located on dark lanes show diverse behavior (e.g. AR3_3 and AR3_2) further suggesting that there is a variation in the underlying magnetic field. Several deductions can be made about the dark appearance of the lanes, which could indicate that energy is being removed from the observed wave frequencies and perhaps converted into the thermal energy of the flare, or scattered into other wave modes with frequencies higher than 8 mHz, or absorbed by the magnetic field in the flare, or dampened by magnetic reconnection. We believe that the correct explanation is that the wave energy is being converted into thermal energy, due to the simultaneous increase in both *GOES* X-ray flux and $H\alpha$ intensity. These possibilities can be investigated by applying the PMM technique to simultaneous magnetograms acquired by GONG. Furthermore, there is a trade-off between signal-to-noise ratio and spa-

tial resolution. Larger subregions increase the signal-to-noise ratio but decrease the spatial resolution. In this paper we chose to have higher spatial resolution in order to investigate oscillations within the narrow dark lanes.

Generally, there is a tendency for an excess of power at low frequencies below 2 mHz compared to higher frequencies. This excess can be as much a factor of 30 for the regions in Figure 3.5, but it is also present in the quiet region in Figure 3.11 at a much lower level (a factor of about 4). Since these are ground-based intensity observations, it is quite possible that some of this excess is caused by fluctuations in the Earth's atmospheric transparency. However, the marked increase in the flaring regions suggests that low-frequency power is enhanced during a flare. If this low-frequency power excess is a feature of strong flares, it may arise from an instability in the chromosphere and provide an early warning of the flare onset.

This pilot project demonstrates that the application of PMMs to $H\alpha$ intensity observations opens up a number of new avenues to explore the physical processes in flares. The temporal and spatial variations of acoustic wave power show intriguing features that contain information about the energy transport and magnetic field variations as a function of height within flaring regions.

There are several paths to follow that will further develop the method. The most informative step is the comparison of the results with the GONG magnetograms. The correlation of changes in oscillatory power with the characteristics of the magnetic field should provide additional information on the underlying physical processes. In addition, the PMM method can also be applied to the magnetograms since they are simultaneously observed at a cadence of once per minute. Additional steps will be the analysis of larger subregions, extension of the PMM method to earlier times to search for flare precursors; application of the method to longer time spans to increase the frequency resolution, analysis of additional cases of strong flares, and accumulation of statistically significant measurements. Eventually, we may be able to construct a new picture of the physics of a flare based on its acoustic

signatures.

Chapter 4

Methodology: AIA Image Processing

In this chapter several steps in the image processing of the AIA data. These steps correct for any artifacts. This study chooses to use JSOC cutouts, therefore saving data space. The flare event of choice was a X3-class flare that occurred on 24-October-2014 at 21:41UT from the NOAA active region AR12192. It was a major active region harboring a giant sunspot group, carrying strong magnetic fields that had a high probability of producing strong explosions. The sunspot group was also facing earth, see Figure 4.1. The X3 flare did not produce a major CME. This active region was a good candidate since it was located near the central meridian of the image and therefore was a good test case for the dissertation study in detecting the behavior of oscillations near an active region. The study used data from the AIA in three different wavelengths corresponding to the different heights within the solar atmosphere: AIA 1700 Å corresponds to the lower photosphere, AIA 1600 Å corresponds to the upper photosphere and AIA 304 Å corresponds to the chromospheric region.

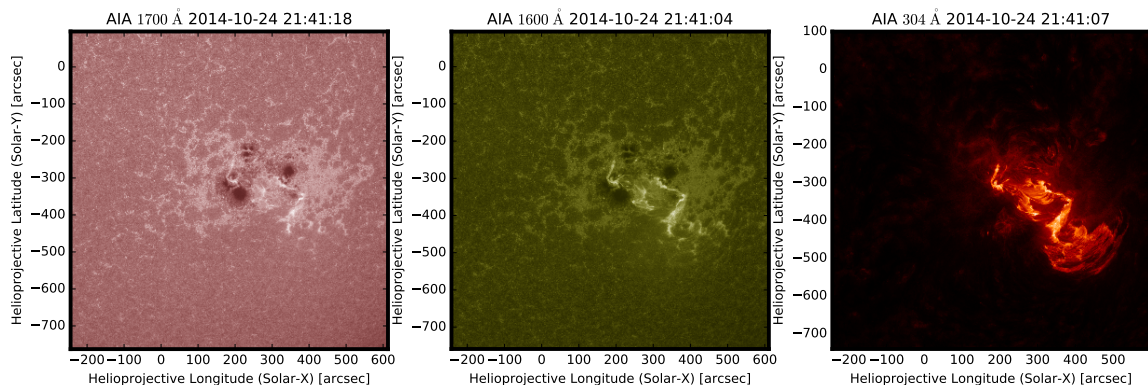


Figure 4.1: AR12192 shown in 1700 Å, 1600 Å and 304 Å wavelengths of the AIA. Active region AR12192 was a major sunspot group that produced a X3-class flare but did not produce a major CME. Credit: SDO/HMI

4.1 Data Acquisition (JSOC) - A Step-by-Step Tutorial

Data acquisition for multi-wavelength SDO's 4096×4096 square pixel images are obtained through the Joint Science Operations Center (JSOC) site, located at Stanford University. JSOC is responsible for the data sources for the AIA and the HMI. In this study the images from three different wavelengths were obtained (1700 Å, 1600 Å and 304 Å). These three wavelengths represent different levels within the solar atmosphere from the lower photosphere (1700 Å), the upper photosphere (1600 Å) to the chromosphere (304 Å). In this section, the acquisition images by a step-by-step guide through the JSOC *Lookdata* tool, will be discussed. Since JSOC will distribute all requested data in one final folder, only one wavelength at a time will be accessed. For this tutorial downloading images for the AIA 1600 Å wavelength is the method of choice. Since each 4096×4096 pixel full disk image is too large in storage size (~35 Megabytes uncompressed) to use for computation, JSOC cutouts of the full disk images with the *Lookdata* tool will be downloaded.

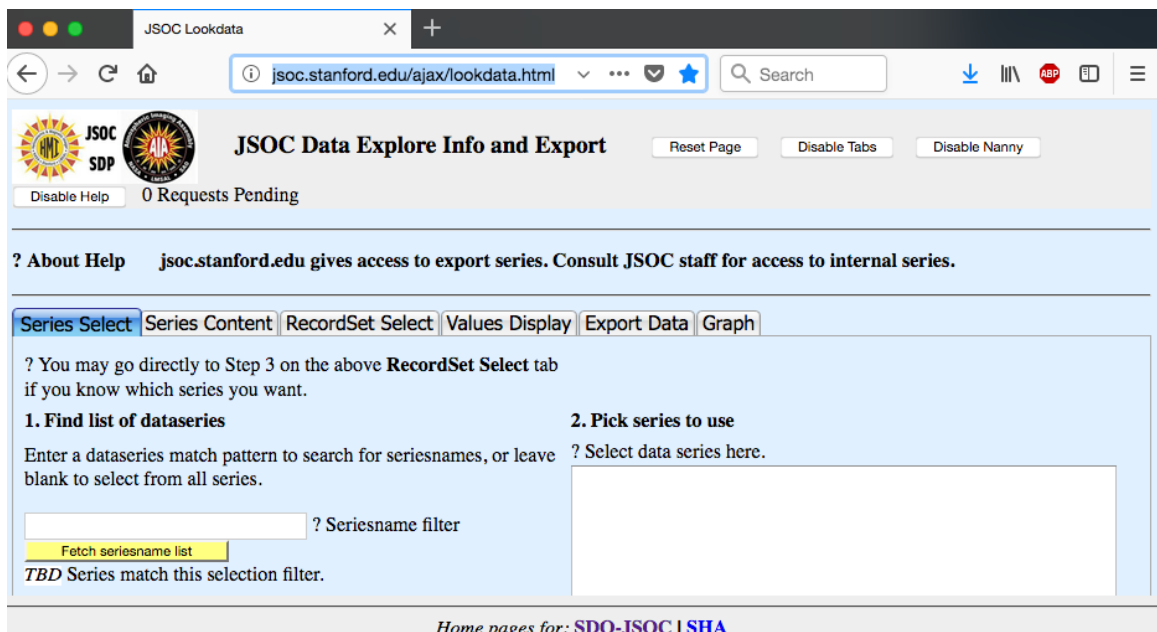


Figure 4.2: JSOC Lookdata site window.

To begin the acquisition go to the JSOC site,* in order to use the *Lookdata* tool is required (see Figure 4.2). Under the *Lookdata* tool the **Series Select** tab starts the process. Under *?Seriesname filter* input field, begin by inputting the requested instrumentation wavelength. Input either “aia.lev1” for level 1 AIA images or “hmi” for all HMI data products. For this example input **aia.lev1** to display all AIA Level 1 images. An important point to remember is the AIA wavelengths have different cadences for different wavelengths, discussed in *Chapter 1: Data Observations in Local Helioseismology*, see *AIA wavelength bands in Table 1.1*. For this example download the AIA 1600 Å wavelength at a cadence of 24 seconds. Once complete, press the **Fetch seriesname list** to display the available data products in the **2. Pick series to use** field. For this example choose **aia.lev_uv_24s --- AIA Level 1, 24 second cadence** for the 1600 Å wavelength (see Figure 4.3).

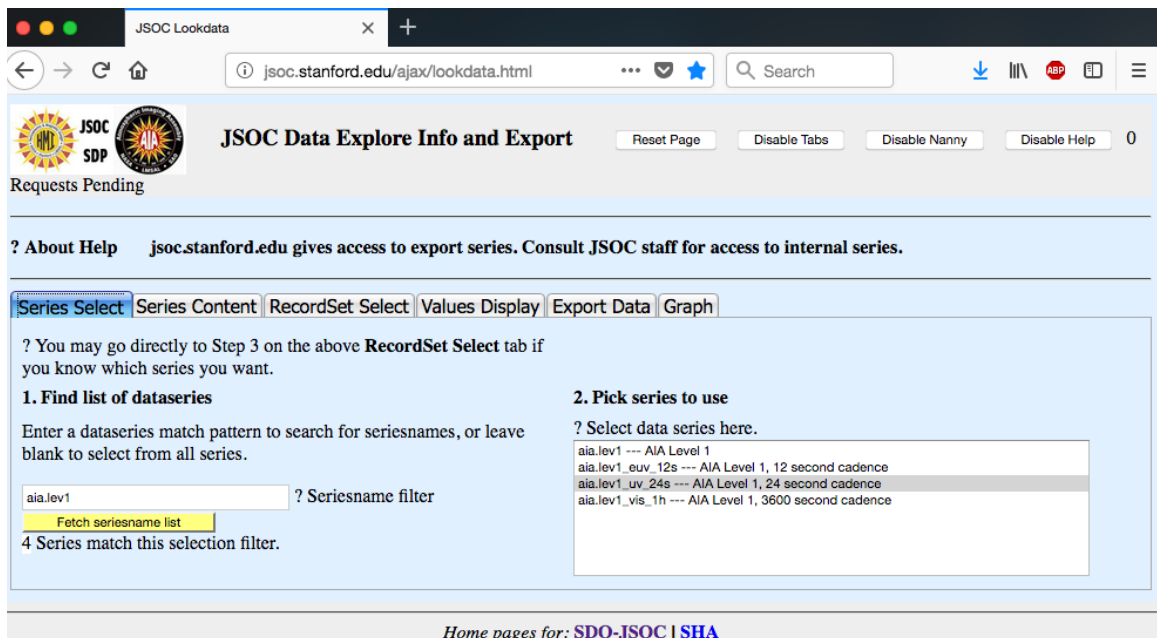


Figure 4.3: JSOC Series Select Tab Window. Begin by inputting either “aia.lev1” for level 1 AIA images or “hmi” to display all HMI data products. And then choose the requested data product.

The *Lookdata* tool will now go to the **RecordSet Select** tab (see Figure 4.4). In this window input the date and times for the requested image time series. Under **3. Se-**

*<http://jsoc.stanford.edu/ajax/lookdata.html>

lect Records and Get Record Count input the required request into the ? input field by this format: `aia.lev1_uv_cadence(s) [DATEYYYY.MM.DD_TIMEHH:MM / Time Series Length (minute or hours)] [Instrument Wavelength]`. Request data for a long time series of 6 hours for the X3 flare that took place in October 2014. For example, the input field would have the format: `aia.lev1_uv_24s [2014.10.24_17:59 / 6h] [1600]`. Then press the **GetRecordCount** button where a display of 900 records were found for this request. Then press the **Fetch Keyword Values for RecordSet** button to move to either the **Values Display** tab or the **Export Data** tab.

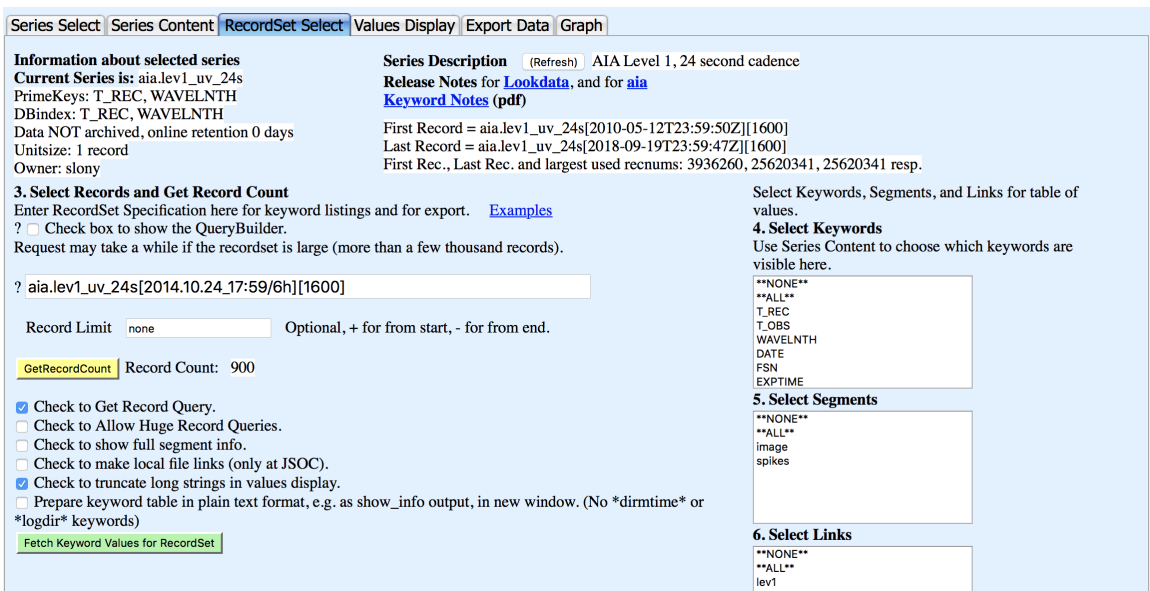


Figure 4.4: JSOC RecordSet Select window.

The **Values Display** tab (see Figure 4.5) displays all the data records that were previously requested. At the top is the starting record then scroll to check the list for all the individual files for the requested time series. Next move to the **Export Data** tab.

Under the **Export Data** tab (see Figure 4.6) press the **Export** button where it will jump to a new export page for data generation.

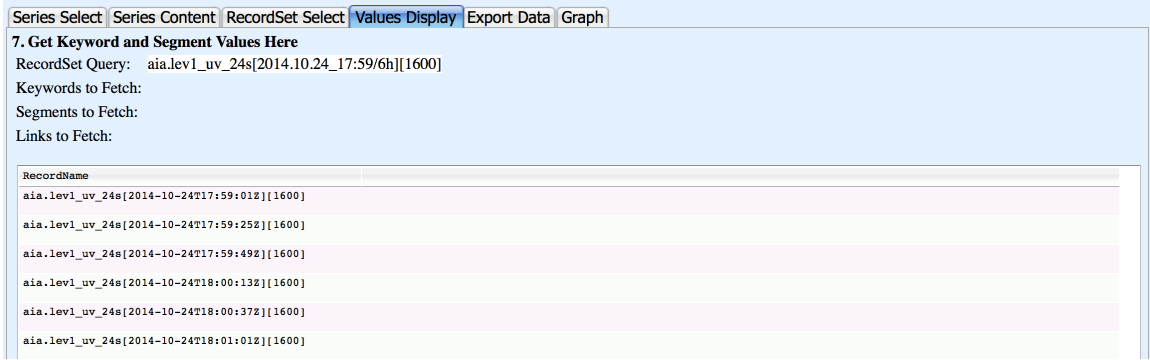


Figure 4.5: JSOC Values Display window.

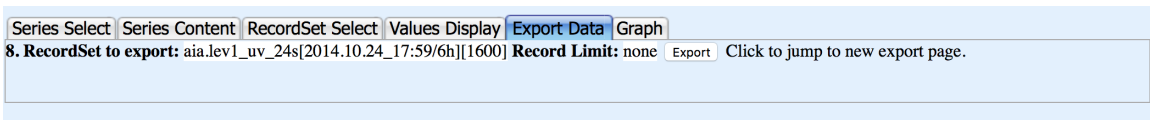


Figure 4.6: JSOC Export Data window.

Within the new **JSOC Export Data** window (see Figure 4.7), there will be a choice of where to retrieve the data from the **Method** field, whether in the form of a url, ftp or a *tar* file containing all the files to be downloaded. Enable processing under the **Processing** field by checkbox option. Then choose the type of file necessary to do the request (FITS, JPEG, MPEG or MP4) under the **Protocol** field.

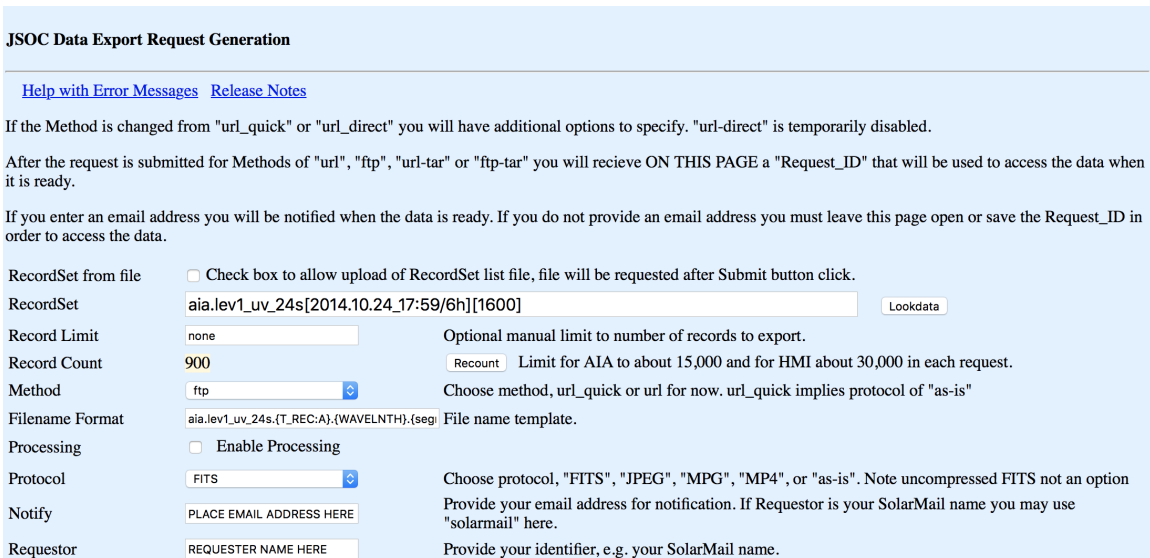


Figure 4.7: JSOC Data Export Request Generation window.

Since it will be necessary to extract the cutout *FITS* files of an active region for a long series of images then enable the **Enable Processing** checkbox under the **Processing** field and choose the **im_patch** check box to extract a sub-frame or cutout of each full disk image. Note, the required center pixel coordinates (**X, Y**) and **Width** and **Height**, were first obtained by downloading a single full disk FITS image of the active region and using an image display program such as *SAOImageDS9* were noted. Within the **Image Patch Extract** fields choose image tracking to track the images, this will also place the active region in place by subtracting the Carrington rotation. Additionally, choose to register the images. Once the coordinate location for the center pixel and the size of the cutout are in place, then press the button. The red **Not Ready** message will then say **OK to submit**. See Figure 4.8 for example of the inputted fields for the requested cutout.

Processing

- no_op - none hide
- aia_scale - Scale image to 0.6 arcsec/pixel
- HmiB2ptr - Convert HMI B_720s to Phi,Theta,R coordinates
- resize - Resize and rotate if needed, use sub-pixel registration
- im_patch - Extract sub-frame
- maproj - Extract a sub-frame and remap to a chosen projection.
- rebin - Rebin with boxcar or gaussian smoothing

IM_Patch

Image Patch Extract - used to export rectangular sub-frames from a sequence of images. The patch may be stationary or tracked at the Carrington rate.
 If only the seriesname is given, the query will be made for the last record only, [\$], unless tracking a from the east limb is requested.
 If the limb checkboxes are checked, tracking will begin or end at the indicated limb(s). If the "register" checkbox is checked, the patch will be interpolated to the desired location. If "register" is not-checked the patch will be exact pixel cutout from the input image.

RecordSet: aia.lev1_uv_24s[2014.10.24_17:59/6h][1600]

Options Tracking, Register, Crop, NOAA AR number:

T_START Check for start at east limb.

T_STOP Check for stop at west limb.

CADENCE

LocUnits Units for X and Y to select center of extracted patch

T_REF Reference time for X,Y to define center of extract patch.

X East-West location of patch center.

Y North-South location of patch center.

BoxUnits Width of extracted patch, Units determined by BoxUnits.

Width Width of extracted patch, Units determined by BoxUnits.

Height Height of extracted patch, Units determined by BoxUnits.

Verify

Figure 4.8: JSOC *im_patch* field for image processing for cutouts.

Once the cutout image processing is complete, then choose FITS file for the **Protocol** field (see Figure 4.7). Provide an email address and requestor name so that a notification can be sent when the data files are ready to download. Next choose the white button, which will turn green. To complete the process, press the green

Submit Export Request button. The request could take a few minutes to several hours depending on the time the request was made and the number of images requested. Once the data request is ready an email will be sent to the address provided that will indicate the ftp site location. From there data can be downloaded straight forward onto a computational device. The data can also be transferred using the *WGET* protocol.

4.2 Stage 1 Image Processing - Uncompressing and Dividing by the Image Exposure Time

When the JSOC image cutouts data are retrieved from JSOC of the three AIA wavelengths, all the files are in a Rice compressed format with each 1400×1400 pixel cutout at 3.9 Megabytes. However, the IDL *readfits* routine used in reading the images may have an issue in detecting the images when initiated. So the images will have to be uncompressed out of the Rice compressed format. One way to do this is to use IDL's *read_sdo* routine, a part of the *SSWIDL* library, by reading in the images. When this is done, an uncompressed version of the fits file is created in the temporary directory. This is usually located under the *VARS* directory on the machine used to run the *read_sdo* routine. The files can be copied to a data directory. The uncompressed files will have the same name as the Rice compressed file, the difference is that the *readfits* routine can now easily read them and the size of each of the files have increased to 15.7 Megabytes. Each image is labeled in the format **AIAYYYYMMDD_HHMMSS_wavelength.fits**, for example a format such as **AIA20141024_175931_0304.fits**. These AIA images are the start of a four stage image processing work flow, see Figure 4.16. This workflow is important because it prepares the images for the analysis stages, and will lessen any spurious results within the data. In the following sections the different stages of image processing procedures will be discussed.

Each of the three wavelengths of the AIA images to be analyzed (1700 Å, 1600 Å and 304 Å) are stored in a separate directory, see Figure 4.9. Originally, data for six hours near

the X3 flare event on 24-October-2014 was collected from an observation time of 17:59UT to 23:59UT. For analysis purposes, only two hours of data encompassing the main flare event time of 21:41UT where one hour encompasses before the event time at 20:40UT and after the event time at 22:40UT. The image processing procedures in this chapter was carried through on the six hour set of data.

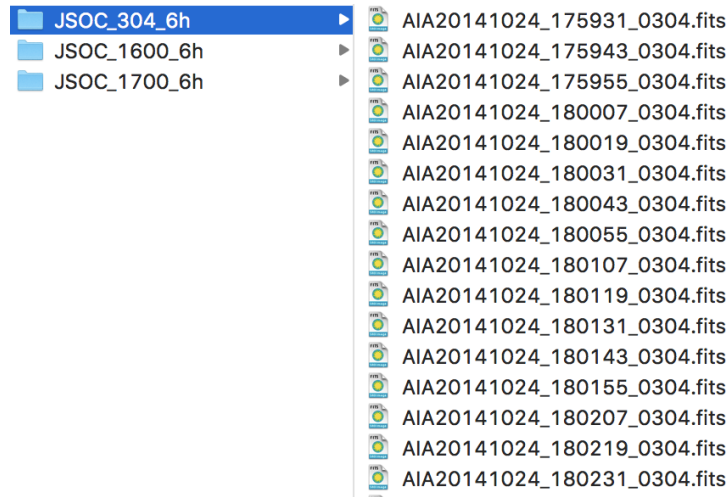


Figure 4.9: Uncompressed AIA image files for each AIA analyzed wavelength.

The counts value on a pixel image can contain instrumental artifacts which complicate surface brightness measurements. A common approach is to divide the counts image by an exposure map to re-scale all parts of the image to the same relative exposure to effectively remove instrumental artifacts from a counts image within the specified band or wavelength (Houck, 2015). Around solar flares the exposure times are usually shortened. An IDL program *exposureaia.pro* was created to divide each image in the data series by the image exposure time. The exposure time can be found in the image header. IDL's *sxpar* routine is used to extract each image exposure time in the AIA images, labeled as 'EXPTIME' and entered into a variable name called *exposure_time*. A *forloop* is created to read in the image data cube with IDL's *readfits* routine. The data cube is then divided by the *exposure_time* variable that stored the 'EXPTIME' for each image. The new images were then written out using IDL's *writefits* routine and classified as Stage 1 image processing images as **C1_AIA20141024** is written in the preamble of the image filename.

Each image is filed in it's corresponding wavelength file under the C1IMAGES directory for Stage 1 image processing, refer to Figure 4.10.

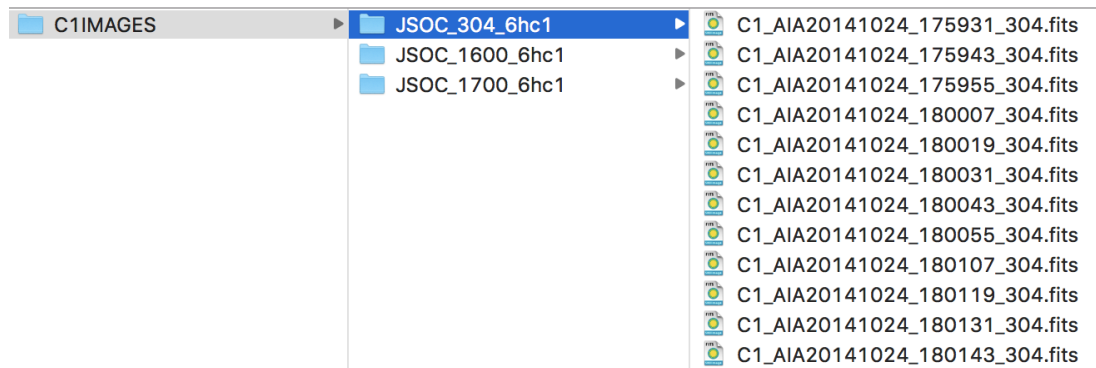


Figure 4.10: Stage 1 image processing images are placed in the C1IMAGES directory.

4.3 Stage 2 Image Processing - Linear Interpolation on Missing Frames

In the last section the images with their counts divided by the exposure time was done for all three AIA wavelengths (1700 Å, 1600 Å and 304 Å) and filed under the C1IMAGES directory, see Figure 4.10. They are used in the second stage of the image processing workflow. Stage 2 of the image processing workflow of the AIA images accounts for any missing frames through an interpolation process. This will be discussed in this section.

Occasionally, in a set series of image files there might be some frames missing due to instrumental maintenance or issues that may occur in the in the instrument's life time. If there is not a long gap in the total time of the missing images, such as five minutes, or a large quantity of such images missing near a flare event, then the missing images can be accounted for by filling in the missing images through image interpolation. The process of image interpolation takes into account the number of missing image frames, the known image frame before the first missing frame, and the known image frame after the last missing frame. The interpolation technique in this study found during a corrective search, a case of two missing frames, and another case for three missing frames. The case for the three missing frames will be discussed below. In the case of two missing frames the

process is similar and can be replicated with a few augmentations in the linear interpolation formulas, see the set of equations in 4.1.

To understand the concept of linearly interpolating images, think of the slope of a line and combine it with two known images KI_1 and KI_2 with all the pixel values contained in the images. Each pixel within each of the two known images are going to have either a positive or a negative slope of the intensity for each pixel contained in the two images. The missing images have to account for the change in the gradation in pixel intensity as it changes from the first known image KI_1 to the second known image KI_2 . If the change of gradation in pixel intensity is thought of as a slope, that change can be linearly interpolated. In the case of three missing images, the first known image KI_1 will have a value of zero to reflect that there is no change in pixel intensity since it is also the starting image frame. The second known image KI_2 will have a value of one since this will be the end image in the missing series. For the three missing images, MI_1 , MI_2 and MI_3 , the change is dependent on the placement distance of the images between KI_1 and KI_2 . Figure 4.11 illustrates the change in a distance and coincides with the change in gradation of the pixel intensity and will be dependent on the slope from zero to one and the order of the missing images. Considering the last statement, the change in gradation of the MI_1 will be $\frac{1}{4}$, for MI_2 will be $\frac{1}{2}$ and for MI_3 will be $\frac{3}{4}$. The placement of numbers for MI_1 , MI_2 and MI_3 will be the coefficients for the gradation in pixel intensity and is shown in the set of equations in 4.1.

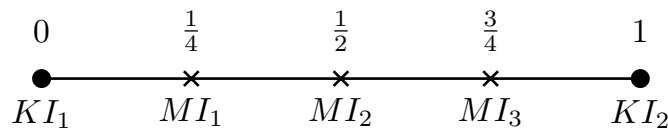


Figure 4.11: Linear interpolation illustration. Case for three missing images. Where KI_1 is Known Image 1, KI_2 is Known Image 2, and MI_1 , MI_2 , and MI_3 are missing images 1,2, and 3 respectively.

$$\begin{aligned}
MI_1 &= KI_1 - \frac{1}{4}(KI_1 - KI_2) \\
MI_2 &= KI_1 - \frac{1}{2}(KI_1 - KI_2) \\
MI_3 &= KI_1 - \frac{3}{4}(KI_1 - KI_2)
\end{aligned}
\tag{4.1}$$

First missing frames have to be detected so the intensity of a test pixel at the same location within each frame of the total set of images in each of the AIA wavelength image stacks has to be plotted, see Figure 4.12. There were two IDL codes created for this *timeadjustaia.pro* and *plotpix.pro*. The first routine *timeadjustaia.pro* checks the separation between the time stamps set in the file names, that correspond to the observation time set in the image header. The difference in times should reflect the cadence of the instrument wavelength, for example 24 seconds for the 1700 Å, 1600 Å and 12 seconds for the 304 Å wavelength. *timeadjustaia.pro* will print out the difference in time stamps, and if there is any discrepancy the printed list will indicate a “0” for image separation times if diverted from the cadence values coinciding with the appropriate image stack wavelength. The second routine *plotpix.pro* is designed as a checker program to plot the intensity values of a test pixel set at a certain location to see if there are any zero values detected in the time series plot of the image stack, this then could indicate missing frames, see Figure 4.11. Inspection of the frames around the location of where the plot showed zero values, need to be done to determine if any images are missing. To carry through the linear interpolation on missing frames, an IDL code *interpolpix.pro* was created to make the missing 2-dimension image frames. The two known images KI_1 and KI_2 were used, along with set of equations in 4.1 defining the missing frames MI_1 , MI_2 and MI_3 . The difference between the two known images, $KI_1 - KI_2$, is multiplied by the gradation coefficients in pixel intensity and is then subtracted from KI_1 for each missing frame. IDL will create three missing frames with the *writefits* routine. To amend the missing header files an IDL program *headermod.pro* which calls IDL’s *SXP* routine

will modify headers by changing the observation date to the respective missing frame date.

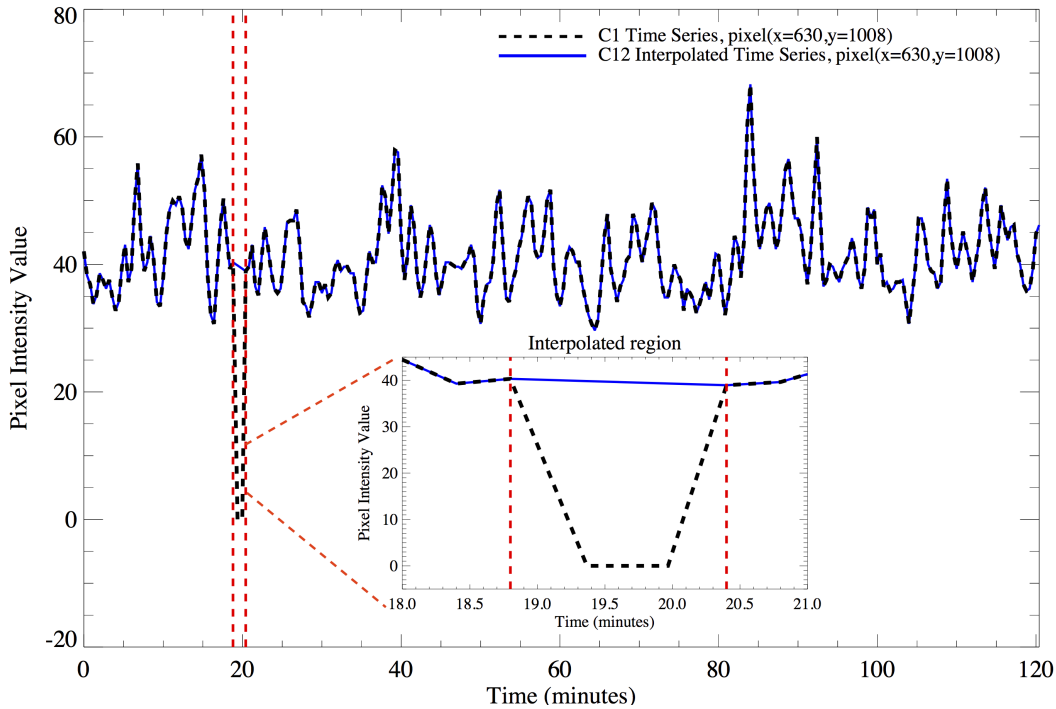


Figure 4.12: Linear interpolation done on three missing frames within the time series. The missing image files correspond to times at: 20:59:38, 21:00:02, and 21:00:14 in the image stack). The *plotpix.pro* routine is used to check image stack time series. The *interpilix.pro* is used to calculate the interpolated frames and then the headers are corrected using *headermod.pro*.

Each of the missing frames is then manually placed back into the corresponding total image wavelength stack. Then rerun a plot of the time series for a test pixel through the entire image stack and plot with the original missing image time series. Once the image stack is corrected, all the files are renamed and classified as **C12_AIA20141024** and is written in the preamble of the image filename by using a Bash script. These images are then filed in their appropriate wavelength files and in the C12IMAGES directory, indicating Stage 2 image processing was carried out, as in Figure 4.13.

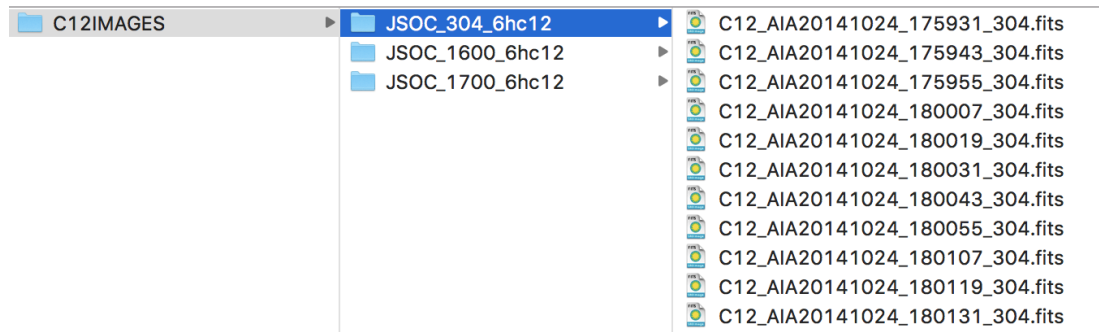


Figure 4.13: Stage 2 image processing images are placed in the C12IMAGES directory.

4.4 Stage 3 Image Processing - Creating Superpixel Images

After linear interpolating any missing image frames for all three wavelengths and are then filed in the C12IMAGES directory, the next stage will incorporate making superpixels out of the Stage 2 images. Superpixels are created to spatially sample regions more accurately by a single pixel instead of spatially averaging the pixels within each frame. Each image in the three wavelengths are cutouts of 1400×1400 pixels in size. Those images are rescaled where five pixels in the original Stage 2 images are rescaled down to one pixel in the Stage 3 image processed images. An IDL created rescaling routine *resizedataaia.pro* converts all the pixels in the cutouts by using IDL's *congrid* routine to rescale the images using a near neighbor interpolation. So the original 1400×1400 pixel images are rescaled down to 280×280 pixel images. The rescaling routine wrote the images out for the entire six hour set of data into the Co280_6hr directory and then files for a two set of data was created in the Co280_2hr directory, see Figure 4.14. The entire set of rescaled images were filed under the C123CoIMAGES, where the images are classified as **C123Co280_AIA20141024** and is written in the preamble of the image filename by IDL's *writefits* routine within the rescaling routine.

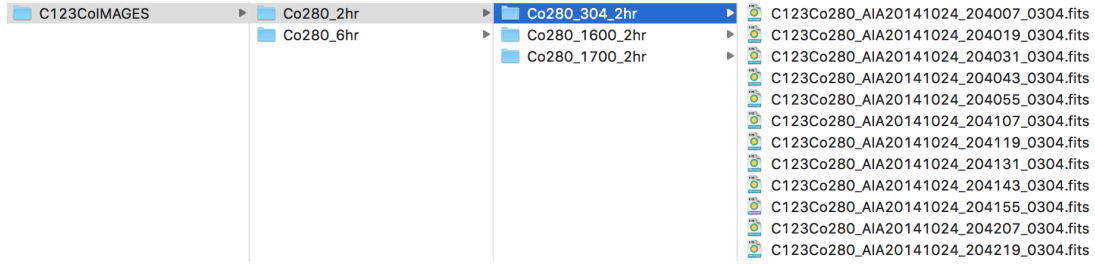


Figure 4.14: Stage 3 image processing images are placed in the C123CoIMAGES directory.

4.5 Stage 4 Image Processing - Image Average Subtraction

The final stage in the AIA image processing workflow will incorporate subtracting the average from the images. This Stage 4 process was done for all three AIA wavelengths within the Co280_2hr directory. The concept of subtracting the average from each image in the image stack, $x_{SA}(t)$ is shown in equation 4.2 and requires the average taken by the sum of the total image stack, $\langle \sum TimeSeriesImages \rangle$, divided by the total number of images contained in the image stack, $\sum n_files$.

$$x_{SA}(t) = Images_{TS}[i] - \frac{\langle \sum TimeSeriesImages \rangle}{\sum n_files} \quad (4.2)$$

An IDL routine *subtractaverage.pro* was created that calls IDL's *moment* routine there calling the average of the image stack array, that will be in the form of a 2-dimensional array. A *forloop* is created that encompasses the *moment* routine to subtract the average from each image in the total image stack in the time series. Then the *writefits* routine writes out the Stage 4 images into the C1234CoIMAGES directory. These image files are classified as **ASC1234Co280_AIA20141024**.

The complete workflow for the image processing procedures on the AIA from Stage 1 to Stage 4 is summarized in the Figure 4.16 flowchart. The Stage 4 images contained in the C1234CoIMAGES directory are used in analyzing Power Map Movies and analysis regions discussed in the next two chapters.

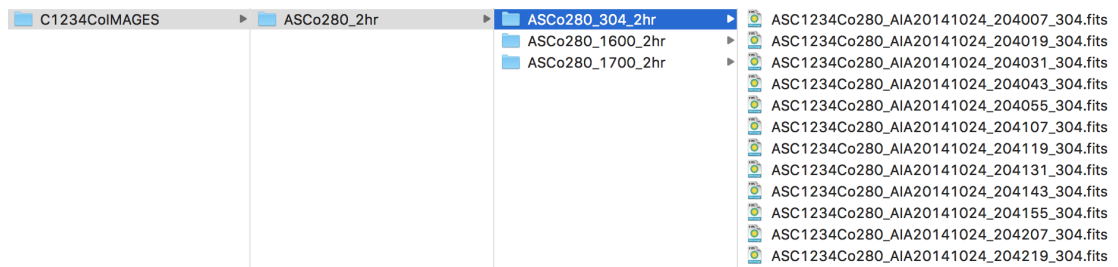


Figure 4.15: Stage 4 image processing images are placed in the C1234CoIMAGES directory.

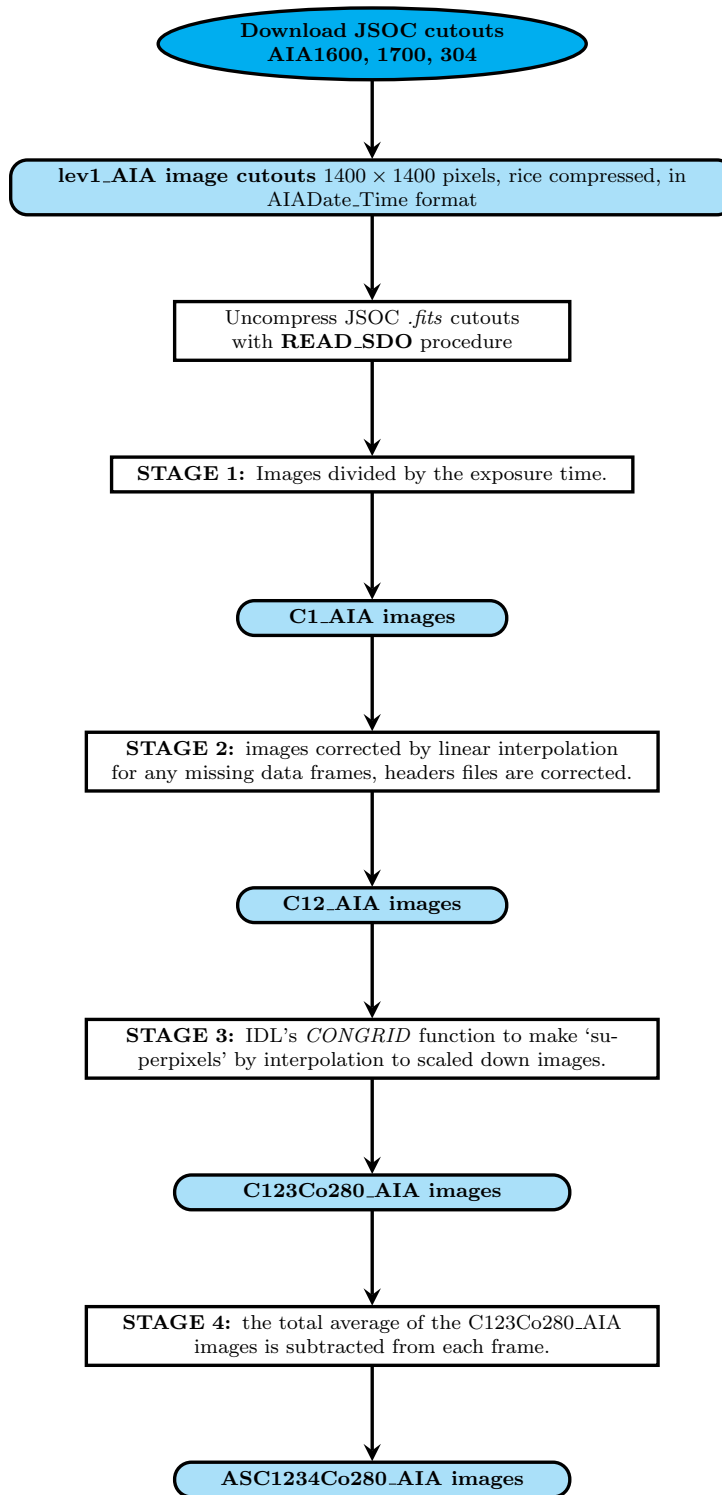


Figure 4.16: AIA image processing flowchart.

Chapter 5

Methodology: higher resolution, higher cadence images (SDO data)

5.1 Power Map Movies of SDO AIA 1700 Å, 1600 Å and 304 Å

Helioseismology is concerned with the observation of waves, as they affect light from the outer layers of the Sun, to infer the structure and dynamics of the otherwise invisible deeper layers. By simultaneously studying the oscillations in multiple wavelengths of light – hence at different heights in the atmosphere – it is therefore possible to probe the layers of the solar atmosphere (Howe *et al.*, 2012). There are many wave interactions taking place at multiple layers, especially during a solar flare event. Helioseismic studies aimed at understanding the behavior of waves and their interaction, especially during flaring events, can aid in finding a connection between wave behavior and interactions of wave processes that could either be the source of the flare event or the origin of a catalyst to the magnetic reconnection process.

In Helioseismology it is of paramount importance to be able to observe wave behavior in frequency space, utilizing the Fourier Transform to take the time-based light signals and decompose them into fundamental frequency wave signals. Wave signals are measured by the power of the signals derived from the Fourier Transform. Moving power maps are utilized and generated by running a windowed Fast Fourier Transform (FFT) algorithm on a pixel by pixel basis along a time series of 2-dimensional images to study the frequency distribution of spectra in multiple wavelengths. The multi-wavelength 4048×4048 pixel images are obtained from the Solar Dynamics Observatory (SDO) launched on February 2010, consisting of the Atmospheric Imaging Assembly (AIA) instrumentation and the Helioseismic Magnetic Imager (HMI) instrumentation (Pesnell *et al.*, 2012). The moving power map technique or Power Map Movies (PMMs) was first developed by Jackiewicz and

Balasubramaniam (2013) in which they studied $H\alpha$ data from NSO's ISOON telescope. The first clear observations of helioseismic waves produced by a flare is by Kosovichev and Zharkova (1998), taken from data with NASA's SOHO Michelson Doppler Imager. The PMM technique of Jackiewicz and Balasubramaniam (2013) was incorporated in the analysis and then the analysis was further evolved by extracting information out of the PMMs such as in the study done by Monsue *et al.* (2016) in which they study the wave interactions around solar flares using GONG $H\alpha$ detectors. In this study the broad frequency distribution is analyzed along with other techniques of wave tracking to isolate a propagating MHD source wave on the surface of the Sun triggered by a flaring event.

The power map movie is a series of time evolved stacked images of the frequency domain, or the power spectra of the original images in the time series of images. From these images analysis of the changes in power around active regions can be compared to the quiet regions. In order to obtain the power map movie the FFT is done on a pixel by pixel basis. There are several stages where one code will call another; these will either be in the form of ROI codes or wrapper codes, refer to Chapter 2. At the time this was the most effective way to handle the data, since many text files containing the data arrays need to be handled in order to process the information of many pixels.

There is an observed outward propagation of a waveform seen in the individual binned frequencies of the PMMs between 2–4 mHz. The waveform is embedded in the time series encapsulating the flare event and appears as a brightening that seems to be moving away from the flare. This is especially seen in the 304 Å chromospheric line. The feature is more subtle in the 1700 Å and 1600 Å wavelengths. The main goal of the methods discussed in this chapter is to track the apparent waveform.

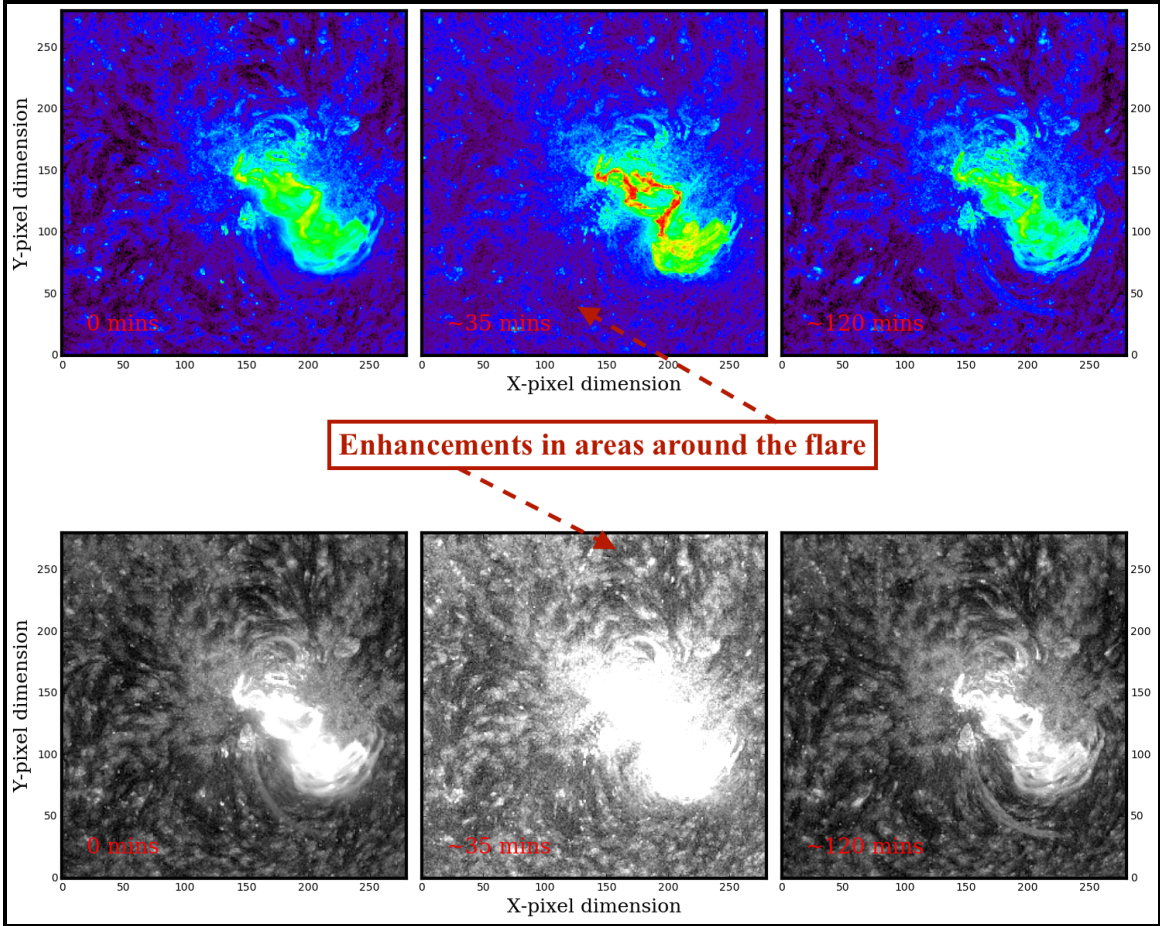


Figure 5.1: (*Top*) In the AIA 304 Å wavelength Power Map Movies at 2–4 mHz there is an overall enhancement of the regions around the flare. This enhancement is observed in the movies to have a radial movement which propagates outward from the flare. This enhancement is also seen in the AIA 1700 Å and 1600 Å wavelengths, but has a more subtle appearance. (*bottom*) Grey-scale images are scaled to bring out the appearance of the enhancements. Python’s `ImageEnhance.Brightness(image)` class from the Python Imaging Library (PIL) is utilized to augment the image contrast in this figure.

5.2 Random Sampling Method

5.2.1 Data Analysis Procedure

In the previous approach, acoustic oscillations were observed within the chromosphere by observing PMMs in the $H\alpha$ wavelength, see Figure 5.1. NSO’s GONG $H\alpha$ network data was utilized, with a cadence of 60 seconds and a Nyquist frequency of 8.33 mHz. Samples near the active regions and within the solar flare were taken to study the frequency

distribution. In the approach the Fourier acoustic PMM observation dark structures were observed in the flaring events over sunspots (Monsue *et al.*, 2016). Those dark structures were believed to be connected to areas of concentrated magnetism through their characteristic absorption of acoustic power within the flare.

The previous GONG H α was evolved to utilizing higher cadence data from NASA's SDO, by combining acoustic observations in a multi-wavelength approach to find a correlation within different frequency bands of the acoustic oscillations around active regions. The initial study involved plotting the binned frequency distribution of each PMM around interesting areas in active region AR12192. The main 280×280 pixel image was reduced to a 125×125 pixel region of interest, encapsulating the active region.

In this analysis the AIA 1600 Å, AIA 1700 Å, and AIA 304 Å images, as well as HMI dopplergrams and HMI magnetograms was used. These different AIA wavelengths were chosen since their wavelengths correlate to the different heights within the solar atmosphere from the photosphere to the chromosphere. The measurements were chosen to bracket an X3 flare in AR12192, on 24-October-2014, at 21:41 UT. The active region was observed while it was close to the central meridian to reduce projection effects. The images were obtained from the JSOC cutout service, discussed in the Chapter 4. The original size of the images for analysis were 1400×1400 pixels. Each AIA image was divided by its exposure time. Missing images were interpolated from the surrounding images to produce a uniform time step. The initial time series for each data cube lasts two hours. The lower-resolution images used in the current analysis were created by spatially averaging the JSOC data, also discussed in the Chapter 4. There were three sampling regions taken, R1, R2 and R3, see Figure 5.2. Three regions (labeled as R1, R2, and R3 in the PMM image below in Figure 5.2) were chosen for the moving power-map analysis. A rectangular windowed 1-D FFT was performed on each spatial pixel in regions R1, R2, and R3, producing a temporally-varying power spectrum at each location.

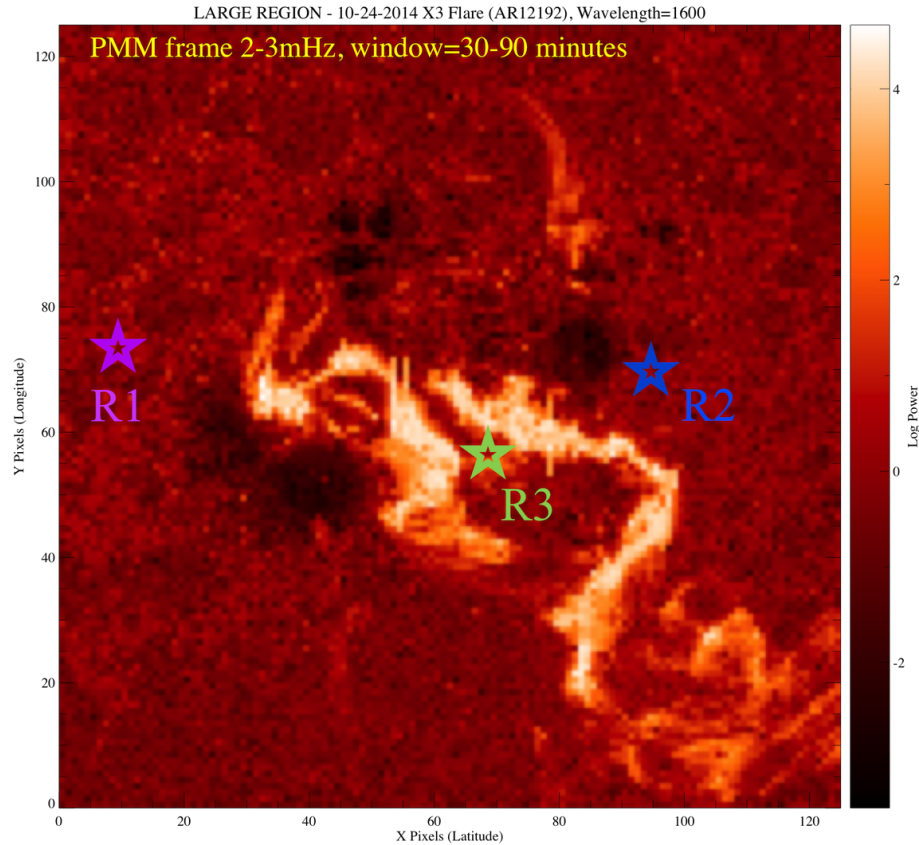


Figure 5.2: A power map frame of three sampled regions R1, R2 and R3 around the October 24, 2014 X3 flare.

5.2.2 Results: Random Sampling Method

The previous GONG $H\alpha$ study has evolved to utilize higher cadence data from NASA's SDO by combining the acoustic observations in a multi-wavelength approach to find a correlation within different frequency bands of the acoustic oscillations around active regions. The initial study involved plotting the binned frequency distribution of each PMM around interesting areas in active region AR12192. Through this multi-wavelength approach there have been observations of higher frequency acoustic waves in the form of wave pulses in the AIA 1700 Å, AIA 1600 Å and HMI Doppler channels, see Figures 5.3, 5.4 and 5.5. Although their origin is uncertain it is thought that these waves are a form of MHD waves traversing outwardly from the flare. The goal in this study is to track the MHD waveform

by taking several sampling around interesting areas and by studying the Fourier spectra in the power maps around the flaring region.

The behavior of the power as a function of frequency and time strongly depends on the location of the analysis area, the temporal behavior of the intensity in the area and the measured wavelength. There are observed enhancements in the lower frequency bands for all measured wavelengths (AIA 1700 Å, AIA 1700 Å, AIA 304 Å and HMI dopplergram, see Figures 5.3, 5.4 and 5.5). Oscillatory behavior is clearly exhibited in the 1600 Å, 1700 Å wavelength and the HMI dopplergram. The behavior of the power in the 304 Å wavelength seems saturated by the flaring activity.

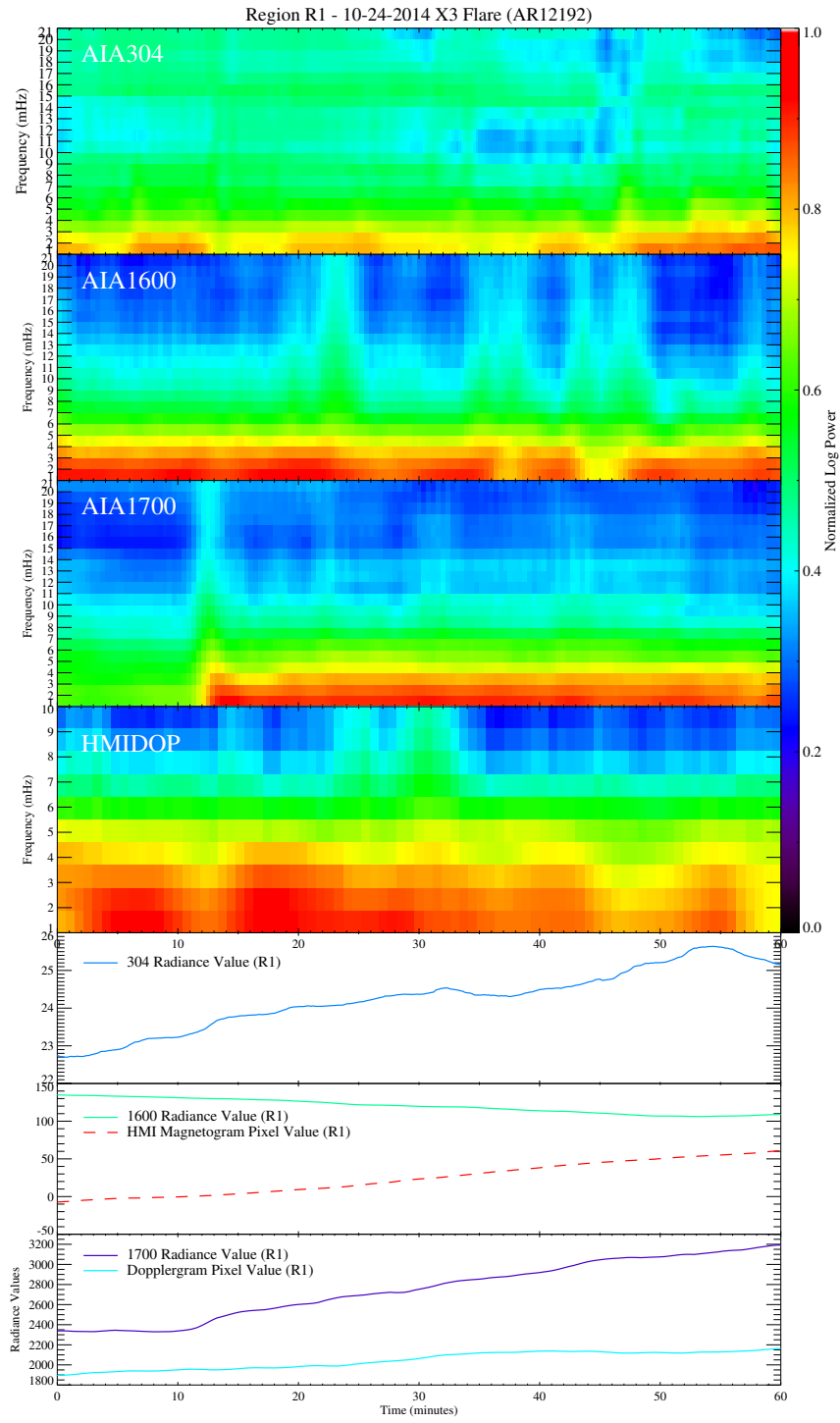


Figure 5.3: Multi-wavelength image of AR12192 at sample R1.

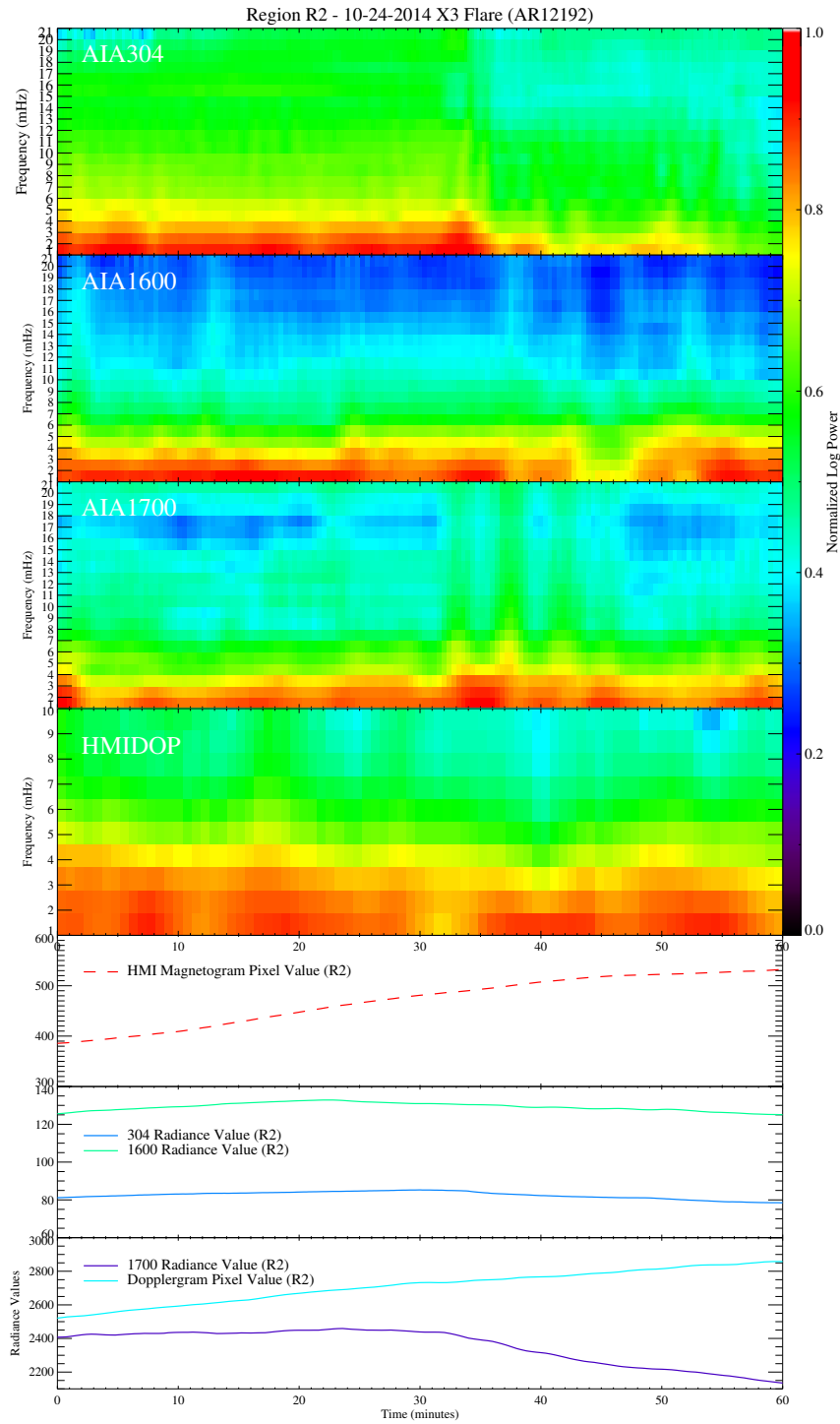


Figure 5.4: Multi-wavelength image of AR12192 at sample R2.

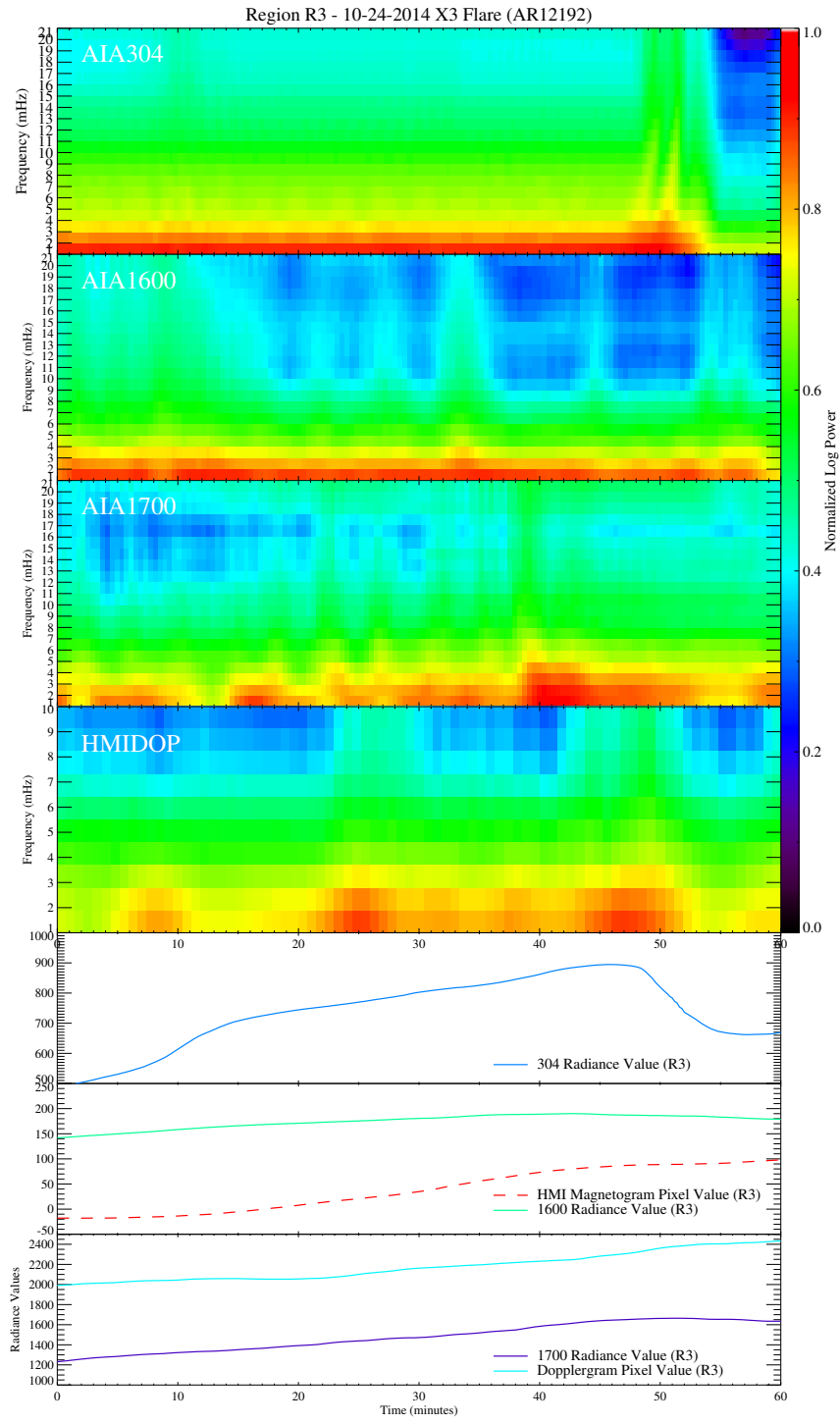


Figure 5.5: Multi-wavelength image of AR12192 at sample R3.

5.3 Triangulation Tracking of a Radially Propagating MHD Wave in the AIA 1600 Acoustic Power Maps in Active Region 12193

Published in: *Research Notes of the AAS (RNAAS)*, Volume 2, Issue 1 (2018)

DOI: 10.3847/2515–5172/aab49f

For decades it has been established that the amount of energy released by solar flares excites the acoustic oscillations propagating on the surface of the Sun (Wolff, 1972). It is believed that these flares can excite velocity oscillations in active regions, especially those regions where a higher class solar flare has taken place (Kumar *et al.*, 2006). However, questions arise as to how the behaviors of acoustic oscillations within such a chaotic environment can birth other waves of the MHD type. *Can we observe such events?*

We employed a method first devised by Jackiewicz & Balasubramaniam (2013) and then studied further by Monsue *et al.* (2016) in which we observe an active region in the spatial-frequency domain as it evolved through time, therefore creating a power map movie (PMM). We chose an X3-class solar flare that occurred on October 24, 2014 at 21:41 U.T., in active region NOAA AR12192. Through PMMs, we were able to study the spatial and temporal frequency information per pixel within the AIA1600 wavelength images, from NASA’s Solar Dynamics Observatory (Pesnell *et al.*, 2012), by running the Fast Fourier Transform (*FFT*) on each pixel. Our observation window is two hours of images, surrounding the flare. We set the window length to run the FFT to one hour as we move through the datacube of the 1600 images, enabling us to study the broadband behavior of the acoustic oscillations within the frequency bands of 1–21 mHz. We reached a Nyquist frequency observation limit of ~ 21 mHz, since the AIA1600 cadence is 24 seconds. We also averaged the intensity for each pixel to 5-spatial pixels for each 1600 image frame before running the FFT. We observed in the 2–4 mHz PMMs of the AIA1600 images a radially propagating enhancement occurring during the flaring event. We suspected that this propagating enhancement is due to the creation of a MHD wave moving out away from the

flare. We studied this closer by devising a way to triangulate the movement of the MHD wave by taking a 90° triangular sampling to see how the pixels behaved by constructing a spectrogram at each sampled region (e.g. Figure 5.6). For a sampling of spectrograms of some of the regions (A1, A3, O3, O1), we were able to see oscillatory behavior. However, we are unable to conclude if this oscillatory behavior is attributable to the MHD wave, or aliasing due the behavior of the FFT.

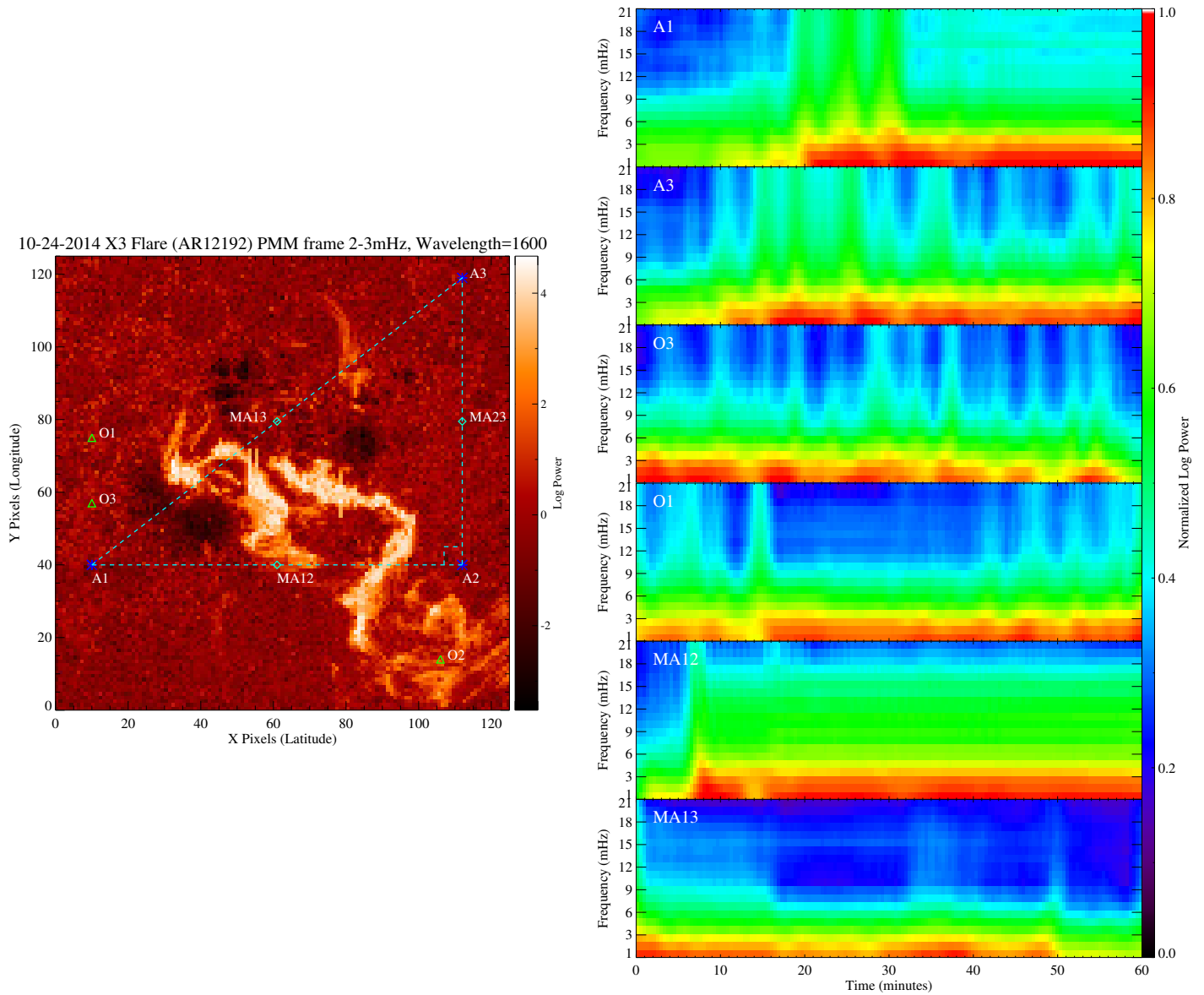


Figure 5.6: (*Left*) Illustrated above is a PMM frame (the region is measured in power) in the 2–3 mHz band, windowed at 30–90 minutes. Sampled 90° triangular region in flaring region AR12192 (AIA1600 wavelength). The large region of interest is 125×125 pixels encompassing the active flare region. (*Right*) Spectrogram plots of corresponding regions, A1, A3, O3, O1, MA12 and MA13.

5.3.1 Results: Additional Areas for Triangulation Tracking

This section covers additional regions that were not documented in the previous section. The sampled 90° triangular region in flaring region AR12192 was taken in the AIA1600 \AA

wavelength. And an additional sampling of three other regions (O1, O2 and O3) as a test. Plots for the sampled pixel region are found in Figure 5.6 through Figure 5.8. At vertices A1 and A3, the opposite corners of the triangle (see Figure 5.6), there is an observed pulsating behavior. The cutoff/break of power takes place before the pulsating behavior for A1 (around 10 minutes) and for A3 (around 2 minutes). For O3, the region closest to vertex A1, the pulsation is similar in behavior to vertex A3. However, the break occurs at the end of O3, whereas the break occurs at the beginning of A3. For region O1 a break in power occurs between 17 and 38 minutes for the higher frequencies above 8 mHz. In the plots, MA12 the midpoint region near the flare has a boost in power in its overall distribution. The behaviors of MA13 and MA23 are more like quiet regions, see Figure 5.7 and 5.8.

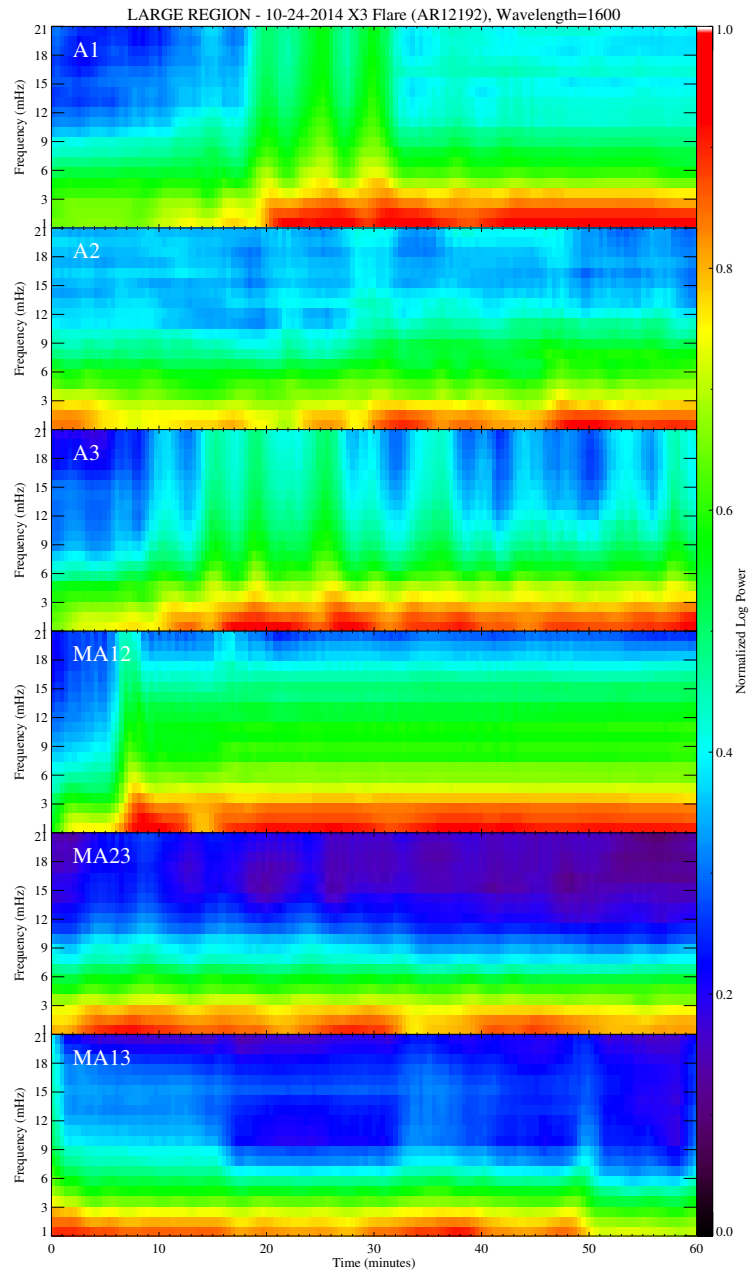


Figure 5.7: Additional sampled regions for the three vertices A1, A2 and A3 and their corresponding midpoints MA12, MA23, MA13.

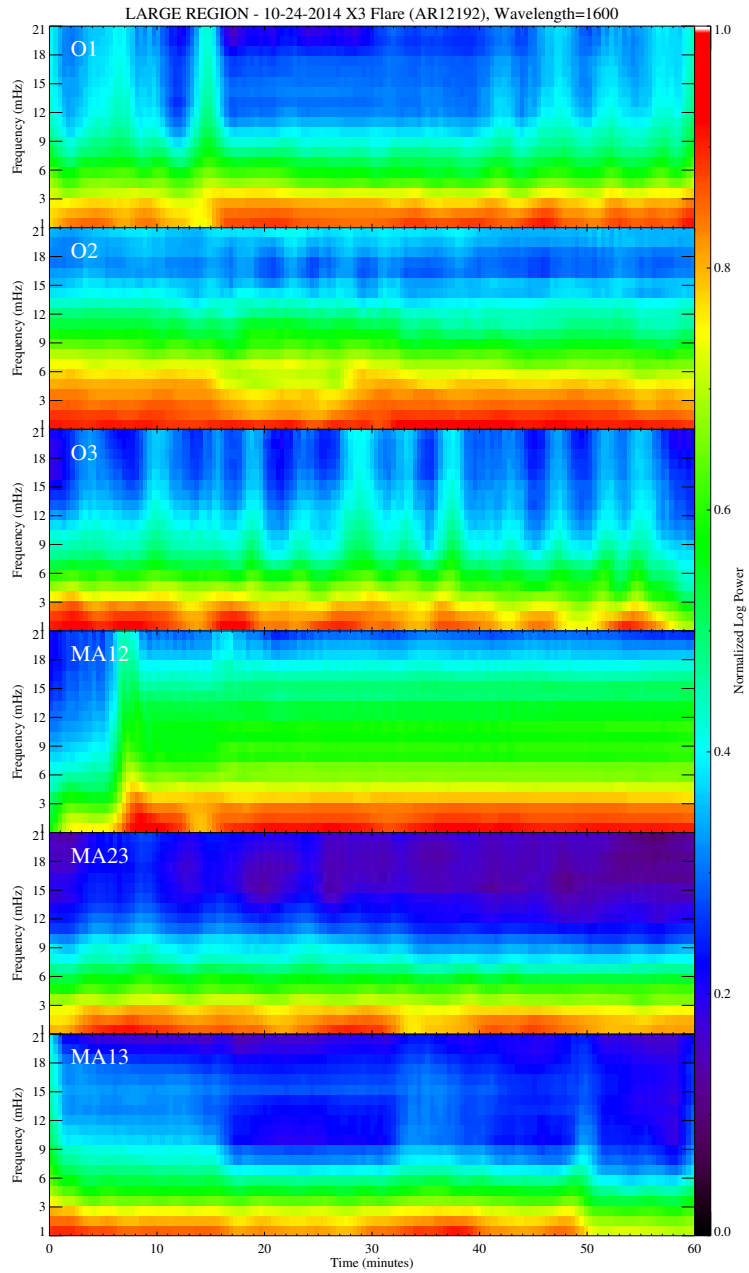


Figure 5.8: Additional sampled regions for the three test points in the outer region of the triangle O1, O2 and O3 and the corresponding midpoints MA12, MA23, MA13 of the triangular region.

5.4 Caveats and lessons learned from previous methods

The random sampling and triangulation analyses within this chapter was a great start in learning how to handle multi-wavelength data. The two analyses also created a starting point to learn about the basic properties of utilizing the FFT. Both the random sampling and triangulation methods proved interesting in detecting a form of oscillations. But unanswered questions remain on the type of oscillations being detected in the data. Even though the studies took precautionary steps in avoiding any sort of noise contamination in the data, through many stages of image preparation, the measurement tool (FFT) chosen can cause issues in how it is used. Such types of issues can be in the form of aliasing from the FFT. A rectangular window was used in both the random sampling and triangulation methods, but with the binning of 1 mHz frequencies this might have alleviated some of the aliasing issues from the FFT. Also, the window size chosen in both analyses was always an hour in size, and a question arose about the frequency resolution at a window size of an hour. The next chapter will address lessening any aliasing that may arise from the FFT by now adding an apodization function to the rectangular window. The next chapter will also address which window size is appropriate for the measurements being taken. Another issue that arose with the past analyses involves the methods of processing the data with the FFT by taking the frequencies at 1 mHz bins that took an abundant amount of time. As a solution, the next chapter will address utilizing a more efficient way of processing the data, by gathering the data through IDL and then utilizing the advanced array manipulation and object oriented programming packages from Python to do the final stages in the analyses.

In both analyses of random sampling and triangulation there needs to be many other areas chosen. However, a bias may be formed from just randomly choosing different areas to sample and this in turn causes issues in knowing which is the right area to choose even if interesting areas are chosen. There were so many other areas that would need to be measured, but the processing of so many other areas might prove to be too arduous. This brings up the issue of losing too much information. A solution to this issue would be to

devise a way to be able to sample efficiently without losing any information. This will also be addressed in the next chapter, by devising a novel way of sampling most of the 2-dimensional image.

Chapter 6

Methodology: Sector Sampling Method Around Active Region AR12192

6.1 Sector Sampling Concept Philosophy

In this chapter a novel approach is discussed to analyze the acoustic oscillations around active regions. The developmental process from the last chapter involved getting to this stage in the analysis by learning from and improving the previous methods. The ultimate goal is to see if the power map movies correlate with the new approach set out in this chapter and to study any anomalies that arise. As discussed in the last chapter in section 5.4 – *Caveats and lessons learned from previous methods*, a major area of concern in the analysis is that the sampling methods are either too random or there are not enough sampling areas chosen. Additionally, there may be biasing or aliasing issues arising from the FFT measurements if spatial averaging is not taken appropriately; this can cause an inaccurate measurement in the power that may have lower values. And with these issues being considered a more effective method would therefore need to be designed. This will be discussed in this section.

When designing a method the sampling has to be treated as equal and any bias has to be eliminated with random sampling. Upon investigation of the solar flare event both the spatial location and the event time has to be taken into consideration. The spatial, time domains and energy have to be conserved in order for the measurement to be effective. Additionally, the Fourier analysis has to be conserved by preserving the properties of the Fourier transform. If all these concerns are taken into consideration then an effective analysis can be designed.

The Fourier transform (FT) in equation 6.1, is used in decomposing a function of time

or signal $x(t)$ into the signal's component frequencies.

$$X(\omega) = \int_{-\infty}^{+\infty} x(t)e^{-j\omega t} dt, \quad \omega = 2\pi f \quad (6.1)$$

The FT is the frequency domain representation of the original signal, by breaking up the signal into a linear combination of sines and cosines. Because the FT is a linear superposition of sines and cosines, it has the property of linearity. The reverse of the FT is in the inverse Fourier transform equation 6.2, in which an operation reverses the frequency domain representation by combining the contributions of all the different frequencies to recover the original function of time, $x(t)$.

$$x(t) = \int_{-\infty}^{+\infty} X(\omega)e^{j\omega t} d\omega \quad (6.2)$$

The FT should also have to be able to have converted to a relative time-measurement, therefore taking the conservation property of time into consideration. This is done by taking the discrete Fourier transform (DFT), where the signal is sampled at discrete intervals by truncating the original signal. The general form of the DFT is represented with no window function in equation 6.3, for the N-point DFT of a sequence $x[0], x[1], \dots, x[N-1]$, where $f_k = k/N$ and $k = 0, 1, \dots, N-1$ (Brigham, 1974; Kandhasamy, 2010),

$$X(f_k) = \sum_{n=0}^{N-1} x(n)e^{-j2\pi f_k n} \quad (6.3)$$

In the process of DFT (or FT), there is only one constraint that has to be satisfied by $X(f_k)$ and $x(k)$ and that is Parseval's theorem connecting the total energy in the time and frequency domains. Parseval's Theorem is an energy conservation theorem that says that a signal contains the same amount of energy regardless of whether that energy is computed in the space/time domain or in the Fourier/frequency domain (Scherbaum, 1994). Parseval's

theorem in the language of the DFT states,

$$\sum_{k=0}^{N-1} x^2(k) = \frac{1}{N} \sum_{n=0}^{N-1} |X(f_k)|^2 \quad (6.4)$$

In the analysis, the spatial dimensions must be conserved so as not to create any bias or voids in the spatial sampling. The 2-dimensional image can be treated as a conformal map. A conformal map preserves the angles, see Figure 6.1, otherwise known as invertible. For example, when transforming from one coordinate system, $x - y$ to another, $u - v$, the angles θ and ϕ have to remain the same from one transformation to the other. This translates to the analysis if a problem is mapped from the $x - y$ plane to the $u - v$ plane; certain physical characteristics in the spatial dimension in the $x - y$ plane could be lost when the problem is mapped to the $u - v$ plane, therefore affecting the measurements. It is important that the angles are conserved.

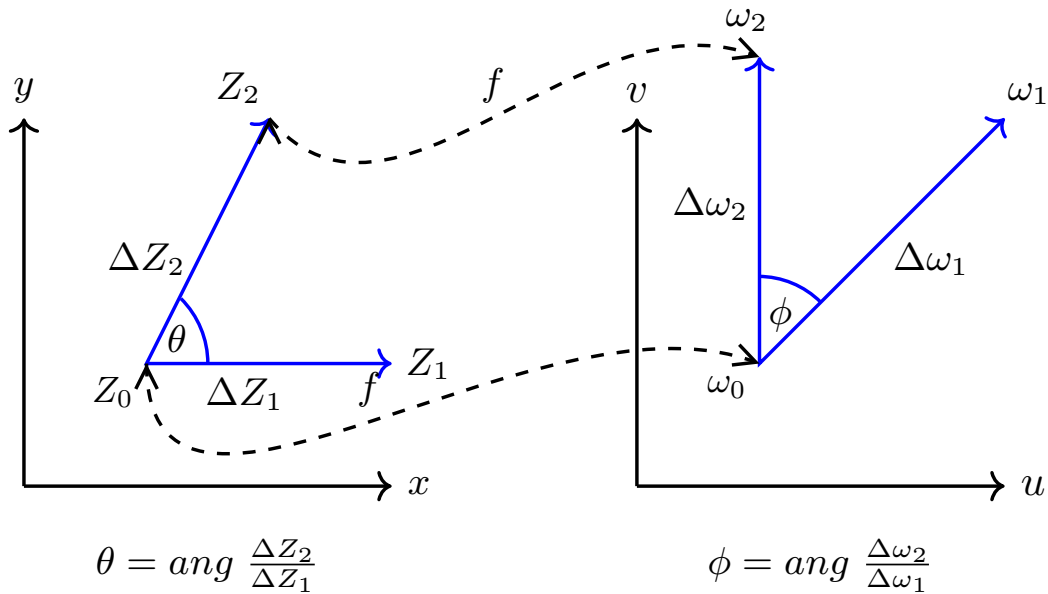


Figure 6.1: Conformal mapping preserves the angles on different coordinate systems.

To expand on the conformal mapping concept implies that both the spatial dimension and physical characteristics have to be conserved during the analysis and to do that will

involve utilizing an annular sampling method, see Figure 6.2. This implies that the 2-dimensional image along with the pixels in the $x - y$ plane will then be mapped to a angular polar plane. To preserve the spatial nature, pixels can be averaged in a angular basis such as in a sector angle, where the pixels are grouped in a annular sampling. However, the area of each annular sampling has to contain the same amount of pixels as the sampling is moving out, preserving the angle. In the analysis, dividing the sectors into 45-degree measurements was sufficient in that it produced eight major regions as the sample was taken from 0° back to 360° . The space between sectors are close, therefore eliminating any voids in the analysis

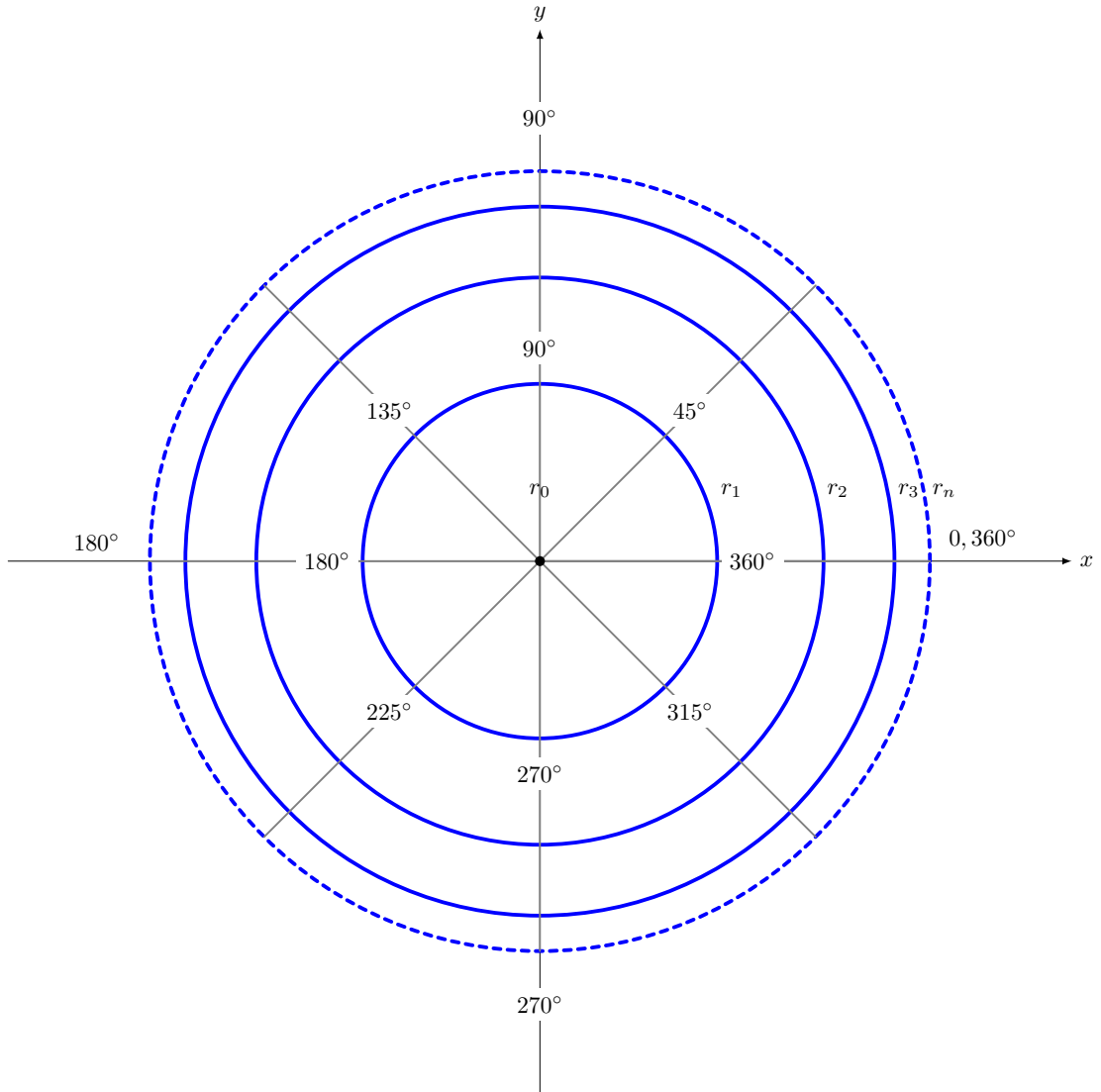


Figure 6.2: Sector sampling method.

To facilitate comparisons of sectors, the radii are selected to enclose the same number of pixels within each sector. The distance between the radii moving out will be different, see Figures 6.2 and 6.3. Figure 6.3 illustrates the change in distance between the radii within each sector as the sampling moves out. In the analysis, the location of r_0 will be close to the center of the 2-dimensional image were a designated center pixel will be determined. The generalized equation for the variable radius length is,

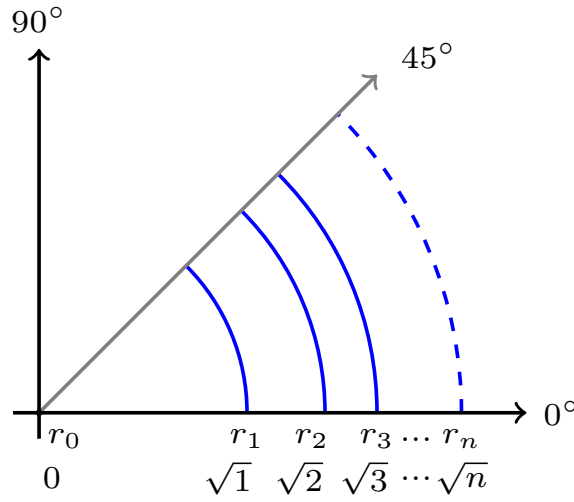


Figure 6.3: The distance between the radii in the sector sampling will vary therefore conserving the value of the pixels contained in each sector region.

$$r_n = \sqrt{2r_{n+1}^2 - r_{n+2}^2} \quad (6.5)$$

When the variable radius (equation 6.5) is set with respect to the primary r_0 and secondary r_1 radius, and $r_0 = 0$ and $r_1 = 1$ is set to solve for r_2 , the equation becomes,

$$r_2 = \sqrt{2r_0^2 - r_1^2} = \sqrt{2(0)^2 - (1)^2} = \sqrt{2} \quad (6.6)$$

Since the first three coefficients ($r_0 = 0, r_1 = 1, r_2 = \sqrt{2}$) are found, the other r_n coefficients can be found by continuing on with $r_3 \rightarrow r_n$ by substituting in the past coefficients.

The sector sample can be expanded to many radii so that the variable radii can be thought of as an expansion series as in equation 6.7,

$$\begin{aligned} r_0, r_1, r_2, r_3, r_4, r_5, r_6, r_7 \dots r_n \\ 0, 1, \sqrt{2}, \sqrt{3}, \sqrt{4}, \sqrt{5}, \sqrt{6}, \sqrt{7} \dots \sqrt{n} \end{aligned} \tag{6.7}$$

And this indicates that for each radius in an n number of samples, the radius will then jump a distance of the \sqrt{n} . Such that,

$$r_n = \sqrt{n} \tag{6.8}$$

6.2 Windowing or Apodization on Time Series

6.2.1 Windowing and the Uncertainty Principle

In particle physics, an elementary particle does not have precise position and momentum. The better one determines the position of the particle, the less precisely is known at that time, and vice versa. In signal processing, this rule translates into the fact that a signal does not simultaneously have a precise location in time and precise frequency (Wang, 2015).

A time signal $x(t)$ contains the amplitude of the signal at any given moment in time, t . However, there is no frequency information given explicitly in $x(t)$. If we take the Fourier transform of the signal $X(\omega) = \mathcal{F}[x(t)]$ we obtain the complete global information of the frequency domain in terms of the magnitude and phases of the frequency component at any given frequency, ω . However, there is no temporal information available within the spectrum of when certain frequency contents appear explicitly. We have either the temporal or spectral information contained in the signal, but never both.

To address this situation we can use a windowed Fourier transform, otherwise called the *short-time Fourier transform (STFT)*. When we take the STFT of $x(t)$, a time window function $w(t)$ truncates $x(t)$ into shorter time intervals, and sets $x(t) = 0$ outside of the time intervals. Then the signal is transformed to the frequency domain. This defines the spectral characteristics within a particular time window. In the time domain, the windowed signal is:

$$x_w(t) = x(t) w(t) \tag{6.9}$$

Following the convolution theorem, the frequency domain representation of equation 6.9 corresponds to the following:

$$W_w(\omega) = X(\omega) W(\omega) \tag{6.10}$$

where $\mathbf{X}_w(\omega) = \mathcal{F}[x_w(t)]$ is the spectra of $x_w(t)$ and $\mathbf{W}(\omega) = \mathcal{F}[w(t)]$ is the spectra of $w(t)$. All the frequency components present in the spectrum $\mathbf{X}_w(\omega)$ exist inside the time window, and the narrower the time window, the better the temporal resolution. However, the spectrum of $\mathbf{X}_w(\omega)$ of the windowed signal is a “blurred vision” of the true signal spectrum $\mathbf{X}(\omega)$ due to the convolution with the window’s spectrum $\mathbf{W}(\omega)$. Additionally, while the temporal resolution can be increased by narrowing the window $w(t)$, the frequency resolution will be reduced due to the expanded spectrum $\mathbf{W}(\omega)$. Similarly, narrowing $\mathbf{W}(\omega)$ to increase the frequency resolution causes poorer temporal resolution by widening the window.* An illustration of this can be found in Figure 6.4 that describes several different spectra taken of a sampled sector averaged 1600 Å light curve. We run the STFT, or windowed FFT, on the sectorized light curve at different sizes.

*A mathematical proof of the Heisenberg Uncertainty Principle and the Fourier Transform can be found in the Appendix Section.

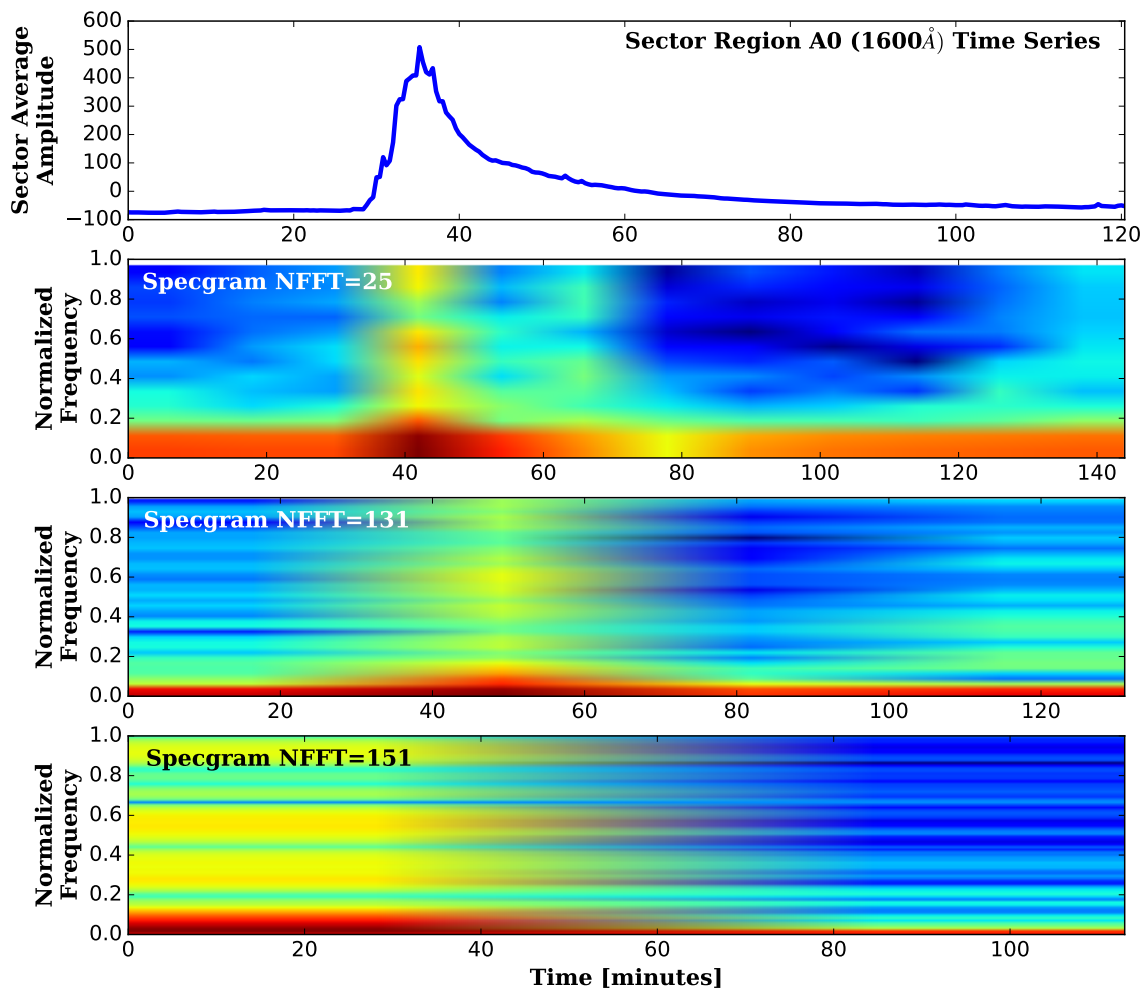


Figure 6.4: Because the STFT is simply applying the Fourier transform to pieces of the time series of interest a drawback of the STFT is that it will not be able to resolve events if they happen to appear within the width of the window. In this case, the lack of time resolution of the Fourier transform is present. In general, one cannot achieve simultaneous time and frequency resolution because of the Heisenberg Uncertainty Principle. In particle physics, an elementary particle does not have precise position and momentum. The better one determines the position of the particle, the less precisely is known at that time, and vice versa. For signal processing, this rule translates into the fact that a signal cannot simultaneously have a precise value in time and precise frequency. In the figure we use *SPECGRAM()* in the *PyLab* library to illustrate this. The bottom plots show a higher frequency resolution with the larger window length of 151 elements and the top plot shows a lower frequency resolution with window length of 25 elements, but are able to resolve the presence of the pulse. This illustrates the importance of choosing the right window length.

6.2.2 Window Functions

When the FFT computes the Fourier transform function, recall Equation 6.1, to measure the frequency component of a signal $x(t)$, the analysis is based on a finite set of data. The actual FFT assumes that it is a finite data set, a continuous spectrum that is one period of a periodic signal. For the Fourier transform both the time domain and the frequency domain have a circular topology in nature, so the two endpoints of the time waveform are interpreted as though they were connected together.[†] Furthermore, the function is thought of as continuous with the integral taken on the function over the interval $-\infty$ to $+\infty$. When the measured signal is periodic and an integer number of periods matches the acquisition time interval, the Fourier transform agrees with the assumption of continuity. However, the majority of times the measured signal is not an actual integer number of periods. The finite length of the measured signal may result in a truncated waveform with different characteristics from the original continuous time signal. This finiteness can introduce sharp transition changes into the measured signal. The sharp transitions are thought of as discontinuities, where the endpoints of the signal are discontinuous. These ‘artificial’ discontinuities show up in the FFT as high-frequency components not present in the original signal. These frequencies can be much higher than the Nyquist frequency and are aliased between 0 and half the sampling rate. Therefore, the spectrum of the computed FFT is not the actual spectrum of the original signal, but a smeared version. It appears as if energy at one frequency leaks into other frequencies. This phenomenon is known as spectral leakage, which causes the fine spectral lines to spread into wider signals. Windowing is a mechanism to reduce the spectral leakage distortion in the Fourier transform due to the edge effects (discontinuities) of the finite sample window within the time series (Priemer, 1991; Marven and Ewers, 1996; Robinson and Silvia, 1978).

[†]See explanation in the Appendix of how the Fourier transform is derived from Euler’s Equation.

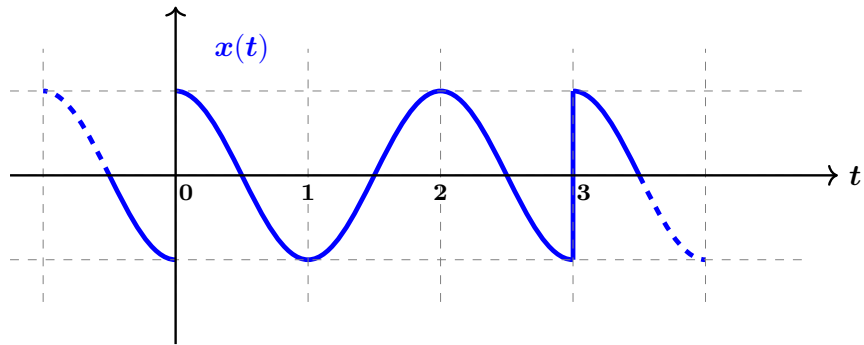


Figure 6.5: Periodic signal function $x(t)$ with discontinuities at $t = 0$ and $t = 3$.

Windowing minimizes the edge effects of the computed FFT over a noninteger number of cycles and reduces the amplitude of the discontinuities at the boundaries of each finite sequence. Windowing consists of multiplying the time signal by a finite-length window with an amplitude that varies smoothly and gradually toward zero at the edges. This makes the endpoints of the waveform meet and, therefore, results in a continuous waveform without sharp transitions. There are several varieties of window functions that can be applied depending on the signal. Three functions will be discussed below: rectangular window, Hanning window and the cosine taper.

The rectangular window function $w_R(t)$, also known as the Boxcar function, is the simplest window function and is defined by:

$$w_R(t) = \begin{cases} 1, & 0 \leq t < T_0 \\ 0, & \textit{otherwise} \end{cases} \quad (6.11)$$

equivalent to replacing all but the analyzed values of a data sequence by zeros, making it appear as though the windowed function suddenly turns on and off. A diagram of a rectangular window function appears in Figure 6.6. $x_w(t) = x(t) w_R(t)$ is regarded as being one period of a periodic function for which the Fourier series coefficients (or spectrum) are obtained using the FFT. In other words, the function shown in Figure 6.5 is a peri-

odic extension of $x_w(t)$, where $w_R(t)$ truncates the signal $x(t)$ to the sampled interval $0 \leq t < T_0$ to obtain $x_w(t)$.

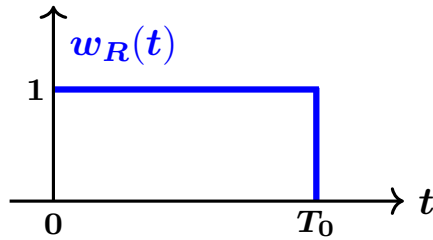


Figure 6.6: Rectangular window function (also known as the Boxcar function).

The Hanning window has the shape of one cycle of a $\cos(x) + 1$ function making the values always positive. The Hanning window of the sampled time series forces the ends to zero and has a value of one at the center of the window.

$$w_{Hann}(t) = \frac{1}{2} - \frac{1}{2} \cos\left(\frac{2\pi}{T_0}t\right), \quad 0 \leq t < T_0 \quad (6.12)$$

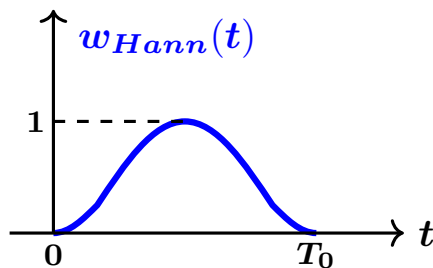


Figure 6.7: Hanning (raised cosine) window function.

The cosine taper window, otherwise called the Tukey window, is given by Equation 6.13.

$$w_{cos}(t) = \begin{cases} \frac{1}{2} \left\{ 1 - \cos \left(\frac{2\pi}{2\tau} t \right) \right\}, & 0 \leq t \leq \tau \\ 1, & \tau \leq t \leq T_0 - \tau \\ \frac{1}{2} \left\{ 1 - \cos \left(\frac{2\pi}{2\tau} (t - T_0) \right) \right\}, & T_0 - \tau \leq t < T_0 \end{cases} \quad (6.13)$$

The duration τ of the taper is usually chosen to be $\tau = T_0/10$ (Priemer, 1991). The shape of the cosine taper window is flat throughout most of the time domain t . A taper length can be specified which determines the amount of time that the window maintains a value of one, between the intervals of $0 \leq t \leq \tau$ and $T_0 - \tau \leq t < T_0$. The advantage of a cosine taper window is that the amplitude of a transient signal in the time domain is less likely to be altered compared to using Hanning, explained further below.

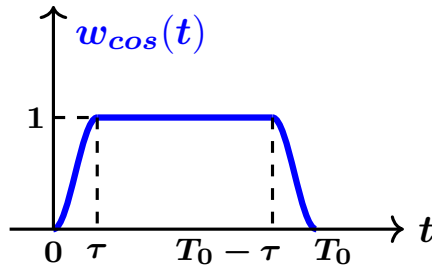


Figure 6.8: Cosine taper (Tukey) window function.

The frequency response of a window function is a continuous spectrum with a main lobe and side lobes (Figure 6.9 bottom panel). The main lobe is centered at each frequency component of the time-domain signal $x(t)$, while the side lobes approach zero. The height of the side lobes indicates the effect the windowing function has on frequencies around the main lobes. The side lobe response of a strong signal can overpower the main lobe response of a weaker signal. This response is known as spectral leakage. Window functions with lower side lobes reduce leakage in the measured FFT but tradeoff with an increase in the

bandwidth of the main lobe (National Instruments, 2016; Vakman, 1998).

The FFT is being implicitly windowed by a rectangular (boxcar) function, since the windowed Fourier transform is the Fourier transform of the window function onto itself. The transform of the rectangular window is a *Sinc* function, in other words $\text{sinc}(x) = \frac{\sin(x)}{x}$. A window in the time domain results in a convolution in the frequency domain transform of the window. This has the effect of convolving the input set with a *Sinc* function in the frequency domain, therefore creating new frequency components. The high side lobes of the *Sinc* function make it difficult to discern different amplitudes because the ripples of the *Sinc* function are observed as leakage. This can be thought of as dynamic range in terms of discernible amplitude of the frequency analysis. The rectangular window has the lowest dynamic range and has the highest level of spectral leakage. Other choices in windows will increase the dynamic range by reducing the side lobes of the window function such as the case with the Hanning window and the cosine taper (Tukey). As shown in Figure 6.9, the frequency response (spectrum) of the three described window functions.

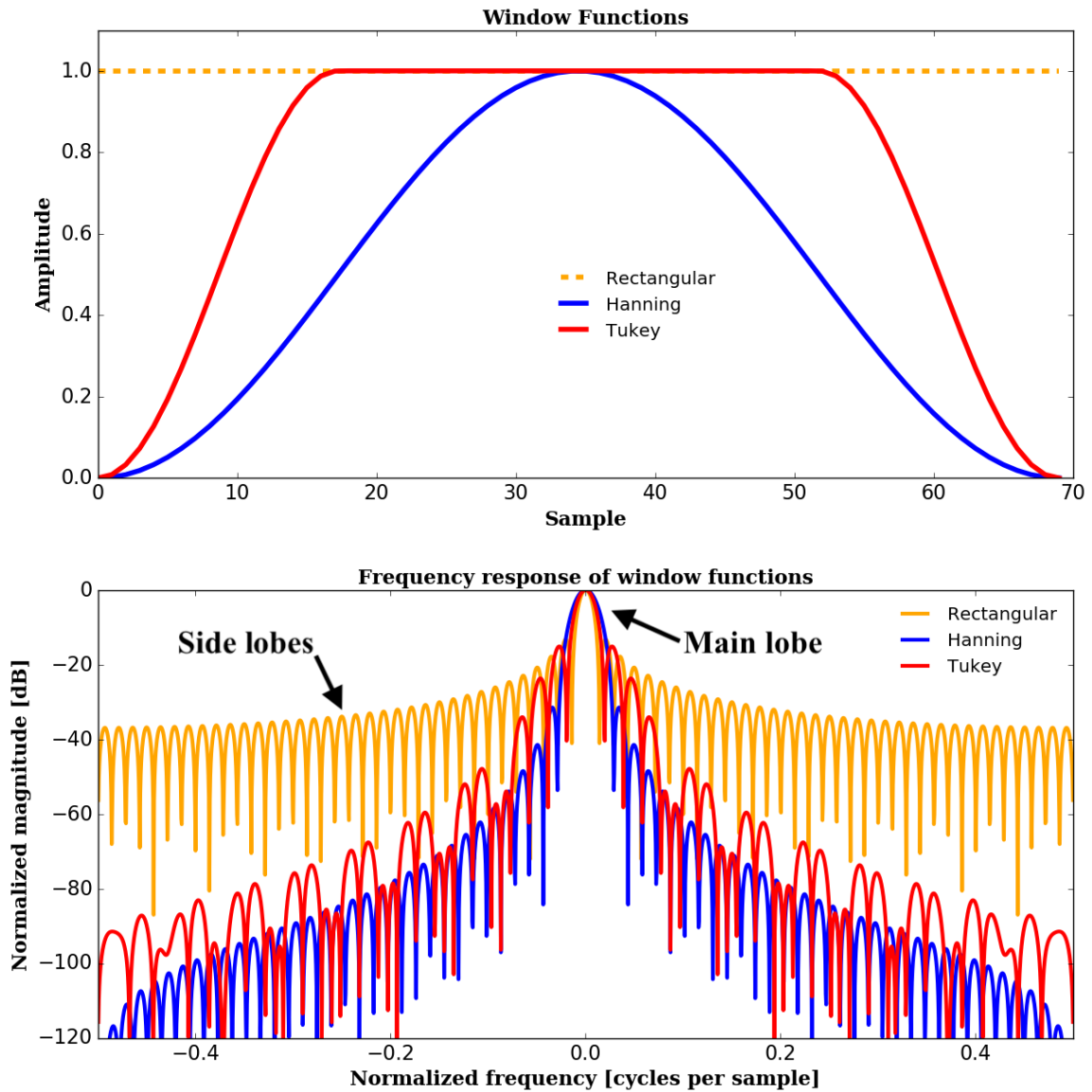


Figure 6.9: (Top) Three window functions rectangular, Hanning and Tukey from Python's *SCIPI* library with a sampling size of 70. (Bottom) The frequency response of the three window functions: rectangular, Hanning and Tukey. The rectangular window contributes the most spectral leakage because of the high side lobes of the *Sinc* function. The Tukey window is thought of as the middle ground between the two other windows. The Hanning has the lowest side lobes, and can cause loss of information in the spectrum.

The Hanning dynamic range is lower than the Tukey and the rectangular window and will attribute to a loss of signal information by distorting the wave form being analyzed by modulating the amplitude (shown in Figure 6.10 Bottom panel), or the variation in amplitude of the signal over the sampled time record (Marven and Ewers, 1996). Amplitude Modulation in a wave form results in the side lobes reducing the frequency resolution by 50%. The Hanning window should never be used with short transient signals but with continuous signals or smooth functions, where there are infinite possible values for time t in the sampled region of $x(t)$. The reason is that the Hanning window shape will distort the shape of the transient, and the frequency and phase content of a transient is intimately connected with its shape. Since the Hanning window distorts both the signal amplitude and energy, window correction factors are used to try and compensate for the effects of applying a window to data. There are both amplitude and energy correction factors for the Hanning window. The amplitude correction factor is 2.00, while the energy correction factor is 1.63. Correction factors are applied in the frequency domain by multiplication of all the amplitude values across the spectrum. It is possible to correct both the amplitude and energy content of the windowed signal to equal the original signal. However, both corrections cannot be applied simultaneously (Siemens PLM Software Inc, 2017; Azima DLI, 2009).

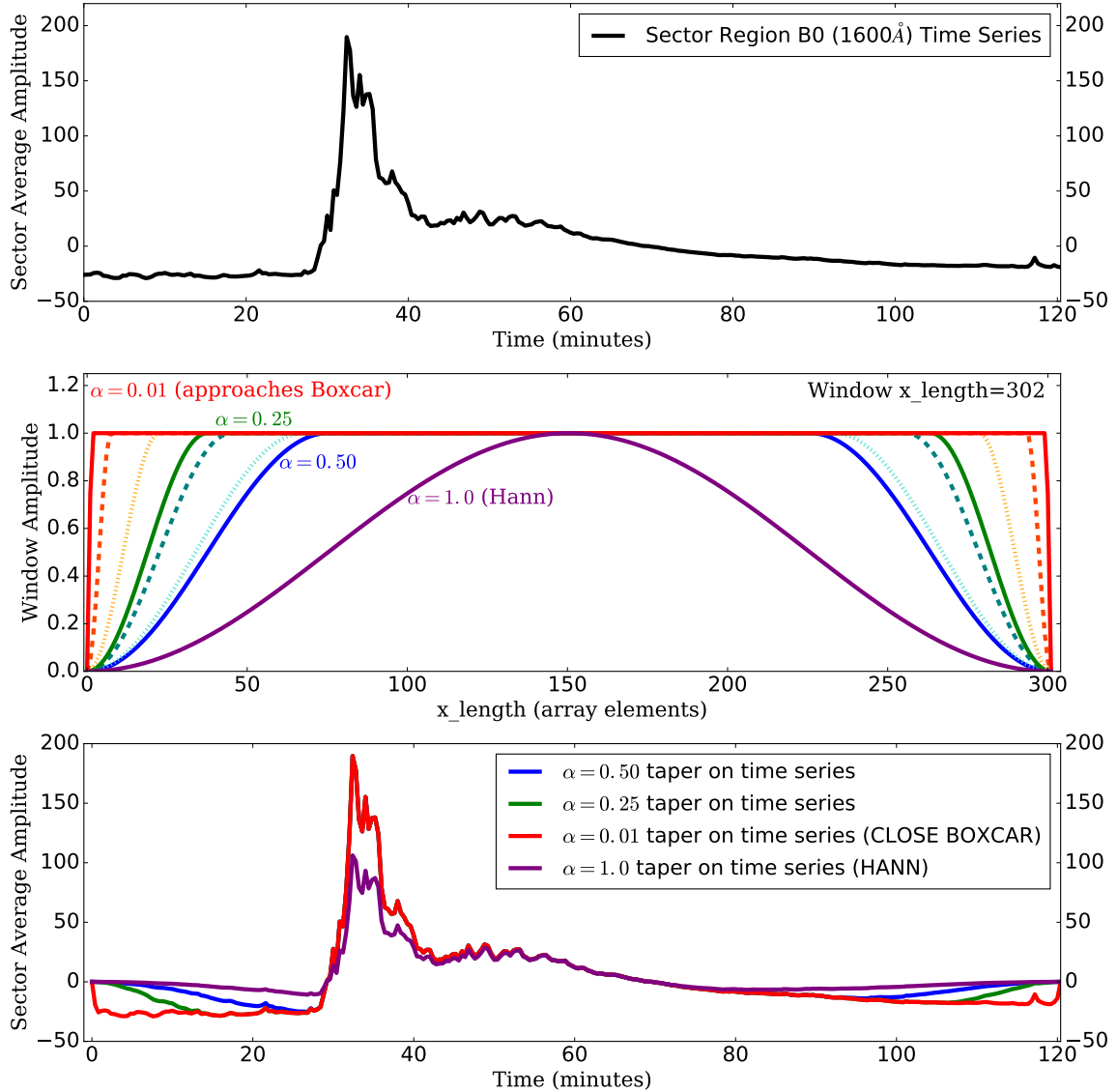


Figure 6.10: The Fourier transform does not give any information on the time at which a frequency component occurs. One approach which can give information on the time resolution of the spectrum is the Short Time Fourier Transform (STFT), where a moving window is applied to the signal and the Fourier transform is applied to the signal within the window as the window is moved. The choice of window is very important with respect to the performance of the STFT in practice. *(Top)* A time series of a sector sampled region BR0, the flare event in this time series is seen to take place around 35 minutes. *(Middle)* Several window functions are depicted: the Hanning window (Hann), several versions of the Tukey or tapered cosine window where alpha is the coefficient to change the gradient of the tapering of the window. *(Bottom)* The window functions are applied to the time series at the top to get a tapering of the time series at the edges. The windowing technique reduces spectral leakage and ringing when the FFT is applied to the time series. Notice the time series in which the Hanning function is used is less at the intensity peak. To correct for this we need to multiply the Hanning function by a gain coefficient to all the window components. The resulting solutions on the Hanning function will look similar to the Tukey function.

6.3 Data Analysis Procedures

6.3.1 Creating sector time series data (in IDL)

The procedures for creating sectorized sampled light curves involve sectorized sampling light curves with the average subtracted, where $x_{SA}(t) = x(t) - \langle x \rangle$, where $\langle x \rangle$ represents the average of all the elements in x . The procedures begin with the AIA subtracted averaged intensity images classified as ASCo280_2hr at the beginning of the filename with a pixel array size of 280×280 . On the set of 2-dimensional images that comprise the two hour time series, the average of all the pixels is taken in an angular sector region on the 2-dimensional image, see Figure 6.11. The procedures for doing this rely on designing a procedure to mask an angular sector on a 2-dimensional image. This program is called *sector.pro* and is created in IDL. Within *sector.pro*, a function *wedge_mask.pro* is included that transforms the rectangular coordinate system (x, y) into polar coordinates (r, θ) . A map of the all the pixels within the rectangular system as the transformation \mathcal{T} defined by $(x, y) = \mathcal{T}(r, \theta) = (r \cdot \cos \theta, r \cdot \sin \theta)$ is created. In other words, the polar conversion equations created by $(x, y) = \mathcal{T}(r, \theta)$ begins with equations 6.14,

$$\begin{aligned}x &= r \cdot \cos \theta \\y &= r \cdot \sin \theta\end{aligned}\tag{6.14}$$

where r is the radius and a form of the Pythagorus Theorem, $r = \sqrt{x^2 + y^2}$. The transportability has to be taken into account that the mask sector has the ability to move anywhere around the 2-dimensional image and by accounting for the location of a center pixel coordinate (x_0, y_0) not at the origin (0,0) of the 2-dimensional image array. In rectangular cartesian coordinates the equation of a circle of radius r centered on (x_0, y_0) is:

$$r^2 = (x - x_0)^2 + (y - y_0)^2\tag{6.15}$$

With the equation of a circle (equation 6.15) for a center pixel coordinate (x_0, y_0) the rectangular transformed polar coordinates, $(x, y) = \mathcal{T}(r, \theta)$, are now converted to the polar transformation $(x_0 + r \cdot \cos \theta, y_0 + r \cdot \sin \theta)$ for the x and y coordinates. So the polar conversion equations with the center pixel coordinate located at (x_0, y_0) now become equation 6.16,

$$\begin{aligned} x &= x_0 + r \cdot \cos(\theta) \\ y &= y_0 + r \cdot \sin(\theta) \end{aligned} \tag{6.16}$$

Within *wedge_mask.pro* the central pixel (x_0, y_0) is designated, the change in radius Δr with the primary radius coordinate of the sector r_0 and the secondary radius coordinate of the sector r_1 , which determines the sector length. Recall, variable radii equation 6.5, see equation 6.17,

$$r_n = \sqrt{2r_{n+1}^2 - r_{n+2}^2} \tag{6.17}$$

where the radius r_n is calculated up to the given r_{max} . In the analysis, the primary coordinate $r_0 = 0$, the secondary coordinate $r_1 = 50$ and $r_{max} = 125$ since the diameter of the image array is 280. Additionally, the change in angular size $\Delta \theta$ denoted by starting angular coordinate θ_0 and the end angular coordinate θ_1 is inputted, this determines the size of the angle. The *wedge_mask.pro* function will store the masked sector pixels of each image. We then call it in *sector.pro* within a *forloop*. To create the mask, the 2-dimensional image array is multiplied by the mask where *wedge_mask.pro* is called. Within the loop we use IDL's *WHERE* function to differentiate the masked pixels and then take the average of the masked sector pixels within the image. Below is an example of the loop within *sector.pro* that calls the function *wedge_mask.pro*.

```
FOR i=0, n_files-1 DO BEGIN
  images = readfits(filenamees[i], Header, /SILENT)

  mask = WEDGEMASK([nx=280,ny=280],[radius_0 , radius_1 ],
                  [theta_0 , theta_1 ], center_pixel=[x0,y0])
```

```

sector = images * mask
...

```

ENDFOR

The area of the sector of an annulus for each sector region moving out of the angle θ has to be conserved, in other words the number of pixels in each annuli moving out in the larger analysis angle will be similar. For example, for a $\theta = 45^\circ$ sampling around the sequential annuli the angle will remain the same moving out, but the area \mathcal{A} (and number of pixels in each region) in each 45° sector will be different if the change in radii is kept constant to the initial change in radii. If the number of pixels are to remain the same, the distance between the radii will vary and the area \mathcal{A} of the sector will be kept the same. The area of a sector \mathcal{A}_{sector} is,

$$\mathcal{A}_{sector} = \pi(r_1^2 - r_0^2) \cdot \frac{1}{N} \quad (6.18)$$

where N equals the number of total sectors divided equally around the entire circular annulus. In our study, the entire annulus is divided into eight sectors, each equaling $\theta = 45^\circ$.

The two hour time series ASCo280 images have an image stack at a set cadence of 12 seconds for the AIA 304 Å wavelength, and 24 seconds for the AIA 1600 Å, 1700 Å wavelengths. Each image in the stack is 2-dimensions and the whole image stack is 3-dimensions running in the time direction. The *sector.pro* procedure will run the partitioned window through the 3-dimensional data cube stack partitioned and jumped by the appropriate wavelength cadence. A wrapper program *sectorcall.pro* was designed to do this by calling the sector program *sector.pro* in a loop to repeat the sector calculation. In other words, the wrapper program runs through the data cube by extracting the sector pixels by the *wedge_mask.pro* function and then taking the average of those pixels at the boundary values of the variable radius at $r_n = \sqrt{n}$, see equation 6.7. It also takes the area of the sector, in equation 6.18, and prints out the results for verification that each cal-

culated sectorized region moving out in the angle are equal, therefore conserving the area.

The calling procedure portion for the *sectorcall.pro* wrapper is found below,

```
FOR N=0,6 DO BEGIN
    radius_0 = SQRT(((N)*R1^2) - (R0)^2)
    radius_1 = SQRT(((N+1)*R1^2) - (R0)^2)

    SECTOR, radius_0 , radius_1 , theta_0 , theta_1 , x0 , y0

    sector_area = (! pi/8) * ((radius_1^2) - (radius_0^2))

    print , 'Area of sector: ', sector_area
ENDFOR
```

The *sectorcall.pro* wrapper writes the output to a *.dat* file containing two 1-D column arrays with one column containing the sector average for all the images in the time series and the second column containing the reference time (in minutes) starting at zero and calculated from extracting the observation time from each image header file using IDL's *SXPAR* function.

304 Å Sector Sampling— Regions A, B, C, D, E, F, G, H

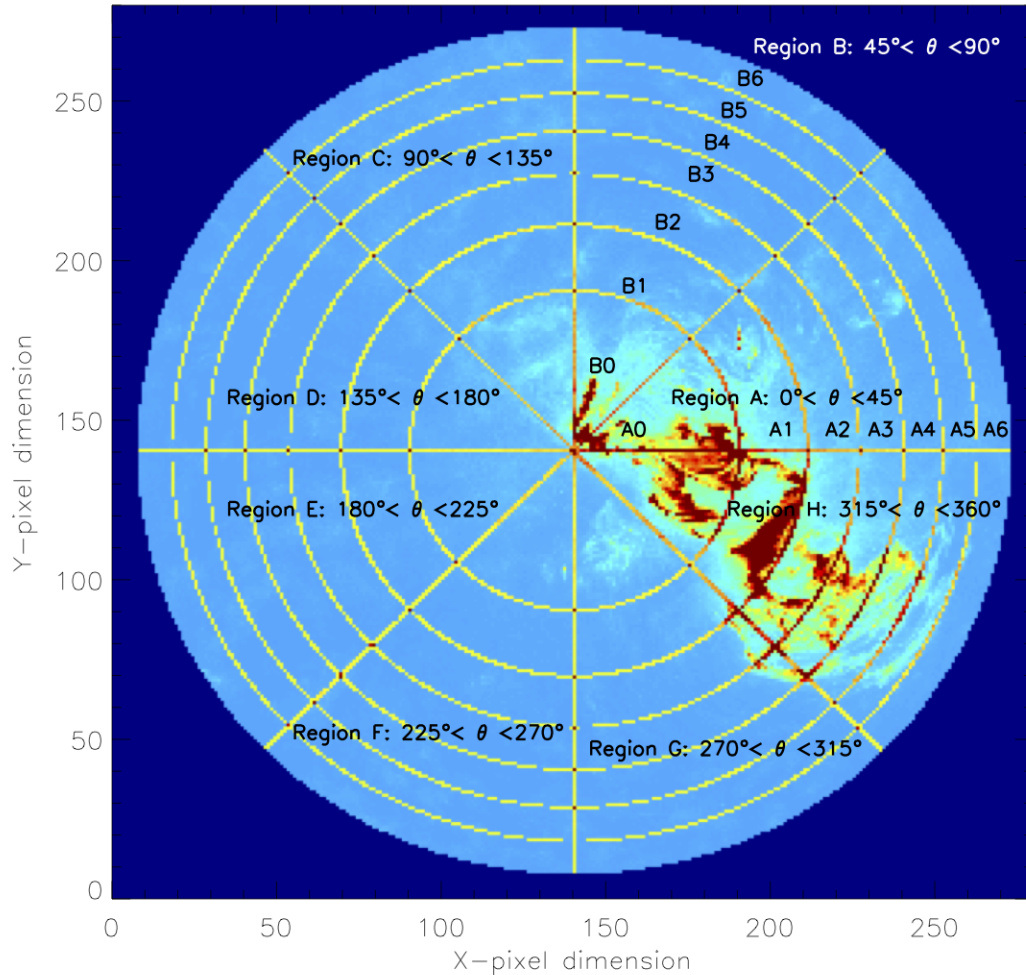


Figure 6.11: 304 Å sector sampling map. Each sectorized region (accurately represented on the image) the average is taken for the intensity pixels through a 3-dimensional image stack in the time series. Each sectorized averaged region produces a light curve.

6.3.2 Running the FFT on sector time series (in Python)

For the next phase of the sector averaged light curves, Python is the language of choice. The data analysis on sectorized light curves can be handled with ease through an interactive Python environment known as the Jupyter notebook application. Through this interactive computational environment, rich text can be added within the notebook along with exe-

cutting code and performing mathematical computation that will produce plots. There are several additional advantages in using Python. One advantage of using Python for analysis is the use of the NUMPY package for array manipulation. The NUMPY package supports object oriented programming through the manipulation of multidimensional arrays in Python known as tuples, which in turn allows all the analysis codes to be executed without the use of *for* loops. However, the data rate on the notebook has to be increased to handle the load of codes contained within one notebook. There is a way to set the data rate of the notebook before initiating it. An initiating command that regulates the data rate for the Jupyter notebook can be set within the Python startup configuration file. Or it can be initiated within the Bash shell on the command line by the command:

```
bash$ jupyter notebook -- NotebookApp.iopub_data_rate_limit=1000000000
```

For the analysis code, a notebook is created for each analyzed wavelength of sector averaged light curves. Within each notebook the code for each angled sector group or sector annular group, is analyzed within one cell of the Jupyter notebook. Each cell can produce multiple stacked plots corresponding to the associated sector region. As a procedural example to produce one plot, and the anatomy of a singular analysis code contained within one cell of the Jupyter notebook – this will be explained from here on out. The code begins with the calling of several packages to run the code: NUMPY, SCIPY and additional packages for plot utilization, such as MATPLOTLIB. We use the FFT in the SCIPY package. Here is a code snippet of the package call at the beginning of the code:

```
import numpy as np
import matplotlib.pyplot as plt
from scipy import signal
from scipy.fftpack import fft, ifft
```

Before the data files can be read, two procedures have to be defined within the code: a definition for a rolling window and a definition for the tapered Tukey window function. Both functions will call NUMPY arrays to define the analyzed window within the time series. For the rolling window a variable for the size, shape and strides are defined within

the function. The *rolling_window.def* procedure then returns a moving window of the extracted rectangular data window jumped through the time series.

$$W_{Tuk}(x) = \begin{cases} \frac{1}{2} \left\{ 1 + \cos\left(\frac{2\pi}{\alpha}[x - \alpha/2]\right) \right\}, & 0 \leq x < \frac{\alpha}{2} \\ 1, & \frac{\alpha}{2} \leq x < 1 - \frac{\alpha}{2} \\ \frac{1}{2} \left\{ 1 + \cos\left(\frac{2\pi}{\alpha}[x - 1 + \alpha/2]\right) \right\}, & 1 - \frac{\alpha}{2} \leq x \leq 1 \end{cases} \quad (6.19)$$

The returned values of *rolling_window.def* are then inputted into the tapered Tukey function *tukeywindow.def* in which the window size and the taper function α are defined. Equation 6.19 is used within the Python definition of the Tukey window, $W_{Tuk}(x)$. This version of the Tukey window, $W_{Tuk}(x)$, is similar to the *tukeywin* version in MATLAB[‡]. As explained in the last section on *Window Functions*, the Tukey or cosine taper uses three cases in equations 6.13 and 6.19 to produce a taper around a rectangular window or Boxcar function, equation 6.11. Within the code the Tukey function will return the array values of the window with the taper applied, from the defined window size and the taper size, α . In the analysis $\alpha = 0.25$ is applied.

```
#DEFINITION: Rolling window
def rolling_window(x: ndarray, window_length):
    ...
    return np.lib.stride_tricks.as_strided(x: ndarray, shape=shape
, strides=strides)

#DEFINITION: Tukey Taper Window Function
def tukeywindow(window_length: ndarray, alpha=n: integer):
    ...
    return window
```

The numerical values for the time array and sector average in the *.dat* files are then inputted using NUMPY, and defined as two column NUMPY arrays for time (*mintime*) and sector average for each sector sampling (*data*). A variable *tukeytaperwin* is

[‡]Explanation of MATLAB'S *tukeywin* function can be found at: <https://www.mathworks.com/help/signal/ref/tukeywin.html>

defined that calls *tukeywindows.def* and input the values for the Tukey window. Then a variable *tukeyvals* calculates the Tukey tapered window onto the data segments of the time series.

```
tukeytaperwin=tukeywindow(window_length=n:integer, taper_size,
    alpha=n:integer)

timewindows=np.array(rolling_window(mintime:ndarray,
    window_length= n:integer))
datawindows=np.array(rolling_window(data:ndarray, window_length=
    n:integer))

tukeyvals=datawindows*tukeytaperwin
```

After the data window containing all sector averages within the window is defined, the outputted frequency arrays are determined from the inputted data window. The Nyquist frequency has to be determined for each cadence data set. The Nyquist frequency ($f_{nyquist}$, equation 6.20), is defined as the highest frequency that the sampled signal can unambiguously represent. The Nyquist frequency depends on the cadence of the data set. Based on equation 6.20, the Nyquist frequency for the AIA 1600 Å and 1700 Å wavelengths is 20.833 mHz, and the Nyquist frequency for 304 Å wavelength is 41.667 mHz.

$$f_{nyquist}(mHz) = 1000 \cdot \frac{1}{2} \cdot \frac{1}{T_S} = \frac{500}{T_S} \quad (6.20)$$

The Nyquist frequency is used to determine the maximum observable frequency in the data set. Then the maximum time variable of the time series, *maxtime*, is defined based on the final value in the time array of the sector averaged light curves of 120.4 minutes. The sampling frequency is defined and based on the maximum time variable and the frequency conversion is based on minutes. A NUMPY array is created to calculate and store the frequency values for each time cadence measurement of the reference time array (in minutes) multiplied by the sampling frequency in the sector average file. The outputted frequency will be the frequency of the real values of the FFT up to the Nyquist frequency

and converted to millihertz values.

```
maxtime=120.4    #maximum time value (in minutes) for data
samp_frequency = 1.0/(60*maxtime)
frequency = np.array(np.arange(0,data.size))*samp_frequency
...
outfrequency = frequency[np.arange(0,(frequency.size/2)+1)]*1000
```

The goal of calculating the FFT on the spectrum averaged time series is to investigate the power spectrum of each individual light curve to detect any hidden signals. To reiterate, the general form of the DFT is represented with no window function in equation 6.21, for the N-point DFT of a sequence $x[0], x[1], \dots, x[N-1]$, where $f_k = k/N$ and $k = 0, 1, \dots, N-1$ (Kandhasamy, 2010),

$$X(f_k) = \sum_{n=0}^{N-1} x[n] \exp(-j2\pi f_k n) \quad (6.21)$$

The Power Spectra is calculated as the magnitude squared of the DFT. This yields the Power Spectral Density, $P(f_k)$ (equation 6.22) of the function (Marven and Ewers, 1996; Kandhasamy, 2010),

$$P(f_k) = \frac{1}{N} \left| \sum_{n=0}^{N-1} x[n] \exp(-j2\pi f_k n) \right|^2 \quad (6.22)$$

The PSD will produce the power values and can be represented as a time-frequency-power spectrogram representation in the X-Y-Z plane (coordinating with time-frequency-power respectively) when the window function (see Figure 6.12) is applied.

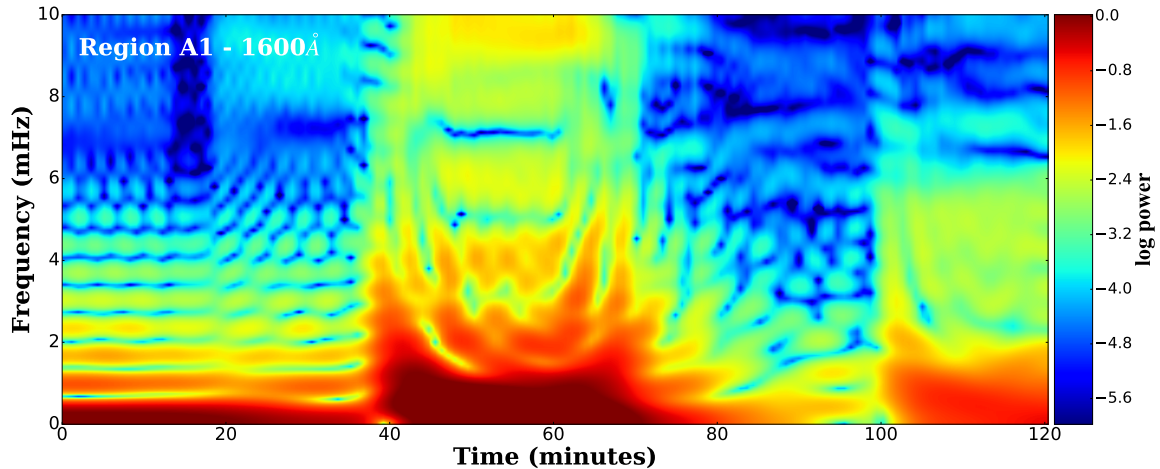


Figure 6.12: A spectrogram plot for sector averaged region A1 in the 1600 Å wavelength. The power values of the PSD are represented as a time-frequency-power spectrogram representation in the X-Y-Z plane coordinating with time-frequency-power respectively.

To calculate the real part the FFT within Python, NUMPY's *fft.rfft* routine is utilized to calculate the real side or values of the FFT without returning the complex values. To calculate the the amplitudes of the power (*POWERAMPLITUDE*) the FFT will be evaluated from the *tukeyvals*. The computed FFT values will produce multidimensional arrays or tuples for the entire set of windowed time series segments. The FFT also has to normalized by the data window size, $1/N$.[§] The PSD is then calculated from the amplitudes of the FFT (*POWERAMPLITUDE*), producing the power values in a variable called *outpower*, that is in the form of a tuple. The *outfrequency* variable is also calculated from the procedures explained above. The two variables, *outpower* and *outfrequency* will produce array values that can be plotted as an image using Python's Matplotlib package, where the logarithmic scale can be applied.

```
N = data.size
POWERAMPLITUDE = (1.0/N)*np.fft.rfft(tukeyvals,N)
outpower = np.abs(POWERAMPLITUDE[np.arange(0,(data.size/2)+1)])
**2
outfrequency = frequency[np.arange(0,(frequency.size/2)+1)]*1000
```

[§]Futher explanations on normalization Python's FFT is found in the Appendix section.

6.4 Results: Sector Sampling Method

6.4.1 Sector Sampling Method Interpretations

There are several observations seen in the overall measurements using the sector method. This section will discuss some of the interesting observations found in the process. Periodic reference will be made to Figure 6.11 in visualizing a map of the sector sampling locations along with the data attained from each sector region. To reiterate, the sampling is taken 3-dimensionally, such that Figure 6.11 is a 2-dimensional representation of each sector region superimposed on a 3-dimensional stack of images two hours in length. The data was handled for each region from Region A through Region H. Each region around the entire circle was sliced up into 45 degree increments. Within each 45 degree slice per region, sector sampling was done to take the average pixel value per frame through the stack of images within the 45 degree sector. Each sector region was separated into seven sector regions, starting from the center of the image and moving outward close toward the edge of the image. For each sector region moving out within the 45 degree slice the area is conserved and the number of pixels are the same for each sampled sector within each region. Each sector superimposed onto the 3-dimensional stack of images produces a light curve of the pixel average per image frame within the two hour time series. For each of the three analyzed AIA wavelengths (1700 Å, 1600 Å and 304 Å), there was a total of 56 light curves from the sector sampling. Each light curve produces a spectrogram plot in which the windowed FFT was performed, totaling 56 spectrograms. A total of 168 individual spectrograms were produced from all three wavelength analyses. Through this thorough sampling the spatial dimensions are conserved and all regions surrounding the flare covered, such that there is not a space of missing data.

The main observed phenomena is the change in power relative to the location of the solar flare. As the sampled region is within the flaring regions A, H and G, the power is high and then decreases as the location of the sample is moving outward away from

the flare. To visualize this, the spectrograms of the sectorized regions are grouped around their corresponding annulus. There is a total of six annuli from annulus regions 0 to 6, this is covered in Figures 6.17 through Figures 6.23 in section 6.4.2 – *Sector Sampling Method - Multi-wavelength Annular Sampling*. The analysis was done this way as the most appropriate way to visualize the data as a whole and visualize and compare individual sectorized annulus regions located near the flare as opposed to moving away from the flare around the annulus. The generalized behavior of the boost in power due to ignition of power is well known and is supported by many researchers (Ambastha *et al.*, 2003b; Kumar *et al.*, 2006, 2011) and was covered in Chapter 1, sections 1.5.3 – *Acoustic power around solar active regions* and sections 1.5.4 – *Excitation of p-modes by solar flares*. In all the spectrogram plots within the lower frequencies of 0 to 4 mHz, where most of the global p-modes reside there is a boost in power at those lower modes indicated by the red color within the spectrogram plots. There is a subtle undulation of the modes when looking at each spectrogram plot that is definitely shown in the lower modes of 0 to 4 mHz. As the sector sampling is in a region within the flare such as regions H, G and A, the overall mode behavior within the spectrogram seems to “stratify” as if observing a binning effect. The cause of this effect is unknown at the moment. As a side note, the black dashed line within each spectrogram indicates the time within the time series where the flare event took place, this event time was close to the middle of the time series.

In observing 45 degree slice per region, such as Region A in the 1600 Å wavelength, as in Figure 6.13, the power is higher for the flaring regions A0 and A1, but lessens as the 45 degree sectorized regions move out away from the flare. Within the quieter regions of A2 through A6, the power seems to undulate and subtly rises and lowers. This subtle undulation is also seen in the time-distance plots of the 304 Å intensity and 2–4 mHz PMM sampling found in the next section, especially within the quieter regions, see Figures 6.26 and Figures 6.25. However, the signal of the flare seems to saturate this subtle feature. The origin of this subtle feature is unknown but could be a feature of the global modes. The

acoustic p-modes can be observed with the highest power within each spectrogram from 0 to 4 mHz. There is a clear acoustic cutoff observed within each spectrogram plot by the blue areas of decreasing power, this acoustic cutoff happens at 5.33 mHz. An example of acoustic cutoff can be clearly seen in regions A0 in the spectrogram, of Figure 6.13, and other spectrogram regions.

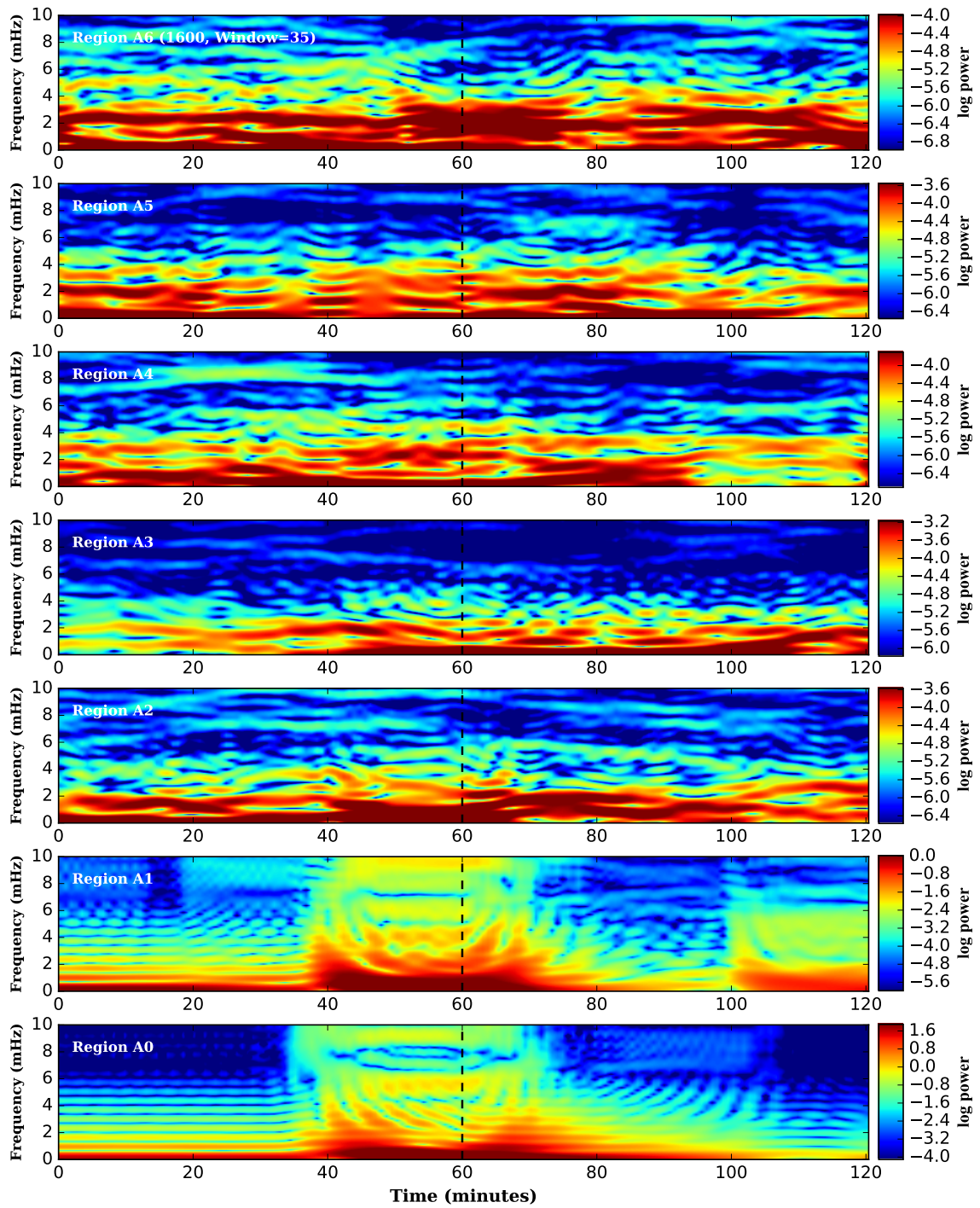


Figure 6.13: 1600 Å sector region A, a 45° sector slice, where the sampling was taken between $0^\circ \leq \theta \leq 45^\circ$. The power is greatest at sector region A0 and gradually lessens moving out to sector region A6.

In observing a single annulus such as Annulus 1 in Figure 6.14, the power can be visualized as varying from higher values near the flaring region H1, G1 and A1 and then decreasing to lower values when moving away from the flare as in regions B1, C1, D1, E1 and F1. Within the flare the power seems to be increasing in a 'U' shaped feature that seems to be only observed within the flare, see regions A1, H1 and G1 in Figure 6.14. Furthermore, the flare seems to cause excitation of the power to go beyond the acoustic cutoff. This could be an indication of magnetohydrodynamic processes occurring to the modes and could be an indication of scattering of the modes that cause mode mixing thereby creating magnetoacoustic waves. In region A1 in Figure 6.14, there is a secondary flaring event occurring after 100 minutes, since the flare that occurred on 24-October-2014 was a ribbon type flare seen with two bands.

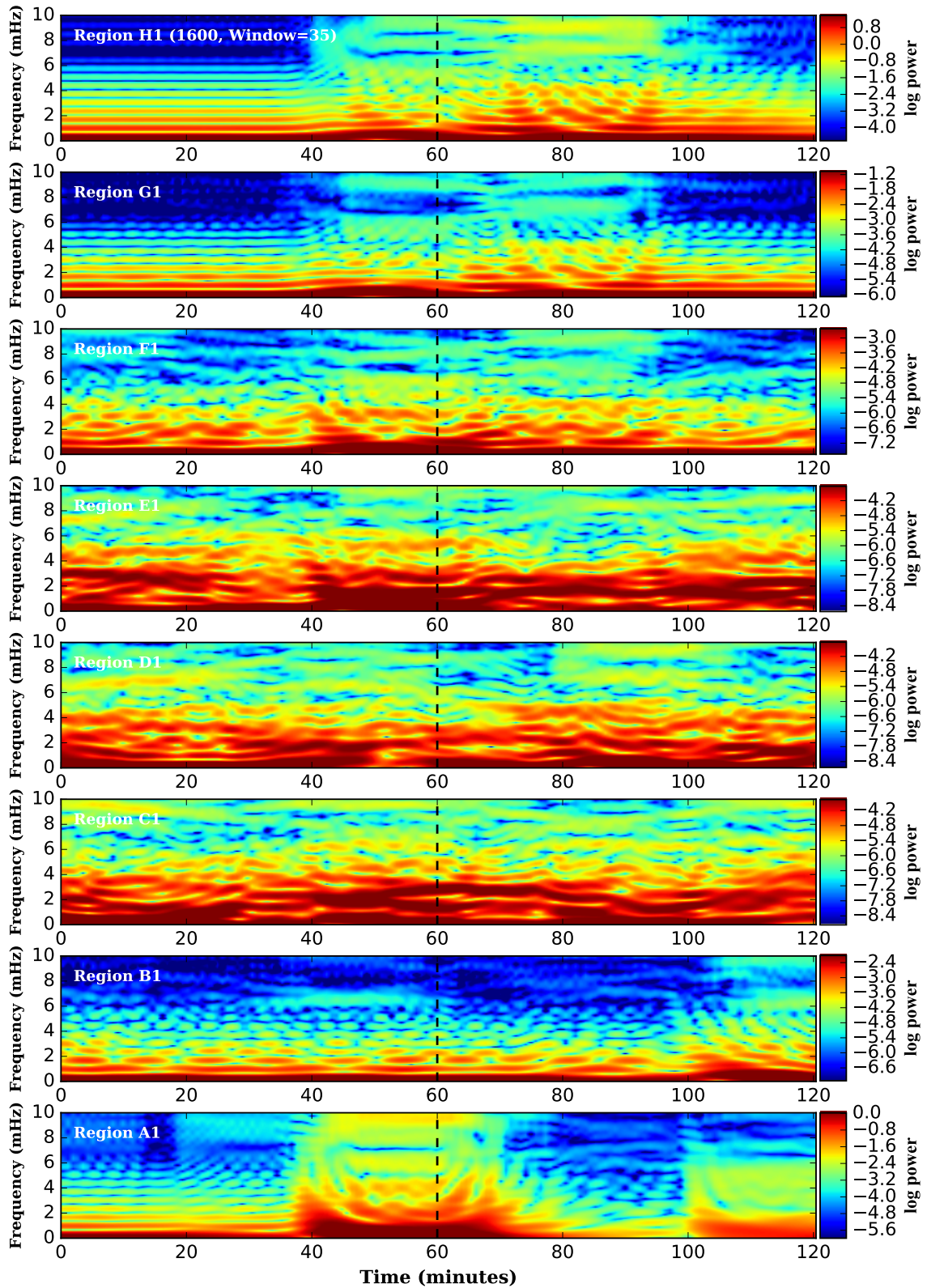


Figure 6.14: 1600 Å sector annulus 1 sampling. The power is the highest for regions H1, G1 and A1 and then lowering when moving away from the flare as in regions B1, C1, D1, E1 and F1.

On the discussion of spurious features, a look at individual spectrograms aligned in a multi-wavelength plot as in Figures 6.15 and 6.16. Within region E1 in the 304 Å spectrogram (top plot in Figure 6.15) there is an absorption feature seen between 40 and 55 minutes. There is also a strong absorptive feature seen in the region C0 in Figure 6.16 between 60 and 80 minutes, see the top plot in Figure 6.16. This absorptive feature only occurs in the 304 Å wavelength and is not observed in any of the 1700 Å and 1600 Å spectrogram plots. The absorptive features could indicate a characteristic of the chromospheric lines, since these type of features were observed also within the GONG H α spectrogram plots discussed in Chapter 3. This study has not been able to correlate if this absorptive feature could be due to concentrated magnetic processes occurring at the time and location of these observed phenomena. Within a running difference movie created from the PMMs in the 304 Å wavelength, there were observed arches of plasma running along magnetic fields lines. However, the location where the bands of plasma occurred was away from region E1. Additionally, there is an apparent similarity between the 1700 Å and 1600 Å spectrograms from each sectorized region, since both wavelengths are close to each other and both are within the photospheric measurements.

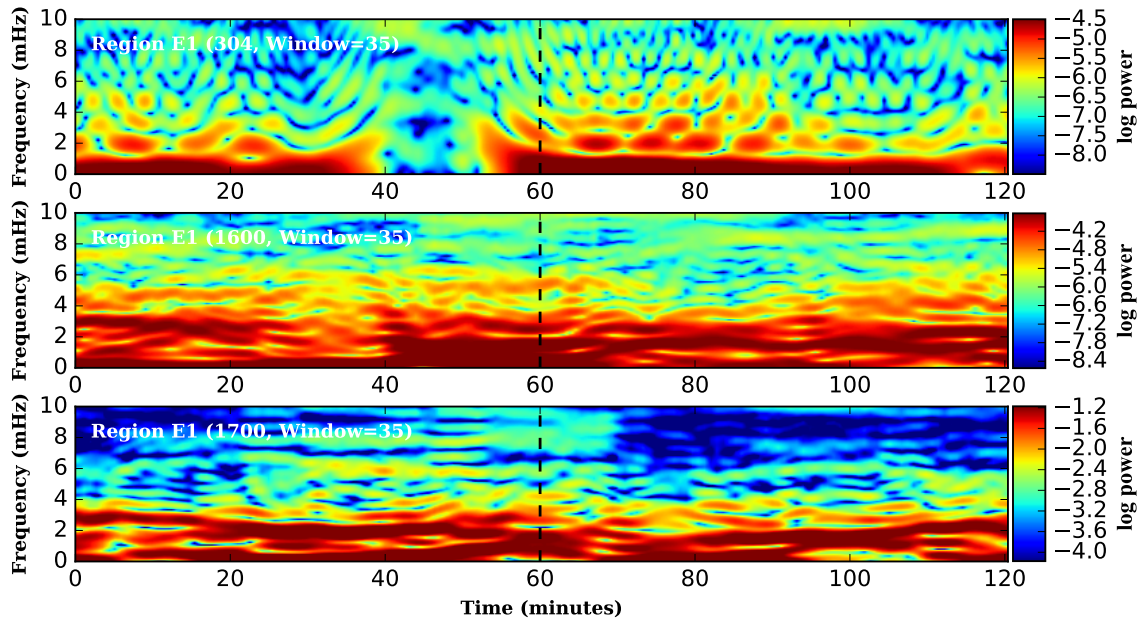


Figure 6.15: Multi-wavelength region E1 in the AIA 1700 Å (lower photosphere), AIA 1600 Å (upper photosphere) and 304 Å (chromosphere). All three wavelengths are windowed at the same size, 35 data size points in the time direction.

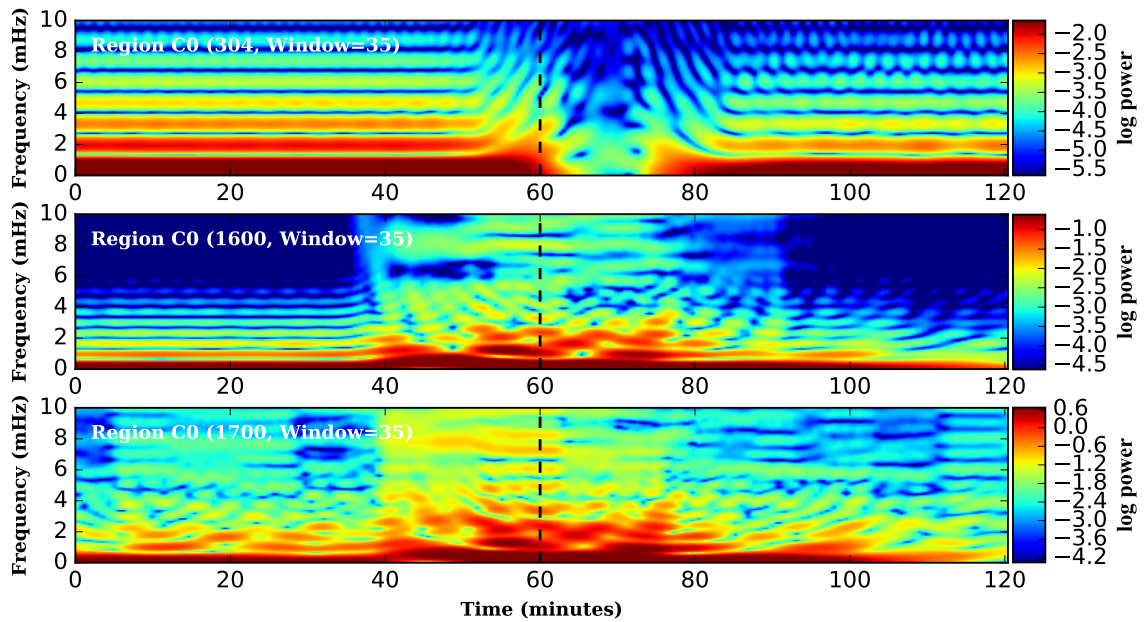


Figure 6.16: Multi-wavelength region C0 in the AIA 1700 Å (lower photosphere), AIA 1600 Å (upper photosphere) and 304 Å (chromosphere). All three wavelengths are windowed at the same size, 35 data size points in the time direction.

6.4.2 Sector Sampling Method - Multi-wavelength Annular Sampling

The plots in this section are multi-wavelength plots of the entire sector region map in Figure 6.11 corresponding to the 1700 Å (lower photosphere), 1600 Å (upper photosphere), 304 Å (chromosphere)). These multi-wavelength plots in Figure 6.17 through Figure 6.23 are of the sectored annuli moving out from annulus 0 to annulus 6. These plots are for reference.

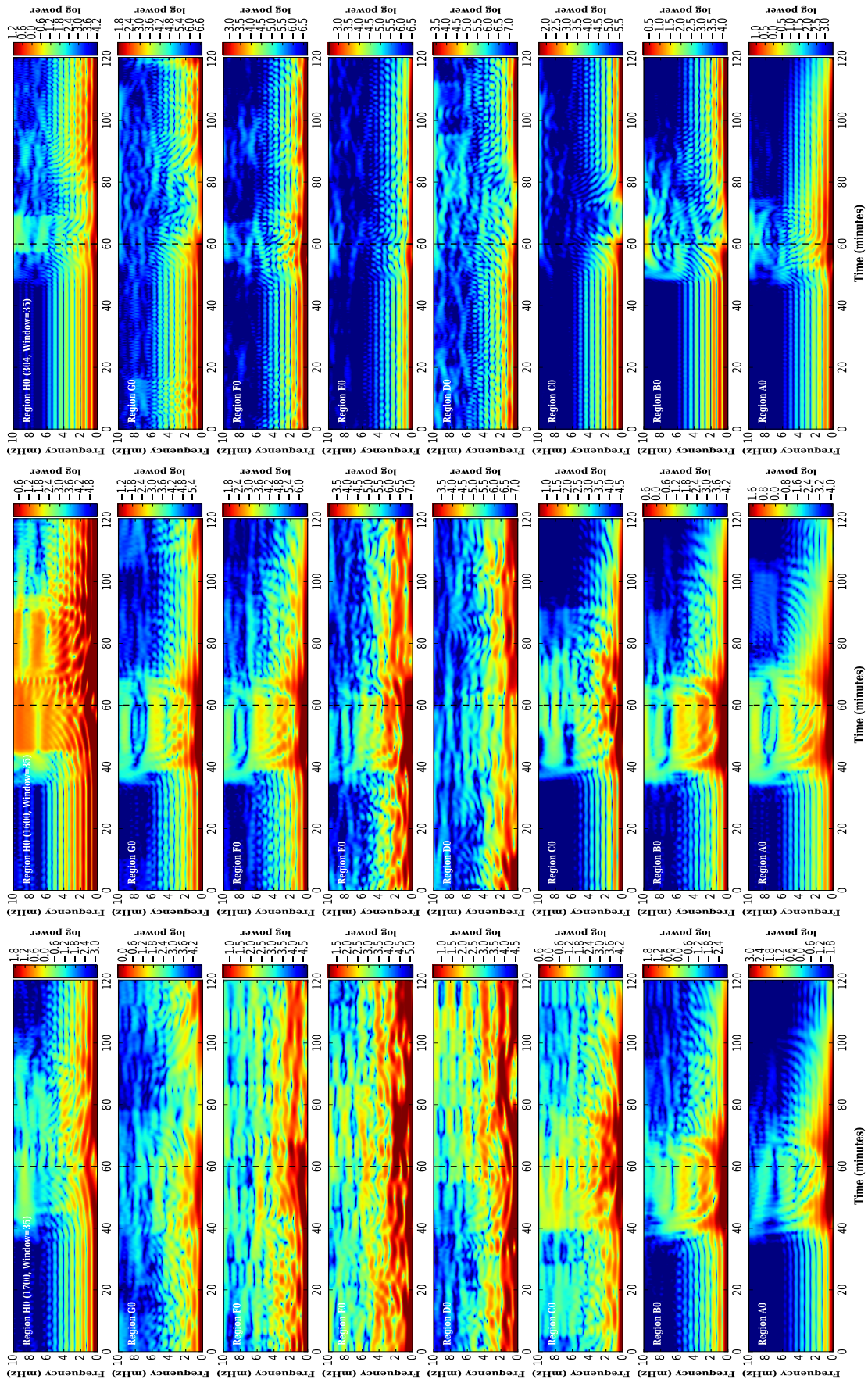


Figure 6.17: Multi-wavelength Annulus 0 (1700 Å (lower photosphere), 1600 Å (upper photosphere), 304 Å (chromosphere)). The black 'dashed' line indicates the time of the main flare event. The Power is in Log Power.

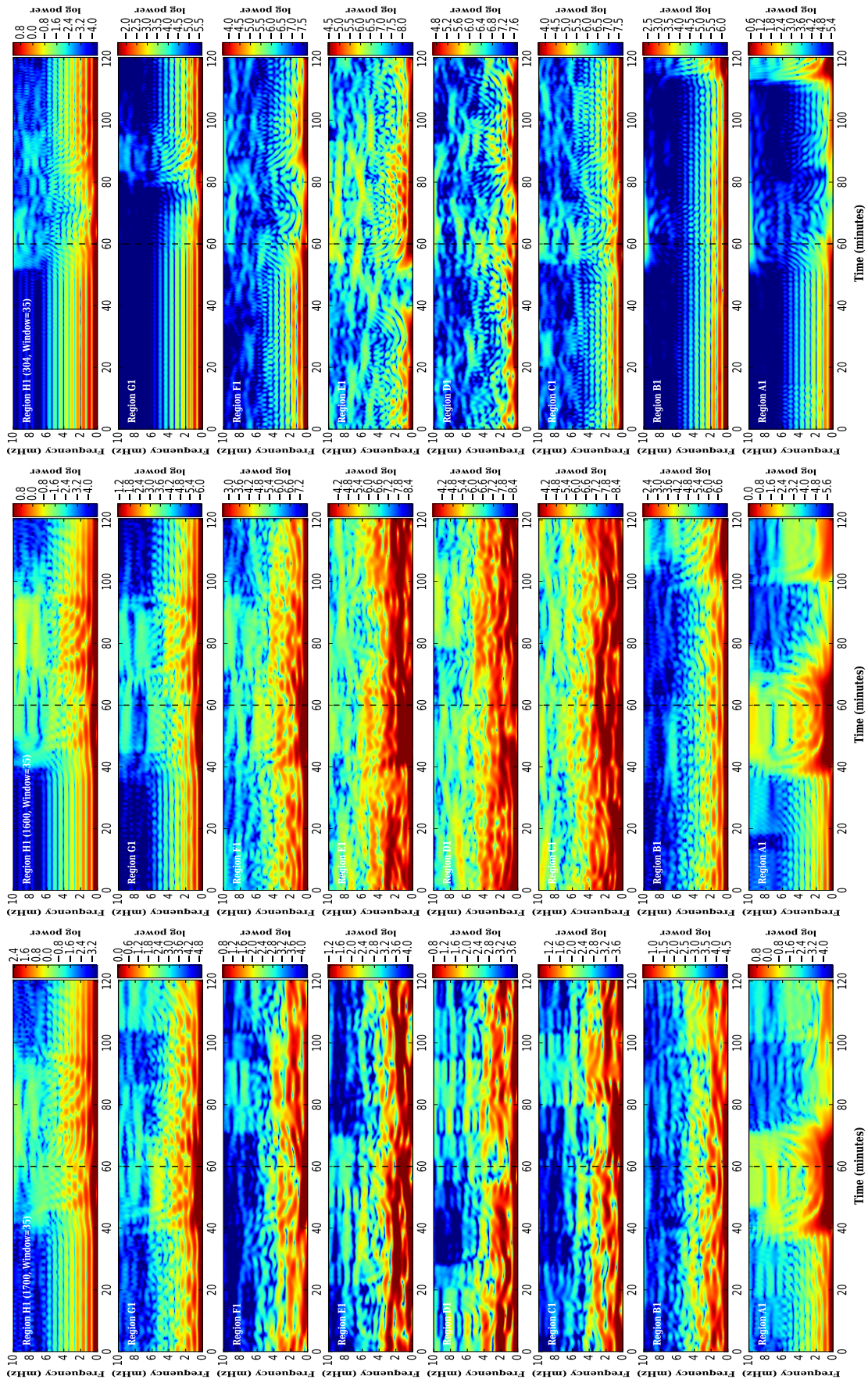


Figure 6.18: Multi-wavelength Annulus 1 (1700 Å (lower photosphere), 1600 Å (upper photosphere), 304 Å (chromosphere)). The black ‘*dashed*’ line indicates the time of the main flare event. The Power is in *Log Power*.

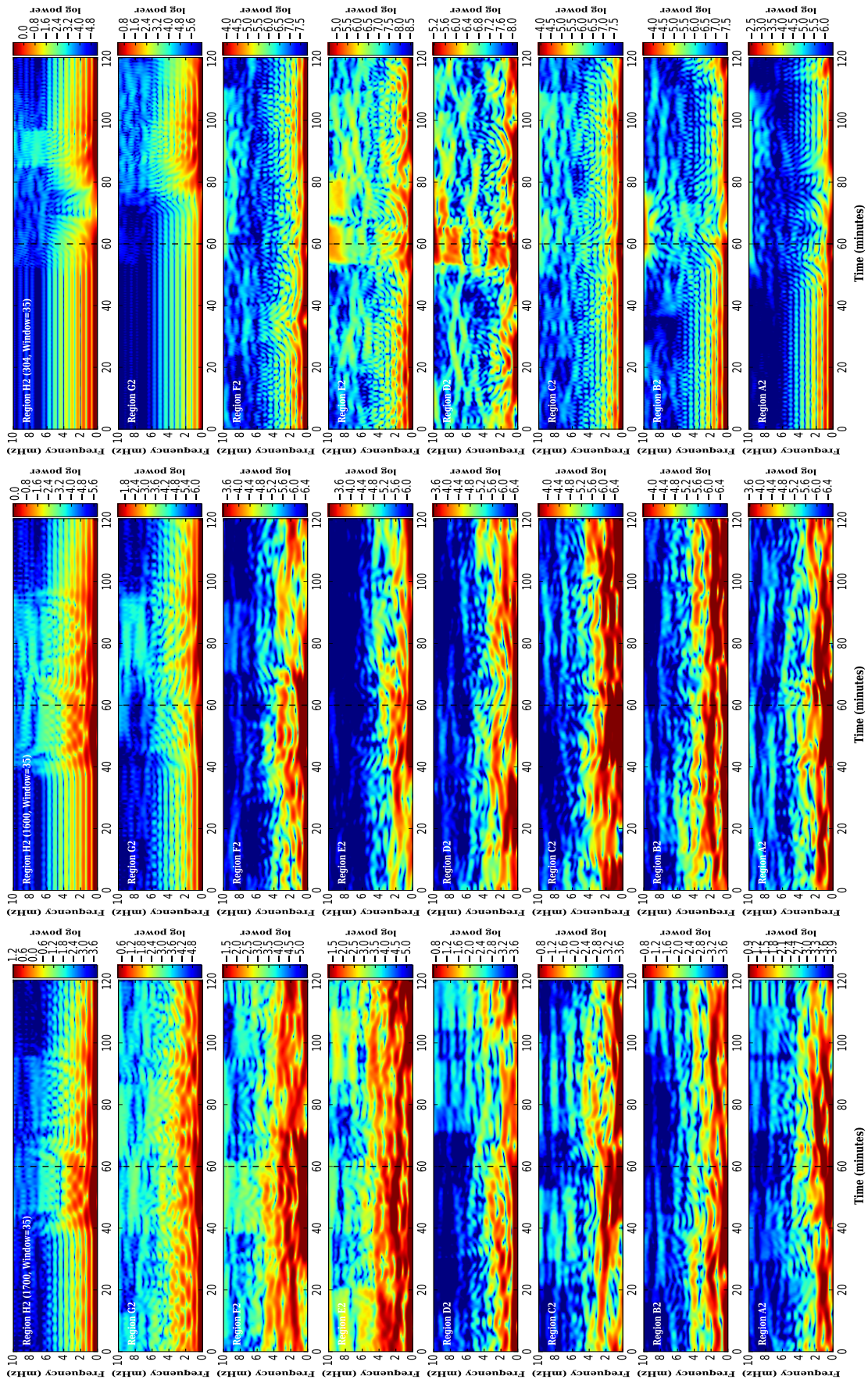


Figure 6.19: Multi-wavelength Annulus 2 (1700 Å (lower photosphere), 1600 Å (upper photosphere), 304 Å (chromosphere)). The black ‘dashed’ line indicates the time of the main flare event. The Power is in *Log Power*.

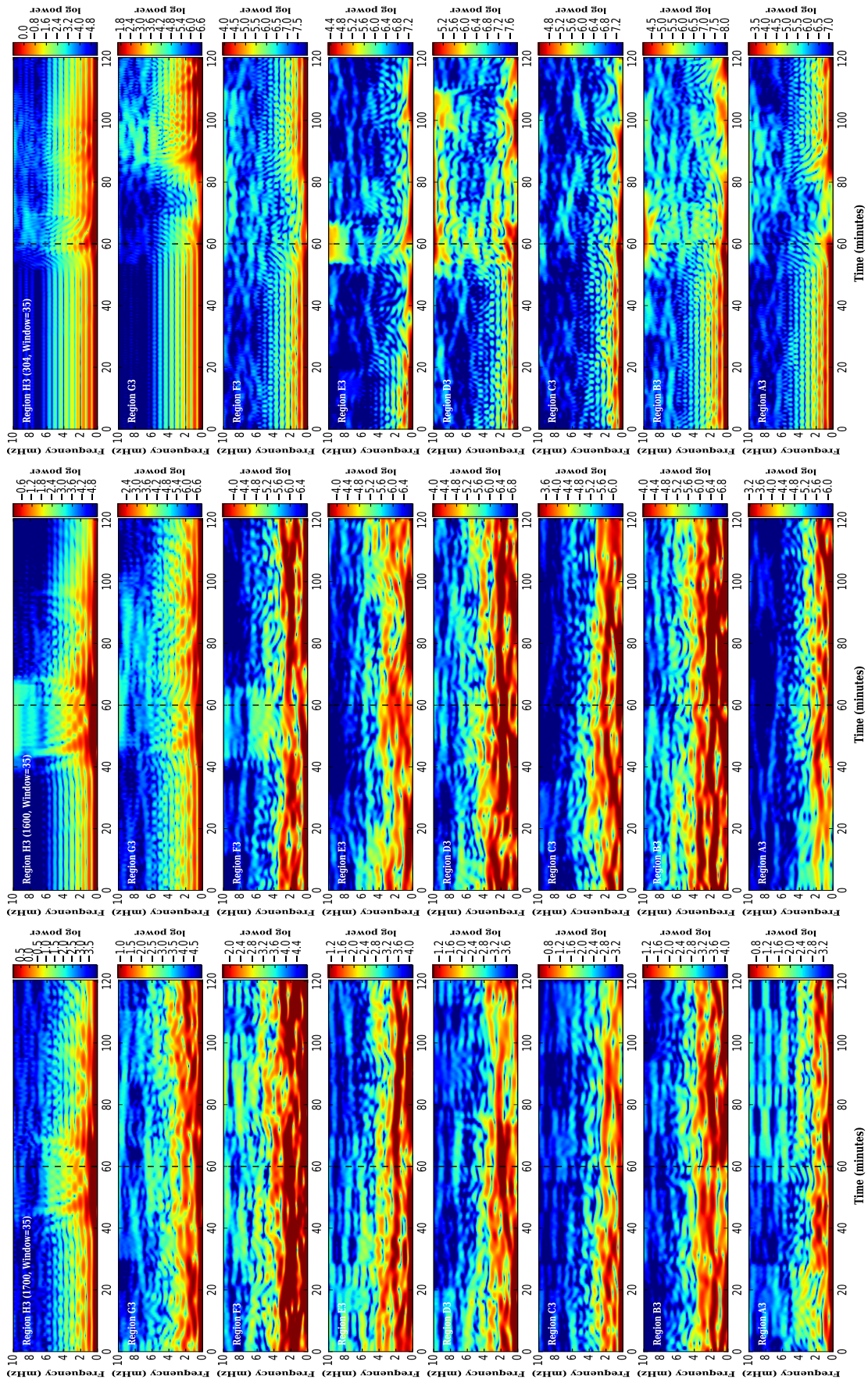


Figure 6.20: Multi-wavelength Annulus 3 (1700 Å (lower photosphere), 1600 Å (upper photosphere), 304 Å (chromosphere)). The black 'dashed' line indicates the time of the main flare event. The Power is in Log Power.

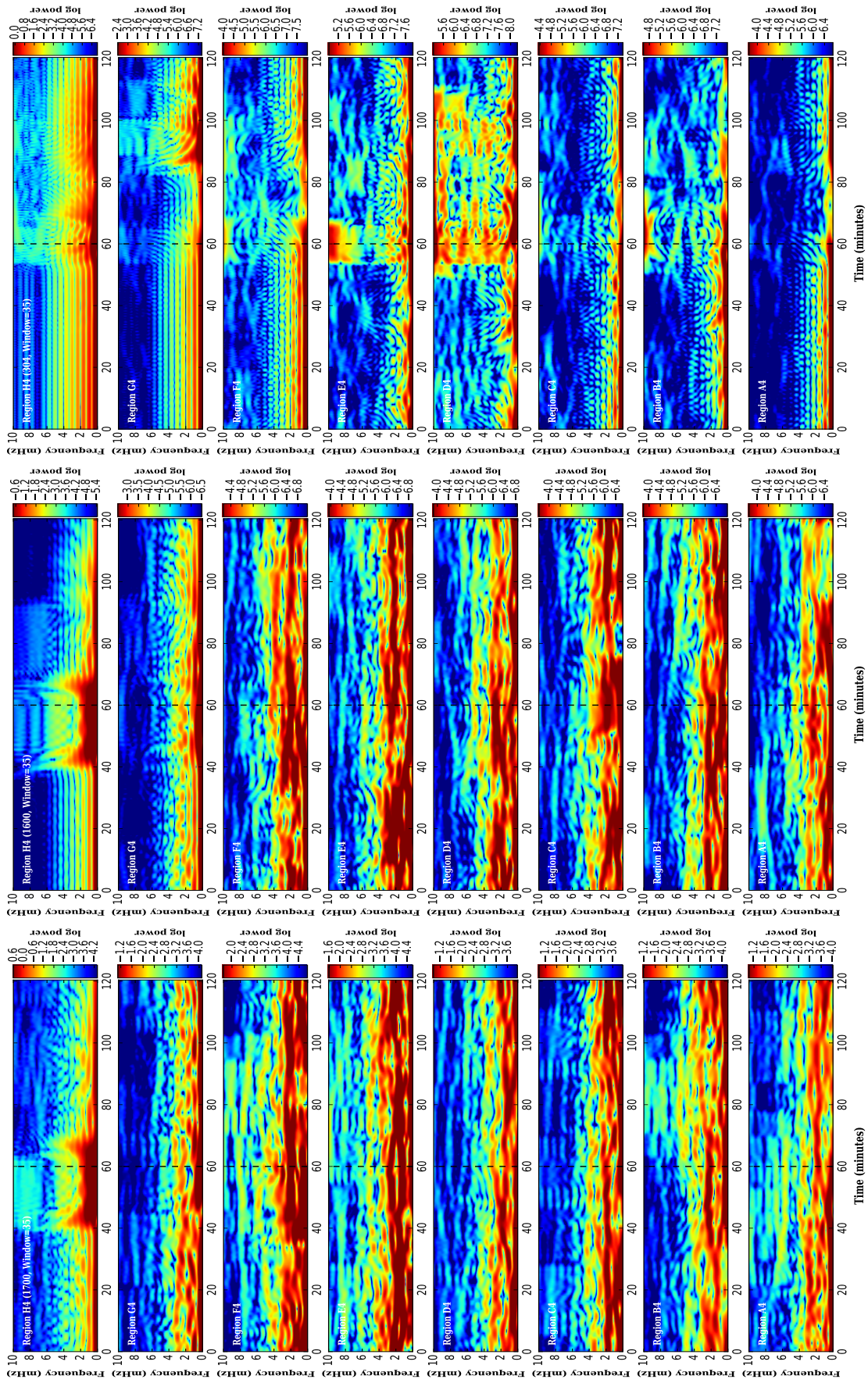


Figure 6.21: Multi-wavelength Annulus 4 (1700 Å (lower photosphere), 1600 Å (upper photosphere), 304 Å (chromosphere)). The black ‘*dashed*’ line indicates the time of the main flare event. The Power is in *Log Power*.

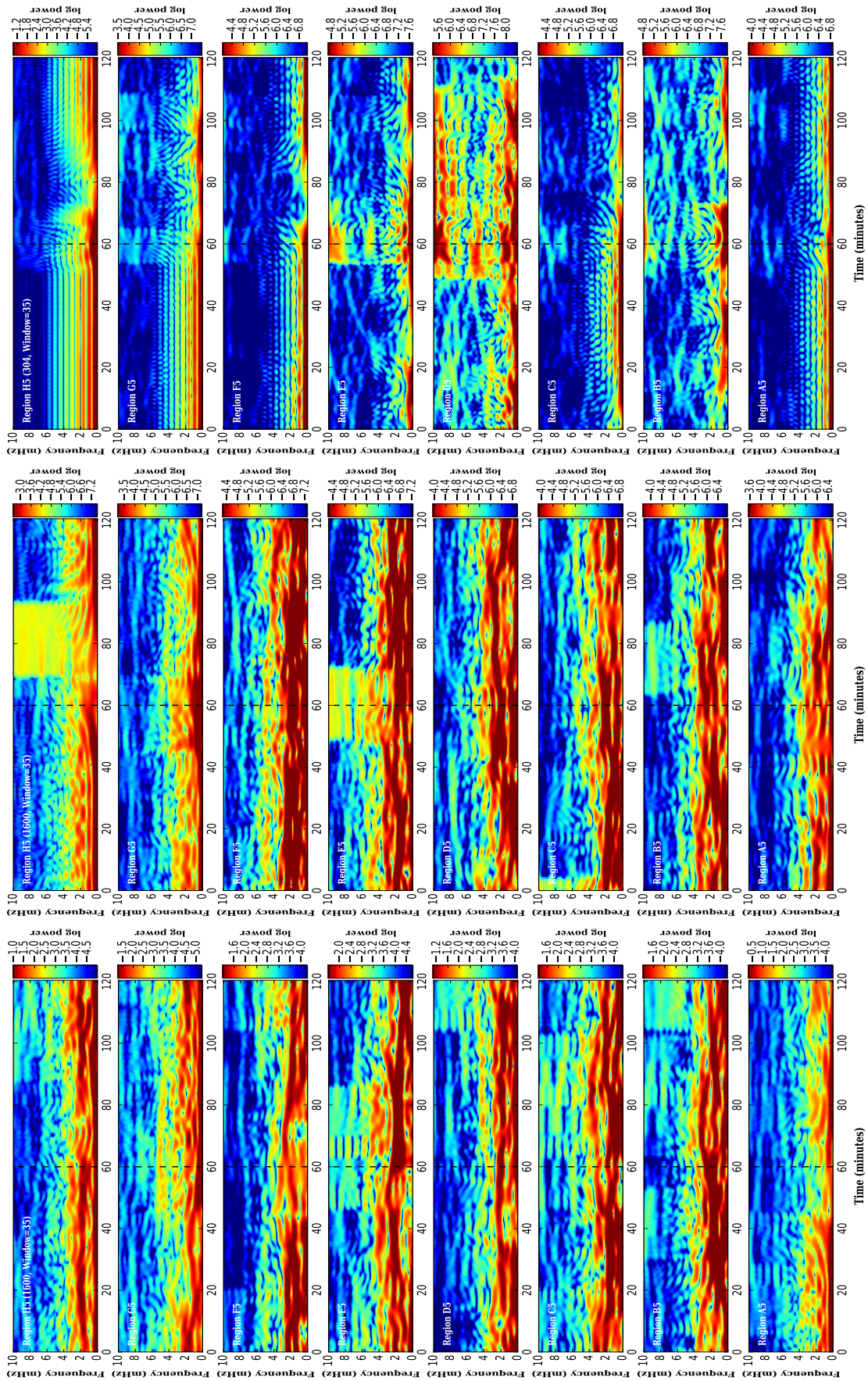


Figure 6.22: Multi-wavelength Annulus 5 (1700 Å (lower photosphere), 1600 Å (upper photosphere), 304 Å (chromosphere)). The black ‘dashed’ line indicates the time of the main flare event. The Power is in *Log Power*.

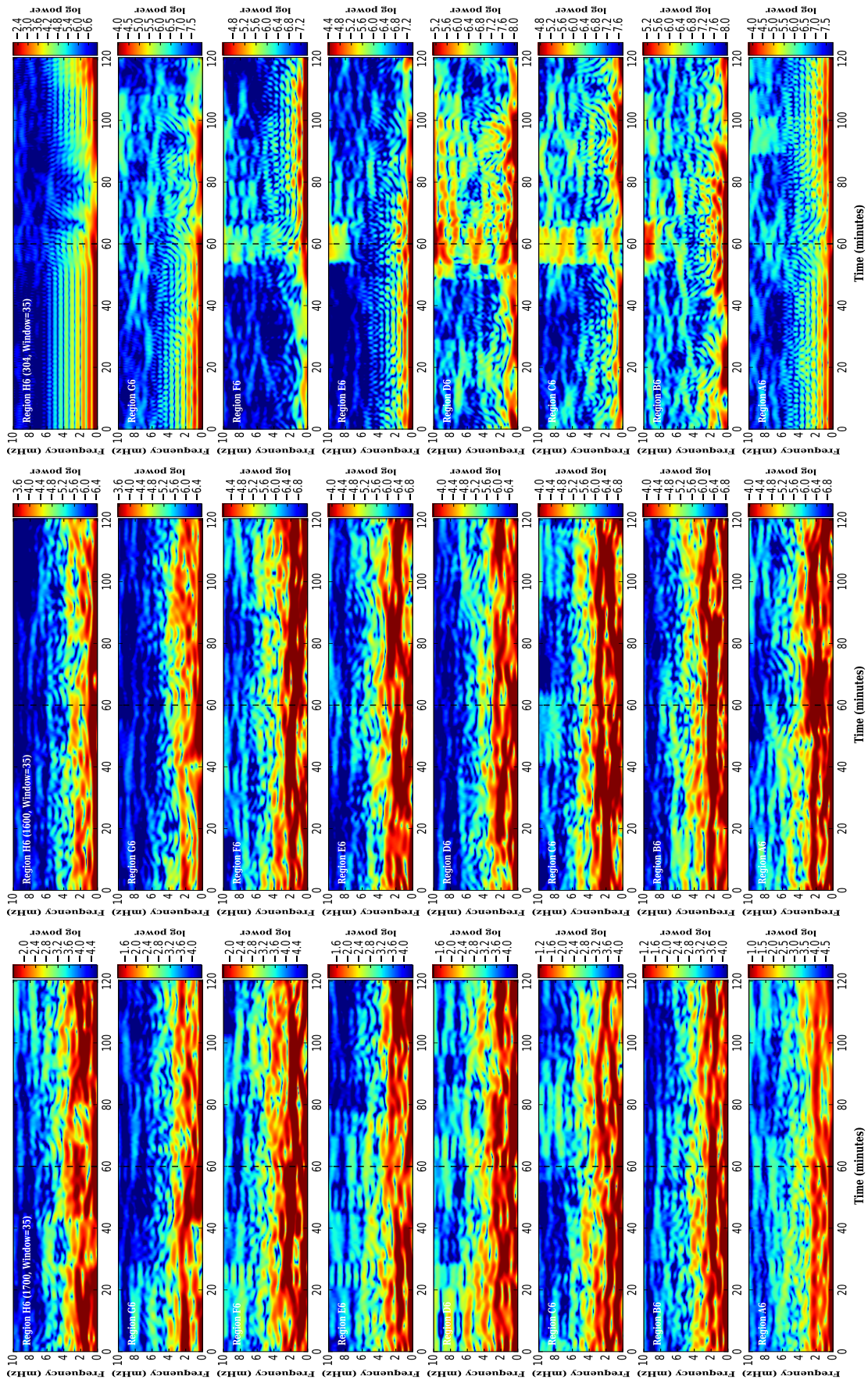


Figure 6.23: Multi-wavelength Annulus 6 (lower photosphere), 1600 Å (upper photosphere), 304 Å (chromosphere). The black ‘dashed’ line indicates the time of the main flare event. The Power is in Log Power.

6.5 Results: Time-Distance Helioseismology Measurements on AR12192

It is known that during flares there is an enhancement in the 3-minute modes (5.33 mHz) when the 5-minute (p-modes) rise from the photosphere to the chromosphere. In this section the goal is to investigate the brightening feature seen especially in the 304 Å PMMs between 2–4 mHz. In previous studies such as the previous triangulation method, there was no detection of the subtle brightening feature mentioned in section 5.1 *Power Map Movies of SDO AIA 1700 Å, 1600 Å and 304 Å* in Chapter 5. Triangulation was chosen as a way to track the feature that could be an MHD wave moving out away from the flare, and investigate if there were any anomalies that could indicate likewise. However, the first triangulation did not indicate the wave feature, and there could also be a bias in the study because of lack of spatial information in the sampling. In the time-distance analysis the approach is carried out by incorporating the sector sampling method, but instead of a 45 degree sampling, the angle is a much thinner angle of 5 degree sampling. Additionally, in the last sector sampling the 45 degree sampling was divided into 7 sectors moving out from the center of the image to near the edge. In this time-distance method with the thin sector 5 degree angle, 25 very small sectors are used instead. The center pixel of the image is kept the same as in the previous sampling, and three small angle samplings are taken with the first sample at $90^\circ \leq \theta \leq 95^\circ$, the second sample at $225^\circ \leq \theta \leq 230^\circ$ and the third sample at $315^\circ \leq \theta \leq 320^\circ$. Notice in the sector map in Figure 6.11, in regard to the three thin sector angles, the shape appears as an upside-down ‘Y’, but the edge of the sampling would be more of a triangular shape. The triangular shape would be thought of as a more advanced application of the triangulation method with the spatial data conserved and not missing any information. In this section the observations are discussed. This is a first trial of time-distance method using the 304 Å wavelength with both PMMs between 2–4 mHz and the intensity images; however, more samplings with the other wavelengths will have to be taken 1700 Å and 1600 Å to see if there is any correlation between the three wavelengths from the previous multi-wavelength sector sampling method. Current

observations are discussed below.

The flaring region is an interesting region to study and this section will begin with the third sample located at $315^\circ \leq \theta \leq 320^\circ$. In Figure 6.24, the 304 Å wavelength intensity analysis is plotted on the left and the 2–4 mHz PMM analysis is plotted on the right. The average was not subtracted from the intensity images, and so the Stage 3 C123Co280 AIA images were used, because the features were seen more clearly than the subtracted average images. These plots are localized at the center pixel of the image and would be marked as the origin at zero. The distance is measured in arcseconds from the centerpixel moving out to the edge. The images were 280×280 pixels in size and the calculations had to be converted back to the original JSOC AIA cutout 4096×4096 square pixel image size where each pixel has a value of 0.6 arcseconds. In the 280×280 pixel images a 1×1 pixel in that image will equal a 5×5 pixel in the JSOC AIA cutout image. Those conversions of the pixel values per arcsecond were multiplied by the radii values moving out of the 5 degree sampling angle. Since the value of the pixels are average between the radii, this causes the values to be binned and created a light curve for each 25 sector sample. These 25 light curves are then combined into a 2-dimensional image. Additionally, for the 2–4 mHz PMM the window size was 35 frames, to coordinate with the last sector sampling, and jumped one frame to produce the movie.

Between the angle $315^\circ \leq \theta \leq 320^\circ$ a portion of the flare can be seen in the 304 Å intensity images (right Figure 6.24) beginning after 35 minutes. Interestingly, in the 304 Å PMM (left Figure 6.24) the flaring region is shown that correlates with the location of the 304 Å intensity image. The location of the power is spread out more around the 304 Å PMM than in the 304 Å intensity flaring region, indicating the mode enhancements in the area around the flare. The PMM power measurements are able to detect subtle flaring features that appear after 60 minutes between 75 and 105 arcseconds. Furthermore, in the 304 Å PMM there appears a brightening occurring before the main onset of the flare from 150 to 324 arcseconds. These results are preliminary, but it would be interesting to compare

them to the 1700 Å and 1600 Å wavelengths. This will be done in the future.

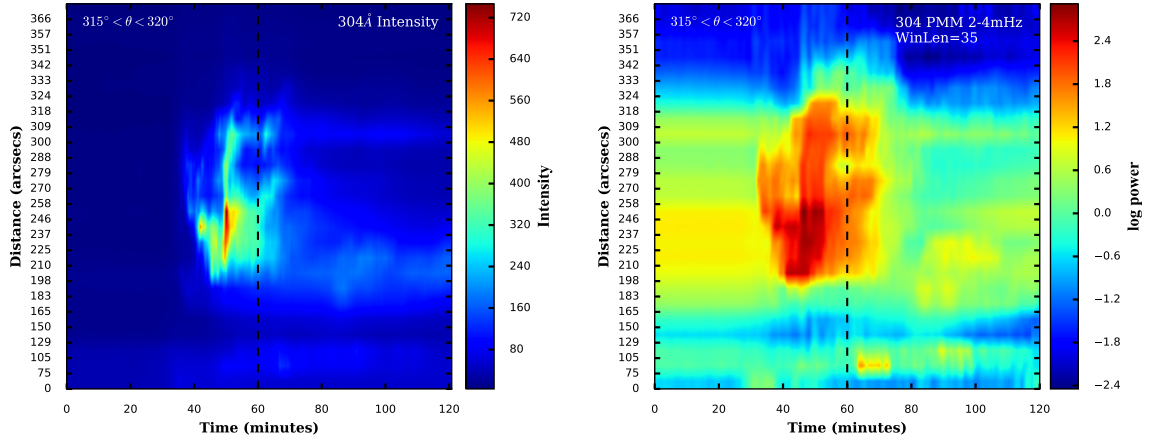


Figure 6.24: Time-distance plot between $315^\circ \leq \theta \leq 320^\circ$.

In the next sampling between $225^\circ \leq \theta \leq 230^\circ$ (see Figure 6.25), some flaring can be seen after 20 minutes for both the intensity and PMM frame, but in this region it was more quiet than active as in the region in Figure 6.24. Additionally, there seems to be some sort of activity taking place between 279 to 356 arcseconds for both the intensity and also the PMM frames. However, the feature shows up more in the PMM plot (see Figure 6.25 right). Interestingly, there is a vertical brightening feature that occurs after 20 minutes and seems to be linked to the flaring behavior from 0 to 105 arcseconds. This subtle vertical brightening feature could be indicative of the brightening feature seen from the MHD wave feature moving out away from the flare in the PMMs. However this brightening feature in the plot has no slope and it seems to occur instantaneously indicated by the sharp vertical shape of the feature. However, one could say that the speed of the MHD wave could be so fast that the limitation of the windowing size at 35 frames may not have been able to detect the subtle slope. Further studies will have to be incorporated to test that hypothesis. In both plots a subtle horizontal undulation from 0 to 120 minutes is seen in the time-distance plots of the 304 Å intensity and 2-4 mHz PMM sampling found, where the darker part of the undulation takes place from 165 to 279 arcseconds, and the brighter part from 279 to 361 arcseconds. This undulation is detected only for the samplings incorporating most of

the the quieter regions of Figures 6.25 and 6.26. An important point to consider is that the undulation does not seem to be an artifact, because it also appears at the $90^\circ \leq \theta \leq 95^\circ$, an area away from the flare and rotated at a different angle. Another important point to note is that the undulation seems to agree with the subtle change in power seen in the quieter regions in the main sector samplings discussed in the last section *6.4.1– Sector Sampling Method Interpretations*.

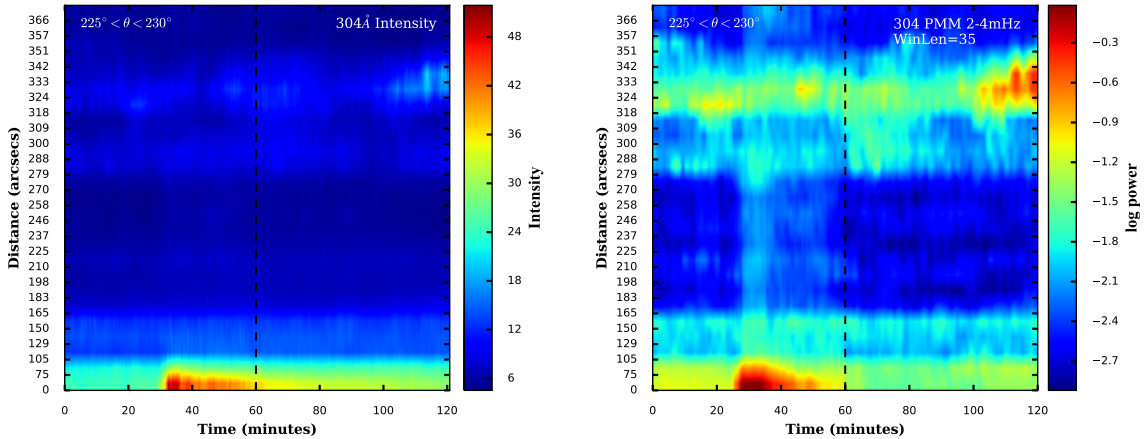


Figure 6.25: Time-distance plot between $225^\circ \leq \theta \leq 230^\circ$.

The sampling located at $90^\circ \leq \theta \leq 95^\circ$, was the quietest region of all three samples, see Figure 6.26. The flaring is between 0 and 75 arcseconds from the center pixel of the image. Again, the horizontal undulation is clearly seen in both the 304 Å intensity and 2-4 mHz PMM sampling, and yet the sample is rotated 135 degrees from the $225^\circ \leq \theta \leq 230^\circ$ sample. Subtle brightening features can be seen in the 304 Å PMM after 320 arcseconds, and could be indicative of subtle active processing happening away from the flare. These measures look promising, however, further measurements have to be taken, especially on the 1700 Å and 1600 Å wavelengths.

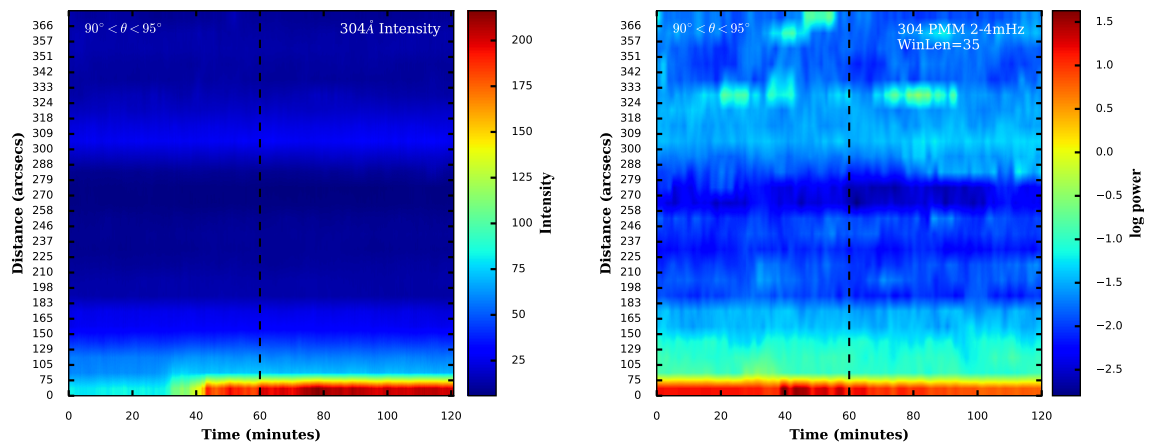


Figure 6.26: Time-distance plot between $90^\circ \leq \theta \leq 95^\circ$.

Chapter 7

Conclusion

This dissertation study involves an observational approach on the effects of solar flares on oscillations and investigates acoustic p-modes and other wave mode oscillation frequency and power in active regions with various imaging techniques such as power map movies and sampling techniques to study the power frequency distribution. The techniques presented in this dissertation are novel and build on the foundations of helioseismology. The Sun, our nearest star, is a chaotic dynamic system affecting the entire Solar System and space weather is a concern as it affects habitability on Earth. Helioseismology originated from seismology detection on Earth and has offered the ability to probe the inside and farside of our star. Over the years there have been many discoveries both from ground based and space based observations, which complement the theoretical predictions. As helioseismology expands, probing the different layers of the Sun's atmosphere may prove to be fruitful and could explain the coronal heating mystery.

Chapter 1 covers a review of the literature in the field, especially with regard to local helioseismology. It gives a historical review and some insights on recent works within the field. Chapter 2 is an introduction to ground based observations utilizing the GONG network with information on data processing of images. Chapter 3 presents results taken from analyses of the chromosphere around active flaring regions with GONG $H\alpha$. Chapter 4 evolves the work to multi-wavelength measurements involving SDO AIA and HMI data and explains the image data processing pipeline. Chapter 5 builds on the GONG work by taking multi-wavelength (AIA 1700 Å, 1600 Å and 304 Å) samples of interesting areas around flaring active regions and studying the frequency distribution from the photosphere to the chromosphere. Chapter 6 takes the work even further by incorporating sound scientific theory in reducing any form of bias in the study, by utilizing a sector sampling ap-

proach. Moreover, this chapter furthers one's appreciation on the merging of fundamental physics concepts with observational techniques.

Appendix A

Scientific and Mathematical Background

A.1 Wave Fundamentals

A.1.1 Fundamentals – the Anatomy of a Wave

For a cyclical process such as oscillatory waves, frequency, f is defined as cycles per unit time, t ; and time, or the period measured in seconds, is the amount of time it takes to complete one cycle:

$$t = \frac{1}{f} \quad (\text{A.1})$$

Therefore, the frequency is measured in cycles per unit time or hertz.

Think of the simplest form of a two-dimensional standing wave, such as a vibrating string. The frequency at which the string vibrates has its own characteristic vibrational mode or standing wave pattern. These patterns are only created within the object or instrument at specific frequencies of vibration; these frequencies are known as harmonic frequencies or just harmonics. The harmonics of the wave are measured as multiples of the base frequency (Table A.1). As the wave oscillates up and down there are regions where the displacement is zero; these are called the nodal points. The places on the string that move the most are called the anti-nodal points (Morin, 2009).

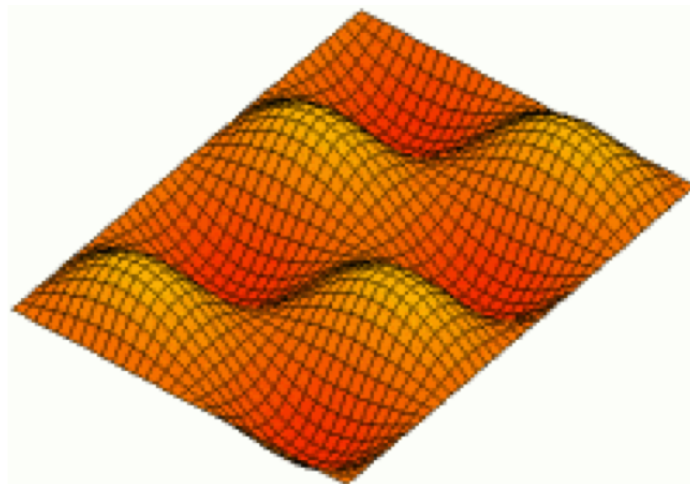


Figure A.1: A segment of a three-dimensional standing wave. Notice that the nodes would now be curves (Alexandrov, 2008).




Harmonic Order (N)	Nodes	Anti-nodes	Pattern
N = 1	2	1	
N = 2	3	2	
N = 3	4	3	

Table A.1: The harmonic order of the fundamental frequency, nodes and anti-nodes of different order standing waves (Morin, 2009).

A.1.2 Spherical Harmonics and Eigenvalues

Regarding the two-dimensional wave, the nodes are points on the wave with zero-dimension (a point). Consider expansion to the three-dimensional case, where the nodes would no longer be points on a two-dimensional wave but now curves on a three-dimensional surface (see Figure A.1). This expansion is necessary since the study of Helioseismology deals with three-dimensional standing waves in a chaotic system. The Sun has radial symmetry or symmetry around a central point. Remember, the fundamental frequency has its

own characteristic vibrational mode or standing wave pattern. Therefore, if there is only a single mode then the period is simple to determine, especially if it is radially symmetric. However, for cases where there are a number of modes in existence, it then becomes more complex and non-radial, and the switch has now been made to quantum mechanics. The modes can be described in terms of spherical harmonics.

The spherical harmonics are characterized by an eigenfunction with three frequency eigenvalues: n , ℓ and m . The order, given by n , is the number of nodes in the radial direction from the surface to the center of the Sun. The harmonic degree, ℓ , indicates the number of node lines on the surface, which is the total number of planes slicing through the Sun (see Figure A.2). The third number, m , tells how many of the surface nodal lines cross the equator and also gives the phase; m runs from $-\ell$ to $+\ell$ because of the direction of the waves. The number m , describes the number of planes slicing through the Sun longitudinally (north to south poles) (Antia *et al.*, 2003; Christensen-Dalsgaard, 2003; National Solar Observatory, 2010). The spherical harmonics $Y_\ell^m(\theta, \phi)$, with latitude θ (the angular distance from the polar axis) and longitude ϕ can be defined as

$$Y_\ell^m(\theta, \phi) = (-\ell^m) c_{\ell m} P_\ell^m(\cos \theta) e^{im\phi} \quad (\text{A.2})$$

P_ℓ^m is the Legendre function, and $c_{\ell m}$ is the normalization function found to be

$$c_{\ell m}^2 = \frac{(2\ell + 1)(\ell - m)!}{4\pi(\ell + m)!} \quad (\text{A.3})$$

ℓ , the degree measures the total horizontal wave number k_h on the surface by

$$k_h = \frac{\sqrt{\ell(\ell + 1)}}{R} \quad (\text{A.4})$$

R is the radius of the Sun. We can also find the wavelength with the wave number (Christensen-

Dalgaard, 2003)

$$\lambda = \frac{2\pi}{k_h} \quad (\text{A.5})$$

The small oscillations of a sphere can be represented by a linear superposition of eigenmodes, each characterized by a set of three quantum numbers n , ℓ , and m . For example, the frequencies of solar oscillatory waves depend on the dynamics and internal structure. The pressure can then be written as:

$$p(r, \theta, \phi, t) = p_0(r) + \sum_{n,\ell,m} A_{n\ell m} R_{n,\ell,m}(r) Y_\ell^m(\theta, \phi) e^{-i\omega_{n\ell m} t} \quad (\text{A.6})$$

where r is the radius, θ and ϕ are spherical-polar coordinates and t is time. $A_{n\ell m}$ is a complex mode amplitude, and $R_{(n,\ell,m)}(r)$ is the radial eigenfunction of the mode. The corresponding modal frequency, $\omega_{n\ell m}$, and the radial dependence $R_{(n,\ell,m)}(r)$ define the eigenfunction. Again, The three quantum numbers n , ℓ and m specify the eigenmode of oscillation (Antia *et al.*, 2003).

A.2 Time Series Data Techniques

The scientific analysis of time series has a long history. Spectrum analysis of time series commenced in 1664 when Isaac Newton decomposed a light signal into frequency components by passing the signal through a glass prism. The mathematical foundations of spectral analysis developed in 1898, when Michelson and Stratton obtained the Fourier Transform of a harmonic analyzer device based on springs. But it was John Tukey's development of the Fast Fourier Transform that revolutionized spectral analysis (Brillinger, 2002).

A.2.1 Fourier analysis and the classical Fourier transform

Helioseismology works with time series data that needs to be transformed from its temporal components to frequency components. To do this a Fourier Transform algorithm

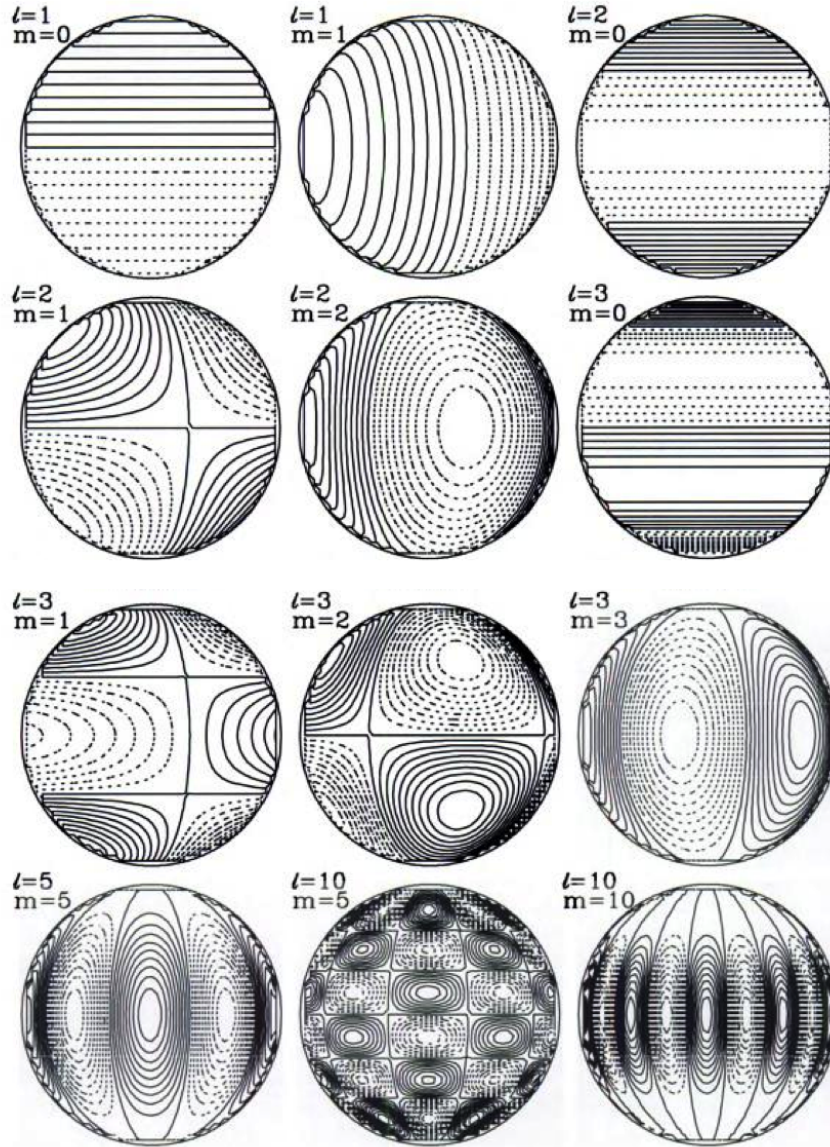


Figure A.2: Contour plots for the real part of spherical harmonics $Y_\ell^m(\theta, \phi)$ projected on the solar disk. ℓ , indicates the number of node lines on the surface, which is the total number of planes slicing through the Sun. The number m , describes the number of planes slicing through the Sun longitudinally north to south. The small oscillations of a sphere can be represented by a linear superposition of eigenmodes (Antia *et al.*, 2003).

is used. Once the information is transformed into its frequency spectrum we can describe the signal by its power spectrum. We use the Fourier transform to convert a time varying signal $x(t)$ from the time domain to the frequency domain $x(\omega)$ (Heiles, 2005).

To understand how the Fourier transform works we begin with a simple oscillating

signal, $x(t)$, and the signal is observed from time, $t = 0$ to $t = T$ (Christensen-Dalsgaard, 2003).

$$x(t) = a_0 \cos(\omega_0 t - \delta_0) \quad (\text{A.7})$$

The equation for the Fourier transform is:

$$x(\omega) = \int_0^T x(t) e^{i\omega t} dt \quad (\text{A.8})$$

Working with the transform and substituting the equation of $x(t)$ to transform it into the frequency domain gives*

$$x(\omega) = \frac{T}{2} a_0 \left\{ e^{i[\frac{T}{2}(\omega + \omega_0) - \delta_0]} \text{sinc} \frac{T}{2} (\omega + \omega_0) + e^{i[\frac{T}{2}(\omega - \omega_0) - \delta_0]} \text{sinc} \frac{T}{2} (\omega - \omega_0) \right\} \quad (\text{A.9})$$

where,

$$\text{sinc}(x) = \frac{\sin(x)}{x} \quad (\text{A.10})$$

The power spectrum of $x(\omega)$ is then,

$$P(\omega) = |x(\omega)|^2 \quad (\text{A.11})$$

or the square of the Fourier transform.[†] A representation of the power spectrum of the $\text{sinc}(x)$ function is found in Figure A.3.

*Further elaboration on the process from equation A.8 to A.9 equation is found in APPENDIX C.

[†]Since the power spectrum is a real value, this takes care of the complex part of the Fourier transform, so the power spectrum is the Fourier transform multiplied by its complex conjugate (Heiles, 2002).

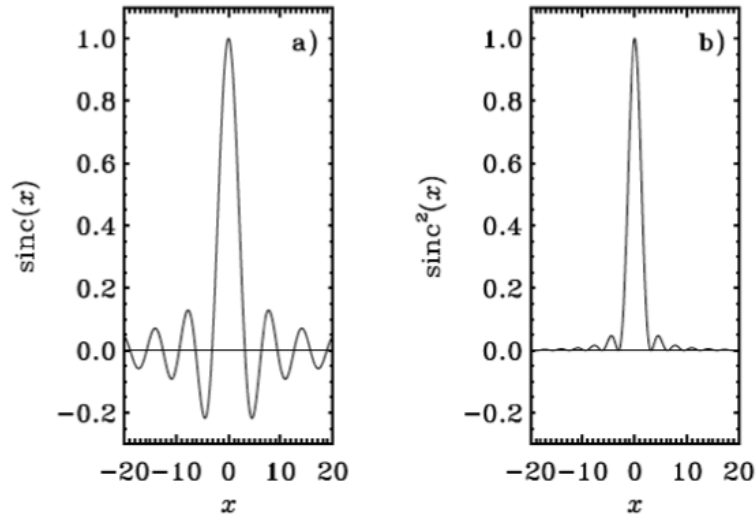


Figure A.3: The $\text{sinc}(x)$ function plotted on the left and the power spectrum of the $\text{sinc}(x)$ function plotted on the right (Christensen-Dalsgaard, 2003).

A.2.2 The Discrete Spectrum and the FFT

When there is a signal in which the spectrum is to be determined, we sample the incoming signal sequentially in time, at regular intervals called the sampling interval, t_{sample} . Equivalently, the signal is sampled at a regular rate called the sampling frequency

$$\nu_{\text{sample}} = \frac{1}{t_{\text{sample}}} \quad (\text{A.12})$$

In discrete sampling, the signal has to be limited in bandwidth. Furthermore, the highest frequency in its spectrum must be limited to an upper cutoff frequency. For example, there is a signal bandwidth of A to B mHz, or the length of the signal. The signal sample must be periodically fast enough that $\nu_{\text{sample}} \geq 2B \text{ mHz}$, this is also known as the Nyquist criterion. When sample rate is ν_{sample} , the maximum signal frequency that can be reproduced is the *Nyquist* frequency, or (Heiles, 2005):

$$f_N = \frac{\nu_{\text{sample}}}{2} \quad (\text{A.13})$$

The Fourier transform converts the time domain to the frequency domain. Equation A.8 represents a continuously sampled signal where an integral is used. However, to compute the Fourier transform digitally, the discrete Fourier transform (DFT) for the discretely sampled signals is necessary. The DFT will be the same as equation A.8, but instead the integral will be replaced by a summation sign. There are two parameters needed to satisfy discrete sampling:

- 1) the bandwidth must have a limit of $f_N \geq \frac{v_{sample}}{2}$
- 2) for the Fourier-transformed power spectrum, the spectral resolution must be the reciprocal of the total time over which the Fourier transform is calculated, $\Delta v = \frac{1}{T_{total}}$

The DFT is regarded as a computational algorithm that takes N numbers in one domain and creates N complex numbers in another domain. Suppose there is a desire to split the discrete Fourier transform into smaller parts, then the utilization of the Fast Fourier Transform will be handy. The Fast Fourier Transform (FFT) is an efficient way of calculating the DFT - helping in computation time and more numerical accuracy[‡]. For example, there are 2^N data points to be computed. The procedure could already be laborious. The DFT is split into $\frac{2N}{2}$ pieces, each containing only two numbers. Then both pieces are put back together again. This process will only require $N \log_2 N$ operations, a much smaller number of operations, resulting in few roundoff errors since there are fewer operations (Heiles, 2005; McClellan *et al.*, 2003).

A.3 Linearity of the FFT

By linearity of the DFT, averaging the signals in time and then taking the DFT of the average is equivalent to averaging the DFTs of the signals.

- $x_n[l] : l^{th}$ – trial time domain sample at time n

[‡]In depth information is given on IDL's FFT algorithm in *Methodology*

- $X_k[l] : l^{\text{th}}$ – trial frequency domain sample at frequency k

The “average” signal in the time domain is given by $\frac{1}{L} \sum_{l=0}^L x_n[l]$. Taking its DFT, we have

$$\sum_{n=0}^{N-1} \frac{1}{L} \sum_l x_n[l] e^{-\frac{i2\pi kn}{N}} \quad (\text{A.14})$$

Switching the order of the summations, we can write

$$\frac{1}{L} \sum_{l=0}^L \sum_{n=0}^{N-1} x_n[l] e^{-\frac{i2\pi kn}{N}} \quad (\text{A.15})$$

but this is the same as averaging the DFTs of each trial.

$$\frac{1}{L} \sum_{l=0}^L X_k[l] \quad (\text{A.16})$$

Appendix B

Mathematical Formulas and Proofs

B.1 Euler's equation and the Fourier Transform

Euler's Identity:

$$e^{iy} = \cos y + i \sin y \quad (\text{B.1})$$

$$\cos x = \frac{e^{ix} + e^{-ix}}{2} = \operatorname{Re}(e^{ix}) \quad (\text{B.2})$$

$$\sin x = \frac{e^{ix} - e^{-ix}}{2i} = \operatorname{Im}(e^{ix}) \quad (\text{B.3})$$

$$|e^{ix}| = 1 \quad (\text{B.4})$$

Fourier Transform:

$$X_k = \sum_{n=0}^{N-1} x_n \cdot e^{-i2\pi kn/N} \quad (\text{B.5})$$

$$x_n = \frac{1}{N} \sum_{k=0}^{N-1} X_k \cdot e^{-i2\pi kn/N} \quad (\text{B.6})$$

The Fourier Transform on \mathfrak{R} : the Fourier integral

The analysis equation:

$$\hat{f}(s) = \int_{-\infty}^{\infty} f(x) e^{-2\pi isx} dx \quad (\text{B.7})$$

The synthesis equation:

$$f(x) = \int_{-\infty}^{\infty} \hat{f}(s) e^{2\pi isx} ds \quad (\text{B.8})$$

The differentiation operator: Write the synthesis equation for $f(x)$ and differentiate both

sides using integration by parts.

$$\hat{f}'(s) = \int_{-\infty}^{\infty} f'(x)e^{-2\pi isx} dx \quad (\text{B.9})$$

$$= f(x)e^{-2\pi isx} \Big|_{-\infty}^{\infty} - (-2\pi is) \int_{-\infty}^{\infty} f(x)e^{-2\pi isx} dx \quad (\text{B.10})$$

$$= 0 - 0 + 2\pi is \int_{-\infty}^{\infty} f(x)e^{-2\pi isx} dx \quad (\text{B.11})$$

$$= 2\pi is \hat{f}(s) \quad (\text{B.12})$$

B.2 Laplace's Equation and Conformal Mapping (Proof)

Derivation taken from a lecture course on Conformal Mapping (Gross, 1971).

The main purpose of this proof is see what happens in ordinary transformations from an algebraic point of view and to see how conformal mapping preserves the solution of Laplace's Equation. Therefore enabling the application of conformal mapping.

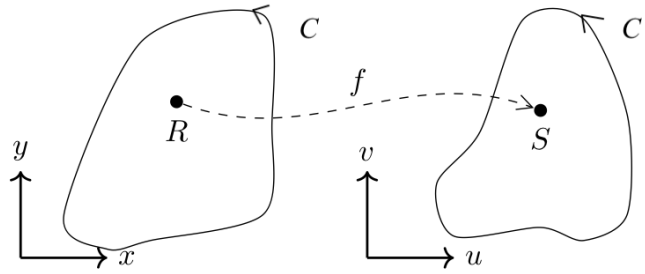


Figure B.1: Conformal mapping and Laplace's equation.

Principle: By the definition of conformal mapping, if $f : R \rightarrow$ where $f = u + iv$ is analytic and $f'(z) \neq 0$ then $T_{xx} + T_{yy} = 0$ if and only if $T_{uu} + T_{vv} = 0$. In the first plane, see Figure B.1 right side, $T = T_0(x, y)$ on $C \rightarrow T = T_0(x(u, v), y(u, v))$ on C' . So $T = T_1(u, v)$. Solve for $T(u, v)$ in S , then $T(x(u, v), y(u, v))$ is a solution in R .

Proof: Assume u and v are continuously differentiable functions of x and y .

$$\begin{aligned} u &= u(x, y) \\ v &= v(x, y) \end{aligned} \tag{B.13}$$

Part I.

Take the Laplacian of x . By the chainrule,

$$T_x = T_u u_x + T_v v_x \tag{B.14}$$

Take the Laplacian,

$$\begin{aligned} T_{xx} &= [T_u u_x + T_v v_x]_x \\ T_{xx} &= (T_u u_x)_x + (T_v v_x)_x \end{aligned} \quad (\text{B.15})$$

By the Product Rule,

$$T_{xx} = T_u u_{xx} + (T_u)_x u_x + T_v v_{xx} + (T_v)_x v_x \quad (\text{B.16})$$

Since $(T_u)_v$ and $(T_v)_x$ are single functions in which to apply the Chain Rule. By the Chain Rule,

$$\begin{aligned} (T_u)_x &= (T_u)_u u_x + (T_u)_v v_x \\ (T_v)_x &= (T_v)_u u_x + (T_v)_v v_x \end{aligned} \quad (\text{B.17})$$

Replace $(T_u)_x$ and $(T_v)_x$ expressions back into the Laplacian T_{xx} :

$$\begin{aligned} T_{xx} &= T_u u_{xx} + [(T_u)_u u_x + (T_u)_v v_x] u_x + T_v v_{xx} + [(T_v)_u u_x + (T_v)_v v_x] v_x \\ T_{xx} &= T_u u_{xx} + T_{uu} u_x^2 + T_{uv} u_x v_x + T_v v_{xx} + T_{vu} u_x v_x + T_{vv} v_x^2 \end{aligned} \quad (\text{B.18})$$

Note: since it is symmetric to \mathbf{x} and \mathbf{y} , the Laplacian T_{yy} will be similar. Just replace all the ' \mathbf{x} 's in the expression with ' \mathbf{y} 's, so that,

$$T_{yy} = T_u u_{yy} + T_{uu} u_y^2 + T_{uv} u_y v_y + T_v v_{yy} + T_{vu} u_y v_y + T_{vv} v_y^2 \quad (\text{B.19})$$

Next, prove T_{yy} has symmetry with T_{xx} by working out T_{yy} . Starting from the beginning, by the Chain Rule,

$$T_y = T_u u_y + T_v v_y \quad (\text{B.20})$$

Take the Laplacian,

$$T_{yy} = [T_u u_y + T_v v_y]_y \quad (\text{B.21})$$

$$T_{yy} = (T_u u_y)_y + (T_v v_y)_y$$

By the Product Rule,

$$T_{yy} = T_u u_{yy} + (T_u)_y + T_v v_{yy} + (T_v)_y v_y \quad (\text{B.22})$$

Remember, $(T_u)_y$ and $(T_v)_y$ are single functions. Again for single functions apply the Chain Rule,

$$(T_u)_y = (T_u)_u u_y + (T_u)_v v_y \quad (\text{B.23})$$

$$(T_v)_y = (T_v)_u u_y + (T_v)_v v_y$$

Replace $(T_u)_y$ and $(T_v)_y$ expressions back into the Laplacian T_{yy} :

$$T_{yy} = T_u u_{yy} + [(T_u)_u u_y + (T_u)_v v_y] u_y + T_v v_{yy} + [(T_v)_u u_y + (T_v)_v v_y] v_y \quad (\text{B.24})$$

And proved,

$$T_{yy} = T_u u_{yy} + T_{uu} u_y^2 + T_{uv} u_y v_y + T_v v_{yy} + T_{vu} u_y v_y + T_{vv} v_y^2 \quad (\text{B.25})$$

Part II.

Add the Laplacians of T_{xx} and T_{yy} together,

$$\begin{aligned} T_{xx} + T_{yy} &= T_u u_{xx} + T_{uu} u_x^2 + T_{uv} u_x v_x + T_v v_{xx} + T_{vu} u_x v_x + T_{vv} v_x^2 \\ &\quad + T_u u_{yy} + T_{uu} u_y^2 + T_{uv} u_y v_y + T_v v_{yy} + T_{vu} u_y v_y + T_{vv} v_y^2 \end{aligned} \quad (\text{B.26})$$

$$\begin{aligned} T_{xx} + T_{yy} &= T_{uu} u_x^2 + T_{uu} u_y^2 + T_{vv} v_x^2 + T_{vv} v_y^2 + T_{uv} u_x v_x + T_{uv} u_y v_y \\ &\quad + T_{vu} u_x v_x + T_{vu} u_y v_y + T_u u_{xx} + T_u u_{yy} + T_v v_{xx} + T_v v_{yy} \end{aligned} \quad (\text{B.27})$$

Collect like terms,

$$\begin{aligned} T_{xx} + T_{yy} &= T_{uu}(u_x^2 + u_y^2) + T_{vv}(v_x^2 + v_y^2) + T_{uv}(u_x v_x + u_y v_y) \\ &\quad + T_{vu}(u_x v_x + u_y v_y) + T_u(u_{xx} + u_{yy}) + T_v(v_{xx} + v_{yy}) \end{aligned} \quad (\text{B.28})$$

By continuity, combine the T_{uv} and T_{vu} terms,

$$\begin{aligned} T_{xx} + T_{yy} &= T_{uu}(u_x^2 + u_y^2) + T_{vv}(v_x^2 + v_y^2) + 2T_{uv}(u_x v_x + u_y v_y) \\ &\quad + T_u(u_{xx} + u_{yy}) + T_v(v_{xx} + v_{yy}) \end{aligned} \quad (\text{B.29})$$

Part III.

For the case of conformal mapping form the complex valued function $f = u + iv$ where $f \rightarrow$ will be analytic and by the definition of conformal mapping,

$$\begin{aligned} f' &= u_x + iv_x \\ u_x &= v_y, u_y = -v_x \end{aligned} \quad (\text{B.30})$$

follows these three cases

Case I:

$$|f'|^2 = u_x^2 + i^2 v_x^2 \quad (\text{B.31})$$

$$= u_x^2 + v_x^2 \quad (\text{B.32})$$

$$= u_x^2 + u_y^2 \quad (\text{from } u_y = -v_x) \quad (\text{B.33})$$

$$= v_y^2 + v_x^2 \quad (\text{B.34})$$

Case II: Since $f = u + iv$ is analytic:

$$u_{xx} + u_{yy} = v_{xx} + v_{yy} = 0 \quad (\text{B.35})$$

Case III: $u_x v_x + u_y v_y = v_y v_x - v_x v_y = 0$ because $u_x = v_y$ and $u_y = -v_x$

In regards to the Laplacian

$$T_{xx} + T_{yy} = T_{uu}(u_x^2 + u_y^2) + T_{vv}(v_x^2 + v_y^2) + 2T_{uv}(0) + T_u(0) + T_v(0) \quad (\text{B.36})$$

$$T_{xx} + T_{yy} = T_{uu}(|f'|^2) + T_{vv}(|f'|^2) \quad (\text{B.37})$$

$$= (T_{uu} + T_{vv})|f'|^2 \quad (\text{B.38})$$

$$\therefore f'(z) \neq 0, \quad T_{xx} + T_{yy} = 0 \iff T_{uu} + T_{vv} = 0 \quad \text{q.e.d.}$$

B.3 Heisenberg's Uncertainty Principle and the Fourier Transform

Derivation taken from a lecture course on Fourier Analysis (Merryfield, 2009).

If $f(t)$ is a function that exists in some region of time – a signal that dies away as t tends to $\pm\infty$ – then we can observe it and approximate when this signal occurs. Similarly, we can look at its Fourier transform $\hat{f}(\nu)$ and in nearly the same way tell just what its frequency is. We cannot specify the “when” perfectly, since the signal lasts for some length of time; we cannot specify the frequency exactly, for very nearly the same reasons. We have seen that a function that is very narrow in time has a Fourier transform that is very wide in frequency, and vice versa. There seems to be some kind of reciprocal relationship between the widths (the uncertainties) of the time and the frequency. The quantitative version of this is the following inequality:

The Heisenberg Uncertainty Theorem: *Suppose that f is a function in L^2 of the line with all of the following properties: $\|f(t)\|^2 = 1$, $tf(t) \in L^2$, and $\nu\hat{f}(\nu) \in L^2$. Define the following numbers*

The average value of t :

$$m_t = \int_{-\infty}^{\infty} t|f(t)|^2 dt \quad (\text{B.39})$$

The uncertainty of t :

$$\sigma_t = \left[\int_{-\infty}^{\infty} (t - m_t)^2 |f(t)|^2 dt \right]^{\frac{1}{2}} \quad (\text{B.40})$$

The average value of ν :

$$m_\nu = \int_{-\infty}^{\infty} \nu|\hat{f}(\nu)|^2 d\nu \quad (\text{B.41})$$

The uncertainty of ν :

$$\sigma_\nu = \left[\int_{-\infty}^{\infty} (\nu - m_\nu)^2 |\hat{f}(\nu)|^2, d\nu \right]^{\frac{1}{2}} \quad (\text{B.42})$$

Then,

$$\sigma_t \sigma_v \geq \frac{1}{4\pi} \quad (\text{B.43})$$

The fact that $\|\mathbf{f}(t)\|^2 = 1$ – that is, $\int_{-\infty}^{\infty} |\mathbf{f}(t)|^2 dt = 1$ – makes the function $|\mathbf{f}(t)|^2$ a *probability density function* for t considered as a random variable. Given that, the definition of the average value of t and the uncertainty of t are the standard probabilistic definitions of *mean* and *standard deviation*. Plancherel's Theorem now specifies that $\int_{-\infty}^{\infty} |\hat{\mathbf{f}}(\nu)|^2 d\nu = 1$, so that $|\hat{\mathbf{f}}(\nu)|^2$ is also a probability density function for ν as a random variable, and we can compute its mean and standard deviation. The use of the square of a function, rather than the function itself, as the probability density function is justified in a course on quantum mechanics, but it makes some sense to us here – how else would we get a positive function?

Proof:

First assume that both m_t and m_v are zero. Then,

$$1 = \int_{-\infty}^{\infty} |f(t)|^2 dt \quad (\text{B.44})$$

Integrate equation B.44 by parts, where

$$u = |f(t)|^2 = f(t)\overline{f(t)} \quad (\text{B.45})$$

$$du = f'(t)\overline{f(t)} + f(t)\overline{f'(t)} \quad (\text{B.46})$$

$$= 2 \operatorname{Re}(f(t)\overline{f'(t)}) \quad (\text{B.47})$$

$$dv = dt \quad (\text{B.48})$$

$$v = t \tag{B.49}$$

The boundary terms of this integration by parts will have $uv = t|f(t)|^2$; the integrability of $t^2|f(t)|^2$ forces this to go to zero as $t \rightarrow \pm \infty$ so that these boundary terms contribute zero. Then,

$$v = t \tag{B.50}$$

$$1 = \int_{-\infty}^{\infty} |f(t)|^2 dt = -2 \operatorname{Re} \int_{-\infty}^{\infty} t f(t) \overline{f'(t)} dt \tag{B.51}$$

$$\leq 2 \left| \int_{-\infty}^{\infty} |f(t)|^2 dt \right| \quad \text{since } |\operatorname{Re} z| \leq |z| \tag{B.52}$$

$$\leq 2 \left(\int_{-\infty}^{\infty} |t f(t)|^2 dt \right)^{\frac{1}{2}} \left(\int_{-\infty}^{\infty} |f'(t)|^2 dt \right)^{\frac{1}{2}} \tag{B.53}$$

The last line above is justified by the Cauchy-Schwarz inequality $\langle u, v \rangle \leq \|u\| \|v\|$. The first factor of (B.53) is just what we are seeking since it is σ_t . To understand the second factor, we apply Plancherel's Theorem so that it becomes the L^2 norm of the Fourier transform of $f'(\nu)$, which by equation (B.12) is $2\pi i \nu \hat{f}(\nu)$, thus

$$1 \leq 2 \left(\int_{-\infty}^{\infty} |t f(t)|^2 dt \right)^{\frac{1}{2}} \left(\int_{-\infty}^{\infty} |f'(t)|^2 dt \right)^{\frac{1}{2}} \tag{B.54}$$

$$1 \leq 4\pi \left(\int_{-\infty}^{\infty} t^2 |f(t)|^2 dt \right)^{\frac{1}{2}} \left(\int_{-\infty}^{\infty} \nu^2 |\hat{f}(\nu)|^2 d\nu \right)^{\frac{1}{2}} \tag{B.55}$$

$$1 \leq 4\pi \sigma_t \sigma_\nu \tag{B.56}$$

$$\sigma_t \sigma_\nu \geq \frac{1}{4\pi} \quad q.e.d. \tag{B.57}$$

Appendix C

Important Procedures

C.1 Normalizing IDL's FFT to Python's Numpy FFT procedure

The reference site to normalize the *FFT* is documented from a site written by Alex Rudy.* The site may not exist in the future, see documentation on normalizing the FFT below:

C.1.1 FFT Normalization

Different FFT implementations often have different normalization parameters. Most FFTs will be defined such that a forward transform followed by an inverse transform will result in the same values. However, implementations tend to apply the normalization at different points. This document describes the normalizations applied by each FFT, and their implications for the Fourier transform reconstructor (FTR).

We can use the IDL FFT definition to clarify our FFT normalization. This document shows how to modify other FFT normalizations so that they match the IDL normalization, the canonical one used in this algorithm.

C.1.2 IDL Normalization

IDL defines the FFT (here) as

$$F(u) = \frac{1}{N} \sum_{x=0}^{N-1} f(x) \exp \left[-j \frac{2\pi ux}{N} \right] \quad (\text{C.1})$$

*Site link: <http://ftr.readthedocs.io/en/latest/FTR/fftnormalization.html#idl-normalization>

and the inverse FFT as

$$f(x) = \sum_{u=0}^{N-1} F(u) \exp \left[j \frac{2\pi ux}{N} \right] \quad (\text{C.2})$$

The important part of this definition for our purposes is the factor of $\frac{1}{N}$ which is applied to the forward transform. When we apply the spatial filters used in the Fourier transform reconstructor, we apply two forward transforms (one for x , one for y), and one backwards transform. Collecting only the factors of $\frac{1}{N}$, we get two factors due to the two forward transforms which are added together. No factor is included in the inverse transform. The normalization factor for the full FTR filter is $\frac{2}{N}$.

C.1.3 Numpy Normalization

Python's **numpy** defines the forward FFT as[†]

$$A_k = \sum_{m=0}^{n-1} a_m \exp \left\{ -2\pi i \frac{mk}{n} \right\} \quad k = 0, \dots, n-1. \quad (\text{C.3})$$

and the inverse FFT as

$$a_m = \frac{1}{n} \sum_{k=0}^{n-1} A_k \exp \left\{ -2\pi i \frac{mk}{n} \right\} \quad m = 0, \dots, n-1. \quad (\text{C.4})$$

Comparing this definition to the one used by IDL, we can see that the normalization is applied as a $\frac{1}{n}$ factor in the inverse transform. Comparing to the IDL implementation, when we apply the two forward transforms, then add them, and apply a single reverse transform, we find that the total normalization is $\frac{1}{n}$. Therefore, we should multiply the Fourier transform of the phase estimate by 2 to match the normalization used by IDL.

[†]see link <https://docs.scipy.org/doc/numpy/reference/routines.fft.html#implementation-details>

BIBLIOGRAPHY

- Alexandrov, A. (2008). Two Dimensional Standing Wave - code done in Matlab. https://commons.wikimedia.org/wiki/File:Two_dim_standing_wave.gif. Online; accessed 25 November 2016.
- Ambastha, A., Basu, S., and Antia, H. M. (2002). Effect of flares on solar oscillations characteristics. In Wilson, A., editor, *From Solar Min to Max: Half a Solar Cycle with SOHO*, volume 508 of *ESA Special Publication*, pages 43–46.
- Ambastha, A., Basu, S., and Antia, H. M. (2003a). Effects of flares on solar oscillation characteristics. In Sawaya-Lacoste, H., editor, *GONG+ 2002. Local and Global Helioseismology: the Present and Future*, volume 517 of *ESA Special Publication*, pages 219–222.
- Ambastha, A., Basu, S., and Antia, H. M. (2003b). Excitation of Solar p-mode Oscillations by Flares. *Bulletin of the Astronomical Society of India*, 31:319–320.
- Antia, H. M., Bhatnagar, A., and Ulmschneider, P., editors (2003). *Lectures on Solar Physics*, volume 619 of *Lecture Notes in Physics*, Berlin Springer Verlag.
- Appourchaux, T., Belkacem, K., Broomhall, A.-M., Chaplin, W. J., Gough, D. O., Houdek, G., Provost, J., Baudin, F., Boumier, P., Elsworth, Y., García, R. A., Andersen, B. N., Finsterle, W., Fröhlich, C., Gabriel, A., Grec, G., Jiménez, A., Kosovichev, A., Sekii, T., Toutain, T., and Turck-Chièze, S. (2010). The quest for the solar g modes. *Astron. Astrophys. Rev.*, 18:197–277.
- Archontis, V. (2008). Magnetic flux emergence in the Sun. *Journal of Geophysical Research (Space Physics)*, 113:A03S04.
- Azima DLI (2009). The Hanning Window. <http://www.azimadli.com/vibman/thehanningwindow.htm>. Online; accessed 18 August 2018.
- Balmforth, N. J. and Gough, D. O. (1990). Effluent stellar pulsation. *Astrophys. J.*, 362:256–266.
- Basu, S., Antia, H. M., and Bogart, R. S. (2004). Ring-Diagram Analysis of the Structure of Solar Active Regions. *Astrophys. J.*, 610:1157–1168.
- Bogdan, T. J. and Judge, P. G. (2006). Observational aspects of sunspot oscillations. *Philosophical Transactions of the Royal Society of London Series A*, 364:313–331.
- Braun, D. C., Duvall, Jr., T. L., and Labonte, B. J. (1987). Acoustic absorption by sunspots. *Astrophys. J. Lett.*, 319:L27–L31.
- Braun, D. C. and Lindsey, C. (2001). Seismic Imaging of the Far Hemisphere of the Sun. *Astrophys. J. Lett.*, 560:L189–L192.

- Braun, D. C., Lindsey, C., Fan, Y., and Fagan, M. (1998). Seismic Holography of Solar Activity. *Astrophys. J.*, 502:968–980.
- Brigham, O. E. (1974). *The Fast Fourier Transform*. Prentice-Hall, Inc.
- Brillinger, D. R. (2002). John w. tukey’s work on time series and spectrum analysis. *Ann. Statist.*, 30(6):1595–1618.
- Chakraborty, S., Rabello-Soares, M. C., Bogart, R. S., and Bai, T. (2011). Investigating the correlation between high-frequency global oscillations and solar flares. *Journal of Physics Conference Series*, 271(1):012048.
- Chen, H.-R., Chou, D.-Y., Chang, H.-K., Sun, M.-T., Yeh, S.-J., LaBonte, B., and Team, t. T. (1998). Probing the Subsurface Structure of Active Regions with the Phase Information in Acoustic Imaging. *Astrophys. J. Lett.*, 501:L139–L144.
- Chou, D.-Y., Liang, Z.-C., Yang, M.-H., Zhao, H., and Sun, M.-T. (2009a). Measurements of Absorption, Emissivity Reduction, and Local Suppression of Solar Acoustic Waves in Sunspots. *Astrophys. J. Lett.*, 696:L106–L109.
- Chou, D.-Y., Sun, M.-T., Huang, T.-Y., Lai, S.-P., Chi, P.-J., Ou, K.-T., Wang, C.-C., Lu, J.-Y., Chu, A.-L., Niu, C.-S., Mu, T.-M., Chen, K.-R., Chou, Y.-P., Jimenez, A., Rabello-Soares, M. C., Chao, H., Ai, G., Wang, G.-P., Zirin, H., Marquette, W., and Nenow, J. (1995). Taiwan Oscillation Network. *Solar Phys.*, 160:237–243.
- Chou, D.-Y., Yang, M.-H., Zhao, H., Liang, Z.-C., and Sun, M.-T. (2009b). Spatial Distributions of Absorption, Local Suppression, and Emissivity Reduction of Solar Acoustic Waves in Magnetic Regions. *Astrophys. J.*, 706:909–916.
- Christensen-Dalsgaard, J. (2002). Helioseismology. *Reviews of Modern Physics*, 74:1073–1129.
- Christensen-Dalsgaard, J. (2003). Lecture notes on Stellar Oscillations (Fifth Edition). <http://astro.phys.au.dk/~jcd/oscilnotes/>. Online; accessed 5 December 2016.
- Christensen-Dalsgaard, J., Duvall, Jr., T. L., Gough, D. O., Harvey, J. W., and Rhodes, Jr., E. J. (1985). Speed of sound in the solar interior. *Nature*, 315:378–382.
- Claverie, A., Isaak, G. R., McLeod, C. P., van der Raay, H. B., and Cortes, T. R. (1979). Solar structure from global studies of the 5-minute oscillation. *Nature*, 282:591–594.
- De Pontieu, B., Title, A. M., Lemen, J. R., Kushner, G. D., Akin, D. J., Allard, B., Berger, T., Boerner, P., Cheung, M., Chou, C., Drake, J. F., Duncan, D. W., Freeland, S., Heyman, G. F., Hoffman, C., Hurlburt, N. E., Lindgren, R. W., Mathur, D., Rehse, R., Sabolish, D., Seguin, R., Schrijver, C. J., Tarbell, T. D., Wülser, J.-P., Wolfson, C. J., Yanari, C., Mudge, J., Nguyen-Phuc, N., Timmons, R., van Bezooijen, R., Weingrod, I., Brookner, R., Butcher, G., Dougherty, B., Eder, J., Knagenhjelm, V., Larsen, S., Mansir, D., Phan, L., Boyle, P., Cheimets, P. N., DeLuca, E. E., Golub, L., Gates, R., Hertz, E., McKillop, S., Park, S., Perry, T., Podgorski, W. A., Reeves, K., Saar, S., Testa, P.,

- Tian, H., Weber, M., Dunn, C., Eccles, S., Jaeggli, S. A., Kankelborg, C. C., Mashburn, K., Pust, N., Springer, L., Carvalho, R., Kleint, L., Marmie, J., Mazmanian, E., Pereira, T. M. D., Sawyer, S., Strong, J., Worden, S. P., Carlsson, M., Hansteen, V. H., Leenaarts, J., Wiesmann, M., Aloise, J., Chu, K.-C., Bush, R. I., Scherrer, P. H., Brekke, P., Martinez-Sykora, J., Lites, B. W., McIntosh, S. W., Uitenbroek, H., Okamoto, T. J., Gummin, M. A., Auker, G., Jerram, P., Pool, P., and Waltham, N. (2014). The Interface Region Imaging Spectrograph (IRIS). *Solar Phys.*, 289:2733–2779.
- Deubner, F.-L. (1975). Observations of low wavenumber nonradial eigenmodes of the sun. *Astron. Astrophys.*, 44:371–375.
- Donea, A.-C., Braun, D. C., and Lindsey, C. (1999). Seismic Images of a Solar Flare. *Astrophys. J. Lett.*, 513:L143–L146.
- Duvall, Jr., T. L., Dziembowski, W. A., Goode, P. R., Gough, D. O., Harvey, J. W., and Leibacher, J. W. (1984). Internal rotation of the sun. *Nature*, 310:22–25.
- Duvall, Jr., T. L. and Gizon, L. (2000). Time-Distance Helioseismology with f Modes as a Method for Measurement of Near-Surface Flows. *Solar Phys.*, 192:177–191.
- Duvall, Jr., T. L. and Harvey, J. W. (1983). Observations of solar oscillations of low and intermediate degree. *Nature*, 302:24–27.
- Duvall, Jr., T. L., Jefferies, S. M., Harvey, J. W., and Pomerantz, M. A. (1993). Time-distance helioseismology. *Nature*, 362:430–432.
- Elliott, I. (1969). Power Spectra of H α Doppler Shifts. *Solar Phys.*, 6:28–40.
- Evans, J. W. and Michard, R. (1962). Observational Study of Macroscopic Inhomogeneities in the Solar Atmosphere. III. Vertical Oscillatory Motions in the Solar Photosphere. *Astrophys. J.*, 136:493.
- Fossat, E., Boumier, P., Corbard, T., Provost, J., Salabert, D., Schmider, F. X., Gabriel, A. H., Grec, G., Renaud, C., Robillot, J. M., Roca-Cortés, T., Turck-Chièze, S., Ulrich, R. K., and Lazrek, M. (2017). Asymptotic g modes: Evidence for a rapid rotation of the solar core. *Astron. Astrophys.*, 604:A40.
- Frazier, E. N. (1968). A Spatio-Temporal Analysis of Velocity Fields in the Solar Photosphere. *Z. Astrophys.*, 68:345.
- García, R. A., Turck-Chièze, S., Jiménez-Reyes, S. J., Ballot, J., Pallé, P. L., Eff-Darwich, A., Mathur, S., and Provost, J. (2007). Tracking Solar Gravity Modes: The Dynamics of the Solar Core. *Science*, 316:1591.
- Gizon, L. and Birch, A. C. (2005). Local Helioseismology. *Living Reviews in Solar Physics*, 2:6.
- Gonzalez Hernandez, I., Patron, J., Chou, D.-Y., and TON Team (1998). On the Reliability of Ring Diagram Analysis. *Astrophys. J.*, 501:408.

- Gough, D. O. (1982). A Review of the Theory of Solar Oscillations and its Implications Concerning the Internal Structure of the Sun. In Cox, J. P. and Hansen, C. J., editors, *Pulsations in Classical and Cataclysmic Variable Stars*, page 117.
- Gough, D. O. and Toomre, J. (1983). On the detection of subphotospheric convective velocities and temperature fluctuations. *Solar Phys.*, 82:401–410.
- Gross, H. I. (1971). Lecture notes in Calculus Revisited - Conformal Mapping. <https://archive.org/details/CalculusRevisitedPart3-ConformalMapping>. Faculty of Center for Advanced Engineering Study at Massachusetts Institute of Technology. Online; accessed 10 April 2017.
- Gumley, L. (2001). *Practical IDL Programming*. Elsevier Science.
- Gurman, J. B., Leibacher, J. W., Shine, R. A., Woodgate, B. E., and Henze, W. (1982). Transition region oscillations in sunspots. *Astrophys. J.*, 253:939–948.
- Harris Geospatial Solutions (2017). IDL. <https://www.harrisgeospatial.com/docs/fft.html>.
- Hart, A. B. (1954). Motions in the Sun at the photospheric level. IV. The equatorial rotation and possible velocity fields in the photosphere. *Mon. Not. Roy. Astron. Soc.*, 114:17.
- Hart, A. B. (1956). Motions in the Sun at the photospheric level. VI. Large-scale motions in the equatorial region. *Mon. Not. Roy. Astron. Soc.*, 116:38.
- Harvey, J. W., Duvall, Jr., T. L., Jefferies, S. M., and Pomerantz, M. A. (1993). Chromospheric Oscillations and the Background Spectrum. In Brown, T. M., editor, *GONG 1992. Seismic Investigation of the Sun and Stars*, volume 42 of *Astronomical Society of the Pacific Conference Series*, page 111.
- Heggland, L., Hansteen, V. H., De Pontieu, B., and Carlsson, M. (2011). Wave Propagation and Jet Formation in the Chromosphere. *Astrophys. J.*, 743:142.
- Heiles, C. (2005). Discreetly fine times with discrete fourier transforms (DFT's with DFT's) or “why does that FFT output look so weird??”. <http://ugastro.berkeley.edu/radio/2016/handout.links/fourierc.pdf>. Online; accessed 5 December 2016.
- Hill, F. (1988). Rings and trumpets - Three-dimensional power spectra of solar oscillations. *Astrophys. J.*, 333:996–1013.
- Hill, F. (2008). Helioseismology and the solar cycle: Past, present and future. *Journal of Astrophysics and Astronomy*, 29:75–84.
- Hindman, B. W. and Brown, T. M. (1998). Acoustic Power Maps of Solar Active Regions. *Astrophys. J.*, 504:1029–1034.
- Hindman, B. W. and Jain, R. (2008). The Generation of Coronal Loop Waves below the Photosphere by p-Mode Forcing. *Astrophys. J.*, 677:769–780.

- Houck, J. (2015). An introduction to exposure maps. http://cxc.harvard.edu/ciao/download/doc/expmap_intro.ps. Accessed: 2018-07-08.
- Howe, R., Jain, K., Bogart, R. S., Haber, D. A., and Baldner, C. S. (2012). Two-Dimensional Helioseismic Power, Phase, and Coherence Spectra of Solar Dynamics Observatory Photospheric and Chromospheric Observables. *Solar Phys.*, 281:533–549.
- Jackiewicz, J. and Balasubramaniam, K. S. (2013). Solar H α Oscillations from Intensity and Doppler Observations. *Astrophys. J.*, 765:15.
- Jain, R., Gascoyne, A., and Hindman, B. W. (2011). Interaction of p modes with a collection of thin magnetic tubes. *Mon. Not. Roy. Astron. Soc.*, 415:1276–1279.
- Jain, R., Gascoyne, A., Hindman, B. W., and Greer, B. (2014). Five-minute Oscillation Power within Magnetic Elements in the Solar Atmosphere. *Astrophys. J.*, 796:72.
- Jain, R., Tripathy, S., Bharti, L., and Kumar, B. (1999). H α Intensity Oscillations in Solar Flares. In Rimmele, T. R., Balasubramaniam, K. S., and Radick, R. R., editors, *High Resolution Solar Physics: Theory, Observations, and Techniques*, volume 183 of *Astronomical Society of the Pacific Conference Series*, page 531.
- Jain, R. and Tripathy, S. C. (1998). Detection of H α Intensity Oscillations in Solar Flares. *Solar Phys.*, 181:113–120.
- Jensen, J. M. (2003). Time-distance: what does it tell us? In Sawaya-Lacoste, H., editor, *GONG+ 2002. Local and Global Helioseismology: the Present and Future*, volume 517 of *ESA Special Publication*, pages 61–70.
- Kandhasamy, S. (2010). DFT, PSD and MATLAB. https://labcit.ligo.caltech.edu/~ethrane/Resources/signals/shivaraj_DFT.pdf. Online; accessed 5 May 2018.
- Karoff, C. and Kjeldsen, H. (2008). Evidence That Solar Flares Drive Global Oscillations in the Sun. *Astrophys. J. Lett.*, 678:L73–L76.
- Khomenko, E., Centeno, R., Collados, M., and Trujillo Bueno, J. (2008). Channeling 5 Minute Photospheric Oscillations into the Solar Outer Atmosphere through Small-Scale Vertical Magnetic Flux Tubes. *Astrophys. J. Lett.*, 676:L85–L88.
- Khomenko, E. and Collados, M. (2015). Oscillations and Waves in Sunspots. *Living Reviews in Solar Physics*, 12:6.
- Kneer, F. and von Uexkuell, M. (1983). Brightness oscillations of the sun’s chromosphere in K and H-alpha. *Astron. Astrophys.*, 119:124–130.
- Kneer, F. and von Uexkuell, M. (1985). Oscillations of the sun’s chromosphere. II - H-alpha line centre and wing filtergram time sequences. *Astron. Astrophys.*, 144:443–451.
- Komm, R. and Hill, F. (2009). Solar flares and solar subphotospheric vorticity. *Journal of Geophysical Research (Space Physics)*, 114:6105.

- Kosovichev, A. G. (2006). Properties of Flares-Generated Seismic Waves on the Sun. *Solar Phys.*, 238:1–11.
- Kosovichev, A. G. (2011). Advances in Global and Local Helioseismology: An Introductory Review. In Rozelot, J.-P. and Neiner, C., editors, *The Pulsations of the Sun and the Stars, Lecture Notes in Physics, Berlin Springer Verlag*, volume 832 of *Lecture Notes in Physics, Berlin Springer Verlag*, page 3.
- Kosovichev, A. G. and Zharkova, V. V. (1998). X-ray flare sparks quake inside Sun. *Nature*, 393:317–318.
- Krishna Prasad, S., Jess, D. B., and Khomenko, E. (2015). On the Source of Propagating Slow Magnetoacoustic Waves in Sunspots. *Astrophys. J. Lett.*, 812:L15.
- Kumar, B., Mathur, S., García, R. A., and Venkatakrisnan, P. (2010). On the Flare Induced High-Frequency Global Waves in the Sun. *Astrophys. J. Lett.*, 711:L12–L18.
- Kumar, B. and Ravindra, B. (2006). Analysis of Enhanced Velocity Signals Observed during Solar Flares. *Journal of Astrophysics and Astronomy*, 27:425–438.
- Kumar, B., Venkatakrisnan, P., Mathur, S., Tiwari, S. K., and García, R. A. (2011). On the Flare-induced Seismicity in the Active Region NOAA 10930 and Related Enhancement of Global Waves in the Sun. *Astrophys. J.*, 743:29.
- Kumar, B., Venkatakrisnan, P., and Venugopalan, K. (2006). On the enhanced velocity oscillations observed during solar flares. In *Proceedings of SOHO 18/GONG 2006/HELAS I, Beyond the spherical Sun*, volume 624 of *ESA Special Publication*.
- Kumar, P. and Lu, E. (1991). The location of the source of high-frequency solar acoustic oscillations. *Astrophys. J. Lett.*, 375:L35–L39.
- Lara, A., Gopalswamy, N., and DeForest, C. (2000). Change in photospheric magnetic flux during coronal mass ejections. *Geophys. Res. Lett.*, 27:1435–1438.
- Leibacher, J. W. (1999). The global oscillation network group (GONG) project. *Advances in Space Research*, 24:173–176.
- Leibacher, J. W. and Stein, R. F. (1971). A New Description of the Solar Five-Minute Oscillation. *The Astrophysical Journal, Letters*, 7:191–192.
- Leighton, R. B., Noyes, R. W., and Simon, G. W. (1962a). Velocity Fields in the Solar Atmosphere. I. Preliminary Report. *Astrophys. J.*, 135:474.
- Leighton, R. B., Noyes, R. W., and Simon, G. W. (1962b). Velocity Fields in the Solar Atmosphere. I. Preliminary Report. *Astrophys. J.*, 135:474.
- Lindsey, C. and Braun, D. C. (1990). Helioseismic imaging of sunspots at their antipodes. *Solar Phys.*, 126:101–115.

- Lindsey, C. and Braun, D. C. (1998). Acoustic Signatures of Subphotospheric Structure Underlying Sunspots. *Astrophys. J. Lett.*, 509:L129–L132.
- Lindsey, C. and Braun, D. C. (2000a). Basic Principles of Solar Acoustic Holography - (Invited Review). *Solar Phys.*, 192:261–284.
- Lindsey, C. and Braun, D. C. (2000b). Seismic Images of the Far Side of the Sun. *Science*, 287:1799–1801.
- LMSAL-AIA (2010). Atmospheric Imaging Assembly. <http://aia.lmsal.com/public/instrument.htm>. Accessed: 08-August-2018.
- Löhner-Böttcher, J. and Bello González, N. (2015). Signatures of running penumbral waves in sunspot photospheres. *Astron. Astrophys.*, 580:A53.
- Martínez González, M. J., Asensio Ramos, A., Manso Sainz, R., Khomenko, E., Martínez Pillet, V., Solanki, S. K., López Ariste, A., Schmidt, W., Barthol, P., and Gandorfer, A. (2011). Unnoticed Magnetic Field Oscillations in the Very Quiet Sun Revealed by SUNRISE/IMaX. *Astrophys. J. Lett.*, 730:L37.
- Marven, C. and Ewers, G. (1996). *A Simple Approach to Digital Signal Processing*. John Wiley & Sons, Inc.
- Mason, D., Komm, R., Hill, F., Howe, R., Haber, D., and Hindman, B. W. (2006). Flares, Magnetic Fields, and Subsurface Vorticity: A Survey of GONG and MDI Data. *Astrophys. J.*, 645:1543–1553.
- McClellan, J. H., Schafer, R. W., and Yoder, M. A. (2003). *Signal processing first*. Pearson/Prentice Hall.
- McIntosh, S. W. and Jefferies, S. M. (2006). Observing the Modification of the Acoustic Cutoff Frequency by Field Inclination Angle. *Astrophys. J. Lett.*, 647:L77–L81.
- Merryfield, K. G. (2009). Lecture notes in Fourier Analysis. <http://web.csulb.edu/~kmerry/>. Faculty of Mathematics at California State University, Long Beach. Online; accessed 5 August 2018.
- Monsue, T., Hill, F., and Stassun, K. G. (2016). Temporal Evolution of Chromospheric Oscillations in Flaring Regions: A Pilot Study. *Astron. J.*, 152:81.
- Morin, D. (2009). Harvard Lecture Notes on Physics. <http://www.people.fas.harvard.edu/~7Edjmorin/book.html>. Online; accessed 5 December 2016.
- National Instruments (2016). Understanding FFTs and Windowing. <http://www.ni.com/white-paper/4844/en/>. Online; accessed 5 December 2017.
- National Solar Observatory (2010). GONG and Helioseismology. <http://gong.nso.edu/info/helioseismology.html>.

- Pekeris, C. L. (1939). The Propagation of a Pulse in the Atmosphere. *Proceedings of the Royal Society of London Series A*, 171:434–449.
- Pesnell, W. D., Thompson, B. J., and Chamberlin, P. C. (2012). The Solar Dynamics Observatory (SDO). *Solar Phys.*, 275:3–15.
- Plaskett, H. H. (1916). A Variation in the Solar Rotation. *Astrophys. J.*, 43:145.
- Priemer, R. (1991). *Introductory Signal Processing*, volume 6 of *Advanced Series in Electrical and Computer Engineering*. World Scientific, 1 edition.
- Rajaguru, S. P., Couvidat, S., Sun, X., Hayashi, K., and Schunker, H. (2013). Properties of High-Frequency Wave Power Halos Around Active Regions: An Analysis of Multi-height Data from HMI and AIA Onboard SDO. *Solar Phys.*, 287:107–127.
- Rempel, M. and Schlichenmaier, R. (2011). Sunspot Modeling: From Simplified Models to Radiative MHD Simulations. *Living Reviews in Solar Physics*, 8:3.
- Richardson, M., Hill, F., and Stassun, K. G. (2012). No Evidence Supporting Flare-Driven High-Frequency Global Oscillations. *Solar Phys.*, 281:21–35.
- Robinson, E. and Silvia, M. (1978). *Digital Signal Processing and Time Series Analysis*, volume 53 of *Lecture Notes in Earth Sciences*. Holden-Day, Inc., 1 edition.
- Scherbaum, F. (1994). *Basic Concepts in Digital Signal Processing for Seismologists*, volume 53 of *Lecture Notes in Earth Sciences*. Springer-Verlag Berlin Heidelberg, 1 edition.
- Scherrer, P. H., Bogart, R. S., Bush, R. I., Hoeksema, J. T., Kosovichev, A. G., Schou, J., Rosenberg, W., Springer, L., Tarbell, T. D., Title, A., Wolfson, C. J., Zayer, I., and MDI Engineering Team (1995). The Solar Oscillations Investigation - Michelson Doppler Imager. *Solar Phys.*, 162:129–188.
- Scherrer, P. H., Schou, J., Bush, R. I., Kosovichev, A. G., Bogart, R. S., Hoeksema, J. T., Liu, Y., Duvall, T. L., Zhao, J., Title, A. M., Schrijver, C. J., Tarbell, T. D., and Tomczyk, S. (2012). The Helioseismic and Magnetic Imager (HMI) Investigation for the Solar Dynamics Observatory (SDO). *Solar Phys.*, 275:207–227.
- Shibata, K., Tajima, T., Steinolfson, R. S., and Matsumoto, R. (1989). Two-dimensional magnetohydrodynamic model of emerging magnetic flux in the solar atmosphere. *Astrophys. J.*, 345:584–596.
- Siemens PLM Software Inc (2017). Window Types: Hanning, Flattop, Uniform, Tukey, and Exponential and Window Correction Factors. <https://community.plm.automation.siemens.com/>. Online; accessed 20 August 2018.
- Ulrich, R. K. (1970). The Five-Minute Oscillations on the Solar Surface. *Astrophys. J.*, 162:993.

- Vakman, D. (1998). *Signals, Oscillations, and Waves - A Modern Approach*. Artech House.
- Vandakurov, Y. V. (1968). The Frequency Distribution of Stellar Oscillations. *Soviet Astron.*, 11:630.
- Wang, H., Qiu, J., Denker, C., Spirock, T., Chen, H., and Goode, P. R. (2000). High-Cadence Observations of an Impulsive Flare. *Astrophys. J.*, 542:1080–1087.
- Wang, R. (2015). Heisenberg uncertainty principle. <http://fourier.eng.hmc.edu/e161/lectures/fourier/node2.html>. Accessed: 2018-08-18.
- Wilhelm, K., Lemaire, P., Curdt, W., Schuhle, U., Marsch, E., Poland, A. I., Jordan, S. D., Thomas, R. J., Hassler, D. M., Huber, M. C. E., Vial, J.-C., Kuhne, M., Siegmund, O. H. W., Gabriel, A., Timothy, J. G., Grewing, M., Feldman, U., Hollandt, J., and Brekke, P. (1997). First Results of the SUMER Telescope and Spectrometer on SOHO - I. Spectra and Spectroradiometry. *Solar Phys.*, 170:75–104.
- Wolff, C. L. (1972). Free Oscillations of the Sun and Their Possible Stimulation by Solar Flares. *Astrophys. J.*, 176:833.
- Woodard, M. F. (2002). Solar Subsurface Flow Inferred Directly from Frequency-Wavenumber Correlations in the Seismic Velocity Field. *Astrophys. J.*, 565:634–639.
- Zhao, J., Chen, R., Hartlep, T., and Kosovichev, A. G. (2015). Detection of Fast-moving Waves Propagating Outward along Sunspots' Radial Direction in the Photosphere. *Astrophys. J. Lett.*, 809:L15.
- Zhao, J., Felipe, T., Chen, R., and Khomenko, E. (2016). Tracing p-mode Waves from the Photosphere to the Corona in Active Regions. *Astrophys. J. Lett.*, 830:L17.
- Zhao, J., Kosovichev, A. G., and Sekii, T. (2010). High-Resolution Helioseismic Imaging of Subsurface Structures and Flows of a Solar Active Region Observed by Hinode. *Astrophys. J.*, 708:304–313.